



TECHNISCHE UNIVERSITÄT MÜNCHEN  
Max-Planck-Institut für extraterrestrische Physik

## **Gamma-ray burst host galaxies in absorption**

Philip Wiseman

Vollständiger Abdruck der von der Fakultät für Physik der Technischen Universität München zur Erlangung des akademischen Grades eines

**Doktors der Naturwissenschaften (Dr. rer. nat.)**

genehmigten Dissertation.

Vorsitzender: Prof. Dr. Björn Garbrecht  
Prüfer der Dissertation: 1. Priv.-Doz. Dr. Jochen Greiner  
2. Prof. Dr. Stefan Schönert

Die Dissertation wurde am 14.09.2017 bei der Technischen Universität München eingereicht und durch die Fakultät für Physik am 25.10.2017 angenommen.



# *Abstract*

Gamma-ray bursts (GRBs) are bright flashes of high-energy radiation, that for their duration from a fraction of a second to several minutes are among the most luminous sources in the Universe. For the long-duration variant of GRBs, the prompt radiation is thought to be produced as the collapse of a massive, rapidly rotating star into a black hole or neutron star. From the accretion disk around this compact object is launched a highly relativistic jet of electrons, inside which are shells of differing Lorentz factors. It is thought that shocks occur as the shells collide with one another, producing a high-energy non-thermal prompt spectrum. As the jet reaches the circumstellar medium, further, external shocks are created, the non-thermal electron population then cooling via the radiation of synchrotron radiation from the X-ray to the radio regimes, known as the afterglow. With satellites such as *Swift*, GRB afterglows are located to a few arc-seconds precision within minutes of the burst, allowing extensive follow up from ground-based instruments.

The link between GRBs and massive stars means that they necessarily explode in star-forming regions of their host galaxies. Combined with their extreme luminosity, the massive-star association allows GRBs to be used to probe the conditions and characteristics of star-forming galaxies into the distant Universe. One of the principle methods to conduct such research is by measuring the effect on the afterglow light caused by material in the host galaxy that is aligned with the line of sight to the GRB. The two main effects of intervening material are an overall reddening of the ultra-violet and optical spectral energy distribution caused by dust, and spectral absorption lines caused by atoms and ions in the gas phase. This thesis uses both reddening and line absorption extensively in an attempt to characterise the interstellar medium (ISM) of GRB hosts. A brief introduction to GRBs and the characteristics seen in absorption is given in Chapter 1.

The predominant method used in this thesis to extract information about GRB host galaxies is absorption line spectroscopy, which is described in detail in Chapter 2. At redshifts greater than 1.6, most ionic transitions of singly and of triply-ionised metals, as well as the dominant Lyman- $\alpha$  line of neutral hydrogen, are shifted into the optical window visible from Earth, and as such can be observed by large ground-based facilities such as the Very Large Telescope, and its workhorse spectrograph X-shooter. By fitting the absorption lines with Voigt profiles, it is possible to accurately measure the column density of the absorbing gas and its constituent parts. With that information, relative abundances between different species can be measured in order to calculate the relative metal content (metallicity), dust depletion, and ionisation of the absorber.

In Chapter 3 I present a study of the dust characteristics of 19 GRB host galaxies as measured through both reddening and dust depletion. In order to negate ionisation effects, only damped Lyman-alpha absorbers (DLAs;  $N_{\text{H I}} > 10^{20.3} \text{ cm}^{-2}$ ) are included. By using a minimum of four elements as well as the latest dust-depletion sequences, the most comprehensive sample yet of GRB-DLA dust-depletion strengths, dust-corrected metallicities, and dust-to-metals ratios (DTMs) is computed. It is shown that DTM is correlated with metallicity, suggesting that the majority of the dust has been produced by the growth of grains in the ISM, rather than instantaneously with the metals in evolved stellar winds and supernova ejecta. Furthermore, the relationship between dust measured through depletion and reddening is investigated, and it is

found that the two fail to trace each other well.

The spectrum of one particular burst, GRB 080810, is investigated in detail in Chapter 4. The bright afterglow facilitated observations with the high-resolution HIRES spectrograph of the 10 m Keck telescope, providing one of the richest GRB afterglow spectra ever obtained. The analysis focuses on the four distinct absorbing systems at the host redshift of 3.35, all of which have lower-than-average neutral gas column densities, the largest being measured at  $N_{\text{H I}} < 10^{18.35} \text{ cm}^{-2}$ . Using the chemical, kinematic and ionisation characteristics measured from the absorption lines as well as morphological constraints obtained from imaging, inferences are made regarding the physical nature of the four systems. Identified is the excited gas nearby to the GRB explosion itself, as well as a galactic outflow located in a similar region of the host but moving at nearly  $200 \text{ km s}^{-1}$  in the direction of the observer. Also detected is the hot, strongly ionised halo of a foreground galaxy that is approaching the host at  $700 \text{ km s}^{-1}$ , and may already be interacting with it. Finally, a very metal-poor system is found that may be in the process of accreting onto the interacting system, providing some of the first evidence of such near-pristine gas flow onto a star-forming galaxy.

In Chapter 5, the results from the two main studies are discussed further, and in Chapter 6 the prospects for future research of GRB hosts and similar topics with upcoming facilities are outlined.

# Zusammenfassung

Für einen sehr kurzen Zeitraum sind Gammastrahlen-Blitze (engl: GRBs) die hellsten Lichtquellen des Universums. Die in  $\sim 100$  s freigesetzte Energie entspricht dem Energieumsatz der Sonne in ihrer ganzen Lebensdauer. Bei langen Blitzen, die länger als zwei Sekunden dauern, entsteht die prompte Emission durch den Kollaps eines massereichen, schnell rotierenden Sterns in ein schwarzes Loch oder einen Neutronenstern. Aufgrund der Magnetfelder in der Akkretionsscheibe bricht ein relativistischer Jet aus, der sogenannte Feuerball, der aus vielen Schalen mit unterschiedlichen Lorentzfaktoren besteht. Die Schalen kollidieren und es entstehen Schocks, wobei ein nicht-thermisches Spektrum ausgesendet wird. Wenn der Jet das Interstellare Medium (ISM) erreicht, kollidiert er mit der ihn umgebenden Materie wodurch weitere Schocks erzeugt werden. Die beschleunigten Elektronen kühlen durch Synchrotronstrahlung ab und erzeugen dadurch das charakteristische Nachleuchten, welches vom Radio- bis Röntgenbereich beobachtbar ist. Mit heutigen Satelliten wie *Swift* ist es möglich, dieses Nachleuchten mit einer Präzision von Bogensekunden zu lokalisieren, was die weitere Untersuchung mit bodengebundenen Teleskopen erlaubt.

Die Herkunft der GRBs aus massereichen Sternen bedeutet zwangsläufig, dass GRBs in den aktiven Sternentstehungsgebieten ihrer Muttergalaxien explodieren müssen. Zusammen mit ihrer extremen Helligkeit erlaubt es diese Tatsache, GRBs als Sonden zur Erforschung der Charakteristiken von Sternentstehungs-Galaxien des jungen, weit entfernten Universums zu verwenden. Eine der gängigen Methoden dabei ist es, die Auswirkungen von Material wie Gas und Staub in der Herkunftsgalaxie zu messen, welches sich in der Sichtlinie zwischen dem Burst und der Erde befindet. Dabei zeigen sich hauptsächlich zwei beobachtbare Effekte: zum einen verursacht der Staub eine allgemeine Rötung der ultravioletten und optischen spektralen Energieverteilung des Nachglühens und zum anderen erzeugen Atome und Ionen der Gasphase prominente Absorptionslinien. In dieser Arbeit verwenden wir beide Methoden, um das Interstellare Medium in den Herkunftsgalaxien von GRBs zu charakterisieren. Eine kurze Einführung in GRBs und Informationen, die aus Absorptionslinien abgeleitet werden können, finden sich in Kapitel 1.

In Kapitel 2 wird die Absorptionslinien-Spektroskopie detailliert beschrieben. Sie ist eine der hauptsächlich verwendeten Methoden dieser Arbeit, die es ermöglicht, Informationen über GRB-Herkunftsgalaxien zu ermitteln. Bei Rotverschiebungen größer als 1.6, sind die meisten ionischen Übergänge von einfach- und dreifach-ionisierten Metallen ebenso wie die markante Lyman-alpha Linie von neutralem Wasserstoff in den optischen Bereich des Spektrums verschoben. Dieser kann von der Erde aus mit großen bodengebundenen Einrichtungen wie dem Very Large Telescope und seinem Spektrographen X-Shooter beobachtet werden. Durch das Modellieren der Absorptionslinien mit Voigt-Profilen lässt sich die Säulendichte des absorbierenden Gases und seiner Bestandteile messen. Mit dieser Information ist es möglich, das relative Vorkommen unterschiedlicher Elemente zu bestimmen, woraus sich Rückschlüsse auf die Metallizität, die Staub-Verarmung und die Ionisation des absorbierenden Mediums ziehen lassen.

Im Kapitel 3 wird eine Studie der Staub-Eigenschaften von 19 GRB-Muttergalaxien präsentiert, die sowohl durch Rötung als auch Staub-Verarmung gemessen wurden. Um Ionisationseffekte zu vermeiden, werden nur Systeme einbezogen, die als gedämpfte Lyman-alpha Absorbierer identifiziert werden (engl: DLAs;  $N_{\text{H I}} > 10^{20.3} \text{ cm}^{-2}$ ). Die Verwendung von mindestens

vier Elementen sowie der neuesten Dust-Verarmungs-Sequenzen stellt sicher, dass wir hier die bisher umfassendste Stichprobe von Staubverarmungen sowie Staub-korrigierten Metallizitäten und Staub-zu-Metall-Verhältnissen (engl.: DTMs) in GRB-DLA-Systemen berechnen. Es zeigt sich, dass die DTMs mit der Metallizität korrelieren. Dies lässt vermuten, dass der größte Teil des Staubs durch das Wachstum von Staubkörnern im ISM und nicht in einem Sternenwind oder dem Auswurf einer Supernova Explosion produziert wird. Außerdem wird überprüft, ob die beiden Methoden der Verarmung und der Rötung zur Bestimmung des Staubs übereinstimmende Ergebnisse erbringen. Dies ist nicht der Fall.

Das Spektrum eines einzelnen Bursts, dem GRB 080810, wird in Kapitel 4 genau analysiert. Wegen der außergewöhnlichen Helligkeit des Nachglühens war es möglich, hoch-auflösende Spektren mit dem HIRES Spektrographen am 10m Keck Teleskop aufzunehmen. Diese Beobachtungen liefern eines der detailliertesten GRB Spektren, das jemals beobachtet werden konnte. Die Analyse des Spektrums konzentriert sich auf die vier unterschiedlichen Absorptionssysteme, die durch die Mutter-Galaxie bei einer Rotverschiebung von 3.35 erzeugt werden. Alle weisen eine unterdurchschnittliche Säulendichte von neutralem Gas auf: die größte der vier beträgt nur  $N_{\text{HI}} < 10^{18.35} \text{ cm}^{-2}$ . Durch Verwendung der chemischen, der kinematischen und der Ionisationseigenschaften, die in den Absorptionslinien bestimmt werden können sowie den morphologischen Einschränkungen, die aus den Aufnahmen bestimmt werden konnten, werden Rückschlüsse auf die physikalische Natur der vier Systeme gezogen. In der Nähe der GRB-Explosion kann angeregtes Gas identifiziert werden. Außerdem finden wir einen galaktischen Ausfluss in einer benachbarten Region, der sich mit ungefähr  $200 \text{ km s}^{-1}$  auf den Beobachter zubewegt. Ebenso wurde ein heißer, stark ionisierter Halo einer Vordergrund-Galaxie detektiert, die sich auf die Herkunftsgalaxie mit  $700 \text{ km s}^{-1}$  zubewegt und möglicherweise schon mit ihr interagiert. Schließlich wurde ein sehr metallarmes System gefunden, das sich möglicherweise gerade dabei befindet, auf ein anderes, interagierendes System zu akkretieren. Das ist einer der ersten Beweise für einen solchen Fluss von sehr reinem, ursprünglichen Gas auf eine sternbildende Galaxie.

Im Kapitel 5 werden die Ergebnisse der beiden Studien weiter diskutiert, und im Kapitel 6 werden mögliche Zukunftsperspektiven für eine Weiterführung der Forschungsarbeit angesprochen.

# Contents

<b>1</b>	<b>Gamma-ray bursts</b>	<b>1</b>
1.1	Introduction to gamma-ray bursts . . . . .	1
1.1.1	Long and short GRBs . . . . .	1
1.1.2	The GRB/SN connection . . . . .	2
1.1.3	GRB progenitors . . . . .	3
1.1.4	The <i>Swift</i> era . . . . .	3
1.1.5	The fireball model . . . . .	4
1.1.5.1	Prompt emission . . . . .	4
1.1.5.2	Afterglows . . . . .	5
1.1.6	GRBs as cosmic probes . . . . .	8
1.2	GRB host galaxies . . . . .	10
1.2.1	GRB host surveys . . . . .	11
1.2.2	Metallicity . . . . .	12
1.3	Afterglow attenuation . . . . .	13
1.3.1	Damped Lyman-alpha absorbers . . . . .	13
1.3.2	Dust . . . . .	15
1.3.2.1	Dust Depletion . . . . .	15
1.3.2.2	Dust-to-metals ratio . . . . .	16
1.3.2.3	Extinction . . . . .	18
<b>2</b>	<b>Absorption line spectroscopy</b>	<b>21</b>
2.1	Voigt profile fitting . . . . .	22
2.2	Accurately measuring abundances . . . . .	22
2.3	Velocity components and kinematics . . . . .	24
2.4	Ionisation . . . . .	24
2.5	Excitation . . . . .	26
<b>3</b>	<b>Evolution of the dust-to-metals ratio as traced by GRB-DLAs</b>	<b>27</b>
3.1	Introduction . . . . .	27
3.2	Dust depletion . . . . .	29
3.3	Sample and data reduction . . . . .	34
3.3.1	New GRB Spectra . . . . .	37
3.3.2	Hidden saturation . . . . .	38
3.4	Method . . . . .	39
3.4.1	Depletion model fitting . . . . .	39
3.4.1.1	Nucleosynthesis . . . . .	39
3.4.2	Dust-to-Metals Ratio . . . . .	41
3.5	Results . . . . .	42
3.5.1	Metallicity . . . . .	43
3.5.2	Dust-to-Metals ratio . . . . .	44
3.6	Discussion . . . . .	45
3.6.1	The Origin of Dust . . . . .	45

3.6.2	The $A_{V;SED}$ to $A_{V;DTM}$ discrepancy . . . . .	47
3.6.3	Accuracy of $A_{V;DTM}$ - depletion as a reliable tracer of dust . . . . .	47
3.6.4	Accuracy of $A_{V;SED}$ . . . . .	48
3.6.5	Equivalent dust column density . . . . .	49
3.7	Conclusion . . . . .	50
<b>4</b>	<b>Gas inflow and outflow in an interacting high-redshift galaxy: The remarkable host environment of GRB 080810 at <math>z = 3.35</math></b>	<b>55</b>
4.1	Introduction . . . . .	55
4.2	Observations and data reduction . . . . .	56
4.2.1	Keck/HIRES afterglow spectrum . . . . .	58
4.2.2	Late time imaging and spectral observations . . . . .	58
4.3	Analysis of the afterglow spectrum . . . . .	58
4.3.1	Defining the host complex at $z = 3.35$ . . . . .	58
4.3.1.1	HI column densities . . . . .	61
4.3.1.2	Metal column densities . . . . .	63
4.3.2	Intervening systems . . . . .	64
4.4	Results . . . . .	64
4.4.1	System A . . . . .	66
4.4.2	System B . . . . .	67
4.4.3	System C . . . . .	72
4.4.4	System D . . . . .	73
4.4.5	Imaging and emission spectrum . . . . .	73
4.5	Characterising the absorbing systems . . . . .	75
4.5.1	Systems B and C . . . . .	75
4.5.2	Lack of an Fe detection . . . . .	76
4.5.3	System A . . . . .	77
4.5.4	System D . . . . .	78
4.6	Discussion . . . . .	78
4.6.1	Conditions in the interacting galaxies . . . . .	78
4.6.2	GRBs and SNe in interacting systems . . . . .	80
4.6.3	Inflows and outflows . . . . .	80
4.7	Summary and conclusions . . . . .	81
<b>5</b>	<b>Discussion</b>	<b>83</b>
5.1	Dust Properties of GRB host galaxies . . . . .	83
5.1.1	Dust at high redshift . . . . .	84
5.1.1.1	Inaccuracy of $A_{V;DTM}$ . . . . .	84
5.1.1.2	Varying extinction law at high $z$ . . . . .	87
5.1.2	Future work on high- $z$ dust . . . . .	87
5.2	GRBs as probes of inflows . . . . .	88
5.3	Accuracy of absorption and emission line measurements . . . . .	90
5.3.1	Metallicity diagnostics from integral field units . . . . .	91
5.3.2	GRBs as metallicity calibrators . . . . .	91
<b>6</b>	<b>Outlook</b>	<b>93</b>
6.1	GRBs, SLSNe and FRBs in similar hosts - implications for the progenitors . . . . .	93
6.2	The next decade: entering the LSST/JWST/E-ELT era of explosive transients . . . . .	94

*Dedicated to Cousin Jack, who sparked my interest in physics all those  
years ago.*



# Chapter 1

## Gamma-ray bursts

### 1.1 Introduction to gamma-ray bursts

The story of gamma-ray bursts originates in the 1960s, as tensions between the USA and the Soviet Union were high. Nuclear tests in the atmosphere, underwater or in space were banned in 1963. The USA subsequently launched a series of gamma-ray detectors, known as the Vela satellites, in order to make sure the USSR did not contravene the ban with secret tests in space. In 1967, the satellites began picking up short outbreaks of radiation in the MeV energy range which appeared not to be anything like those expected from nuclear tests. When the arrival times of these bursts at multiple satellites were measured, directions for their origin could be determined, and it was discovered that the bursts were coming neither from the Earth nor the Sun — they were cosmic events (Klebesadel et al. 1973).

The following decades passed with the nature of gamma-ray bursts remaining relatively unclear. At the end of the 1970s the *KONUS* experiment hinted at an isotropic distribution of GRBs on the sky (Mazets et al. 1981). During the 1990s, the Burst And Transient Source Experiment (BATSE) instrument on board the Compton Gamma-Ray Observatory detected around 2700 bursts, the isotropic sky distribution of which (Fig. 1.1) proved strong evidence for an extragalactic origin for GRBs. Given the high fluxes recorded, this discovery placed GRBs as some of the most energetic events in the Universe.

The final confirmation of the cosmological origin of GRBs came in 1997 with the BeppoSAX satellite, which for the first time detected a fading X-ray afterglow consistent with the position of the long GRB 970228<sup>1</sup> (Costa et al. 1997). A fading, optical afterglow was also discovered, and deep late-time imaging revealed a faint galaxy at the same position (van Paradijs et al. 1997). Later that year, a spectrum of the optical afterglow of long GRB 970508 was taken, revealing the signature of absorbing material at a redshift of  $z = 0.835$ , suggesting that the GRB must have occurred at least that far away (Metzger et al. 1997).

#### 1.1.1 Long and short GRBs

Both the *KONUS* and *BATSE* samples showed a clear bimodality in the burst duration distribution<sup>2</sup>: there appeared to be two populations of bursts, one with a peak in the distribution at around 0.3 s, and the other at  $\sim 30$  s, with the threshold lying at 2 s (Mazets et al. 1981; Kouveliotou et al. 1993). These two populations were denoted short and long (S/L) GRBs, and the two come from different formation channels that lead to significantly different observed properties: the prompt emission of SGRBs is harder than that of LGRBs; their host galaxy population is not confined only to star-forming galaxies; and no supernova has been observed in connection with an SGRB. It is believed that SGRBs are formed by the merger of two compact objects (two

---

<sup>1</sup>GRBs are named according to the date of their explosion: 970228 exploded on the 28th of February 1997.

<sup>2</sup>The ‘duration’ of GRBs is usually quantified by the parameter  $T_{90}$ : the time that elapses between the 5th and 95th percentiles of their flux.

## 2704 BATSE Gamma-Ray Bursts

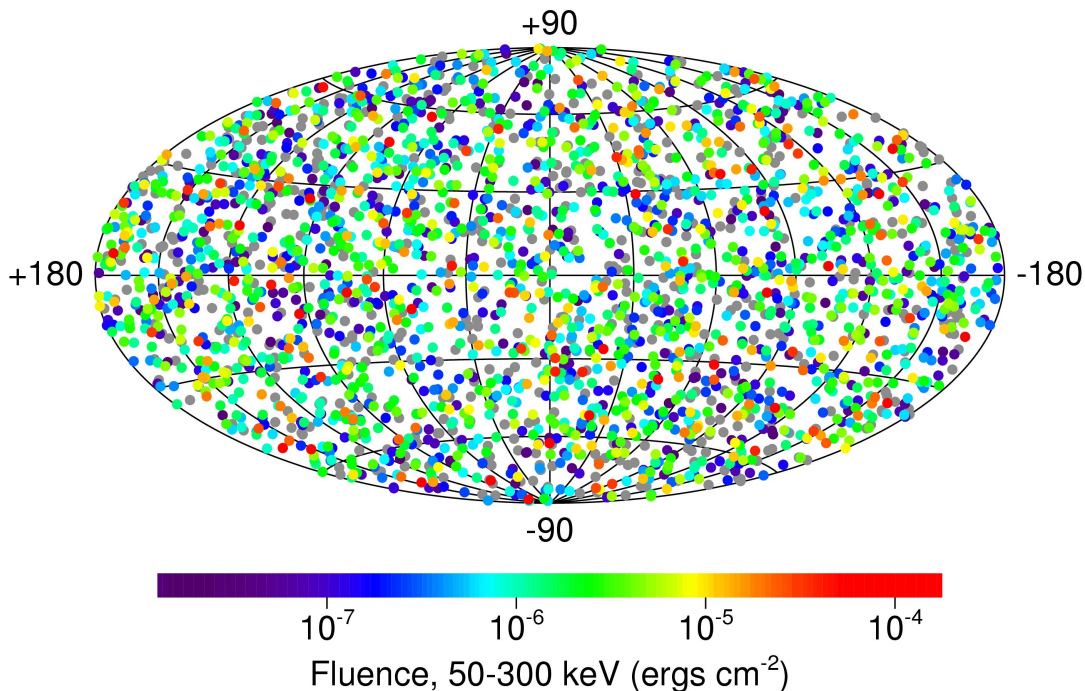


FIGURE 1.1: The isotropic distribution of 2704 GRBs detected during 9 years of BATSE observations, shown in Galactic coordinates. Adapted from <https://heasarc.gsfc.nasa.gov>.

neutron stars (NS) or a neutron star and a black hole, e.g. Nakar 2007; Berger & Edo 2011), while the LGRBs are caused by the collapse of massive stars (“collapsars”; Woosley 1993). The rest of this thesis will concentrate on LGRBs, and unless stated otherwise the term GRB will refer to the long variety.

### 1.1.2 The GRB/SN connection

It was after the first afterglow and host galaxy detections in 1997 that the belief that GRBs were cosmological explosions was confirmed, and soon after a further constraint was placed on their origin. A day after the discovery and localisation of GRB 980425, a brightening transient was found consistent with its location (Galama et al. 1998), as predicted by the collapsar model. The transient turned out to be a supernova (SN) of type Ic, denoted SN 1998bw, a type of core-collapse supernova (CCSN), the spectrum of which displayed neither lines of hydrogen nor helium.

Supernovae are not detected after every GRB, mostly because beyond a fairly low redshift ( $z \gtrsim 1$ ) the supernovae become too faint. However, there are now  $> 30$  GRBs that have been connected with supernovae, of which GRB 030329/SN 2003dh (Hjorth et al. 2003) became the “Rosetta Stone” object, proving that normal LGRBs and CCSNe were connected. While GRB 980425/SN 1998bw was a low luminosity burst, with no detected afterglow, GRB 030329 was much more typical of the population, and SN 2003dh showed very similar spectral features to SN 1998bw. This subject has been well reviewed by numerous authors including Hjorth & Bloom (2012) as well as Cano et al. (2017). This association has been widely accepted as conclusive evidence that long GRBs are caused by the deaths of massive stars. The true nature

of the progenitors and the mechanisms by which their deaths cause GRBs is still hotly debated, and I provide a brief overview of the main points relating to that topic in the following sections.

### 1.1.3 GRB progenitors

The SN connection is a clear indicator that GRBs are caused by the deaths of massive stars. But not all massive stars explode as GRBs — in fact only  $\sim 1\%$  (Woosley & Bloom 2006) of SN Ic produce a GRB (Ic make up only 15% of all CCSNe; Kelly & Kirshner 2012; Graham & Schady 2016). Thus, similar to prompt and afterglow emission, the attributes of the progenitor stars of GRBs are constrained by a set of observables and theoretical predictions.

Firstly, the star must be extremely massive ( $> 10M_{\odot}$ ), such that the mass of the core is above the Chandrasekhar limit ( $> 1.4M_{\odot}$ ) and can form a black hole. Secondly it must be rapidly spinning in order for the accretion disk formation and jet launching mechanisms to be successful (e.g. Woosley 1993; Woosley & Bloom 2006; Woosley & Heger 2006). Thirdly, it must have lost its outer envelopes of hydrogen and helium, since these elements are not observed in SNe Ic (e.g. Hjorth et al. 2003; Cano et al. 2014). The lack of outer envelope is also required for the jet to successfully break out of the infalling stellar material. Stars that fulfill all of these criteria are Wolf-Rayet (WR) stars (Filippenko 1997). However, not all WR stars produce GRBs. This is likely because the mass loss is in fact too high, such that the angular momentum lost renders GRB formation impossible. Only at low metallicities (for an introduction to metallicity, see Section 3.5.1) is the angular momentum conserved (e.g. Yoon & Langer 2005; Woosley & Heger 2006). GRBs must therefore form from low-metallicity ( $\lesssim 0.3Z_{\odot}$ ) stars, a hypothesis which has been heavily tested and is discussed throughout Chapter 2.

### 1.1.4 The *Swift* era

Numerous space missions have operated in order to detect and study GRBs, including BATSE, BeppoSAX, the High Energy Transient Explorer 2 (HETE-2), as well as the still operational Astro-rivelatore Gamma a Immagini Leggero (AGILE) and INTERNATIONAL Gamma-Ray Astrophysics Laboratory (INTEGRAL). Since 2008, prompt emission has been studied by the Gamma-ray Burst Monitor (GBM; Meegan et al. 2009) and Large Area Telescope (LAT; Atwood et al. 2009), which make up the *Fermi* satellite. The combined energy range of the two detectors spans over seven orders of magnitude, from 8 keV to 300 GeV, allowing the nature of prompt emission to be extremely well studied.

The revolution in the study of GRBs afterglows has for the past decade been driven by the *Swift* satellite (Gehrels et al. 2004). Its Burst Alert Telescope (BAT; Barthelmy et al. 2005) is able to detect transients in the range 15-150 keV to a positional accuracy of around 3 arcminutes. *Swift* is then able to slew to the source and is typically able to begin observing with its X-ray Telescope (XRT; Burrows et al. 2005) and ultraviolet/optical telescope (UVOT; Roming et al. 2005) within 100 s of the BAT trigger. The speed and unprecedented positional accuracy ( $\sim 3''$  with XRT,  $< 0.5''$  with UVOT) allows the rapid follow up with much larger, ground-based facilities, stimulating observations around the globe and across the entire electromagnetic spectrum.

*Swift* detects roughly 2 GRBs per week with the BAT.<sup>3</sup> Of these triggers, nearly 90% are followed up within 300 s with the XRT, with the remaining 10% not immediately observable due to observing constraints such as proximity to the Sun. The time taken by *Swift* to begin follow-up observations is orders of magnitude quicker than by previous satellites such as BeppoSAX and HETE-2, and dramatically increased the afterglow detection rate.  $\sim 96\%$  of BAT GRBs observed with XRT are detected in X-rays (Evans et al. 2009), but only  $\sim 30\text{-}40\%$  of bursts are

<sup>3</sup>Full numbers of *Swift* BAT, XRT and UVOT detections are available online at <https://swift.gsfc.nasa.gov>

detected by UVOT (Roming et al. 2009). Although only a relatively small fraction of the bursts are detected by UVOT, when an afterglow is detected the positional accuracy is typically 0.5–0.6”, allowing unambiguous host galaxy associations to be made (the typical  $\sim 1.5''$  accuracy of enhanced XRT positions, available within hours of the burst, also facilitates confident detections of host galaxies). With ground-based optical and near-infrared (NIR) telescopes, the detection rate increases towards  $\sim 70\%$  (e.g. Greiner et al. 2011), although positional accuracy may not be as good as with UVOT.

### 1.1.5 The fireball model

The predominant model explaining the prompt and afterglow emission of GRBs is the “fireball model”, which is described in the following sections. The fireball model is used to explain both long and short GRB emission, although the mechanisms forming the fireball are different.

#### 1.1.5.1 Prompt emission

Chronologically, the first observed component of a GRB is the flash of high-energy radiation (gamma-rays) that is referred to as the *prompt emission*. The preeminent model of GRB prompt emission is based on three separate observations, namely:

- i The enormous total emitted energy. Typical fluences in the gamma-rays range between  $10^{-4} - 10^{-7}$  erg cm $^{-2}$  (Paciesas et al. 1999). Combined with the cosmological distances travelled by the gamma-rays, the intrinsic, isotropic emission is thus of the order  $\sim 10^{52} - 10^{55}$  erg. For comparison, that is similar to the total energy output of the Sun in its entire lifetime. Given that CCSNe are thought to release up to 100 times more energy in neutrinos and gravitational waves than in electromagnetic radiation, these numbers suggest monumental energy releases. This energy is released in a matter of seconds.
- ii Typically, the timescale on which variations in physical processes are observed is related to the physical scales on which they occur. The time light takes to travel across the system means that any variations on shorter time scales are generally smoothed out. GRB prompt emission is observed to vary on millisecond timescales, suggesting a very compact ( $1 \text{ ms} \times c < 10^8$  cm, compared to  $R_{\odot} \sim 10^{10}$  cm) “central engine” producing the emission.
- iii The spectrum of the prompt emission is not fit by a thermal, black body shape, but a series of power laws. It is parametrised by slope indices  $\alpha$  and  $\beta$ , connected by a smooth break around the energy at which the counts are maximum,  $E_{\text{peak}}$ .

Such a vast energy release in such a small time (points i and ii) makes GRBs for a short while the most luminous objects in the Universe, which can only be explained by gravitational collapse. However, to produce the observed emission from such a small region leads us to the so-called “compactness problem”. The energy density in the fireball that is created at the point of collapse must be so high that positron-electron pair production becomes efficient ( $\gamma \rightarrow e^{-} + p^{+}$ ) for any gamma-rays with  $E_{\gamma} > 1$  MeV. This would lead to the fireball becoming optically thick to gamma-rays, instead creating a photosphere at its surface which would radiate thermally. But according to point iii, the emission is non-thermal, and there is no shortage of radiation above 1 MeV.

The compactness problem is solved by invoking relativistic effects, which are logical given the extreme energy release. If the fireball is accelerated to a relativistic velocity  $v \sim c$ , it has the Lorentz factor:

$$\Gamma = 1 / \sqrt{1 - (v/c)^2}. \quad (1.1)$$

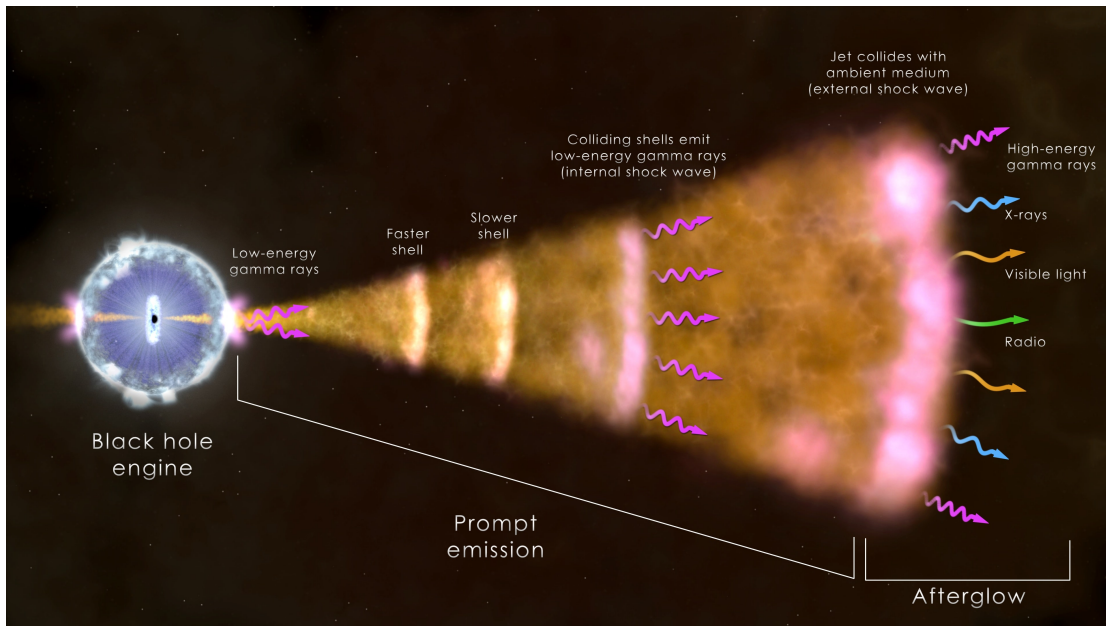


FIGURE 1.2: The fireball model of interacting shells that cause GRB prompt and afterglow emission. Adapted from [www.nasa.gov](http://www.nasa.gov).

Treating the fireball as relativistic now means: the moving size of the fireball is dilated by  $\Gamma^2$ , reducing the density and thus efficiency of pair production; the radiation is not isotropic, but instead is beamed into an angle of  $\Gamma^{-1}$ , meaning that the total energy output is smaller than previously assumed; the observed photons are blueshifted, meaning that in the rest frame the majority have energies  $E_\gamma < 1$  MeV, and thus the pair production is further reduced.

The final piece of the theoretical puzzle is the introduction of a small number of baryons into the scenario. With baryons present, a large fraction of the energy of the fireball is in the kinetic form: the fireball is in fact a highly relativistic jet of particles. Given an inhomogeneous launching mechanism, the jet comprises expanding shells, each with a different  $\Gamma$ . As these shells collide they induce relativistic shocks within the jet, known as *internal shocks*, which in turn transfers kinetic energy back into internal energy of the particles via Fermi acceleration. This energy is then thought to be released via synchrotron radiation, producing the power-law shaped prompt emission we detect.

### 1.1.5.2 Afterglows

Once the mass swept up in front of the jet equals the mass in ejecta, two external shocks are produced: a forward shock into the circumburst medium (CBM), and a reverse shock back through the ejecta (Fig. 1.2). Due to there being more material in the CBM, forward shock lasts longer, especially in the case of a thin shell where the reverse shock crosses the ejecta quickly. The forward shock is thus the dominant of the two. The external shock also radiates via synchrotron emission (Meszaros & Rees 1997), producing an almost featureless spectrum from X-ray to radio wavelengths. The afterglow spectral energy distribution (SED) is described by four power laws joined at three characteristic frequencies: the synchrotron self-absorption frequency  $\nu_a$ , below which photons may be re-absorbed by the synchrotron-emitting electrons; the characteristic synchrotron frequency  $\nu_m$ , where the SED peaks; and the cooling frequency  $\nu_c$ , which is the break between slow and fast cooling electrons. Afterglow decay is also described by a power law (or indeed a series of power laws), so at any one time in any one energy band

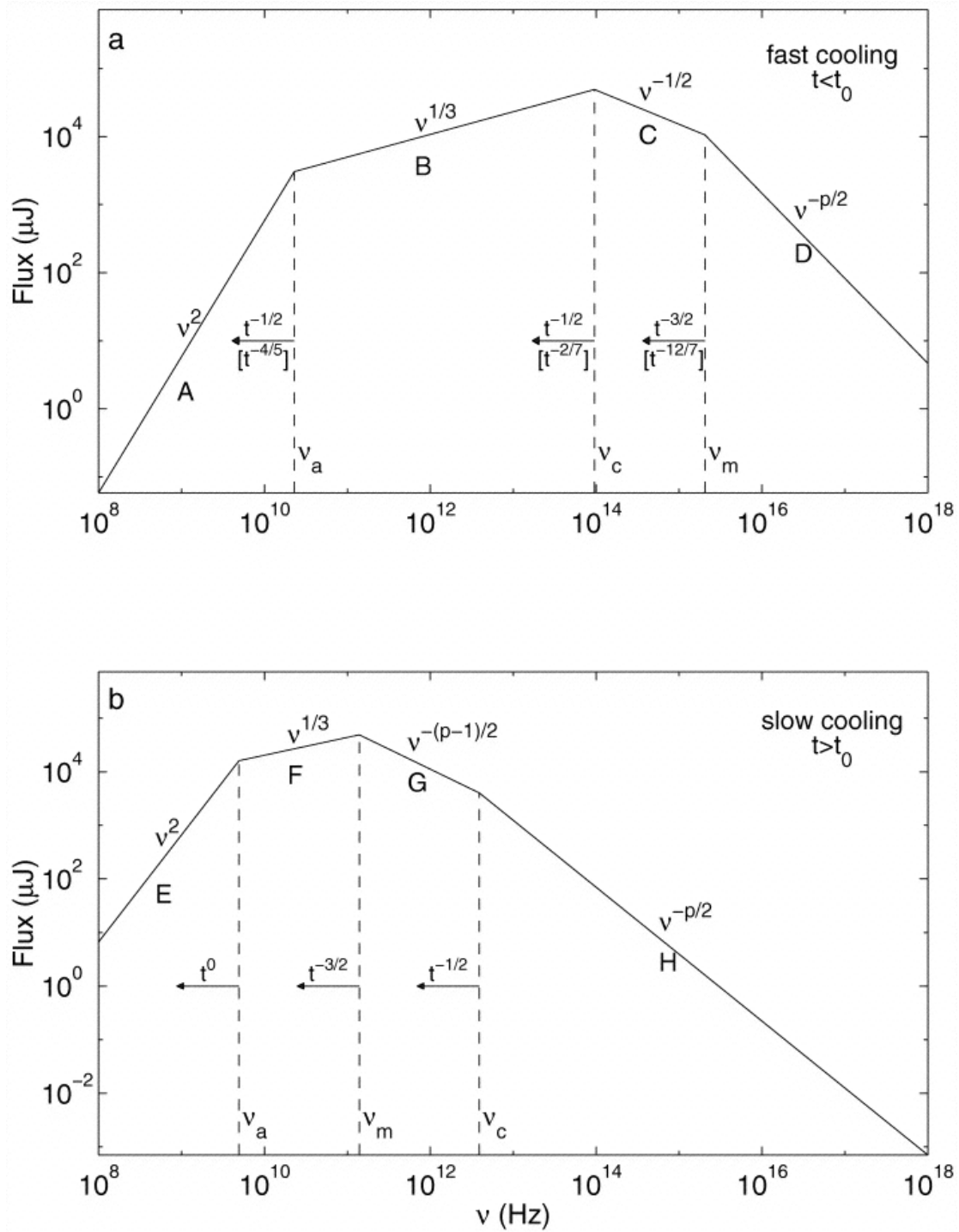


FIGURE 1.3: The GRB afterglow SED in the slow- and fast-cooling regimes, characterised by the relative positions of  $\nu_m$  and  $\nu_c$ . Adapted from Sari et al. (1998).

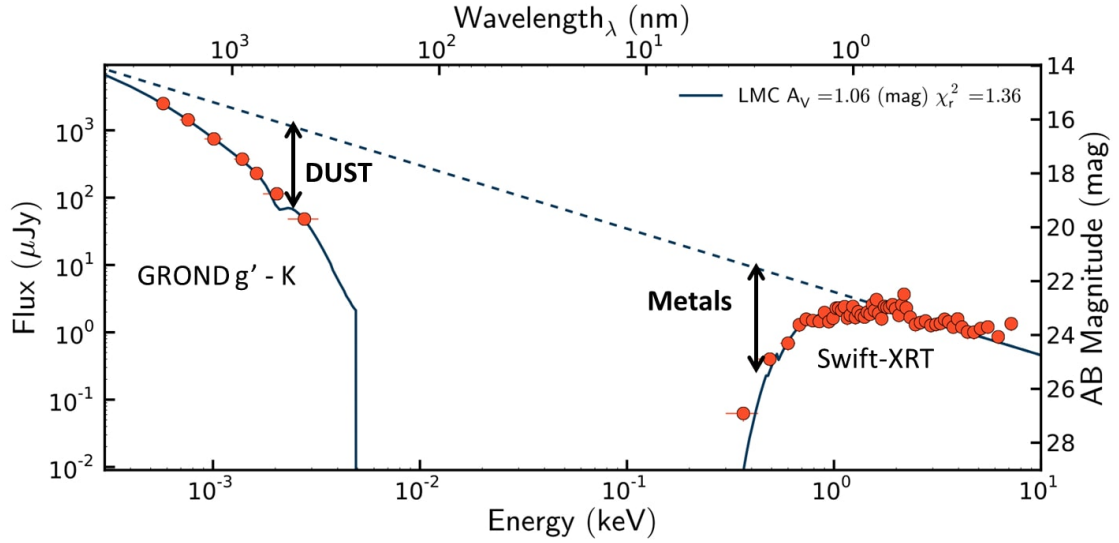


FIGURE 1.4: The broadband SED of GRB 120119A. The soft X-rays are absorbed by metals, while optical photons are absorbed and scattered by dust. The longer wavelength NIR as well as the hard X-rays fix the slope of the afterglow power law, allowing the measurement of equivalent absorbing column of hydrogen in the X-rays ( $N_{\text{H,X}}$ ) as well as the total dust extinction  $A_V$  from the optical. Adapted from Bolmer et al., *in review*.

the flux can be described by:

$$F_\nu(\nu, t) = t^{-\alpha} \nu^{-\beta}, \quad (1.2)$$

where  $\alpha$  and  $\beta$  are the temporal and spectral slopes respectively. Afterglows are usually visible on timescales from hours to days after the onset of the burst, the X-ray from days to weeks, and in some cases radio emission is visible on scales of years.

The characteristics of the observed emission from the forward shock depend on the relative position of the synchrotron frequencies. The positions of the synchrotron frequencies depend on a number of parameters: the total isotropic equivalent energy of the afterglow  $E_{\text{iso}}$ ; the fraction of energy in electrons and in a magnetic field, denoted  $\epsilon_e$  and  $\epsilon_b$  respectively; the radius of the jet is described by the half opening angle  $\theta_0$ ; the electron index  $p$ , which defines the slope of the energy distribution of the Fermi-accelerated electron population; the density and density profile of the CBM, assumed to scale with radius as  $n = Ar^{-k}$ , where  $A$  is a constant and  $k$  is either 0 for a typical ambient interstellar medium (ISM) or 2 for a stellar wind profile. The relative positions of the break frequencies are also dependent on the cooling regime, determined by whether the electron cooling timescale is shorter or longer than the hydrodynamical timescales inside the shock. For fast cooling,  $\nu_m > \nu_c$ . At some point, the majority of electrons will have moved into the slow-cooling regime, such that  $\nu_m < \nu_c$ . The overall spectrum in the two regimes can be seen in Fig. 1.3. Another form of temporal evolution is the so-called “jet break”, which occurs at late times when the relativistic beaming effects subside, causing a sharp steepening of the slope of the power-law decay of the lightcurve.

The evolution of the synchrotron frequencies and their relative positions, as well as the characteristic power-law indices  $\alpha$  and  $\beta$ , are tied together through the closure relations (e.g. Meszaros & Rees 1997; Sari et al. 1998; Racusin et al. 2009). The nature of the relations depend on the internal physics of the jet as well as the external CBM conditions and geometry of the system.

An example of a ground-based instrument dedicated to GRB science is the Gamma-ray Burst Optical and Near-infrared Detector (GROND; Greiner et al. 2008), mounted at the Max Planck Gesellschaft 2.2 m telescope at La Silla Observatory, Chile. GROND operates in seven bands simultaneously - the Sloan  $g'r'i'z'$  optical as well as  $JHK$  near-infrared (NIR) bands. Able to begin observations as quickly as 1 minute after the GRB trigger, GROND can provide light curve and SED information from the very onset of the afterglow (e.g. Fig. 1.4) throughout its evolution. Simultaneous broad band afterglow observations with instruments such as GROND and XRT, and even sub-mm/radio telescopes, can then be used as a powerful test of the fireball model and afterglow physics (e.g. Filgas et al. 2012; Varela et al. 2016).

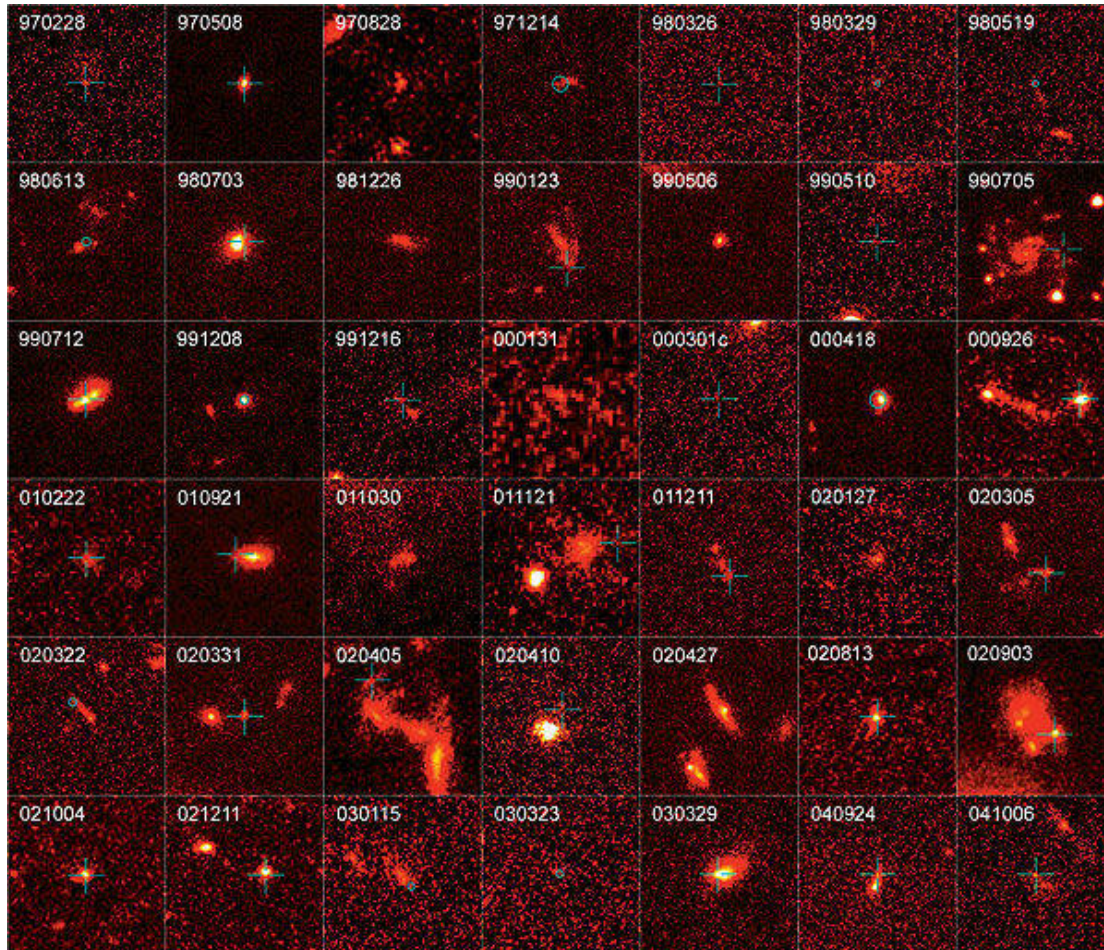


FIGURE 1.5: The hosts of 42 GRBs imaged using *HST*. Adapted from Fruchter et al. (2006).

### 1.1.6 GRBs as cosmic probes

The cosmological distances of GRBs, combined with their observed fluxes, make them for a short period of time the most luminous objects in the Universe. Along with the brightest, most distant active galactic nuclei (AGN), which are known as quasars (QSO), GRBs are the most easily observable sources at high redshift, and this observability opens up a wealth of potential uses for GRBs as probes of the distant Universe. As they are caused by massive stars, GRBs could be tracers of star formation across the Universe (see Section 1.2.1), although substantial uncertainties are present. These include: the theorised low-metallicity preference, insinuating that they might occur less frequently in high metallicity galaxies avoiding a large fraction of

the star formation; dust effects that hinder the detection of afterglows and host galaxies, which also could cause biases against massive, dusty galaxies; an evolving initial mass function (IMF), causing a varying rate of GRBs per unit star formation; and the typically low-number statistics of GRB samples.

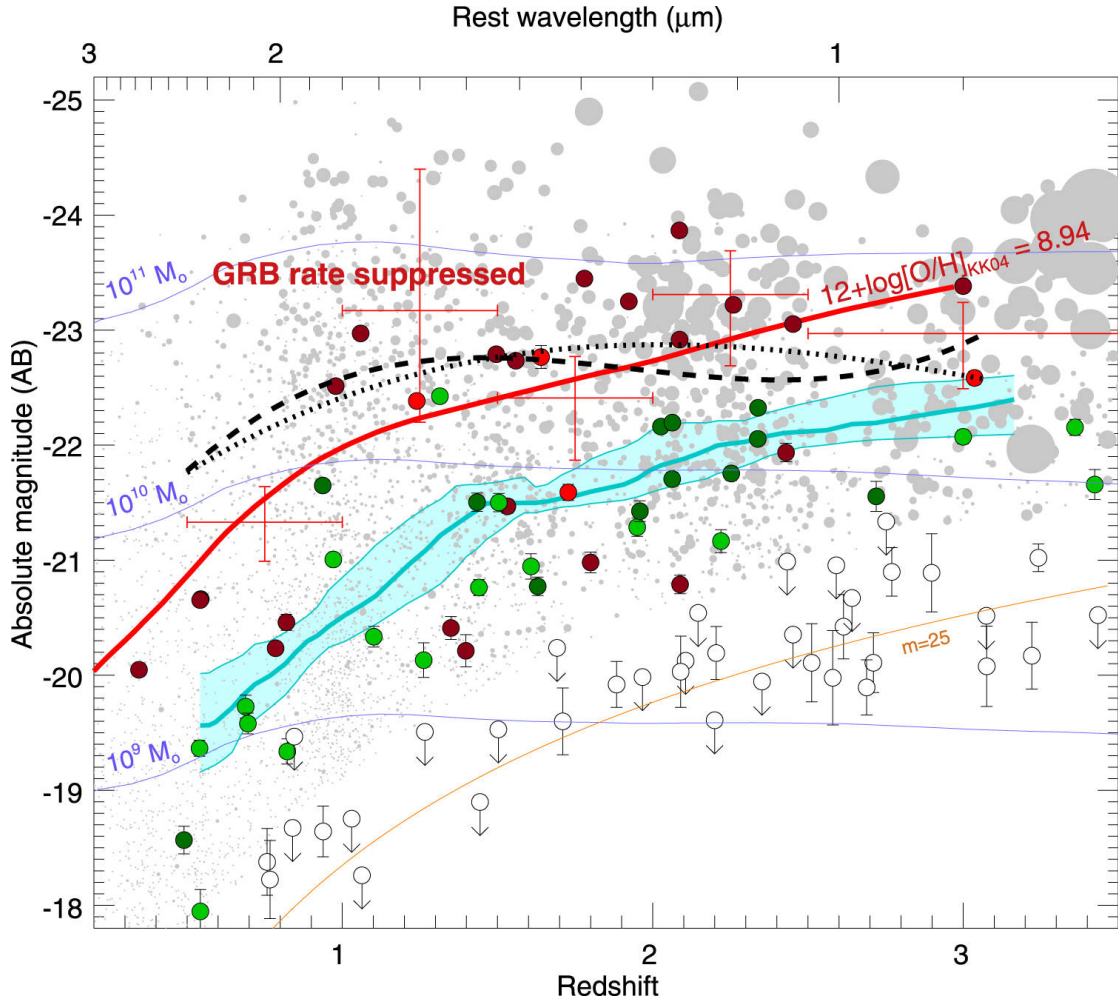


FIGURE 1.6: *Spitzer*  $3.6\mu$  magnitudes for GRB hosts (green: normal afterglows; red: dusty afterglows) and field galaxies (grey; Kajisawa et al. 2011). An apparent magnitude cut of  $m < 24.5$  has been applied to both populations in order to compare the samples only in the regions where both are complete. The cyan curve shows the median magnitude of the GRB host population near that redshift (and  $1\sigma$  bootstrap uncertainty). The dashed and dotted curves show the same property calculated from MODS/GOODS-N and CANDELS/UDS, respectively. GRB hosts are significantly underluminous as a population at all redshifts but especially below  $z < 1.5$ . The red measurements show the best-fit values for  $M_{3.6/(1+z),\text{thresh}}$  a (soft) upper limit for efficient GRB production within a host galaxy. The solid red curve shows the threshold for a metallicity of  $\log(\text{O}/\text{H})+12=8.94$  converted to luminosity. Adapted from Perley et al. (2016c).

Standard candles are objects with a known intrinsic luminosity, such that measurements of their brightness allow distance calculations, which when combined with redshift are plotted on a Hubble diagram and used to determine cosmological parameters. Currently, SNe Ia are the most commonly used objects at the largest distances and were used to detect the accelerated expansion of the Universe (Riess et al. 1998; Perlmutter et al. 1999), but are only visible to

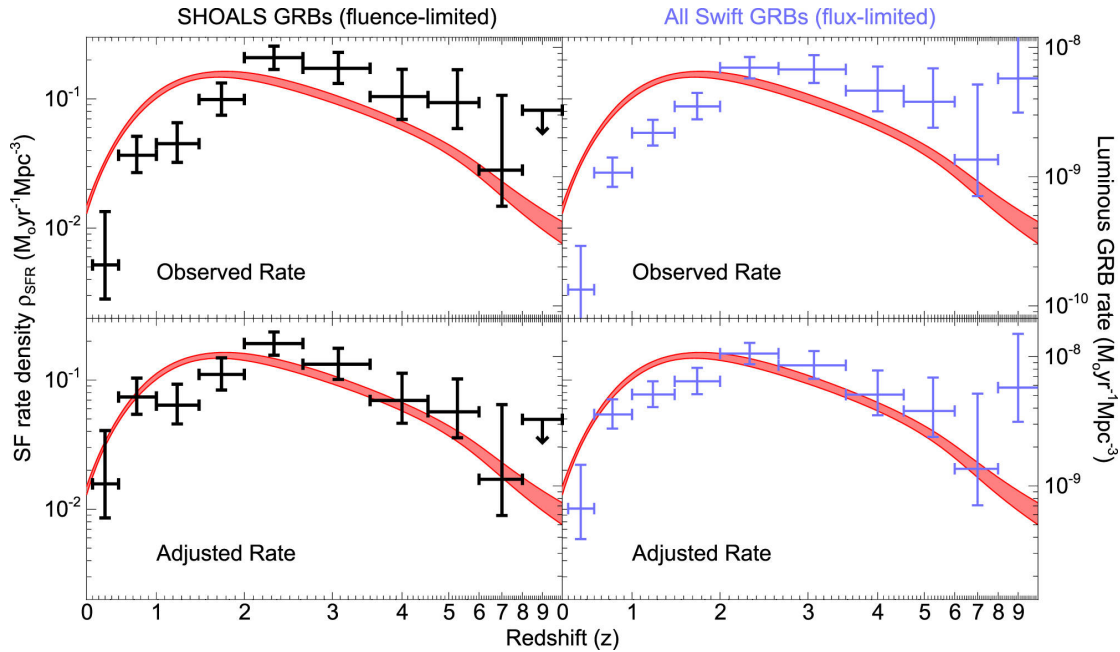


FIGURE 1.7: Comparisons of the GRB rate and SFR across cosmic time. Adapted from Perley et al. (2016c).

$z \sim 1$ . Some authors propose that correlations are detected in GRB prompt emission that could allow them also to be used as standard candles (e.g. Firmani et al. 2005; Lin et al. 2015), which would be extremely useful and would expand the Hubble diagram to much higher redshifts than at present. However, this suggestion is still debated. What is certain is that their extreme brightness allows us to probe the dark, distant, inaccessible reaches of our Universe, and it is this aspect of GRB astronomy that provides the focus for the remainder of this thesis.

## 1.2 GRB host galaxies

As mentioned in the previous sections, long gamma-ray bursts are caused by the deaths of massive stars, and as such must explode in galactic environments. The galaxies in which GRBs explode are known as their hosts. Since the first discovery of a GRB host over 20 years ago, an entire field of research has been dedicated to these galaxies, the highlights of which I present in this section.

Most galaxy samples are selected based on one or more selection criteria, which introduce largely unavoidable biases into the samples. For example, an obvious criterion is that they must be bright enough to be detected by the survey in which they are being studied. Clearly, closer or more intrinsically luminous objects are more likely to be selected. This factor is even stronger when conducting surveys of high redshift galaxies, hindering the ability to make complete and unbiased studies of high redshift galaxy properties. Long gamma-ray bursts offer a way to select galaxies regardless of their luminosity. It has been shown that, due to their origin as massive stars, GRBs trace the cosmic star-formation rate at least to  $z = 3$ , and therefore are an ideal way to select star-forming galaxies at high redshift. As discussed previously in Section 1.1.6, selection effects may be present in samples of GRB host galaxies which must be understood in order to minimise the biases they introduce. Nevertheless, they certainly pick out regions of star formation that may be undetected by conventional surveys of galaxies.

For example, using the *Hubble Space Telescope* (*HST*), Fruchter et al. (2006) showed that GRBs explode in irregular and dwarf galaxies, and tend to occur in the very brightest regions

of the galaxy, suggesting that they trace the youngest and most massive stars (Fig. 1.5). With multi-band photometry, further constraints can be placed on the characteristics of the host. By fitting the observed SED with galactic models, parameters such as stellar mass, star-formation rate and dust extinction can be derived (e.g. Perley et al. 2013, 2016c). This information is crucial if GRBs are to be used as standard tracers of star formation across the Universe, as it must be determined whether or not GRB hosts trace the population of field galaxies. At the most basic of levels, the GRB rate could be used as a proxy for star-formation rate (SFR) over cosmic time, and this hypothesis has formed a heavy part of the literature over the past decade (e.g. Yüksel et al. 2008; Kistler et al. 2009; Robertson & Ellis 2012; Trenti et al. 2012; Michałowski et al. 2012; Elliott et al. 2012; Schulze et al. 2015; Graham & Fruchter 2015; Greiner et al. 2015a; Perley et al. 2013). However, this picture is easily skewed by the introduction of metallicity. The standard “collapsar” model of GRBs requires a progenitor metallicity significantly lower than that of the Sun (typically around  $\sim 0.3Z_{\odot}$ ; Section 1.1.3). For a long time the observations conformed, as GRB hosts proved to be faint, low-metallicity, low-mass, blue, star-forming galaxies (Fruchter et al. 1999; Christensen et al. 2004; Tanvir et al. 2004; Savaglio et al. 2009). However, in recent years a number of surveys have been conducted that have attempted to reduce the inherent biases associated with following up GRBs (Section 1.2.1). A number of observations have complicated the picture somewhat, due to the dedicated follow up of heavily extinguished GRBs (Cenko et al. 2009; Perley et al. 2009; Greiner et al. 2011; Perley et al. 2013): X-ray-localised bursts without a detected optical afterglow. Super-solar metallicities have been observed in a small number of hosts (Elliott et al. 2013; Schady et al. 2015), and follow-up of several bursts revealed massive, red, luminous host galaxies (e.g. Perley et al. 2013; Hunt et al. 2014; Perley et al. 2015).

### 1.2.1 GRB host surveys

To compile complete and unbiased samples of GRB hosts, it is necessary to correct for the biases induced by only selecting hosts of optically detected afterglows, and thus to include hosts of dark bursts. There have been several programmes which have attempted this, including ‘The Optically Unbiased GRB Host’ (TOUGH) survey (Hjorth & Bloom 2012), ‘BAT6’ (Salvaterra et al. 2012), and the ‘*Swift* Gamma-Ray Burst Host Galaxy Legacy Survey’ (SHOALS; Perley et al. 2016a). Most use a combination of imaging and spectroscopy across the electromagnetic spectrum in order to acquire as much information as possible. Using *Spitzer*  $3.6\mu$  luminosities, Perley et al. (2016c) have showed that even with a complete and unbiased sample, GRB hosts tend to be less luminous (and therefore less massive) than the general galaxy population (Fig. 1.6), particularly at low redshift, although attempts have been made to correct for this aversion (Perley et al. 2016c; Fig. 1.7). Schulze et al. (2015), using the TOUGH survey, find that at  $1 < z < 3$  GRBs appear to trace UV star-formation metrics well, contrasting with the result of Perley et al. (2016c). Greiner et al. (2015a) find that, above  $z \geq 2$ , GRBs trace the UV metrics of star formation well, whereas Schulze et al. (2015) find that this is not the case.

A key instrument in the development of GRB host surveys has been X-shooter, a mid-resolution ( $R \sim 8000$ ), optical/NIR spectrograph mounted at the European Southern Observatory (ESO) Very Large Telescope (VLT) on Cerro Paranal, Chile. X-shooter is able to obtain spectra in three bands (UVB, VIS, NIR) simultaneously, providing coverage in the range  $3000 - 25000 \text{ \AA}$ , a much larger coverage than any previous spectrograph of such resolution. Over the past  $\sim 8$  years, the use of X-shooter in the rapid follow-up of GRBs has provided not only redshifts, but also chemical abundances obtained both from absorption (e.g. Cucchiara et al. 2015; Wiseman et al. 2017b) and emission (Krühler et al. 2015). A sample of X-shooter GRB spectra has been compiled that is much larger than obtained by any other instrument of its class, which has been used to study dust depletion (Wiseman et al. 2017b; Chapter 3), dust

extinction (Japelj et al. 2016, Zafar et al. *in prep*), metallicity (Cucchiara et al. 2015) and other host properties (Krühler et al. 2015).

### 1.2.2 Metallicity

As well as probes of star formation, GRB afterglows can also be used as tools to study to other properties of high redshift galaxies such as metallicity (A detailed introduction to metallicity measurements is provided in Chapter 3). In the seconds following the Big Bang, the first elements were formed, in a process known as Big Bang nucleosynthesis (BBN). The very first stars, known as Population III stars, were later formed out of the products of BBN: pure hydrogen, along with traces of deuterium, helium, and lithium. All other elements were produced in the subsequent generations of stars and their associated explosions, and the fraction of them relative to hydrogen is known as the metallicity. Thus the pollution of a galaxy by metals is directly related to the evolution of its stellar populations, as well as inflows and outflows to the galaxy. Briefly, the galaxy is fed by the pristine, primordial gas from the IGM which fuels star formation. When stars explode, they expel metal-enriched material into the circumgalactic medium (CGM) through galactic winds (these winds may also be driven by stellar winds and active galactic nuclei); this enriched material may fall back onto the galaxy, forming a galactic fountain. The evolution of metallicity is thus an indicator of the flow of material in and out of the galaxy as well as its stellar processes. As well as being a cornerstone in theories of galaxy evolution in general, metallicity is also a key concept in the field of GRBs. This is due to the conditions needed to form a GRB in the first place (see Section 1.1.3). Most models point to the threshold metallicity being about 1/3 of the solar value. Because it is not possible to directly measure the metallicity of the GRB progenitor, nor the immediate environment which is fully ionised by the explosion, absorption of the afterglow by nearby strong absorbing systems (typically star-forming regions) residing in the GRB host provide one of the best methods of studying this theoretical threshold observationally. Absorption lines are more sensitive to much lower metallicities than emission lines at the redshifts at which both can be used ( $1.6 \lesssim z \lesssim 2.3$ ) are used, since the emission lines are typically very weak and/or contaminated by strong  $H$ - and  $K$ - band sky lines, and thus diagnostics become unreliable. A detailed explanation of the methods (and pitfalls) of analysing absorption line data in order to measure metal and dust content can be found in Chapter 2.

Large surveys of late time spectroscopy have also been completed, from which a sample has been compiled by Krühler et al. (2015) who used VLT/X-shooter spectra to measure emission lines from 96 hosts, one of the largest samples of host spectra to date. With strong lines such as the Balmer series and forbidden lines of oxygen and nitrogen, among others, they were able to provide independent results for SFR and  $A_V$ . Furthermore, they used strong line diagnostics in order to estimate the metallicity of the star-forming regions of the hosts. Krühler et al. (2015) find an aversion of GRBs occurring in high-metallicity environments, with only 20% of GRBs at  $z < 1$  occurring in  $Z > Z_\odot$  galaxies, below the fraction of total star formation. Graham & Fruchter (2017) find a sharp cut at  $\log(\text{O}/\text{H})+12 = 8.3$ , corresponding to  $0.4Z_\odot$ , with the rate of GRB production per unit star formation 10 - 50 times higher for galaxies with metallicity below this limit. This finding may also explain the aforementioned preference for GRBs to occur in lower-mass galaxies, because it is known through the mass-metallicity relation (MZR; Tremonti et al. 2004) that such galaxies also have lower metallicities. Perley et al. (2016c) find a larger metallicity cut-off of around solar (which is evident in Fig 1.6, although their metallicities were inferred from stellar masses via the MZR). The metallicities measured in all of the works discussed have been inferred either directly or indirectly using emission line diagnostics, which bring with them a significant degree of uncertainty, and the topic is discussed further in Chapter 5.

## 1.3 Afterglow attenuation

As evident in Fig. 1.3, the intrinsic spectrum of a GRB is largely featureless, and composed of a number of power-law components. Any deviation (see Fig. 1.4) from this continuum seen in observations must therefore be caused by material lying between the GRB and the observer. Absorbing and attenuating material can in general be split into three categories: host galaxy, intervening systems, and the Milky Way. The form of this absorption can be broken down further. For example, dust preferentially attenuates and scatters light at blue and ultra-violet (UV) wavelengths compared to the red and NIR bands, causing an effect known as reddening, which I will discuss in Section 1.3.2.3. The drop in flux as a function of wavelength is known as an extinction curve, which can be compared to the intrinsic spectrum in order to determine the amount of dust. This is not simple however, as the effect of extinction itself is relatively smooth and featureless, leading to degeneracies between different models, as well as with the shape of the intrinsic spectrum itself, should the cooling break be located between the optical and X-ray bands. The soft (lower energy) X-rays are also absorbed, an effect caused by line transitions from metals in neutral as well as partly and highly ionised states. Assuming solar abundances one is then able to measure the (lower limit of the) equivalent X-ray absorbing hydrogen column density,  $N_{\text{H,X}}$ .

Strong absorption occurs also in the form of atomic line transitions from atoms and ions in the gas phase, which can be seen in spectra of the afterglow. Atoms/ions each have their own set of transitions, the wavelengths of which are determined by the energy difference between the two electronic levels responsible. When light with the precise wavelength corresponding to that energy difference encounters such an atom or ion, it may be absorbed, promoting the electron to the higher energy state. According to our knowledge of quantum mechanics, the rest-frame vacuum wavelengths ( $\lambda_{\text{vac}}$ ) of these transitions are known to high precision. The observed wavelengths at which they occur determine their redshift by:

$$\lambda_{\text{obs}} = (1 + z) \lambda_{\text{vac}} . \quad (1.3)$$

It is usually assumed that the highest redshift set of lines correspond to absorbing gas in the GRB host galaxy, and in the majority of cases a damped Lyman-alpha absorber is observed. It should be noted that this is only possible above  $z \gtrsim 1.7$ , when the Ly- $\alpha$  line is redshifted into the transparent wavelength window used by ground-based telescopes.

### 1.3.1 Damped Lyman-alpha absorbers

Above a redshift of  $\sim 1.7$ , the Lyman-alpha (Ly- $\alpha$ ) transition of neutral hydrogen (the absorbing photon promoting an electron from  $n = 1$  to  $n = 2$ ) at  $\lambda_{\text{vac}} = 1215.67 \text{ \AA}$  becomes visible from the ground. Hydrogen is over three orders of magnitude more abundant than any other element (apart from helium), and thus Ly- $\alpha$  is often the strongest absorption line in the spectrum. It is so strong that at column densities of  $N_{\text{H I}} > 10^{19} \text{ cm}^{-2}$  the red wing of the line begins to show signs of damping (Fig. 1.8). Above  $N_{\text{H I}} > 10^{20.3} \text{ cm}^{-2}$ <sup>4</sup> the absorption system is called a damped Lyman-alpha absorber (DLA; Wolfe et al. 2005). In DLAs the self-shielding provided by the dense gas is strong enough to reduce ionisation to a negligible level. It can then be assumed that the elemental abundances measured from the neutral or singly-ionised states of metals are representative of the total abundance of that metal. In some DLAs molecular hydrogen ( $\text{H}_2$ ) is also detected through its numerous transitions in the Lyman-Werner bands blueward of Ly- $\alpha$  (e.g. Ledoux et al. 2006b).

<sup>4</sup>For the entire thesis, column densities or their logarithms are given in units of  $\text{cm}^{-2}$

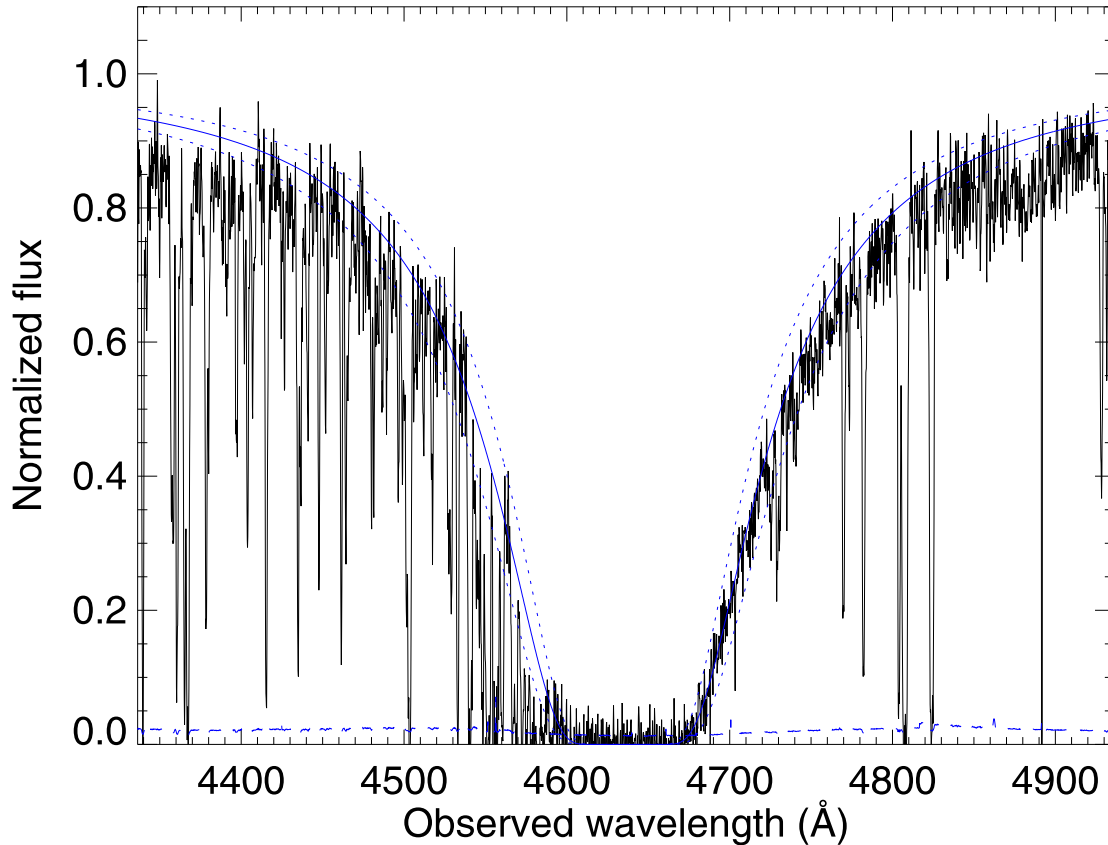


FIGURE 1.8: The Ly- $\alpha$  absorption in the spectrum of GRB 120327A at  $z = 2.8145$ . The column density  $\log N_{\text{H I}} = 22.01 \pm 0.09$ , and as such the damping of the red wing (right hand side) is clearly evident, as is the onset of the Ly- $\alpha$  forest at bluer wavelengths. Adapted from D’Elia et al. (2014).

DLAs were discovered serendipitously in the spectra of distant quasars, but it was soon realised that they are useful probes of the high-redshift Universe. Once dedicated surveys had been completed it became apparent that there was enough neutral gas in DLAs to produce the stellar mass seen in  $z = 0$  galaxies — that is, DLAs could represent the building blocks of the modern Universe (Wolfe et al. 1995). Large samples of DLAs and their characteristics now exist, including Wolfe et al. (1995), Ledoux et al. (2006a), and Prochaska et al. (2007c).

Lines of sight to QSOs cross intervening absorbing systems at random. The vast majority of absorbers belong to the optically thin Ly- $\alpha$  forest, with  $\log N_{\text{H I}} < 17$ . The Ly- $\alpha$  line is typically only mildly saturated (reaches zero flux), but the systems are frequent, their recurrence across a wide redshift range leading to the forest title. Such systems are the result of the trace neutral gas found in dense pockets of the intergalactic medium (IGM). Denser clouds of  $17.3 < \log N_{\text{H I}} < 19$  are referred to as Lyman limit systems (LLSs), due to their total absorption below the Lyman limit ( $n = 1$  to  $n = \infty$ ) at  $911.8 \text{ \AA}$ . LLSs are also highly ionised, and typically show strong absorption from triply ionised metal transitions such as C IV and Si IV. Above  $\log N_{\text{H I}} > 19$  we enter the regime of sub-DLAs, whose Ly- $\alpha$  absorption profiles begin to show signs of damping, but ionisation is still likely to play a significant role. Only above the aforementioned threshold of  $\log N_{\text{H I}} > 20.3$  can ionisation effects be neglected.

The interaction cross section for QSO lines of sight (LOS) is much higher for the outskirts of galaxies (their halos or CGM) than for the dense star-forming regions of the interior. Therefore it is quite rare that QSO spectra reveal a DLA, and when they do they are often fairly metal-poor and do not necessarily trace the inner regions of their high-redshift host galaxies. Indeed, there is

currently significant debate as to what gas the QSO-DLAs *do* actually trace. On the other hand, the massive star origin of GRBs means that they necessarily occur within a star-forming region — the lifetime of the massive progenitors (most models give masses of  $> 40 M_{\odot}$ ) is of the order of a few Myr, shorter than the typical star-forming region lifetime. GRBs occur typically in the gas-rich disk of their hosts and thus their LOS usually pass through dense regions. Indeed, at redshifts greater than 1.7 (the threshold for detecting Ly- $\alpha$  from the ground, and therefore unambiguously identifying DLAs), over 80% of GRB afterglow spectra show a DLA (Cucchiara et al. 2015), and a further 10% a sub-DLA. This tendency to probe the star-forming regions of high-redshift galaxies makes GRB-DLAs extremely useful laboratories in which to explore the conditions in which the earliest stars and galaxies existed.

### 1.3.2 Dust

Dust is a crucial component in the evolution of galaxies, as it is on the surface of dust grains that hydrogen atoms are able to join to form H<sub>2</sub>, the fuel of star-formation. This dust is subsequently irradiated by the newly formed stars, the UV light from which it absorbs and re-emits in the far-infrared (FIR). For this reason it is used to measure the SFR and stellar mass of galaxies in which the UV flux is attenuated. It is also used to infer the mass of gas (by assuming a certain dust-to-gas ratio) in high redshift galaxies for which direct measurements via the hyperfine H I 21 cm line and molecular CO are not possible due to being too faint. Furthermore, the production mechanisms of dust and its physical properties are key ingredients inserted into simulations of the evolution of galaxies. GRBs probe star forming galaxies, and since their lines of sight cross the ISM of these galaxies, they thus provide an excellent laboratory in which to study dust across the history of the Universe, over the peak of cosmic star formation ( $z \sim 2.5$ ; Madau & Dickinson 2014), and even into the Milky Way (Watson 2011).

#### 1.3.2.1 Dust Depletion

Dust depletion is defined as the removal of some metals from the gas phase due to their condensation onto dust grains. Absorption line measurements then return a lower abundance of those metals, compared to the true *intrinsic* abundance of those metals. As mentioned in Section 2.2, different elements deplete with different strengths, which, when combined with nucleosynthetic effects, lead to degeneracies and thus a large uncertainty on metallicity measurements. It is therefore very useful for the study of GRB host galaxies as well as QSO-DLAs to be able to break the degeneracies and subsequently correct for the effects of depletion, as well as using the depletion to study the dust itself. A detailed study on dust depletion in GRB-DLAs is presented in Chapter 3, and to avoid repetition this section shall be kept brief.

Depletion has been known about for many years, appearing in a review by Savage & Mathis (1979), but it is only in the last two decades that it has been comprehensively studied. Savage & Sembach 1996 (SS96) provided a description of depletion in the Milky Way (MW) in which they ascribe one of four dust descriptions to any particular line of sight. This is because the depletion patterns of the elements appear to follow those of the warm halo (WH), warm disk/halo (WDH), warm disk (WD) or cold disk (CD) environments (listed here in order of depletion strength). In each of the cloud types, the depletion of each of eight elements is well known. Soon after, this knowledge of depletion was being applied to GRB hosts (Savaglio 2001; Savaglio et al. 2003; Savaglio & Fall 2004), where the fitting of the SS96 patterns to observed relative abundances provided a method of determining the dust content of the hosts. Other works have used the ratio between just two elements as the dust tracer (e.g. [Fe/Zn]; Vladilo et al. 2006). The seminal work of Jenkins 2009 (J09), turned the discrete, four-type model into a continuous distribution of depletion strengths for 17 elements across lines of sight to 243 MW stars, allowing any and

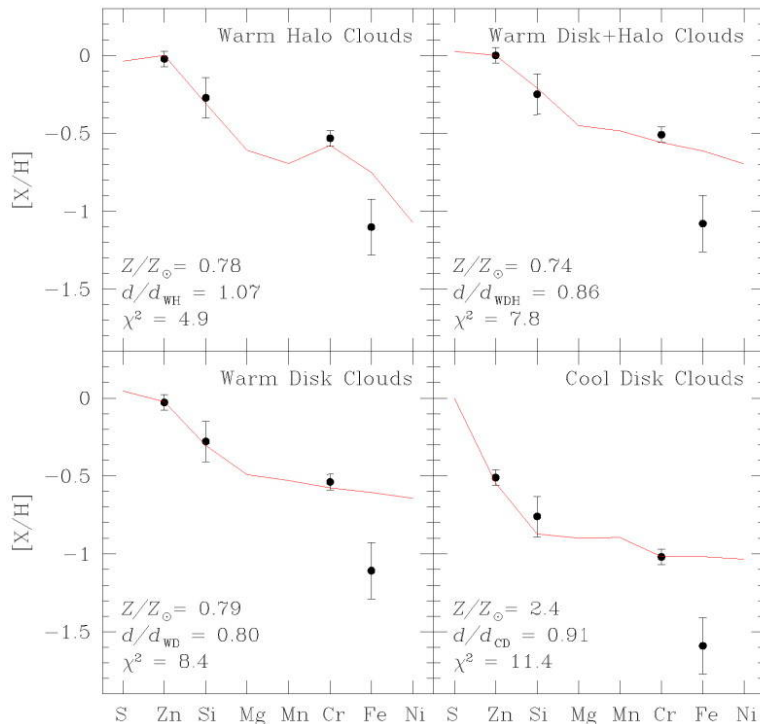


FIGURE 1.9: The dust depletion patterns of GRB 000926 compared to the best fitting SS96 models from the Milky Way. The free parameters of the fit are the metallicity ( $Z/Z_{\odot}$ ) and dust-to-metals ratio  $d$ , here given in terms of that in the respective MW cloud. Adapted from Savaglio et al. (2003).

every sight line to be described by the dust depletion strength factor,  $F_*$ . This work has been regularly used to calculate and correct for dust in GRB hosts (e.g. Sparre et al. 2014; Friis et al. 2015), and has recently been extended to include measurements from the Magellanic Clouds (MCs; Tchernyshyov et al. 2015; Jenkins & Wallerstein 2017) and QSO-DLAs (De Cia et al. 2016). The dust depletion sequences from De Cia et al. (2016) are shown in Fig. 1.10, in which the dust strength is determined by the abundance ratio  $[Zn/Fe]$  (for an explanation of this abundance notation, see Chapter 2).

In Chapter 3, we investigate dust depletion in GRB host galaxies and provide the largest sample of such measurements to date.

### 1.3.2.2 Dust-to-metals ratio

A commonly used parameter throughout astrophysics is the dust-to-gas mass ratio (DTG). It is often used as a conversion factor when measurements of galaxy dust masses are available (from far-IR or sub-mm observations) in order to calculate the molecular gas mass, a crucial measurement in the study of star formation. The DTG is also used in cosmological simulations that model galaxies and also incorporate dust, and it is often held constant throughout the simulations. In more detailed studies, it is seen that the DTG varies between galaxies as well as within them. It scales, for example in the MW, with metallicity (e.g. Dwek 1998; Draine et al. 2007). This relation implies a constant dust-to-metals ratio (DTM), an assumption which is often fed into cosmological simulations of galaxy evolution as well as used to convert between dust and gas masses in the distant Universe.

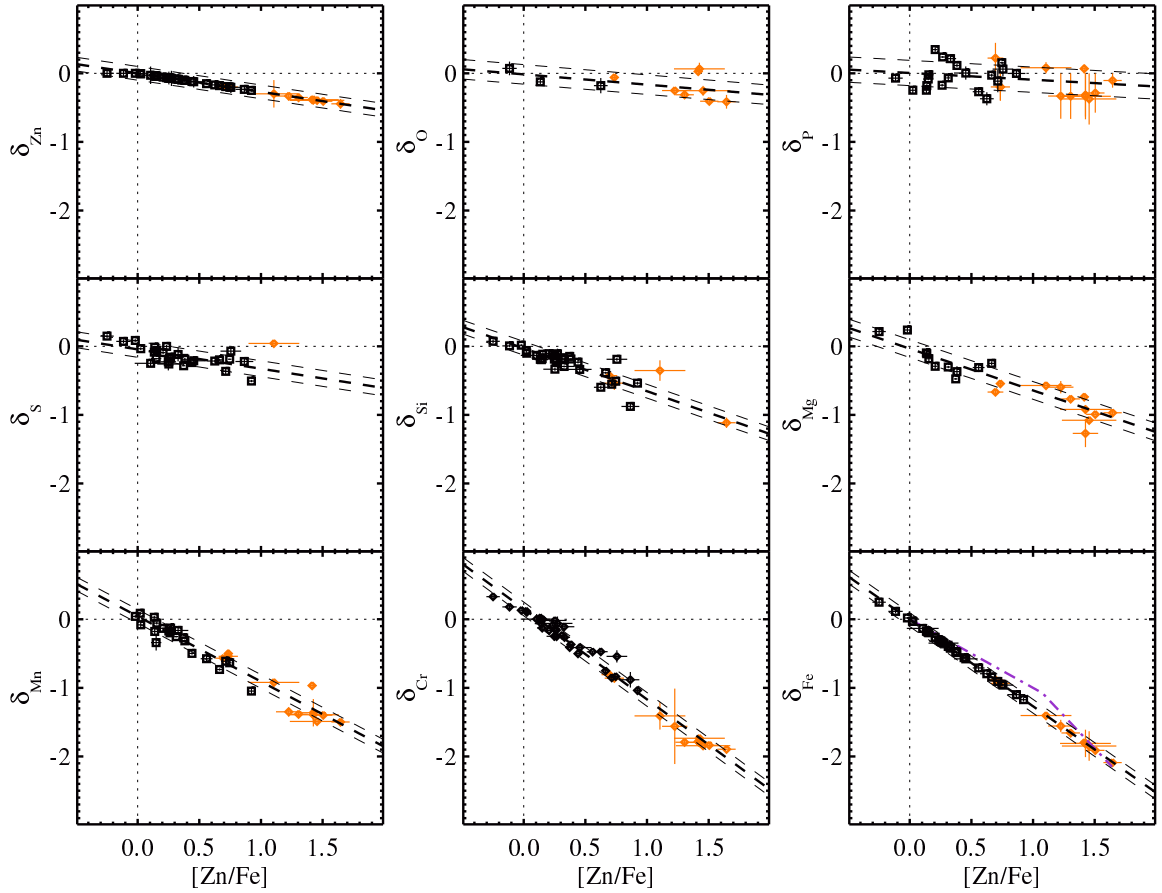


FIGURE 1.10: The dust depletion sequences of a number of elements measured in QSO-DLAs. The depletion  $\delta$  of an element is the logged fraction of that element still remaining in the gas phase; the dust fraction is thus  $1 - 10^\delta$ . The relative value  $[\text{Zn}/\text{Fe}]$  is taken to be the measure of overall dust strength. Adapted from De Cia et al. (2016).

As well as being an important factor in the study of galaxy evolution and star formation the DTM is a useful indicator of the origin of dust. While the gas (i.e. H) in a galaxy typically originates in the IGM and accretes onto the galaxy during its lifetime, the metals and the dust are both formed in the galaxy itself. Metals are formed in the cores of stars and supernova (SN) explosions, and expelled into the ISM via stellar winds and the expanding supernova ejecta. Dust, on the other hand, can be formed in a number of locations:

- i In the atmospheres and winds of post-asymptotic giant branch (AGB) stars.
- ii In the cooling ejecta of SNe.
- iii In situ in the ISM, by metals condensing from the gas phase onto pre-existing grains.

Knowledge of the dust formation process is important not only for understanding the physics of the aforementioned environments, but also for the understanding of the role of dust on longer timescales of galactic evolution. While simulations can predict the evolution of the DTG and DTM (e.g. McKinnon et al. 2016; Aoyama et al. 2017), it is also necessary to conduct observations. The observational signature of the formation process is the relationship between DTM and metallicity. If DTM remains constant with metallicity, then most of the dust has likely been formed in the same place as the metals (because no matter what the metallicity is, the same

fraction of those metals are forming dust). If, however, the DTM correlates positively with metallicity, then most of the dust has been formed in the ISM, because metal-rich environments provide more metals from which the dust can form.

At the highest redshifts, it is expected that almost all of the dust is formed in SNe, and to some extent post-AGB stars. This is because the nucleation sites do not yet exist in the ISM, nor has enough time elapsed for grains to have grown significantly. In the present day, however, many authors believe that grain-growth in the ISM is the dominant mode of dust production (e.g. Draine 2003). GRB-DLAs are a useful addition to the sample of observations of the DTM and metallicity provided by QSO-DLAs and lensed galaxies (e.g. Zafar & Watson 2013; De Cia et al. 2013) especially at high redshift. A more comprehensive overview of the corresponding literature on this subject is presented in Chapter 3, followed by a study of a sample of 19 GRB-DLAs and their metal and dust contents.

### 1.3.2.3 Extinction

As well as the depletion, measurable through absorption lines, dust also absorbs and scatters light in the process known as extinction, making background objects appear fainter and redder. The change in apparent magnitude caused by extinction at wavelength  $\lambda$  is denoted  $A_\lambda$ , whose evolution as a function of wavelength defines the extinction curve:

$$A_\lambda = A_V \eta_\lambda = -2.5 \log_{10} \frac{F_\lambda}{F_\lambda^0}, \quad (1.4)$$

where  $F_\lambda$  and  $F_\lambda^0$  represent the absorbed and intrinsic flux respectively, at wavelength  $\lambda$ .  $A_V$  is the absolute extinction in the  $V$ -band, which normalises the extinction curve described by  $\eta_\lambda$ . The steepness of the extinction curve is determined by the grain-size distribution, which is encompassed in the parameter  $R_V$ , which is known as the absolute-to-selective extinction and quantifies the slope of the curve at UV/optical wavelengths.  $R_V$  and  $A_V$  are related through the expression:

$$R_V = \frac{A_V}{E_{B-V}}, \quad (1.5)$$

where  $E_{B-V} = A_B - A_V$  is the difference in extinction between the  $B$  and  $V$  bands, known as the reddening. The extinction curves along lines of sight in the Milky Way have been measured by Cardelli et al. (1989), and typically show a characteristic bump centered at 2175 Å, which is usually weaker in the LMC and non-existent in the SMC (the feature is however detected along one sight line through the SMC wing; Gordon et al. 2003). Thus not only the slope but also the presence and strength of the bump helps distinguish between extinction laws when fitting GRBs.

Numerous studies have calculated the  $A_V$  of GRB hosts using their SEDs, including Schady et al. (2010); Greiner et al. (2011); Zafar et al. (2011); Schady et al. (2012); Japelj et al. (2016); Bolmer et al. *in review*. Frequently used are SED fitting routines such as XSPEC (Arnaud 1996). In order for the fitting procedure to provide accurate results, the absorption due to foreground (Milky Way) material must be known and provided to the algorithm. Typically the foreground  $A_V$  is taken from all-sky maps such as Schlegel et al. (1998) and Schlafly & Finkbeiner (2011). The soft X-rays are also absorbed in both the host and the Milky Way by metals, the strength of which correlates with the hydrogen column density,  $N_H$ , and this must also be accounted for. In this case,  $N_H$  maps from Kalberla et al. (2005) are typically used.

Fixing the foreground extinction and absorbing column and the redshift leaves a number of free parameters which are left to be fit in the XSPEC routine. These are:

- The spectral index of the unabsorbed SED: GRB spectra are well described by power laws (or broken power laws), the slope of which ( $\beta$ ) can be fixed from photometry in the NIR

and X-ray. If the cooling break frequency  $\nu_c$  lies between the optical and X-ray regimes, the power law is broken and the difference in  $\beta$  is usually fixed at 0.5.

- $E(B - V)$ : Assuming that the dust in the host galaxy is similar to one of the three Local Group galaxies (MW, LMC, SMC) the difference between the unabsorbed power law and the optical/NIR photometric data is then fit by the average extinction laws from those galaxies from Pei (1992). The law with the best fitting reduced chi-squared value is taken, giving the  $E_{B-V}$  and thus  $A_V$ .
- $N_{H,X}$ : Any excess absorption in the soft X-rays that is not accounted for by the column in the MW is attributed to the host.

In the sample by Greiner et al. (2011), most of the SEDs were fit better by a broken than a simple power law, whereas Schady et al. (2010) selected primarily simple power laws in order to remove the degeneracy caused by the unknown location of the cooling break. Most of those afterglows were fit best with SMC-like extinction curves. In Schady et al. (2012), the average GRB extinction curve shows  $A_V < 1$ , SMC or LMC-like steepness but with no obvious sign of the 2175 Å bump. In contrast, bursts with  $A_V > 1$  tended to show MW-like dust and signs of the bump.

Typically,  $A_V$  values are relatively low for GRB hosts (see the above referenced works), with a potential trend to even lower values at higher redshifts (Zafar et al. 2011, Bolmer et al., *in review*). This has been interpreted as a sign of decreasing dust content in the Universe above redshifts of  $\sim 3$ . However, significant selection effects are expected to be at play, since high redshift bursts appear fainter. Heavily extinguished bursts at high redshift are thus less likely to be detected than closer bursts with the same extinction.

In the following chapter, I discuss the measurement technique of absorption line spectroscopy which has been heavily used in the work presented in this thesis. In Chapter 3, I present a study of the dust properties of GRB host galaxies, in which I have compiled the largest sample of dust-depletion measurements in GRB hosts to date, and compared them with dust extinction measurements of the same objects. In Chapter 4, I move to a case study of the single, extraordinary host galaxy of GRB 080810. In Chapter 5, I discuss the results of my work, and in Chapter 6 I discuss the prospects for the future of the field of GRBs, hosts, and other explosive transients.



## Chapter 2

# Absorption line spectroscopy

The predominant method of data analysis used in this thesis is absorption line spectroscopy. The method is a powerful way of extracting information about a foreground absorber that is illuminated by a background source. In this chapter, I will outline the rationale for using the Voigt-profile fitting technique and some of the physical parameters that are attainable, as well as some caveats and ways around them.

In order to provide context for the use of absorption line spectroscopy, I will first describe the physical information that is measured with it. The raw property that is attained from absorption line fitting is the column density of one or a number of different atomic and ionic species, the absorption caused by electronic transitions between energy levels in the atoms and ions of the gaseous absorbing medium. The next logical step is to calculate the metallicity, simply by comparing the abundance of hydrogen to one or many metals. Absorption-derived metallicities are usually written in the relative solar abundance format  $[X/H]$ , where

$$[X/H] = \log\left(\frac{N_X}{N_H}\right) - \log\left(\frac{N_X}{N_H}\right)_\odot, \quad (2.1)$$

and in DLAs  $N_H \approx N_{H\text{I}}$  and for most metals  $N_X \approx N_{X\text{II}}$ . The approximation of the singly-ionised state being dominant applies to many of the heavy elements found in the ISM, for which the ionisation potential of the neutral state is much lower than the 13.6 eV of H I, meaning that even in a DLA there are enough photons with high enough energy to ionise them once. O, N, and C (13.6 eV, 14.5 eV, and 11.3 eV respectively) are however much closer, so in dense regions such as DLAs are dominated by their neutral state. For the entire work the solar abundances given by Asplund et al. (2009) are used, which have been measured to high accuracy and precision with studies of the solar photosphere as well as mass spectroscopy of meteorites in Earth-based laboratories. In fact, the choice of solar abundances would not greatly affect the results, because other sources of error are much more dominant.

The metallicity of a DLA is then relatively simple to calculate, by measuring the column density from the H I and singly-ionised (or neutral) metal absorption lines with a line-fitting method, as described in Section 2.1. There are a number of ways to do this, each with their own caveats, including the curve-of-growth analysis (COG; Spitzer 1978) and the apparent optical depth method (AODM; Savage & Sembach 1991), which both make assumptions about the shape of absorption lines, and both work when the lines are saturated. The most accurate method when the data is of high enough quality and the lines are not saturated is the Voigt profile fitting method. In the interest of conciseness, I will only talk about the Voigt-profile method, as it has been the only one employed throughout the work presented in this thesis. It should be noted, however, that when using multiple methods on the same data, results are found to be consistent (e.g. Cucchiara et al. 2015), although the Voigt-profile fits are the most precise, and therefore preferred when the S/N and/or resolution is good.

## 2.1 Voigt profile fitting

The strength (depth) of an absorption line is determined by the optical depth  $\tau(\nu)$ , which is the product of two factors: the column density  $N$ , which is the number of particles in a column of surface area  $1 \text{ cm}^2$  along the length of the entire absorber; and the cross section  $\sigma(\nu)$ . The cross section is a function of the oscillator strength  $f$ , a dimensionless parameter derived from the quantum mechanical likelihood of the transition from state 1 to state 2 — the Einstein coefficient  $B_{12}$  — and is defined by:

$$f = \frac{h\nu m_e c B_{12}}{(2\pi e)^2} \quad (2.2)$$

where  $h$  is the Planck constant, and  $m_e$  and  $e$  the respective mass and charge of the electron.

Absorption lines are not delta functions, but have a width caused by two broadening mechanisms. One is the finite uncertainty on the electronic energy levels caused by the uncertainty principle, which means the transition can occur at a range of energies and thus frequencies. The probability distribution of these transition frequencies follows a Lorentzian profile, and so causes the Lorentzian or “natural” broadening, shown by the red profile in Fig. 2.1. It normally has a visible effect only at the very high column densities of H I. The second, usually dominant, cause of broadening is Doppler broadening, which is parameterised by the broadening factor  $b$ , usually given in units of  $\text{km s}^{-1}$ . Doppler broadening is caused by the thermal motion of the atoms, whose non-zero relative velocities cause the transition to be either blue or redshifted, and gives rise to the  $b$  parameter:

$$b_{\text{therm}} = \sqrt{2kT/m} \quad (2.3)$$

as well as any turbulent motion in the gas giving rise to the additional  $b_{\text{turb}}$ . These then sum in quadrature via the relation

$$b_{\text{tot}}^2 = b_{\text{turb}}^2 + b_{\text{therm}}^2. \quad (2.4)$$

The Doppler broadening causes a Gaussian line shape, which when convolved with the Lorentzian profile results in the Voigt profile (Fig. 2.1). The oscillator strength  $f$  is known to high precision for most atomic/ionic transitions, and thus the shape of the absorption lines depends on only two free parameters: the column density  $N$  and the broadening parameter  $b$ . For each transition, it is then possible to fit for a range of values for  $N$  and  $b$ , creating expected profiles and comparing them to the observed ones, until the  $\chi^2$  value is minimised indicating the best fit. Depending on the redshift of the burst, many species will have more than one transition available for fitting, each with a unique  $f$  but the same  $N$  and  $b$ . Fitting such lines simultaneously can therefore significantly reduce the error on the fit (typically given simply as the statistical error taken from the  $\chi^2$  minimisation).

## 2.2 Accurately measuring abundances

The singly-ionised states <sup>1</sup> of the majority of the most abundant elements in the Universe, such as C, N, O, Si, Fe and Mg, have transitions in the rest-frame UV (1000 – 3000 Å), meaning at redshifts of  $z \gtrsim 1$  they are shifted into the optical bands which are visible from Earth (the atmosphere is opaque to wavelengths  $\lambda_{\text{obs}} \lesssim 3000 \text{ Å}$ ).

The ideal lines for measuring metallicity must fulfill several criteria. They must be isolated rather than blended with any nearby, unrelated lines in the spectrum which may contaminate the absorption (either those from other lines at the host redshift, from intervening systems, or from the Earth’s atmosphere known as telluric lines). They must be unsaturated — that is, their flux

<sup>1</sup>I shall use standard astrophysical notation for ions for the entire thesis. For example, neutral hydrogen is H I, and singly-ionised iron is Fe II

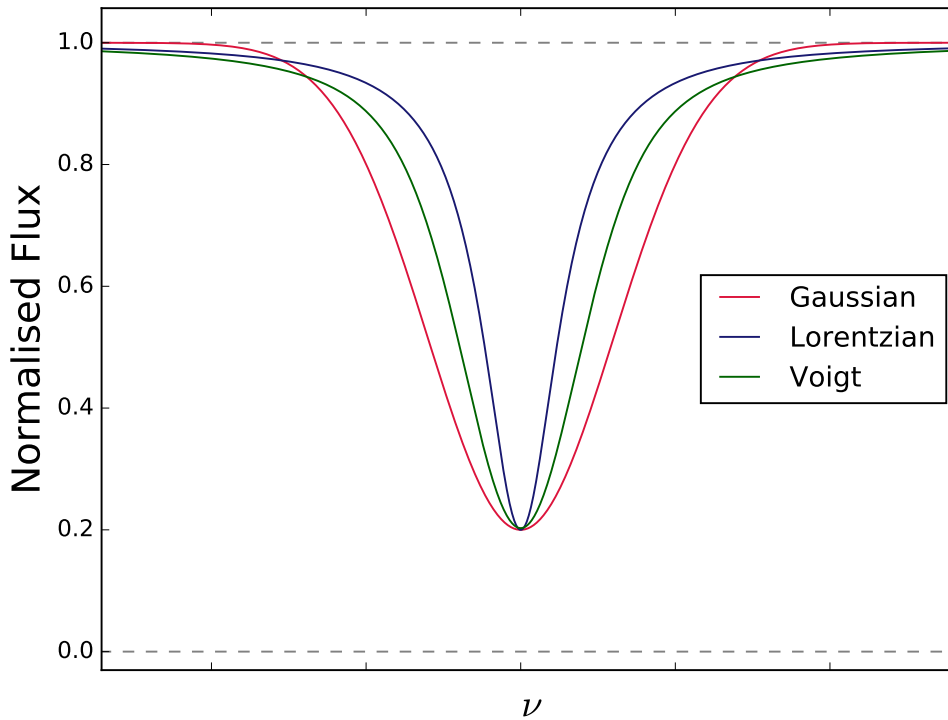


FIGURE 2.1: The Gaussian, Lorentzian and Voigt profiles.

cannot reach zero — because then the depth and shape of the line no longer scales as strongly with  $N$  — although the analysis of Section 3.3.2 shows that saturation effects may be tolerable to some level. Finally, metallicity estimates can be affected by intrinsic variations in the relative abundances in the DLA. One cause of variations is a difference in the nucleosynthetic history of the DLA — that is, the elements have been produced in different ratios in comparison to what is seen in the solar neighbourhood. The most prominent nucleosynthetic effect is the  $\alpha$  enhancement, which refers to an overabundance of the  $\alpha$  elements such as C, N, O, and Si relative to iron-group elements like Fe, Ni, and Zn. Nucleosynthetic effects are however rarely larger than about 0.3 dex in relative abundance. Dust depletion, on the other hand, can be much stronger, and it can be troublesome to find a suitable volatile element which does not easily deplete (condense) into dust grains. More on the details of dust depletion can be found in Section 3.2.

Finding lines that fulfill the above criteria is tricky, and there is no perfect solution. Of the volatile elements, Zn II is blended with Mg I and Cr II at 2026 Å and 2062 Å respectively. High S/N ( $\gtrsim 15$ ) and a good resolution ( $R \gtrsim 8000$ ) is required to break the blend. Si II has several lines but most are usually saturated, and it is also mildly depleted. C and O are so abundant that for all but the lowest metallicity systems all their lines are saturated in both the neutral and first ionisation states. N II has two triplets but they are both located bluewards of Ly- $\alpha$ , meaning they are often hopelessly blended with the Ly- $\alpha$  forest, while the S II  $\lambda\lambda\lambda 1253, 1259, 1260$  are often blended with Ly- $\alpha$  as well as Si II  $\lambda 1260$ . The dust depletion traits of S are also not particularly well known (Jenkins 2009). It has been suggested, for example by De Cia et al. (2016), that P is the best element for measuring metallicity, but its low relative abundance ( $12 + \log(P/H) = 5.41$ , compared to the values of 7.5 for Fe and Si, and 8.69 for O) means its lines are much weaker and often not detected even in relatively high metallicity systems, when the S/N is not good.

Sometimes Si II  $\lambda 1808$  is unsaturated and unblended, and when combined with a measurement of iron to estimate the depletion, it can be used as a good metallicity tracer. Similarly, Fe and Ni have many detectable lines, most of which do not usually saturate. Therefore, with a value for a volatile element measured, metallicity can be well constrained and corrected for dust with the addition of Fe or Ni measurements. The issue of which lines to use for metallicity determination is hotly debated in the literature, examples of which include Vladilo et al. (2011); Rafelski et al. (2012, 2014); Cucchiara et al. (2015), and no consensus has been reached.

### 2.3 Velocity components and kinematics

DLAs are rarely composed of a single cloud of material, but usually several components each with distinct local velocities (and thus different apparent redshifts). While these can be separated by several hundreds of  $\text{km s}^{-1}$ , they can still be blended into one another in the spectrum, due to instrumental broadening. Because GRB afterglows are usually faint objects that fade away within a matter of hours, there is a limit to the resolution of the spectrographs that can be used to observe them, in order to collect enough light per wavelength bin for a good signal-to-noise ratio (S/N) to be achieved. The work of de Ugarte Postigo et al. (2012) used high resolution spectra to measure a mean  $b$ -parameter of  $12.6 \text{ km s}^{-1}$ . It is possible to resolve lines of such width only with the highest-resolution instruments used for GRB science (and DLAs in general), such as the High Resolution Echelle Spectrometer (HIRES) on the 10 m Keck-I telescope in Hawaii or the Ultra-violet and Visible Echelle Spectrograph (UVES) at the VLT. The maximum resolving powers of HIRES and UVES are 85,000 and 110,000 respectively, corresponding to velocity resolutions of around  $v_{\text{FWHM}} \sim 3 \text{ km s}^{-1}$ . This value is often increased significantly by poor seeing (turbulence in the atmosphere). However, only the brightest bursts can be observed with those instruments. Most GRB spectra to date have been obtained with mid-resolution (e.g. VLT/X-shooter;  $v_{\text{FWHM}} \gtrsim 25 \text{ km s}^{-1}$ ) or low-resolution (e.g. VLT/FORS2;  $v_{\text{FWHM}} \gtrsim 120 \text{ km s}^{-1}$ ) spectrographs. Typically then, the intrinsic velocity structure of the DLA is partially (in the case of mid resolution) or totally (in the case of low resolution) blended out, such that the measured  $b$ -parameter is not actually physically meaningful. For sample studies looking at global galactic properties such as metallicity, this blending is not particularly important, and as such samples of GRB-DLA metallicities have been compiled (e.g. Prochaska et al. 2007b; Arabsalmani et al. 2014; Cucchiara et al. 2015; Wiseman et al. 2017b; Chapter 3).

The second problem with the lack of resolution is the the effect known as hidden saturation. This occurs due to the Gaussian broadening effect of the instrument, which smooths out absorption features, making lines which are only mildly saturated appear unsaturated. Measuring  $N$  using such lines leads to an underestimation of column densities, and has been discussed in the context of spectrographs from low to high resolution in works including Prochaska (2006) and Jorgenson et al. (2013). In the work presented in Chapter 3 of this thesis (see also Wiseman et al. 2017b), hidden saturation has been studied in detail using synthetic spectra at the resolution of X-shooter.

### 2.4 Ionisation

Along with the dust and chemical abundances in the ISM, absorption line studies of GRB afterglows can also provide insights into the ionisation properties of the constituent gas. While in DLAs the majority of the metals are found in the singly ionised state, significant absorbing columns of other ionisation states are also regularly observed. C IV and Si IV, for example, are often heavily saturated in DLAs, despite their negligible contribution to the total abundance of C and Si. Other examples include N V and O VI, which may not trace the same gas as that in

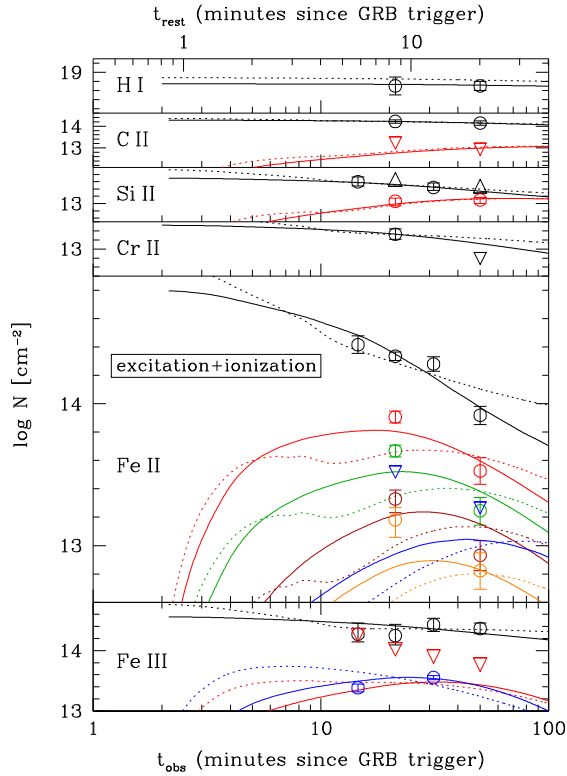


FIGURE 2.2: The varying column densities of the excited and ground states of C II, Si II, Fe II and Fe III in GRB 080310. The open circles are detections, while the open triangles indicate upper or lower limits ( $3\sigma$ ). The different colours denote the different ion levels: black for the ground state and red-green-maroon-orange for the first four excited levels, while the Fe II  $^4F_{9/2}$  and Fe III  $^7S_3$  levels are indicated in blue. The solid and dotted lines correspond to the best-fitting model, assuming the default and an alternative input flux, respectively. Adapted from Vreeswijk et al. (2013).

the DLA, but rather regions of higher temperature in the CGM or in the near vicinity of hot, massive stars. Studies such as Fox et al. (2008) have searched for blueshifted absorption from high-ionisation states that could trace high-velocity outflowing gas that has been ejected from the GRB progenitor, although their results were inconclusive.

A key parameter in absorbers with densities below that of DLAs (i.e. sub-DLAs and LLSs) is the ionisation parameter  $U$ . This parameter quantifies the ionisation state of the absorbing gas by the flux of ionising photons (those with energies  $> 1$  Ryd) per hydrogen atom, and is necessary in order to correct column densities into true abundances when calculating metallicities in ionised systems. With a combination of measurements of ratios between metals in different ionisation states, it is possible to calculate  $U$  using photo-ionisation code such as CLOUDY (Ferland et al. 2017). The code runs based on an assumed UV background due to quasars and hot stars. GRB afterglow spectra are illuminated by the additional source of the GRB itself, and as such modelling the ionisation parameter in low-column density GRB absorbers is extremely complicated. It is for this reason that GRB metallicity and dust studies focus almost entirely on DLAs. Few studies (Fox et al. 2008; Prochaska et al. 2008b; Tanga et al. 2016) have investigated the high-ionisation structure of GRB absorbers; in Chapter 4 I provide a detailed investigation of gas in several ionisation states in the high resolution afterglow spectrum of the bright GRB 080810.

## 2.5 Excitation

In a similar way to ionisation, absorption spectroscopy can allow investigations of gas excitation. In this sense, excitation refers to the promotion of electrons into excited states through fine-structure transitions, and such states are referred to with the \* symbol. For example, Si II\* is the first excited state of Si II. Because the excited states are intrinsically unstable, a strong UV source must be responsible for their production. Although C II\* is often detected in star-forming galaxies (e.g. Wolfe et al. 2003), excited presumably by the young, hot stars, Si II\* appears almost exclusively in GRB afterglows. The reason for this is the UV pumping of the ions into their excited state by the radiation of the afterglow itself (Prochaska et al. 2006; Vreeswijk et al. 2007). Because of the rapid response of modern ground-based telescopes with both imaging and spectroscopy, it is possible to use excited lines to measure the distance to the DLA from the GRB. Required is multi-epoch spectroscopy along with a well-resolved light curve — the differing strengths of identical fine-structure lines (often those of Fe II\*) as well as the declining flux from the afterglow can then be used as input in a CLOUDY model, such as in Fig. 2.2. Results from such analyses have consistently shown GRB-DLAs to be located on scales of a few hundreds of parsecs to over a kiloparsec from the GRB itself (Vreeswijk et al. 2007, 2013; Krühler et al. 2013; D’Elia et al. 2014; Friis et al. 2015)— close enough to share similar global properties such as metallicity and dust content, but not part of the same star-forming H II regions.

Even when multi-epoch spectroscopy is not available, the presence of fine-structure absorption in one or multiple velocity components can indicate which components are closest to the GRB. If the components are well-resolved, it is possible to measure differences in chemistry between them, and thus better characterise systems that appear to be moving towards or away from the GRB (and thus in or out of the galaxy). In Chapter 4, this technique is used extensively to analyse the gas in the complicated, extremely well resolved host system of GRB 080810.

## Chapter 3

# Evolution of the dust-to-metals ratio as traced by GRB-DLAs

As published as P. Wiseman, P. Schady, J. Bolmer, T. Krühler, R. M. Yates, J. Greiner, and J. P. U. Fynbo, 2017, *Astronomy & Astrophysics*, 599, A24, reproduced with permission ©ESO.

### 3.1 Introduction

The abundances and compositions of the dust and metals in the interstellar medium (ISM) can reveal important information about local environmental conditions. Despite the wealth of information on our doorstep regarding the ISM of the Milky Way (MW) and Local Group galaxies, it is also necessary to investigate the ISM in the distant Universe in order to trace its properties in very different environments, as well as its evolution over cosmic history.

One of the key constituents of the ISM is dust. Dust is produced in a range of environments, from the stellar sources of outer envelopes of post-asymptotic giant branch (AGB) stars and the expanding and cooling ejecta of supernova to grain growth and accretion in the ISM. It reveals itself via emission in the far-infrared and sub-mm wavelength range and through absorption and scattering of visible and ultraviolet (UV) light from background sources, and its effect must be corrected for when studying sources that shine through it. For example, everything outside the Galaxy must be observed through the dust of the MW, which has a complex topography (Schlafly & Finkbeiner 2011). It is estimated that up to 30% of all light in the Universe has been reprocessed by dust grains (Bernstein et al. 2002). Dust is also necessary for, and traces, star formation across the Universe (Sanders & Mirabel 1996; Genzel et al. 1998; Peeters et al. 2004; McKee & Ostriker 2007). Conversely, star formation also destroys dust at differing rates (Draine & Salpeter 1979a,b; McKee 1989; Jones et al. 1996; Dwek 1998; Bianchi & Ferrara 2005; Yamasawa et al. 2011). Along with the ISM, dust is present in substantial quantities alongside gas and metals in the circum-galactic medium (CGM; Bouche et al. 2007; Peebles et al. 2014; Peek et al. 2015.) It is therefore of fundamental importance to the theory of star formation and thus galaxy evolution to understand the nature of all dust processes, such as formation, composition, evolution, and destruction, as well as its observational characteristics, both in the local and distant Universe. Since dust is intimately connected to the conditions of the ISM and the properties of gas (Draine 2003), the dust-to-gas ratio (DTG; Bohlin et al. 1978) is a good indicator of the dust content of a galaxy or gas cloud. The dust-to-metals ratio (DTM; Predehl & Schmitt 1995; Güver & Özel 2009; Watson 2011), which is the DTG corrected for the metallicity of the gas, thus describing the fraction of the total metals that are in the solid dust phase, can reveal more about the nature of the dust itself, its production mechanisms, and the processes by which it evolves.

The evolution of the DTM over cosmic time is a tracer of the history of the interplay between gas and dust in the ISM of galaxies, and its distribution in comparison to metallicity can be used to infer clues about the origin of interstellar dust. If all dust and metals were to be produced in and ejected from stars, one would expect the DTM to remain constant in both time and metallicity (e.g. Franco & Cox 1986). In models, this is often assumed (e.g. Edmunds & Eales 1998),

especially in the local Universe (Inoue 2003), and a fairly constant dust-to-metals ratio is indeed observed (Issa et al. 1990; Watson 2011). At higher redshift, Zafar & Watson (2013) found that the DTM in a sample of foreground absorbers to GRBs and quasars tends not to vary significantly over a wide range of redshifts, metallicities, and hydrogen column densities, proposing a universally constant DTM. Chen et al. (2013) find a slow redshift evolution of DTM in lensed galaxies. These findings suggest that most of the dust is produced ‘instantaneously’ in the ejecta of core-collapse supernova (CCSNe), a result supported by recent models by McKinnon et al. (2016), who find that roughly two-thirds of the dust in MW-like galaxies at  $z = 0$  is produced in Type II SNe. These authors all use the traditional method of measuring DTM: the extinction,  $A_V$ , is compared to the equivalent metal column density,  $\log N(\text{H}) + [\text{M}/\text{H}]$ , where  $[\text{M}/\text{H}]$  is the logged metallicity of the gas (see Eq. 3.2).

Other studies use a different definition of DTM, namely by determining the dust fraction  $\mathcal{F}_d$  from the dust depletion (Sect. 3.2) of metals observed in damped Lyman- $\alpha$  absorbers (DLAs) on sight lines to quasars (Vladilo 2004) and GRBs (De Cia et al. 2013). These studies, unlike those using  $A_V$  as their dust quantifier, claim detections of increasing evolution of the DTM with metallicity. This would suggest that the majority of the dust is formed by growth onto grains in the ISM (Draine 2009) rather than simultaneously together with the metals formed in CCSNe and post-AGB star envelopes. Tchernyshyov et al. (2015) use depletion observations in the Small Magellanic Cloud (SMC) to suggest the trend between DTM and metallicity only occurs below a certain metallicity threshold that depends on gas density. Mattsson et al. (2014) provide a comprehensive discussion on the debate from a theoretical standpoint, suggesting that selection effects or statistical fluctuations could explain the differing observed trends, and Feldmann (2015) attempts to model the observed evolution of dust and metal parameters via production, accretion, destruction, as well as gas infall and outflow from the galaxy, and also reproduce an evolution of the DTM at low metallicities. McKinnon et al. (2016) include stellar production and accretion along with destruction by SN shocks and winds driven by star formation in models that predict the DTM of MW-like galaxies.

GRBs are useful tools with which to study trends in the DTM in the distant Universe. They are extremely bright, allowing their detection even at very high redshift (Tanvir et al. 2009), and occur in galaxies with a wide range of dust content and metallicities (e.g. Fynbo et al. 2008; Mannucci et al. 2011; Krühler et al. 2015; Cucchiara et al. 2015). GRBs are massive stellar explosions (e.g. Galama et al. 1998), the afterglows of which are observed to have featureless synchrotron spectra (Meszaros & Rees 1997). This means that any absorption lines or changes to the shape of the spectrum must originate from an absorbing medium between the explosion site and the observer. Typically they manifest themselves in the form of DLAs in the host galaxy of the GRB. A DLA is defined as an absorbing system with  $\log(N(\text{H I})) > 20.3$  (Wolfe et al. 2005), and it has been found that a large proportion of GRB afterglow spectra that lie in the redshift range for the Ly- $\alpha$  transition to fall into the atmospheric transmission window ( $z > \sim 1.7$ ) do indeed fulfil this criterion (e.g. Krühler et al. 2013; Sparre et al. 2014; Friis et al. 2015). With such a large pool of neutral gas, the ionization fraction is so small that the dominant state of the elements used in this analysis is the singly ionized one (Wolfe et al. 2005; Viegas 1995; Peroux et al. 2007), and the measurements of singly ionized metal species are taken to be representative of the total gas phase abundance of these metals in the DLA. We do commonly detect highly ionized species such as C IV and Si IV, both often saturated, which might call the above assumption into question, and Fox et al. (2004) do indeed use the ratio  $[\text{C IV}/\text{O VI}]$  as proportional to the total  $[\text{C}/\text{O}]$ . However, these lines often show broader velocity structure and/or offsets in central velocity than the low-ionization lines (e.g. Fox et al. 2007), suggesting that the gas with a higher ionization state does not trace the same structure as the low-ionization lines. This issue is also addressed in Ellison et al. (2010), and while they suggest that there may be some ionization corrections below  $\log(N(\text{H I})) < 21$ , they are still low, and only two of the

objects in our sample have a neutral hydrogen column density below this value. We thus make no ionization corrections throughout the paper, and take the low-ionization abundances to be representative.

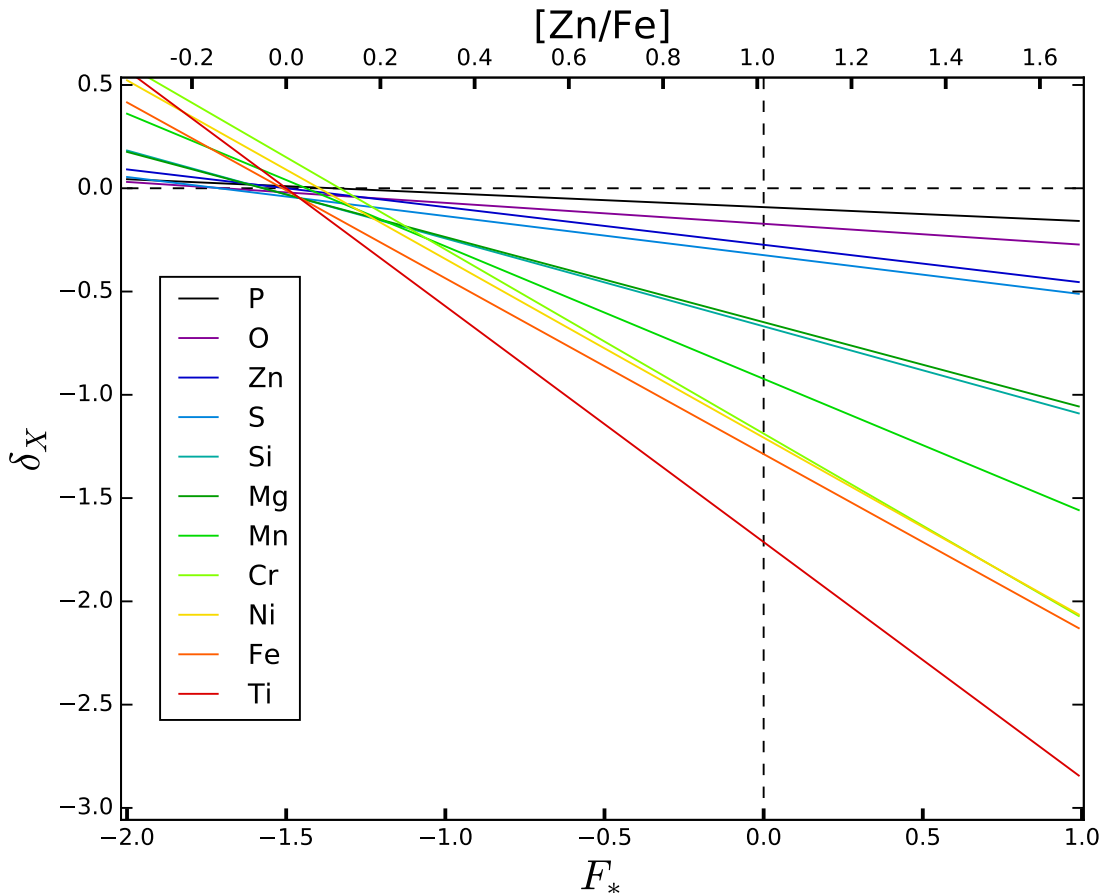


FIGURE 3.1: Depletion  $\delta_X$  is plotted as a function of  $F_*$ . The slope is defined by the parameter  $B$ , and the point of zero-depletion by  $A$ . The elements are listed in order of depletion strength.

In this paper, we present spectral analysis of five previously unpublished GRBs, and we combine them with 14 more GRB-DLAs from the literature, all but three of which have mid- to high-resolution spectroscopy. We compute dust depletion curves using all of the available metals, which we then use to calculate average DTM values, and investigate their relation with metallicity and redshift in order to investigate the evolution of DTM.

The structure of this paper is as follows. In Sect. 3.2 we describe the background and updated methods available to parameterize dust-depletion. The initial sample is presented in Sect. 3.3. In Sect. 3.4 we introduce our method of fitting for depletions in GRB-DLAs, and in Sect. 4.4 we present the results; we discuss the results in Sect. 4.6 and conclude in Sect. 4.7. Throughout the paper we assume the solar abundances from Asplund et al. (2009).

## 3.2 Dust depletion

Using spectroscopy, it is possible to measure the column density of ISM constituents through absorption lines. However, what is achieved here is a measure of the gas phase abundance of that element, as any metal atoms in the dust grains do not contribute to the observed absorption.

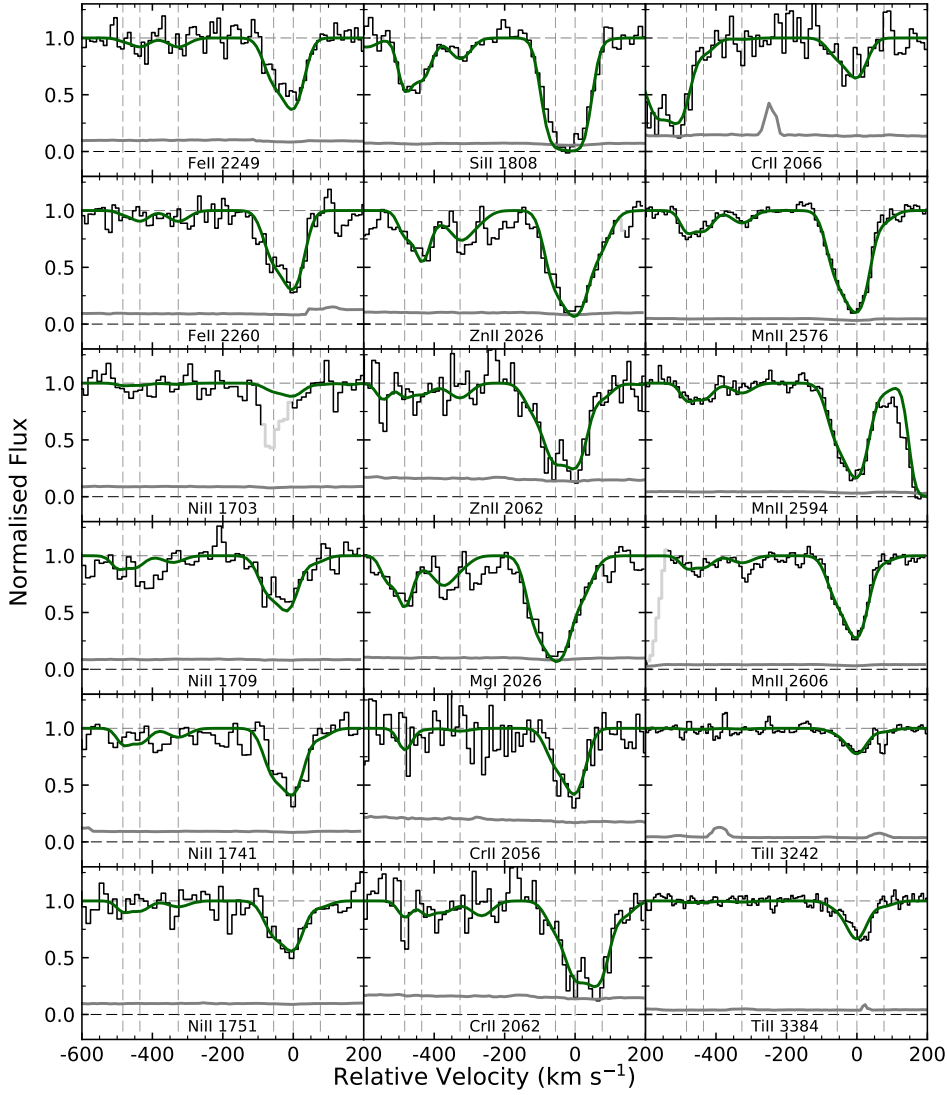


FIGURE 3.2: Metal absorption lines in the X-Shooter spectrum of GRB 120119A. Red dashed lines indicate velocity components. Resolution in VIS arm:  $v = 31.4 \text{ km s}^{-1}$ .

The difference between the observed column and intrinsic, total column density of metal  $X$  is referred to as dust depletion

$$\delta_X = [X/H]_{\text{obs}} - [X/H]_{\text{in}}, \quad (3.1)$$

where a greater amount of element  $X$  is expected to be depleted onto dust grains with increasing negative values of  $\delta_X$ . We use the standard relative abundance notation,

$$[X/Y] = \frac{\log N(X)}{\log N(Y)} - \frac{\log N(X)_{\text{ref}}}{\log N(Y)_{\text{ref}}}. \quad (3.2)$$

To calculate the amount of depletion, we need to know two things: the observed gas-phase abundance of each element, and the total intrinsic (gas + dust) abundance. The observed column densities are obtained from the GRB afterglow spectrum, but the intrinsic values are harder to come by, as we do not know a priori the total column density of a metal in both the gas and solid phase (i.e. dust). It was shown by Savage & Sembach (1996) that different elements deplete

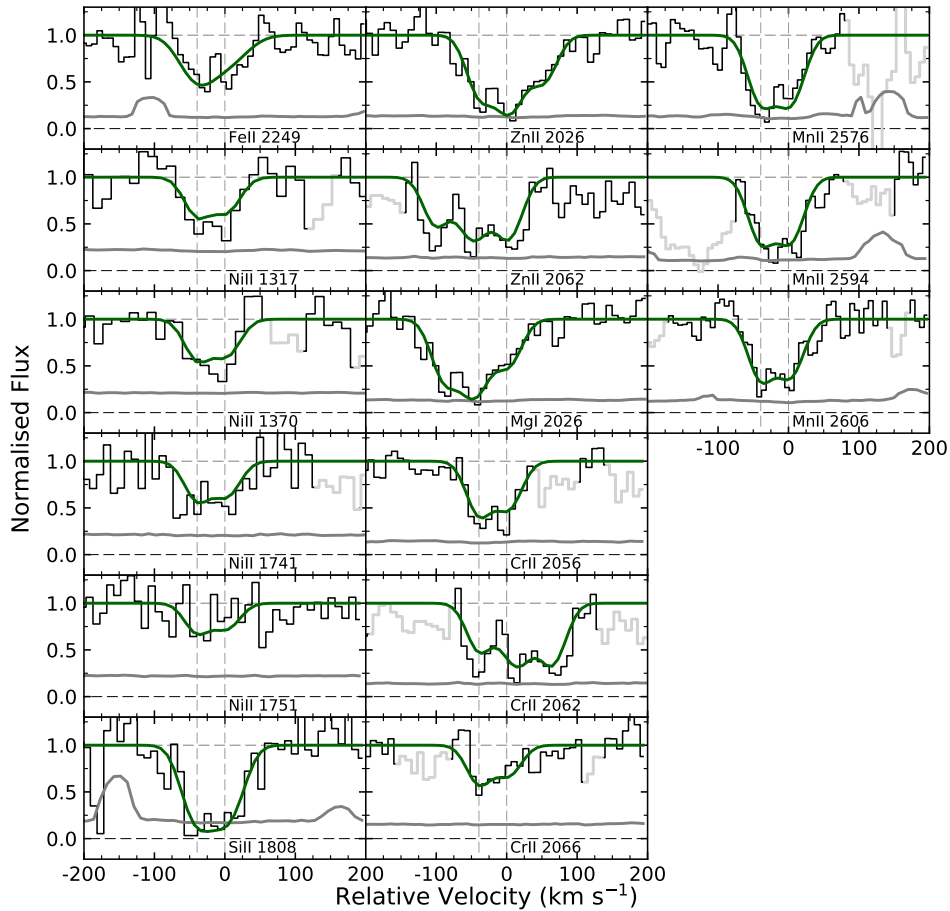


FIGURE 3.3: Metal absorption lines in the X-Shooter spectrum of GRB 120716A. Red dashed lines indicate velocity components. Resolution in VIS arm:  $v = 35.0 \text{ km s}^{-1}$ .

onto dust at different rates. Some elements, such as Fe and Ni, deplete rapidly and are known as refractory elements. Others, such as Zn, P, S, and Si, are almost always entirely in the gas phase and are denoted as volatile. The measured abundance of these volatile elements in this formulation are taken to be a good indicator of the metallicity of the system, and the difference in the relative abundances of a volatile and a refractory element, such as the ratio  $[\text{Zn}/\text{Fe}]$ , is thus a basic quantifier of depletion.

Savage & Sembach (1996) measured the depletions of several elements towards a set of different sight lines in the MW, from the dust-poor warm halo (WH) clouds, increasing in dust content to warm disk+ halo (WDH), warm disk (WD), and finally heavily dusty cold disk (CD) clouds. They reported typical depletion levels of each element for each cloud (Fig. 5 and Table 6 in Savage & Sembach 1996). When investigating depletion in a DLA, fitting each of the MW depletion patterns to the observed relative abundances can be attempted. Since the metallicity and dust-to-metals ratio in the DLA are likely to be different to the MW, they are left as free parameters; the relative abundances expected from the model are adjusted until they best match those of the observed abundances, a method described by Savaglio (2001) and Savaglio et al. (2003). Although these methods provide a basis for depletion studies, it is often found that GRB-DLAs tend not to follow any Local Group depletion patterns particularly well (e.g. D’Elia et al. 2014; Friis et al. 2015).

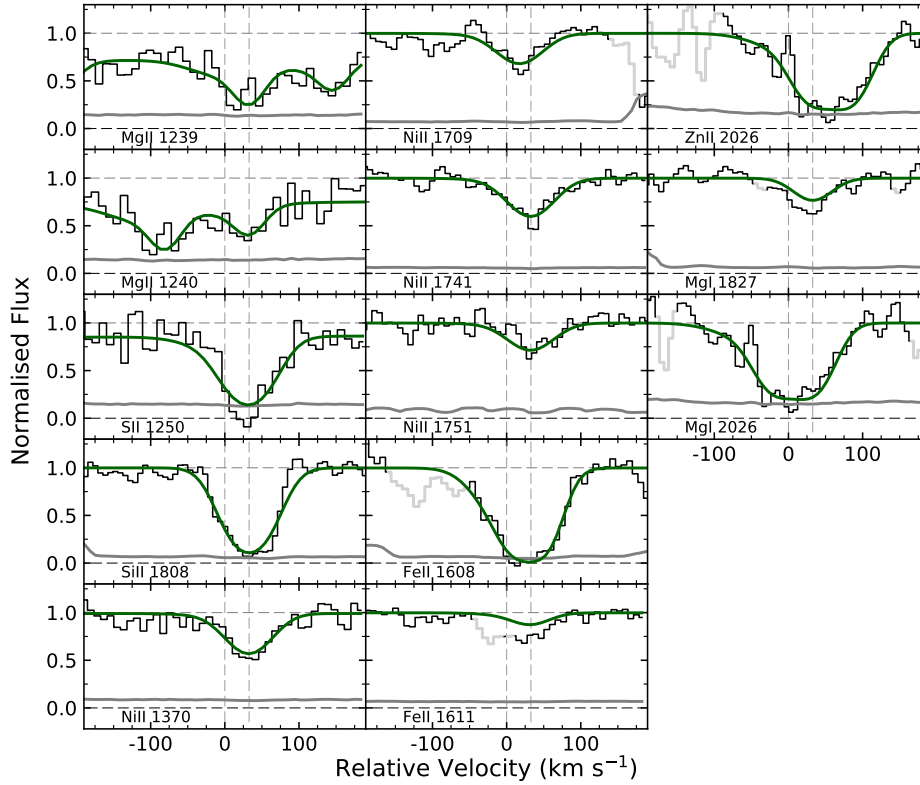


FIGURE 3.4: Metal absorption lines in the X-Shooter spectrum of GRB 120909A. Red dashed lines indicate velocity components. Resolution in VIS arm:  $v = 30.1 \text{ km s}^{-1}$ . The continuum in Mg II 1239/1240 and Si II 1250 is affected by the Lyman- $\alpha$  red damping wing. The extra absorption apparent in Fe II 1611 is from the excited state transition Fe II 5s 1612.

Based on the concept of Savage & Sembach (1996), a more continuous determination of depletion was introduced by Jenkins (2009), based on depletions observed in 17 elements towards stars along 243 MW sight lines. It was found that all elements deplete in a linear fashion, such that the rate of depletion of an element  $X$ ,  $\delta_X$ , can be given as

$$\delta_X = B_X + A_X (F_* - z_X), \quad (3.3)$$

where  $A_X$  is the depletion slope, and  $B_X$  and  $z_X$  are constant offsets. This formulation implies that the difference between the depletion of any two elements should depend only on the value  $F_*$ , the depletion strength factor of the environment. That is, the relative abundances between any set of two or more elements in a single sight line can only be described by one unique value of  $F_*$ , which is then a powerful tool that can be used to calculate an overall, average DTM using multiple elements.

In the Jenkins (2009) formulation,  $F_* = 0$  is given to those sight lines where the least depletion was observed, with  $F_* = 1$  the value for the most depleted MW systems. The  $F_*$  method is also applied to the abundances in the Savage & Sembach (1996) models, with the WH clouds having  $F_* = -0.28$ , whereas  $F_* = 0.90$  in the dusty CD environment.

A study of the Magellanic Clouds (MCs) was presented by Tchernyshyov et al. (2015) who used the  $F_*$  method to ascertain whether depletion slopes and offsets followed the MW trends from Jenkins (2009). Here they combined the offsets  $A_X$  and  $z_X$  into one offset,  $\delta_0$ , which simply describes the level of depletion at  $F_* = 0$ . Compared to the MW, they found differences in the

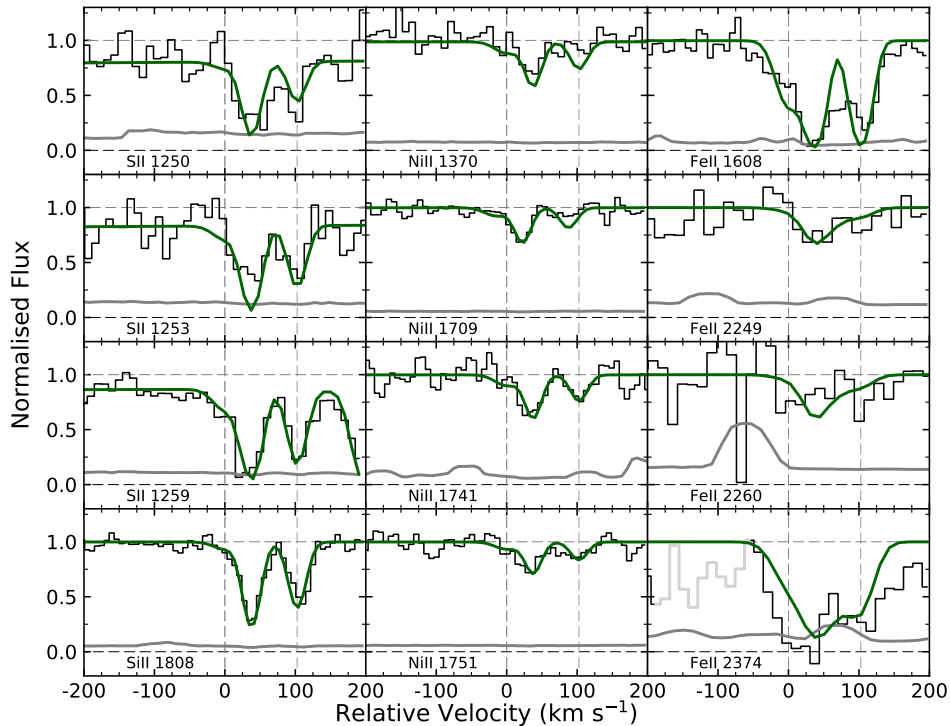


FIGURE 3.5: Metal absorption lines in the X-Shooter spectrum of GRB 130408A. Red dashed lines indicate velocity components. Resolution in VIS arm:  $v = 20.0 \text{ km s}^{-1}$ . The continuum in S II 1250/1253/1259 is affected by the Lyman- $\alpha$  red damping wing.

offsets for the elements P, Zn, Si, Cr, and Fe, and that  $\delta_0$  decreases with metallicity of the sight line. Depletion slope  $A_X$ , however, tends to stay constant. The main interpretation of this is that at lower metallicities, a higher  $F_*$  is needed before metals begin to form dust, although this is based on a fairly small sample covering only the metallicities of the Small and Large Magellanic Clouds.

Recently, the most comprehensive study yet of depletion patterns down to low metallicity and dust content has been conducted by De Cia et al. (2016), detailing depletion sequences of nine elements (P, O, Zn, S, Si, Mg, Mn, Cr, Fe) in 70 QSO-DLAs at redshifts of 1.7-4, and metallicities from the solar value down to  $1/100Z_\odot$ . They use a very similar method to Jenkins (2009): the depletion of each element in each DLA is plotted against  $[\text{Zn}/\text{Fe}]$ , used here as the dust quantifier instead of Jenkins'  $F_*$ , although the two parameters are directly and linearly linked. The Zn is used as a proxy for an undepleted element, but in reality this is not the case. It is corrected for its own depletion by comparing the  $[\text{Zn}/\text{H}]$  and  $[\text{Zn}/\text{Fe}]$  values in the MW. For a measured  $[\text{Zn}/\text{Fe}]$  in a QSO sightline, De Cia et al. (2016) interpolate the MW  $[\text{Zn}/\text{Fe}] - [\text{Zn}/\text{H}]$  relation to find the corresponding Zn depletion. This missing Zn is then added to give a corrected  $[\text{Zn}/\text{Fe}]$  to be used as the final depletion strength indicator for that sight line. To add continuity to the depletion sequences, these QSO data are supplemented with Jenkins' data from the MW, and it can be seen that the high- $z$  data show the same behaviour as – and are a simple continuation of – those from the MW. For each element, De Cia et al. (2016) then use linear regression techniques to fit the depletion sequences and calculate two parameters:  $A$ , the depletion at  $[\text{Zn}/\text{Fe}] = 0$ , and  $B$ , the depletion slope. These depletion sequences are shown in Fig. 3.1. There are distinct clusters of elements: P, O, Zn, and S, which are volatile elements; Cr, Ni, and Fe, which are refractory elements; Si, Mg, and Mn, which lie between the volatile

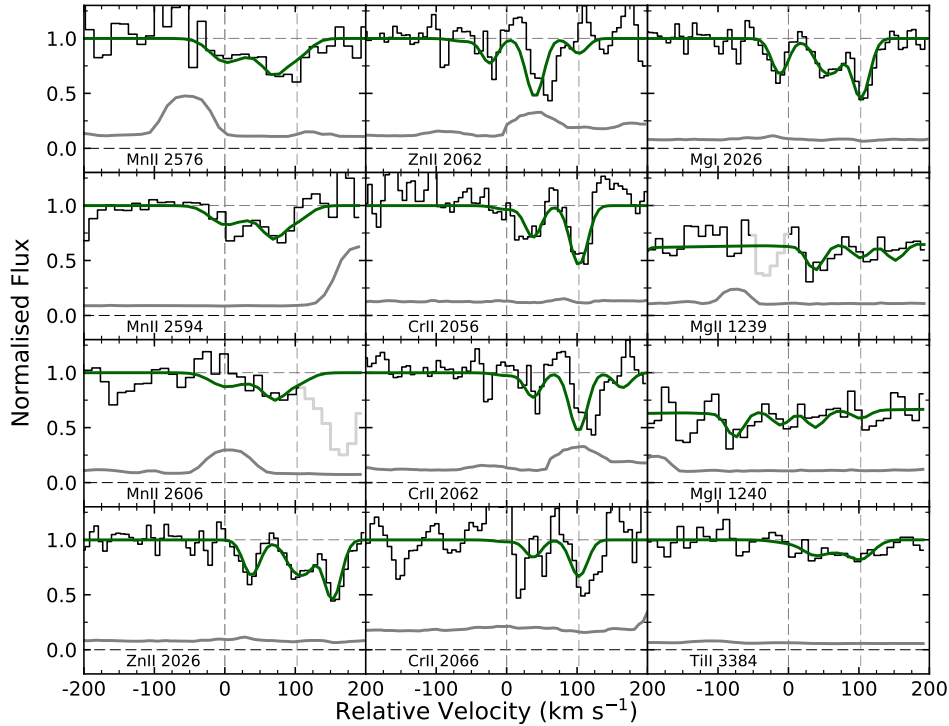


FIGURE 3.6: Metal absorption lines in the X-Shooter spectrum of GRB 130408A. Red dashed lines indicate velocity components. Resolution in VIS arm:  $v = 20.0 \text{ km s}^{-1}$ . The absorption to the right of the Mn II 2606 line is due to telluric absorption.

and refractory elements; and Ti, which seems to lie distinctly below all of the others.

From Fig. 3.1 it can be seen that at  $F_* = 0$  there is still significant depletion ( $\sim 1$  dex), especially in the refractory elements, which shows that even the least depleted MW clouds are more dusty than those in low-metallicity QSO-DLAs. The parameter  $A$  can best be seen as the offset in the relative abundance of the element at the point of no iron depletion,  $[\text{Zn}/\text{Fe}] = 0$ . Since they are all very small, the point at which the depletion starts (i.e.  $\delta_X = 0$ ) is very similar for each element, suggesting that all elements begin forming dust at some distinct threshold in temperature or density.

The analysis from De Cia et al. (2016) shows that the slopes are linear and well determined in the whole range from low metallicity and low dust content right through to the dustiest MW clouds, which we believe is strong evidence that the depletion mechanism works in the same way in all environments, and can indeed always be quantified by a single depletion strength factor. For this reason, we use the slopes from De Cia et al. (2016) for our depletion analysis of the typically low-dust, low-metal GRB-DLA environments in order to calculate DTMs and metallicities, which we describe in Section 3.4.

### 3.3 Sample and data reduction

In order to select our sample, we require GRBs with mid- to high-resolution spectroscopy as this allows us to resolve relatively well the velocity structure of the absorber, thus limiting the effect of unidentified saturation in the lines. The spectrum must also cover the Ly- $\alpha$  line, such that we can verify that it is a DLA, and thus regard any ionization correction as negligible. Finally, we require that the spectrum includes unsaturated detections of at least four singly ionized metals

TABLE 3.1: Hydrogen and metal abundances in our sample of GRB afterglows. Units of column density are  $\log(\text{cm}^{-2})$ .

GRB	$z$	$\log N(\text{Mg})$	$\log N(\text{Si})$	$\log N(\text{P})$	$\log N(\text{Ti})$	$\log N(\text{Cr})$	$\log N(\text{Mn})$	$\log N(\text{Fe})$	$\log N(\text{Ni})$	$\log N(\text{Zn})$	$\log N(\text{S})$
000926	2.04	-	$16.47 \pm 0.05^1$	-	-	$14.34 \pm 0.05^1$	-	$15.60 \pm 0.20^1$	-	$13.82 \pm 0.05^1$	-
050401	2.9	-	$16.5 \pm 0.4^2$	-	-	$14.6 \pm 0.2^2$	-	$16.0 \pm 0.2^2$	-	$14.3 \pm 0.3^2$	-
050730	3.9672	$< 16.08^4$	$15.47 \pm 0.03^4$	-	-	-	-	$15.49 \pm 0.03^3$	$13.69 \pm 0.02^3$	-	$15.11 \pm 0.04^3$
050820A	2.6145	$15.86 \pm 0.05^4$	-	$13.64 \pm 0.04^4$	-	$13.33 \pm 0.02^4$	-	$14.82 \pm 0.12^4$	$13.69 \pm 0.04^4$	$12.96 \pm 0.02^4$	$15.57 \pm 0.04^4$
070802	2.45	-	$16.00 \pm 0.32^5$	-	-	$14.04 \pm 0.40^5$	$13.69 \pm 0.18^5$	$16.16 \pm 0.18^5$	$14.89 \pm 0.28^5$	$13.67 \pm 0.65^5$	-
081008	1.9685	-	$15.75 \pm 0.04^6$	-	-	$13.83 \pm 0.03^6$	-	$15.42 \pm 0.04^6$	$13.74 \pm 0.07^6$	$13.15 \pm 0.04^6$	-
090323	3.567	-	$15.80 \pm 0.05^7$	-	-	-	-	$15.00 \pm 0.05^7$	$14.76 \pm 0.04^7$	$13.57 \pm 0.04^7$	$15.80 \pm 0.02^7$
090809	2.737	$> 16.80^8$	$16.15 \pm 0.07^8$	-	-	-	$13.75 \pm 0.12^8$	$15.75 \pm 0.07^8$	$14.40 \pm 0.07^8$	$13.70 \pm 0.25^8$	-
090926A	2.1071	$> 14.11^9$	$14.80 \pm 0.08^9$	-	-	-	-	$14.86 \pm 0.09^9$	$13.92 \pm 0.13^9$	-	$14.89 \pm 0.10^9$
100219A	4.667	$> 13.72^{10}$	$15.25 \pm 0.25^{10}$	-	-	-	-	$14.73 \pm 0.11^{10}$	-	-	$15.25 \pm 0.15^{10}$
111008A	4.99	-	$> 15.86^{11}$	-	-	-	-	-	-	-	$15.71 \pm 0.09^{11}$
120119A	1.7285	-	$16.67 \pm 0.35^{12}$	-	-	$14.17 \pm 0.11^{11}$	$13.72 \pm 0.08^{11}$	$16.05 \pm 0.05^{11}$	$14.89 \pm 0.18^{11}$	$13.28 \pm 0.21^{11}$	-
120327A	2.8145	$16.34 \pm 0.02^{13}$	$16.36 \pm 0.03^{13}$	$14.19 \pm 0.04^{13}$	$13.18 \pm 0.25^{12}$	$14.21 \pm 0.20^{12}$	$13.99 \pm 0.20^{12}$	$15.95 \pm 0.25^{12}$	$14.77 \pm 0.17^{12}$	$14.04 \pm 0.25^{12}$	-
120716A	2.487	-	$16.48 \pm 0.45^{12}$	-	-	$14.17 \pm 0.02^{13}$	-	$15.78 \pm 0.09^{13}$	$14.61 \pm 0.09^{13}$	$13.40 \pm 0.04^{13}$	$15.74 \pm 0.02^{13}$
120815A	2.358	-	$\geq 16.34^{14}$	-	-	$14.20 \pm 0.26^{12}$	$14.02 \pm 0.26^{12}$	$15.65 \pm 0.45^{12}$	$14.42 \pm 0.22^{12}$	$13.91 \pm 0.32^{12}$	-
120909A	3.929	$\leq 16.55^{12}$	$16.22 \pm 0.32^{12}$	-	-	$13.75 \pm 0.06^{14}$	$13.26 \pm 0.05^{14}$	$15.29 \pm 0.05^{14}$	$14.19 \pm 0.05^{14}$	$13.47 \pm 0.06^{14}$	$\leq 16.22^{14}$
121024A	2.30	-	$> 16.35^{15}$	-	-	-	-	$15.20 \pm 0.18^{12}$	$14.36 \pm 0.13^{12}$	$13.55 \pm 0.32^{12}$	$16.10 \pm 0.18^{12}$
130408A	3.7579	$16.01 \pm 0.21^{12}$	$15.95 \pm 0.22^{12}$	-	-	$14.18 \pm 0.03^{15}$	$13.74 \pm 0.03^{15}$	$15.82 \pm 0.05^{15}$	$14.70 \pm 0.06^{15}$	$13.74 \pm 0.03^{15}$	$> 15.90^{15}$
141028A	2.333	$15.28 \pm 0.27^{12}$	$14.82 \pm 0.33^{12}$	-	-	$12.77 \pm 0.22^{12}$	$13.19 \pm 0.13^{12}$	$15.52 \pm 0.11^{12}$	$14.15 \pm 0.08^{12}$	$12.87 \pm 0.16^{12}$	$15.78 \pm 0.18^{12}$
						$12.98 \pm 0.33^{12}$	$< 13.29^{12}$	$14.23 \pm 0.21^{12}$	$13.34 \pm 0.33^{12}$	$12.38 \pm 0.33^{12}$	-

(1) Savaglio et al. (2003); (2) Watson et al. (2006); (3) Ledoux et al. (2009); (4) Prochaska et al. (2007b); (5) Elíasdóttir et al. (2009); (6) D’Elia et al. (2011); (7) Savaglio et al. (2012); (8) Skúladóttir (2010); (9) D’Elia et al. (2010); (10) Thöne et al. (2013); (11) Sparre et al. (2014); (12) *this work*; (13) D’Elia et al. (2014); (14) Krühler et al. (2013); (15) Friis et al. (2015)

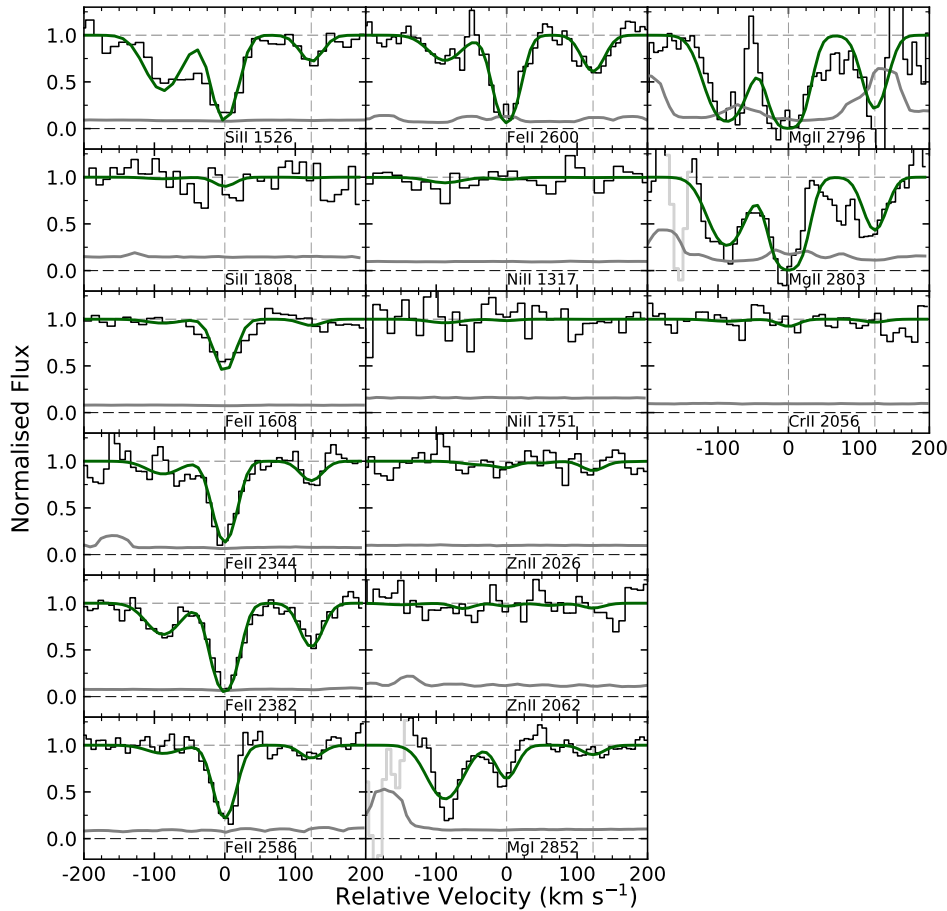


FIGURE 3.7: Metal absorption lines in the X-Shooter spectrum of GRB 141028A. Red dashed lines indicate velocity components. Resolution in VIS arm:  $v = 25.0 \text{ km s}^{-1}$ . The narrow saturated lines in the Mg II 2796/2803 and Mg I 2852 are due to telluric absorption.

in order to increase the precision on a measurement of  $F_*$ .<sup>1</sup>

A state-of-the-art example of an instrument that produces such spectra is X-shooter (Vernet et al., 2011), mounted at ESO’s VLT at Cerro Paranal, Chile. X-shooter operates simultaneously in three spectral arms, namely the bands UVB (3000-5500 Å), VIS (5500-10000 Å), and NIR (10000-25000 Å), thus allowing absorption line metallicity measurements from redshifts  $\geq 1.8$ , and providing a wide spectral range. It operates at a resolving power of around  $R = 8000$ , depending on the arm, slit used, and atmospheric conditions. Twelve GRBs observed with X-shooter pass our selection criteria. Seven of these, GRBs 090809, 090926A, 100219A, 111008A, 120327A, 120815A, and 121024A (references in Table 3.1), have already been published in the literature, and we include them in the sample. In this paper we present the analysis for the remaining five<sup>2</sup>: 120119A, 120716A, 120909A, 130408A, and 141028A (see Sect. 3.3.1). A further two GRBs observed with UVES pass the selection criteria (050730 and 081008, both taken from the literature), and an additional two GRBs observed with Keck

<sup>1</sup>We select GRBs up to the end of 2014. There are more recent GRBs that also pass the selection criteria, but it is beyond the scope of this paper to keep adding to the sample.

<sup>2</sup>Spectra of GRBs 120716A, 120909A, and 130408A have been analysed by Cucchiara et al. (2015), but that work presents column density measurements for only Ly- $\alpha$  and one other element, and does not show line fits and velocity components, as we do here.

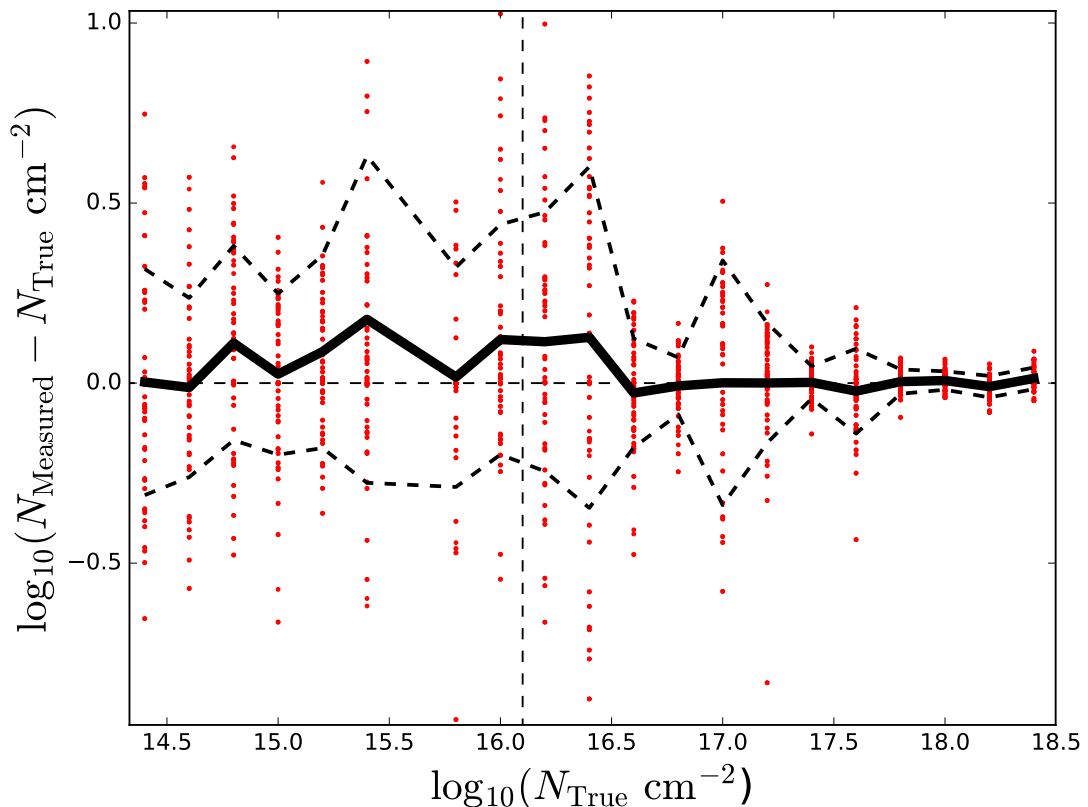


FIGURE 3.8: Difference between the measured column density of Si II  $\lambda 1526$  after convolving with the X-shooter resolution and adding noise at  $S/N = 7.5$ , similar to the lowest quality of our data. The thick black line shows the mean residual, while the dashed curves show the  $1\sigma$  level. The vertical dashed line marks the point at which this line saturates in the original spectrum.

HIRES and ESI have data published and are therefore also included in sample (050820A and 000926, respectively). Unpublished GRBs with Keck high-resolution spectral data cannot be included in the sample since data are not public. In order to help populate the sample with dust-rich sight lines, we add three low-resolution (VLT/FORS) spectra of GRBs 050401, 070802 and 090323, which have high  $N(\text{H})$ , high  $A_V$ , and high metallicity, respectively. However, given the uncertainty in the derived column densities for these GRBs, we distinguish them from the rest of the sample when presenting our results. The final sample of 19 GRBs along with references is presented in Table 3.1; the H I measurements are given in Table 3.2.

### 3.3.1 New GRB Spectra

For the spectra of GRBs 120119A, 120716A, 120909A, 130408A, and 141028A we perform our own analysis on the spectra obtained from X-shooter. The general method used to reduce the raw spectra is based on the standard X-shooter pipeline (Goldoni et al. 2006; Modigliani et al. 2010), which we modify in accordance with the procedures outlined in Krühler et al. (2015), including a correction for telluric absorption using the Molecfit software (Smette et al. 2015). To normalize, we select points on the continuum unaffected by absorption lines, and fit a spline function. Owing to good seeing, the measured resolving power is often larger than the value determined from arc lamp exposures (see e.g. Krühler et al. 2013). We therefore follow the standard procedure, which is to measure the velocity resolution from unsaturated, single telluric

lines. Since there are no telluric lines in the UVB, we use the resolution of those measured in the other two arms, calculating the resolution in the UVB using known conversion factors in line with Fynbo et al. (2011). We perform Voigt-profile fits on the absorption lines using the line-fitting software `VPFit v. 10.2`<sup>3</sup>. At resolutions typically around  $30 \text{ km s}^{-1}$ , we often resolve multiple velocity components, each with distinct  $b$ -parameters. We determine the nature of any such components by fitting singly ionized, unsaturated, and unblended transitions; e.g. Fe II  $\lambda 1611$ , Ni II  $\lambda \lambda 1751, 1741$ , Si II  $\lambda 1808$ , and Mn II  $\lambda 2606$  are often useful transitions. We then fix redshift,  $z$ , and broadening parameter,  $b \text{ km s}^{-1}$ , for each velocity component across all species, leaving column density  $N \text{ cm}^{-2}$  as the free parameter. We present the resulting column densities in Table 3.1, and present a selection of line fits for each GRB in Appendix A.

### 3.3.2 Hidden saturation

An issue that commonly plagues absorption line astronomy, particularly at mid to low resolution and poor signal-to-noise ratio (S/N), is that of hidden saturation. This occurs when a line that is in reality marginally saturated is smoothed out by the instrument resolution and noise to appear unsaturated in the actual observed spectrum. The pitfalls of this have been well documented by e.g. Prochaska (2006); Rafelski et al. (2012); Jorgenson et al. (2013) and Cucchiara et al. (2015), who typically ignore any lines that show any sign that they could be saturated. However, because the basis of our analysis is the use of multiple species to constrain the metallicity and dust depletion, we require measurements of as many lines as possible in the often low S/N GRB spectra.

To investigate and quantify the effect this has on our results we run a set of simulations, similar to those of Jorgenson et al. (2013) who used the apparent optical depth method (AODM). Initially we take the worst-case scenario, and assume the lowest S/N and highest resolution in our GRB sample spectra, which corresponds to  $7.5$  and  $35.0 \text{ km s}^{-1}$ , respectively, in the case of GRB 120716A. We then simulate a set of absorption lines of one transition, namely Si II  $\lambda 1526$ , at a common  $b$ -parameter but with increasing column density so as to straddle the theoretical point at which that line saturates. We choose a  $b$ -parameter of  $10 \text{ km s}^{-1}$  as this represents the smallest value typically seen with higher resolution instruments, with smaller components typically blended (Jorgenson et al. 2013). We create lines starting from unsaturated column densities of  $14.4 \text{ cm}^{-2}$  up to heavily saturated column densities of  $18.4 \text{ cm}^{-2}$ , and convolve with the X-shooter resolution measured in GRB 120716A. We add Gaussian noise at a S/N of 7.5 and use `VPFit` to fit a Voigt profile and measure the column density. The results for 100 trials, with different noise added each time, are plotted in Fig. 3.8. The thick black curve shows that on average the measured column densities are always within 0.2 dex of the true value, with a standard deviation around 0.4 dex. Above  $16.6 \text{ cm}^{-2}$  there is on average no deviation, and above  $14.4 \text{ cm}^{-1}$  the data points have a standard deviation lower than 0.1 dex, reflecting the fitting of the damping wings.

From these simulations, we find that there is only a small loss of accuracy of our column density measurements when lines are saturated, although we do continue to avoid using strongly saturated lines, especially when several components are evident. We also find that the uncertainty on the column densities provided by `VPFit` is often an underestimate compared to that from our simulations. To find the uncertainty for all of our measurements, including those on lines with potential hidden saturation, or evident but mild saturation, we thus conduct a second round of simulations. For each GRB, we take the S/N and resolution measured from the spectrum and simulate the line with the above method 100 times, but this time for only one unsaturated column density of  $15.8 \text{ cm}^{-2}$ . We take the standard deviation of our measurements

<sup>3</sup>VPFit: <http://www.ast.cam.ac.uk/rfc/vpfit.htm>

as the error on a single line measurement for that GRB. For species with multiple lines used, we add the errors from each line in quadrature.

## 3.4 Method

### 3.4.1 Depletion model fitting

Using the concept of linear depletion sequences and  $F_*$  from Jenkins (2009), De Cia et al. (2016) use the observable  $[\text{Zn}/\text{Fe}]$  as their dust indicator. It is possible to directly translate between the two with the relation  $F_* = 1.48 \times [\text{Zn}/\text{Fe}] - 1.50$ . To avoid confusion between  $[\text{Fe}/\text{Zn}]$  as an intrinsic measured value, and “adjusted”  $[\text{Fe}/\text{Zn}]$  as a dust indicator, we use  $F_*$  as our depletion strength factor. For a given metallicity and dust depletion strength, the relative abundance in element  $X$  that we expect to measure according to the model is thus

$$[X/\text{H}]_{\text{exp}} = \delta_X + [\text{M}/\text{H}] = A + B \frac{(F_* - 1.50)}{1.48} + [\text{M}/\text{H}], \quad (3.4)$$

where  $[\text{M}/\text{H}]$  is the metallicity of the system, and  $A$  and  $B$  are the updated linear depletion parameters from De Cia et al. (2016). In a similar way to Savaglio et al. (2003), we vary  $F_*$  and  $[\text{M}/\text{H}]$  to minimize the  $\chi^2$  parameter between the observed abundances and those expected from the model, thus achieving a best fit depletion strength and metallicity. The  $1\sigma$  errors on the parameters are calculated for a single parameter of freedom. Typically, volatile elements such as Zn, P, S, and Si are used as metallicity tracers, often left uncorrected for dust (e.g. Cucchiara et al. 2015). Our method goes one step further: with the large spectral range of X-shooter, we use the information from all of the possible species to fit for dust depletion and thus retrieve a metallicity. We are therefore less sensitive to the pitfalls of only using a particular metallicity tracer.

The errors on  $F_*$  and  $[\text{M}/\text{H}]$  are dependent on the errors on the column densities of H I, each individual element, and on the number of elements included in the dust depletion curve fits. Therefore, when only four elements are available or when the column density measurements are not tightly constrained, the uncertainty on the metallicity and  $F_*$  can be quite large. The 2D chi-squared contour plots are provided in Appendix B. The shape of these plots show elongated confidence regions, which can be seen as a degeneracy between the two parameters. In most cases  $F_*$  and  $[\text{M}/\text{H}]$  are still well constrained, and when this is not the case it is reflected in large errors, for example in GRB 050401.

Unfortunately, De Cia et al. (2016) did not publish measurements for Ni or Ti. Nickel in particular is measured in the majority of our spectra; it is a strongly refractory element with depletion properties similar to Fe, and provides valuable information on the dust content of the DLA. To calculate Zn depletion, De Cia et al. (2016) use the Jenkins (2009) MW data and a least-squares method to fit the slope between  $[\text{Zn}/\text{Fe}]$  and  $[\text{Zn}/\text{H}]$ . We use the same technique with Ni and Ti, using column densities from Jenkins (2009) and orthogonal distance regression to linearly fit the data and retrieve  $A$  and  $B$  parameters. We have seen that the slopes measured down to low dust content are compatible with those measured only in the Galaxy to within the uncertainties, and as such we trust that our Ni and Ti  $A$  and  $B$  values also follow this trend, and provide model values consistent with those for the other elements.

#### 3.4.1.1 Nucleosynthesis

Dust depletion analysis relies on the difference between an observed and an expected, intrinsic abundance for each metal. We use the solar abundances from Asplund et al. (2009) as our reference. This could, however, lead to errors in the depletion calculation. Similar to the composition

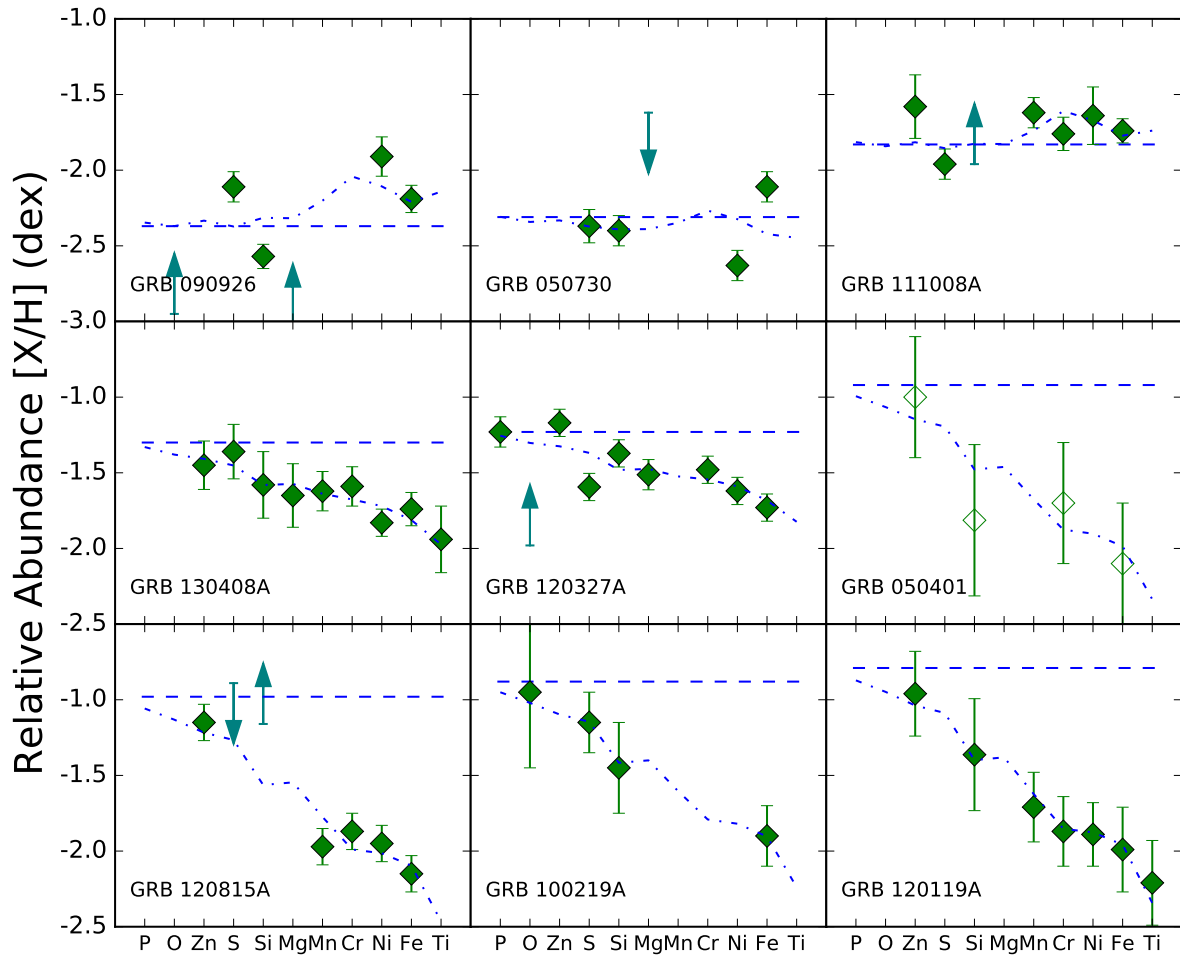


FIGURE 3.9: Dust depletion fits for the nine lowest metallicity GRB-DLAs in our sample. The diamond points are the observed relative abundances, the dot-dashed line follows the expected depletion at a strength of the best fit  $F_*$ , and the dashed line represents the best fit metallicity. Unfilled markers represent low-resolution spectral data (we continue this in all following plots), and squares with up (down) arrows represent lower (upper) limits.

of dust grains, it is perfectly logical to assume that intrinsic abundances in a qqq high-redshift DLA are somewhat different to those observed in the Sun.

One of the most common nucleosynthetic effects at high redshift and low metallicity is an overabundance of  $\alpha$ -elements such as O, Si, S and Mg, in comparison to Fe, often denoted by the factor  $[\alpha/\text{Fe}]$ . The De Cia et al. (2016) depletion patterns have been corrected for these effects, and we adopt their method of applying corrections in our work. In short, this involves applying the observed trend between  $[\text{Zn}/\text{Fe}]$  and  $[\text{Zn}/\text{H}]$  to use  $[\text{Zn}/\text{Fe}]$  as a basic proxy to estimate metallicity. We then use conversions provided by De Cia et al. (2016) which show the nucleosynthetic correction to the abundances at that  $[\text{Zn}/\text{Fe}]$ , based upon their observations alongside those by Lambert (1987); McWilliam (1997); Wheeler et al. (1989), for  $\alpha$ -enhancement, and Wheeler et al. (1989); Mishenina et al. (2015); Battistini & Bensby (2015) for Mn.

Vladilo et al. (2011) calculate the reference abundances in a more theoretical way, using galaxy evolution models to predict metal abundances. It would be interesting to see how such an approach affected our results, but such an analysis is beyond the scope of this paper.

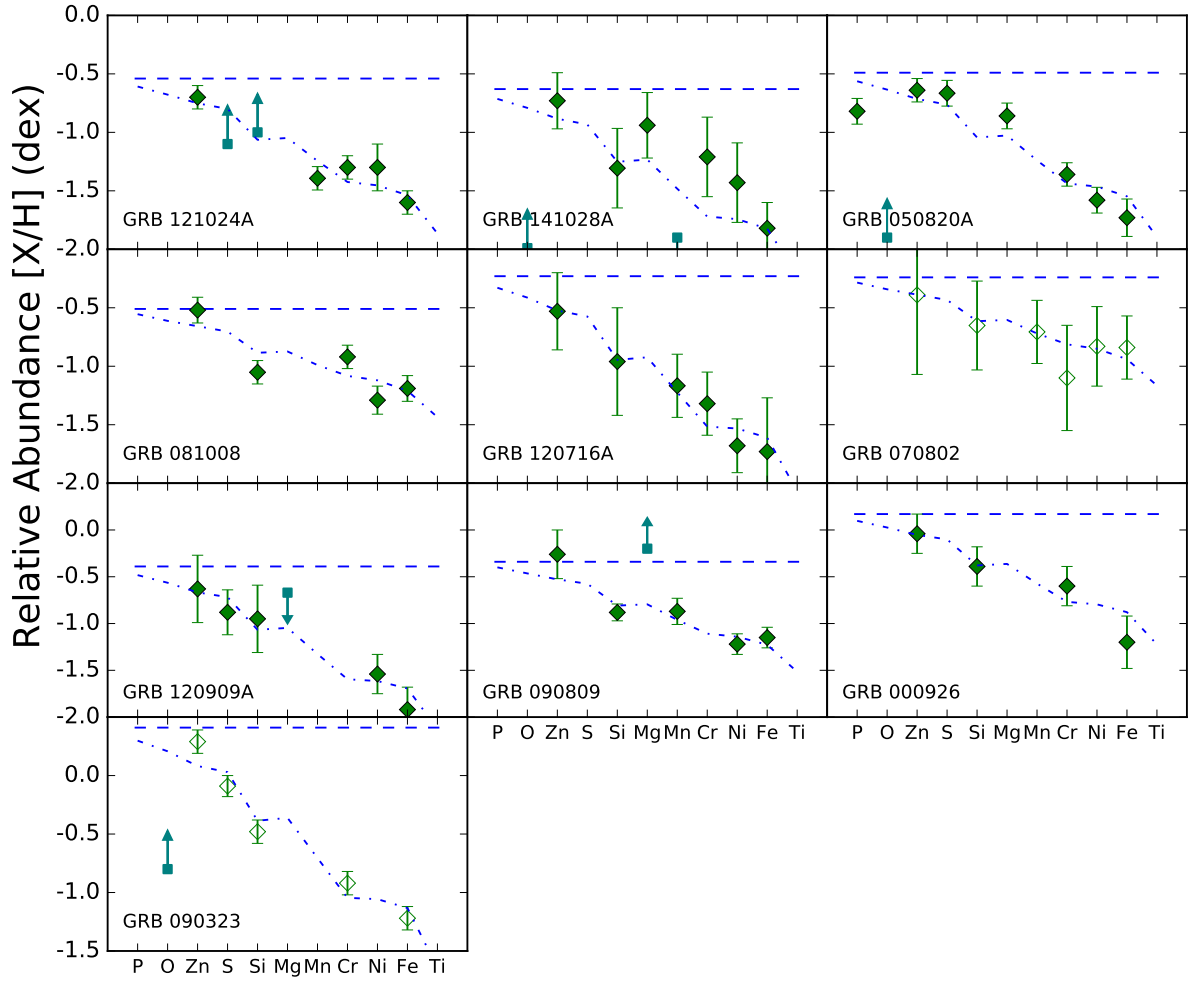


FIGURE 3.10: A continuation of Fig. 3.9 for the ten GRB-DLAs with highest metallicity.

### 3.4.2 Dust-to-Metals Ratio

Rather than comparing dust and metal quantities measured by different means (e.g. Zafar & Watson 2013), or by using only one refractory element to trace the dust, we use the depletion strength factor  $F_*$  along with our best fit  $[M/H]$  and measured  $N(H)$  to calculate the total column densities in dust phase for all 11 elements, including those not measured in the spectrum:

$$N(X)_{\text{dust}} \approx N(H) 10^{[X/H]_{\odot}} 10^{[M/H]} (1 - 10^{\delta_X}) \text{cm}^{-2}, \quad (3.5)$$

where  $\delta_X$  is the depletion in element X as calculated from the best fit  $F_*$ . We can then sum over the elements to find the total dust column density in terms of atoms in the dust phase per  $\text{cm}^2$ .

$$N(\text{dust}) \approx N(H) \frac{Z}{Z_{\odot}} \sum_X 10^{[X/H]_{\odot}} (1 - 10^{\delta_X}) \text{cm}^{-2}, \quad (3.6)$$

and similarly for the total metal column:

$$N(\text{metals}) \approx N(H) \frac{Z}{Z_{\odot}} \sum_X 10^{[X/H]_{\odot}} \text{cm}^{-2}, \quad (3.7)$$

TABLE 3.2: Results of the fitting of the  $F_*$  depletion model to metal column densities from 19 GRB-DLAs. Given uncertainties are at the  $1\sigma$  level.

GRB	$A_V$ (mag)	$\log(N(\text{H}) \text{ cm}^{-2})$	$F_*$	[M/H]	$\mathcal{DTM}$
000926	$0.38 \pm 0.05^1$	$21.30 \pm 0.20$	$-0.28 \pm 0.18$	$0.17 \pm 0.34$	$0.76 \pm 0.07$
050401	$0.45 \pm 0.035^2$	$22.60 \pm 0.30$	$-0.26 \pm 0.31$	$-0.92 \pm 0.68$	$0.76 \pm 0.09$
050730	$\leq 0.17^2$	$22.10 \pm 0.10$	$-1.38 \pm 0.07$	$-2.31 \pm 0.18$	$0.19 \pm 0.02$
050820A	$0.27 \pm 0.05^3$	$21.05 \pm 0.10$	$-0.27 \pm 0.07$	$-0.49 \pm 0.10$	$0.76 \pm 0.06$
070802	$1.23 \pm 0.05^4$	$21.50 \pm 0.20$	$-0.69 \pm 0.18$	$-0.24 \pm 0.80$	$0.59 \pm 0.06$
081008	$\leq 0.08^4$	$21.11 \pm 0.10$	$-0.69 \pm 0.06$	$-0.51 \pm 0.17$	$0.59 \pm 0.04$
090323	$0.10 \pm 0.04^2$	$20.72 \pm 0.09$	$0.30 \pm 0.07$	$0.41 \pm 0.11$	$0.95 \pm 0.07$
090809	$0.11 \pm 0.04^5$	$21.40 \pm 0.08$	$-0.47 \pm 0.07$	$-0.34 \pm 0.25$	$0.68 \pm 0.05$
090926A	$\leq 0.01^6$	$21.60 \pm 0.07$	$-1.7 \pm 0.07$	$-2.37 \pm 0.16$	$0.00 \pm 0.01$
100219A	$0.15 \pm 0.03^7$	$21.14 \pm 0.15$	$-0.31 \pm 0.22$	$-0.88 \pm 0.33$	$0.74 \pm 0.07$
111008A	$0.10 \pm 0.05^7$	$22.30 \pm 0.06$	$-1.58 \pm 0.06$	$-1.83 \pm 0.16$	$0.05 \pm 0.01$
120119A	$1.06 \pm 0.02^8$	$22.44 \pm 0.12$	$-0.14 \pm 0.11$	$-0.79 \pm 0.42$	$0.80 \pm 0.06$
120327A	$\leq 0.02^8$	$22.01 \pm 0.09$	$-0.98 \pm 0.05$	$-1.23 \pm 0.08$	$0.44 \pm 0.03$
120716A	$0.30 \pm 0.15^5$	$21.88 \pm 0.08$	$0.11 \pm 0.16$	$-0.23 \pm 0.55$	$0.88 \pm 0.08$
120815A	$0.08 \pm 0.02^8$	$21.95 \pm 0.10$	$-0.20 \pm 0.07$	$-0.98 \pm 0.22$	$0.78 \pm 0.06$
120909A	$0.16 \pm 0.04^8$	$21.61 \pm 0.06$	$0.01 \pm 0.17$	$-0.46 \pm 0.36$	$0.85 \pm 0.07$
121024A	$0.21 \pm 0.03^8$	$21.85 \pm 0.15$	$-0.34 \pm 0.06$	$-0.54 \pm 0.18$	$0.73 \pm 0.05$
130408A	$0.22 \pm 0.03^8$	$21.76 \pm 0.03$	$-0.91 \pm 0.06$	$-1.30 \pm 0.19$	$0.48 \pm 0.04$
141028A	$0.13 \pm 0.09^5$	$20.55 \pm 0.07$	$-0.18 \pm 0.17$	$-0.50 \pm 0.38$	$0.79 \pm 0.07$

(1) Starling et al. (2007); (2) Schady et al. (2011); (3) Schady et al. (2012); (4) Greiner et al. (2011); (5) *this work*; (6) Rau et al. (2010); (7) Bolmer et al. *in prep*; (8) Greiner et al. *in prep*.

with  $Z/Z_\odot = 10^{[M/H]}$ . We then take the ratio between the dust and total metal column densities, to find a dust-to-metals ratio for the DLA. We can see that metallicity and  $N(\text{H})$  cancel out, such that the DTM calculation is independent of the best fit metallicity and hydrogen column density.

$$\text{DTM} = \frac{N(\text{dust})}{N(\text{metals})} = \frac{\sum_X 10^{[X/H]_\odot} (1 - 10^{\delta_X})}{\sum_X 10^{[X/H]_\odot}}, \quad (3.8)$$

As is customary in DTM analysis, we normalize our values to that of the MW. We compute a Galactic DTM using the same procedure as outlined above, assuming an  $F_*$  of 0.5, as this is the average found in the 243 J09 lines of sight. We denote the MW-normalized value as  $\mathcal{DTM}$ .

We calculate the error on  $\mathcal{DTM}$  by propagating those from the best fit depletion through Eq. 3.8. In particular, the error on the metal fraction,  $10^{\delta_X}$ , is  $10^{\delta_X} \ln 10 \alpha_{\delta_X}$ , where  $\alpha_{\delta_X}$  is the error on the depletion in  $X$ . This is then propagated in quadrature with those from the reference abundances.

### 3.5 Results

The depletion curves for each GRB-DLA are shown in Figs. 3.9 and 3.10, the results of which are presented in Table 3.2, including output values for  $F_*$ , metallicity, and dust-to-metals ratio. The 1, 2, and  $3\sigma$  confidence intervals for the best fit  $F_*$  and  $Z$  values are shown in Figs 3.16 - 3.33.

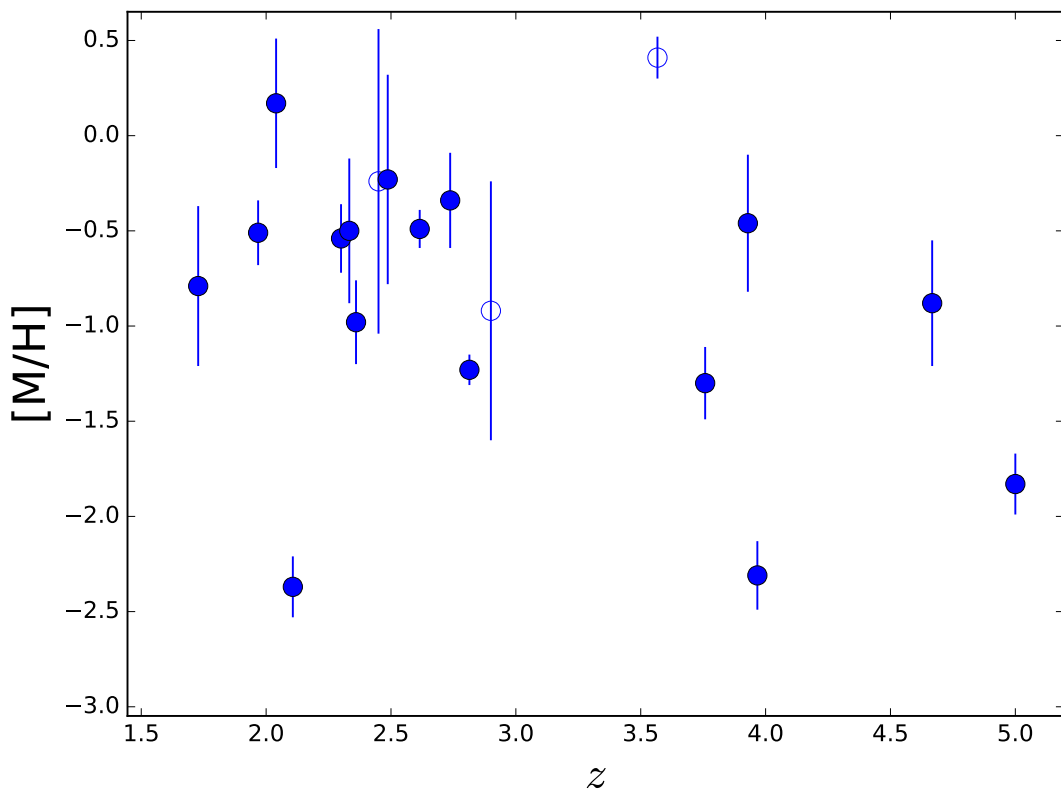


FIGURE 3.11: The metallicity  $[M/H]$  as a function of redshift. Open symbols are those taken from low-resolution spectra.

### 3.5.1 Metallicity

We present dust-corrected metallicities for the 19 GRB-DLAs, including 5 previously unpublished objects. The metallicities range from the very metal-poor  $[M/H] = -2.37$  in GRB 090926A to the supersolar  $[M/H] = 0.41$  in GRB 090323, with a median of  $[M/H] = -0.63$ , which is equal to  $0.25 Z_{\odot}$ , similar to the SMC. The metallicities for all of the GRBs in this sample were presented by Cucchiara et al. (2015) using the apparent optical depth (AOD) method to measure column density. Our metallicities tend to agree with those from that work, although they are typically slightly higher, due to the fact that we make a correction for dust depletion. They find a weak decrease in metallicity with redshift. The metallicity as a function of redshift for our sample is shown in Fig. 3.11. There is no significant trend, although we do note that excluding the low-resolution, supersolar data point at redshift 3.6, there could be a slight decrease in metallicity with redshift, as one would expect given the evolution of galaxies over cosmic time.

The metallicities we derive tend to have a larger uncertainty than those often quoted for GRB-DLAs. Most published metallicities do not account for dust depletion, assuming that volatile elements are good metallicity tracers as they do not deplete strongly into dust. We quote our metallicities with the knowledge that even the most volatile elements deplete to some degree, and in a linear fashion with  $F_*$ , thus giving rise to a larger uncertainty due to a degeneracy between  $[M/H]$  and  $F_*$ . We note that GRBs with detections of numerous species tend to produce a smaller uncertainty on the metallicity than those with only four, since the degeneracy can better be disentangled.

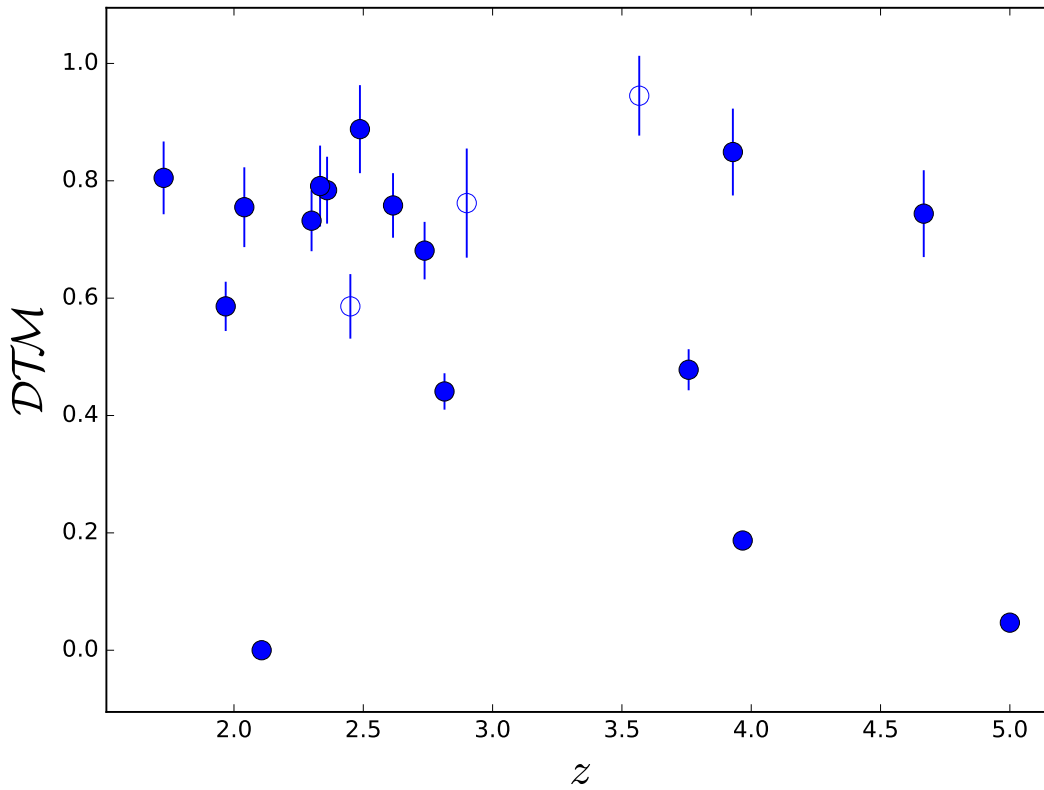


FIGURE 3.12: The  $\mathcal{DTM}$  as a function of redshift.  $z$  error bars are too small to be displayed. There does not seem to be any evolution over the redshift range of 1.7-5, but no conclusions can be drawn with such a small sample.

### 3.5.2 Dust-to-Metals ratio

The  $F_*$  values have a mean of  $-0.52$ , which equates to a  $[\text{Zn}/\text{Fe}]$  of  $0.66$ ,  $0.6$  dex lower than the mean Galactic value of  $1.22$ . This is reflected in a mean  $\mathcal{DTM}$  of  $0.62$ , while the median is  $0.74$ . The standard deviation of  $\mathcal{DTM}$  is  $0.27$ , such that the mean differs from the Galactic  $\mathcal{DTM}$  by nearly  $2\sigma$  while the median is lower at just below  $1\sigma$  significance. This result is similar to the QSO-DLA results from De Cia et al. (2016), whose mean and standard deviation are  $0.70$  and  $0.26$  respectively. GRB 090926A is the only DLA which shows no dust depletion with  $F_* = -1.7$ , which lies to the left of the point where all the depletion slopes cross the axis of zero depletion in Fig. 3.1.

Fig. 3.12 shows the  $\mathcal{DTM}$  plotted against redshift. From this small sample, we don't see any significant trend with redshift. This result is consistent with the hydrodynamical simulations of McKinnon et al. (2016), who find no evolution in the  $\mathcal{DTM}$  at redshifts  $z \geq 1$ . In Fig. 3.13, we plot our  $\mathcal{DTM}$  against metallicity, and find a positive correlation between the two with a Spearman's Rank of  $\rho = 0.63$ , which with 19 data pairs leads to a false-correlation probability of  $0.004$ . There is a potential flattening of the relation, such that above  $[\text{M}/\text{H}] = -1$  there is no real correlation. The potential reasons for this are discussed in the following section.

## 3.6 Discussion

### 3.6.1 The Origin of Dust

Fig. 3.13 shows that the dust-to-metals ratio increases with metallicity. Typically, this would support the view that the dust is formed by grain growth in the ISM (Draine 2009). Mattsson et al. (2014) can also explain this scenario in terms of dust created in stars and supernovae, and then kept in balance by ISM grain growth counteracting dust destruction mechanisms. We also notice a potential flattening of this trend above metallicities of  $0.1Z_{\odot}$ . This flattening is the opposite to what is predicted in the models of Mattsson et al. (2014) and Mattsson (2016) where the DTM is fairly constant (and low) until a critical metallicity of  $0.1 Z_{\odot}$  at which point dust production via grain growth is kick-started and the DTM grows towards the Galactic value at solar metallicity. Our observed trend can instead be explained by a higher rate of dust destruction at lower metallicities. As noted in De Cia et al. (2013), this could be due to the star forming environments that GRBs are known to trace (e.g. Savaglio et al. 2009), which are somewhat different to the solar-like environment of Mattsson (2016). The strong radiation fields in such environments produced by young OB stars and shocks from supernovae (SNe) may destroy dust faster than it can be created by grain growth when the metallicity is low. Another possibility is that the GRB-DLAs are actually tracing dust in the CGM rather than the ISM of their host galaxies where dust evolution is likely to be somewhat different to that in the ISM models referred to previously. Typically, however, the DLAs are located a few hundred parsecs from the GRB site itself (e.g. Hartoog et al. 2013; D’Elia et al. 2014; Friis et al. 2015), and thus located in the ISM of the GRB’s host galaxy.

The amount of dust along the line of sight can also be measured by the effect it has on the spectral energy distribution (SED) of a GRB afterglow. Specifically, the SED is ‘reddened’, and this reddening can be expressed as the total extinction in the  $V$ -band,  $A_V$ . The values for  $A_{V;SED}$  are found by fitting broadband SEDs from the optical to the X-ray regimes (see e.g. Greiner et al. 2011; Schady et al. 2012; Covino et al. 2013; and upcoming papers Bolmer et al. and Greiner et al, both *in prep*). For all bursts from 2007 onwards, we use optical/NIR data from the seven-channel imager GROND (Greiner et al. 2008), and X-ray data from the X-ray Telescope (XRT; Burrows et al. 2005) on board *Swift* (Gehrels et al. 2004). For the pre-GROND bursts, see Schady et al. (2011). A simple power-law or broken power-law is fit to the observed data, and ‘missing’ flux in the bluer visible bands is attributed to dust. This reddening is fit with one of three different extinction laws, namely those from the SMC, LMC, and MW (Pei 1992), and is described by the colour excess,  $E(B - V)$ . This is converted into  $A_{V;SED}$  via the relation

$$A_V = R_V E(B - V), \quad (3.9)$$

where  $R_V$  is the total-to-selective extinction, and is fairly well known for the Local Group extinction curves at an average of 3.08, 3.16, and 2.93 for the MW, LMC and SMC, respectively. It includes silicates and carbonaceous grains and depends largely on the grain-size distribution. Typically, these Local Group extinction laws produce a good fit to GRB SEDs (Schady et al. 2010; Kann et al. 2010; Greiner et al. 2011), although a more complex dust model might fit the extinction curves better. Although the best fit  $A_V$  varies slightly depending on which curve is used, the use of NIR and X-ray data in the SED fit typically provides good constraints on  $A_{V;SED}$ . The extinction law used for the final  $A_{V;SED}$  measurement is that which results in the best  $\chi_{red}^2$  value.

In Fig. 3.14, we plot the metals-to-dust ratio according to the definition of Zafar & Watson (2013), which uses the  $A_V$  as a dust tracer. As in that work, we see no strong trend with metallicity, at odds with the result from Fig. 3.13. We note that our mean metals-to-dust of  $21.65 \text{ cm}^{-2} A_V \text{ mag}^{-1}$  is higher than that from their sample, and we see a higher spread of  $\sigma = 0.46$

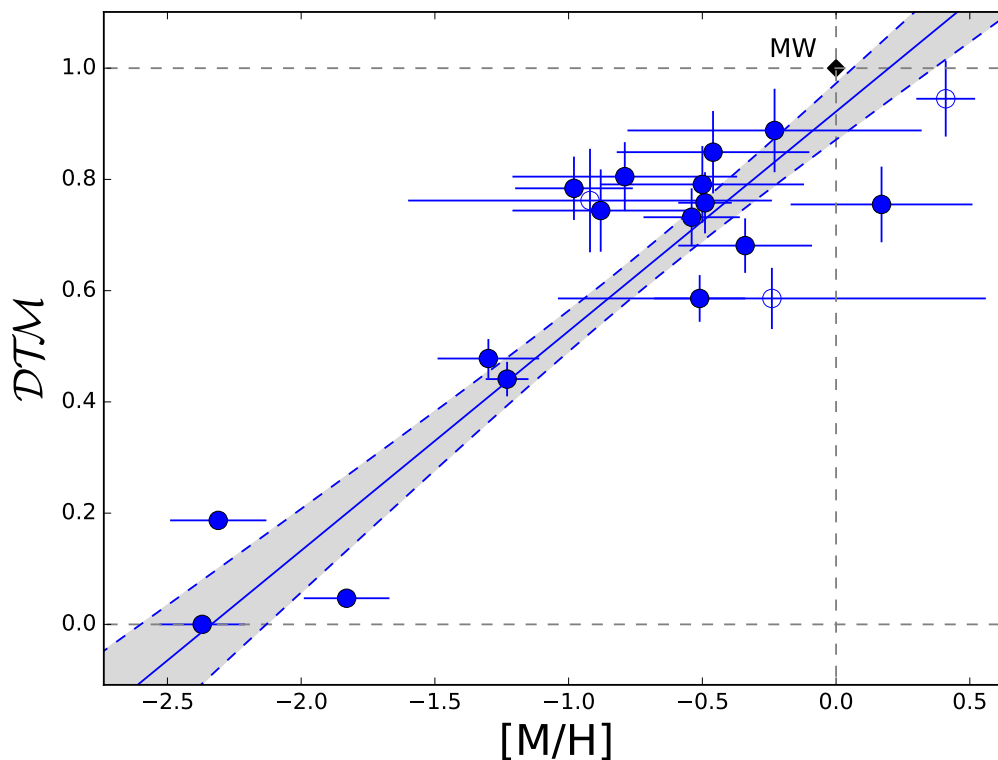


FIGURE 3.13:  $DTM$  as calculated using Eq. 3.8 as a function of metallicity. The dashed line and shaded area is a linear fit to the data and its  $1\sigma$  confidence interval respectively, tracing a significant positive correlation between the two variables. The trend is predominantly set by the lowest metallicity points, with those data points at  $[M/H] > -1$  showing no obvious trend. The Milky Way is shown by a black point at  $[M/H]=0$ ,  $DTM=1$ .

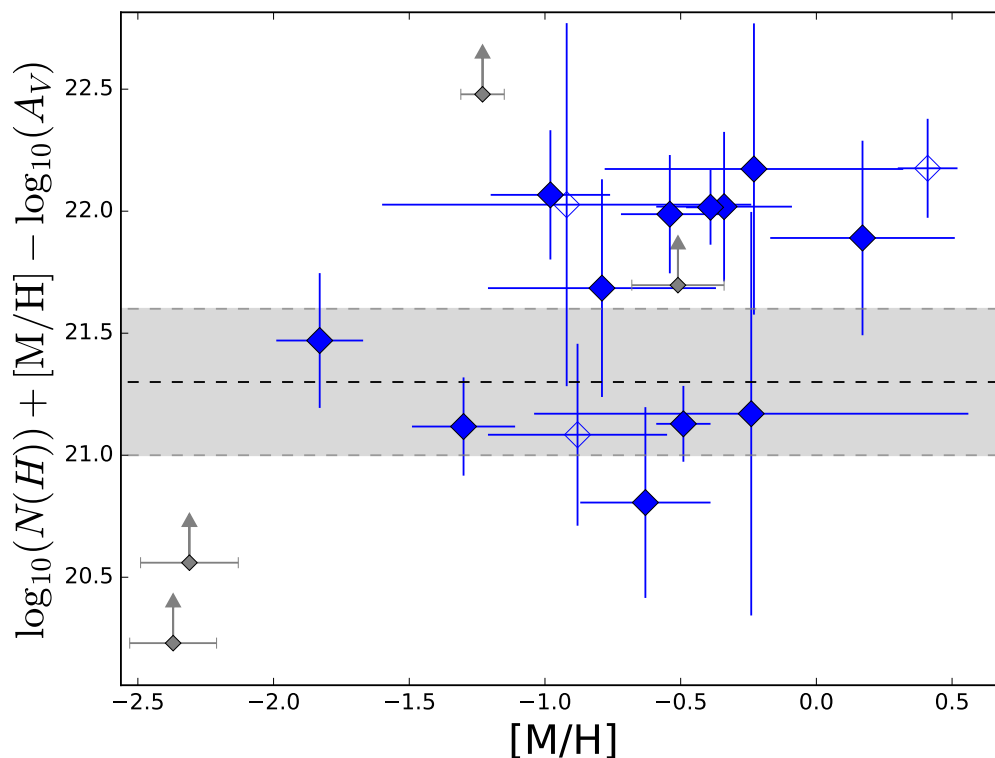


FIGURE 3.14: Metals-to-dust diagnostic used by Zafar & Watson (2013), as applied to our data along with the Local Group average and standard deviation that they quote (dashed line and shaded area).

dex. A Spearman's rank test gives  $\rho = 0.38$  with a false positive probability of  $P = 0.11$ , suggesting that there is perhaps a slight positive correlation, and indeed in the opposite direction to that in our  $\mathcal{DTM}$  method. Given that the metal measurement comes from the same place in both methods, there must be a discrepancy between how the dust is measured, the reasons for which we explore in the following sections.

### 3.6.2 The $A_{V;\text{SED}}$ to $A_{V;\text{DTM}}$ discrepancy

We can see from Figs. 3.13 and 3.14 that depletion and extinction seem either to have different sensitivity, or not to trace the same dust along the line of sight, or properties thereof. To compare these values we look to the relation used to calculate a value of  $A_V$  from a depletion-measured DTM, which we label  $A_{V;\text{DTM}}$ . This is based on the average extinction for a given hydrogen column density in the MW, scaled for DTM and metallicity, as per Savaglio et al. (2003), and using the  $N(\text{H})/A_V$  from Watson (2011)

$$A_V = 0.45 \frac{\text{DTM}}{\text{DTM}_{\text{Gal}}} \frac{Z}{Z_{\odot}} \frac{N(\text{H}) \text{ cm}^{-2}}{10^{21}} \text{ mag}, \quad (3.10)$$

with  $N(\text{H})$  measured in  $\text{cm}^{-2}$ . In the literature there are many cases of GRB afterglows where a direct  $A_V$  measurement from the SED was possible, as well as spectra with measurable depletion, and there is often disagreement between the two values, with the depletion-inferred  $A_V$  usually higher than the SED value (e.g. Watson et al. 2006; Savaglio et al. 2012; Friis et al. 2015). For our sample, we compare our independently measured  $A_{V;\text{SED}}$  values to  $A_{V;\text{DTM}}$  based upon the  $\mathcal{DTM}$ ,  $N(\text{H})$  and  $[\text{M}/\text{H}]$  from our fits, the result of which is shown in Fig 3.15. There seem to be two distinct categories of objects: group (1) are found above the green 1:1 line and make up the majority of the sample and show the known overprediction of  $A_{V;\text{DTM}}$  compared to  $A_{V;\text{SED}}$ , which are best fit by the blue dashed line; group (2) are found below this line and are those whose  $A_{V;\text{DTM}}$  prediction is lower than that measured from the SED. These objects include the known outlier GRB 070802 (Krühler et al. 2008; Elíasdóttir et al. 2009) at an  $A_{V;\text{SED}}$  of 1.23 mag. This underprediction for GRB 070802 is also noted by De Cia et al. (2016), and could be a result of the uncertain column density measurements resulting from low-resolution spectral data.

Including those GRBs with  $A_{V;\text{SED}}$  upper limits, 11 are categorized as overpredictions in group (1), while 6 are definitely in group (2). Of these, one is GRB 070802. The others are GRBs 050820A, 100219A, 111008A, 130408A, and 141028A. GRB 090926A shows negligible dust in both depletion and extinction.

### 3.6.3 Accuracy of $A_{V;\text{DTM}}$ - depletion as a reliable tracer of dust

A potential reason for the discrepancy is touched upon in Zafar & Watson (2013), who mention that while depletion is often based upon Fe, the vast majority of dust mass is composed of O, C, Mg, and Si, arguing that Fe-based depletion measurements may not correctly trace most of the dust. Indeed, Dwek (2016) provide a compelling argument for Fe dust production being different to that of the bulk of the elements; specifically, it is formed by cold grain growth in the ISM rather than in CCSNe and post-AGB star envelopes. In this argument, depletion based upon iron measurements is therefore bound to trace different dust to extinction. However, the linear depletion sequences seen by Jenkins (2009) and De Cia et al. (2016) show that by calculating the  $F_*$  for a particular line of sight, we can get a robust prediction for dust fractions and columns for all elements, including those not measured in the DLA, and thus we incorporate not only the dust compounds traced by iron, but the silicates and carbonaceous grains as well.

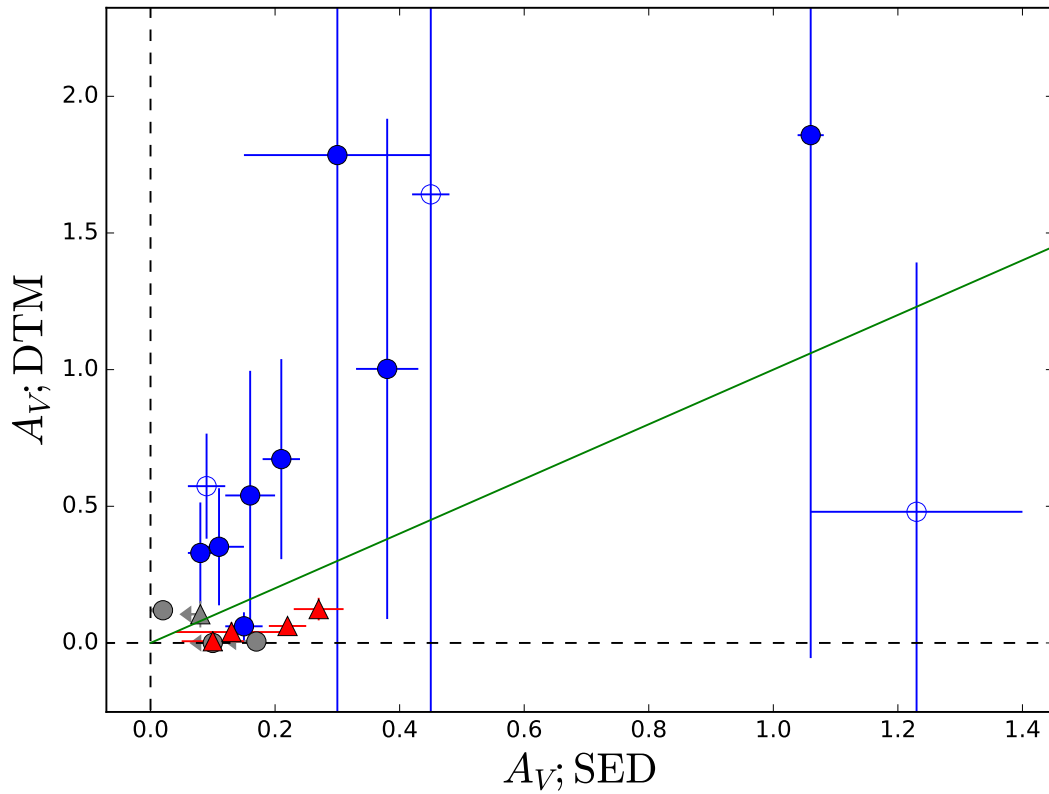


FIGURE 3.15:  $A_V$  as measured directly from the SED against that calculated from the DTM. The green line indicates a 1:1 conversion between the two. Blue circles represent SEDs best fit with a simple power-law, whereas red triangles are used for broken power-law fits. Empty points refer to depletion measured from low-resolution spectra, and grey points are upper limits. Large error bars are due to significant errors in several measured parameters being combined in quadrature.

We have followed the procedure in De Cia et al. (2016) (see Sect. 3.4.1.1) to correct relative abundances for nucleosynthetic effects, such that any discrepancies between our adopted intrinsic abundance and that true to the DLA are likely to be marginal, and certainly not large enough to cause the observed offset in the  $A_{V;DTM}$  prediction.

### 3.6.4 Accuracy of $A_{V;SED}$

Assuming that our depletion measure is indeed a solid representation of the total dust column, we look to  $A_{V;SED}$  for the reason why there could be a discrepancy. The question is whether the Local Group extinction curves are a good fit for GRB-DLAs or whether something other than the MW, LMC, or SMC should be used as their model, such as grey dust (Perley et al. 2008). Indeed, Friis (2015) claim that grey dust extinction, so called because the extinction is weakly dependent on wavelength, could be prominent in up to 25% of GRB-DLAs, including GRB 121024A which is included in our sample. Their reasoning is that a top-heavy grain-size distribution would cause a very flat extinction curve. When fitting a broken power-law SED, there is then a degeneracy between the steepness of the extinction curve (i.e. the  $A_V$ ), and the position of the break between X-ray optical power-law slopes (Schady et al. 2012); one of the solutions is a large amount of grey dust, which corresponds to a large  $A_V$  for a small  $E(B-V)$ . If the extinction in our group (1) DLAs is caused by grey dust, then we may be able to reconcile the

overpredicted  $A_{V;DTM}$  with  $A_{V;SED}$ . However, some of these DLAs show compelling evidence for the contrary:

GRB 120327A is best fit by a simple power law and an SMC-like extinction of  $A_{V;SED} = 0.05$  mag, with  $A_{V;DTM} = 0.18$  mag. The power law removes any degeneracy in the slope of the dust extinction law, and thus excludes the possibility of significant grey dust. Another example is GRB 120815A, whose SED is fit by a power law and SMC-like extinction to give an  $A_{V;SED}$  value of 0.08 mag, which is significantly smaller than the  $A_{V;DTM}$  of 0.44 mag. We find that GRB 121024A is also best fit with a power law. Indeed, Fig. 3.15 shows that only one object that has an overpredicted  $A_V$  was fit with a broken power law.

Although there is strong evidence for dust destruction caused by the GRB itself (Morgan et al. 2014), this would not cause a discrepancy between  $A_{V;SED}$  and  $A_{V;DTM}$ . Any dust that extinguishes the GRB would also be visible in depletion, so if that dust is destroyed it is no longer visible in depletion or extinction.

Intervening systems such as Mg II absorbers are known to contain similar quantities of dust as galaxies (e.g. Ménard & Fukugita 2012), although QSO-DLAs tend to show very little reddening (Krogager et al. 2016a; De Cia et al. 2016). For the group (2) objects, we notice that 050820A, 100219A, 111008A, and 130408A all have intervening absorbing systems. Should these objects have a high dust content, they could significantly affect the SED of the GRB afterglow, such that the reddening caused by dust in the host galaxy itself is indeed smaller, and thus pushes these objects towards the 1:1 line. However, for these intervening systems to be the reason for a much higher  $A_{V;SED}$  than from DTM, they would need to contribute around 80% of the extinction along the line of sight, whereas the systems in our sample are much weaker in metal line absorption than the host DLA (e.g. in GRB 100219A, Thöne et al. 2013). We therefore find it unlikely that a significant amount of the extra extinction is caused by intervening systems.

### 3.6.5 Equivalent dust column density

Having established that depletion is a good tracer of the dust, and with  $A_{V;SED}$  being accurate and reliable, we look to the relation used to calculate  $A_{V;DTM}$ , Eq. 3.10. This is based upon the relation between hydrogen and dust in the Galaxy, where a column of  $N(H) = 10^{21} \text{ cm}^{-2}$  results in an  $A_V$  of 0.45. We note that the value of the Galactic gas-to-dust ratio varies depending on the sample and technique used to measure it. We use the result of Watson (2011). Measurements of this value have been consistent over the past few decades, and include those by Bohlin et al. (1978), Predehl & Schmitt (1995), and Güver & Özel (2009). The value used does not alter the fact that a significant discrepancy is observed. In DLAs, the hydrogen column density is scaled for dust-to-metals ratio and metallicity to take into account the differing dust-to-gas ratios in such environments. However, the discrepancies in Fig. 3.15 show that the scaling between this equivalent dust column density and the  $A_V$  may well be incorrect. That is to say that in DLAs, such a column of dust does not have as much of a reddening effect as in the MW (see e.g. Campana et al. 2009.) This would indeed be solved by the make-up of the dust being different, but this is hard to explain given the well-determined extinction laws that are observed in GRB afterglows, which are consistent with the Local Group extinction laws (Schady et al. 2011; Greiner et al. 2011; Covino et al. 2013). One could argue that the problem arises from using a MW scaling relation with  $A_{V;SED}$  measurements based upon mostly SMC-like extinction laws, but both Magellanic Clouds have similar a  $A_V/N_H$  to that in the MW (Zafar & Watson 2013; Watson 2011).

The reason for the scatter thus remains unclear, and we therefore advise significant caution against basing  $A_V$  predictions on the  $A_V$ -to- $N(H)$  ratio of the MW and Local Group. We also suggest that the discrepancy between the different methods of quantifying dust is the reason for the disagreement between the trend, or non-trend, seen in DTM with metallicity.

### 3.7 Conclusion

Gamma-ray bursts are a unique if somewhat biased probe of the dust-to-metals ratio in the high-redshift Universe. GRBs occur only within certain types of galaxies (Krühler et al. 2015; Perley et al. 2016a), and thus are not totally unbiased probes, although this effect is reduced as redshifts greater than around 2 are reached (Perley et al. 2013; Greiner et al. 2015a; Schulze et al. 2015). They are also complementary to QSO-DLAs, and this work expands our observational knowledge of the DTM into the inner regions of galaxies in the distant Universe. We have used optical/NIR spectroscopy from a sample of 19 GRB afterglows in order to measure the metal and dust content of the DLAs in their host galaxies, including previously un-published metal column densities and metallicities for five objects. By using dust depletion models based on the MW, as well as QSO-DLAs, we have used a thorough method to determine the column densities of dust and of metals in order to calculate a dust-to-metals ratio. We find that the DTM follows a positive trend with metallicity, supporting the theory that a significant amount of dust is formed in situ in the ISM. We have investigated the discrepancy between the results of De Cia et al. (2013) and Zafar & Watson (2013), concluding that  $A_{V;SED}$  and depletion are not analogous measurements of dust. We see the common trend that  $A_{V;DTM}$  is often higher than  $A_{V;SED}$ , which we tentatively suggest could be due to the scaling between depletion-measured DTM and  $A_V$  being different in GRB host galaxies to the MW. We also note a significant number of objects whose  $A_{V;DTM}$  values are underpredictions compared to  $A_{V;SED}$ , and despite seeing what looks like two distinct populations, we are unable to satisfactorily reconcile the two using theories such as grey dust or intervening systems. We thus suggest that, given the large scatter between the two, DTM measured from depletion should not be used as a proxy for  $A_V$ , and encourage further work with larger samples to investigate the problem further.

## Appendix: Confidence levels for depletion fits

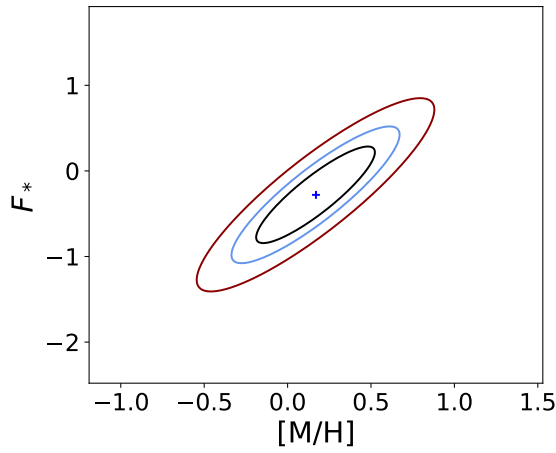


FIGURE 3.16: 1,2,3 $\sigma$  2D confidence levels for GRB 000926

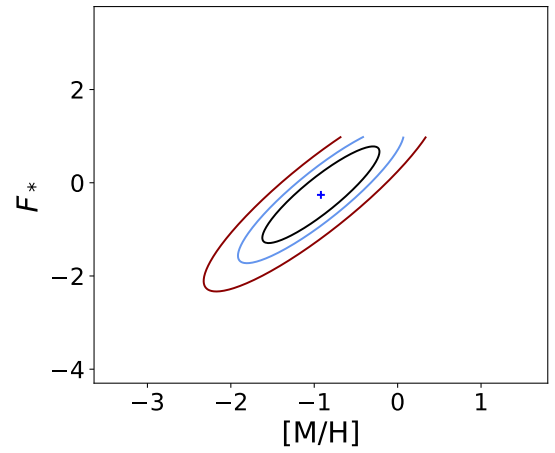


FIGURE 3.17: 1,2,3 $\sigma$  2D confidence levels for GRB 050401

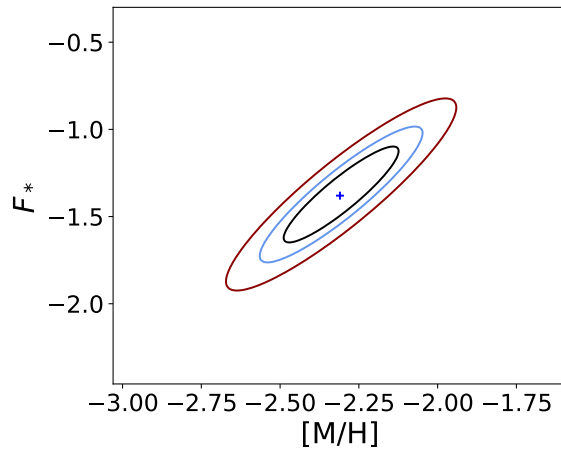


FIGURE 3.18: 1,2,3 $\sigma$  2D confidence levels for GRB 050730

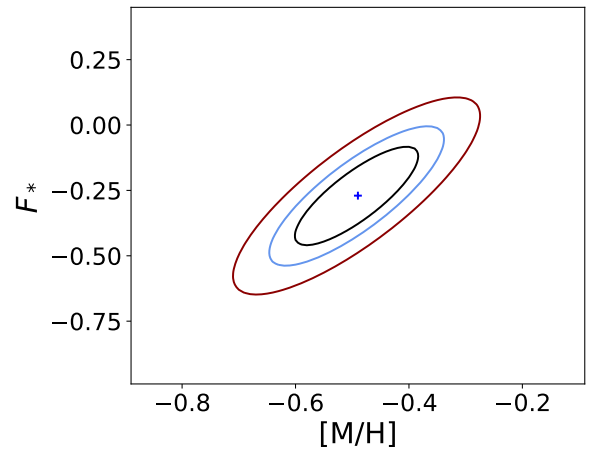


FIGURE 3.19: 1,2,3 $\sigma$  2D confidence levels for GRB 050820

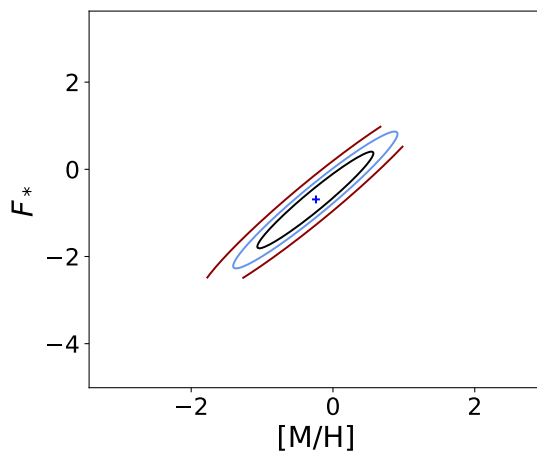


FIGURE 3.20: 1,2,3 $\sigma$  2D confidence levels for GRB 070802

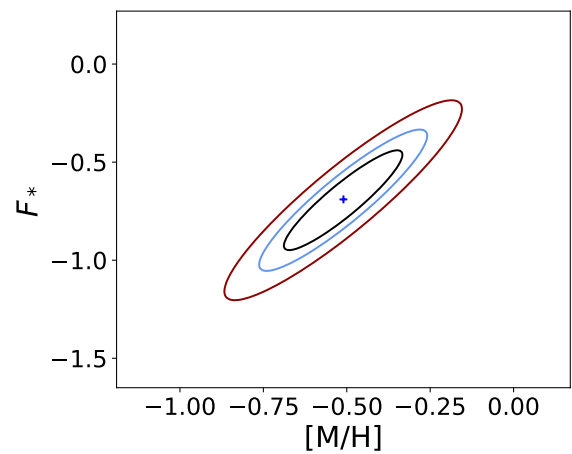


FIGURE 3.21: 1,2,3 $\sigma$  2D confidence levels for GRB 081008

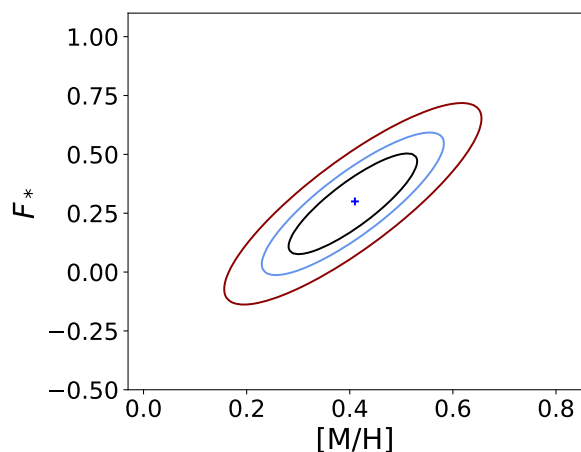


FIGURE 3.22: 1, 2, 3 $\sigma$  2D confidence levels for GRB 090323

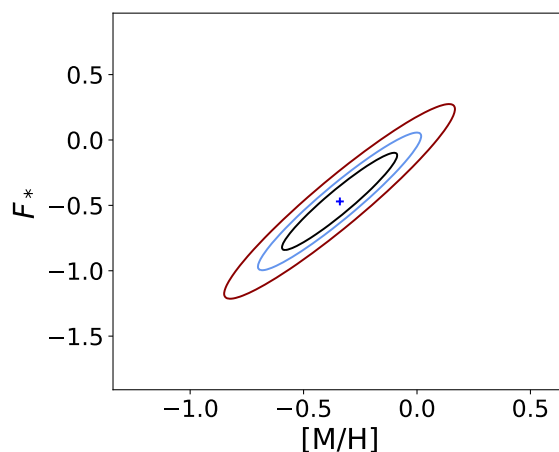


FIGURE 3.23: 1, 2, 3 $\sigma$  2D confidence levels for GRB 090809

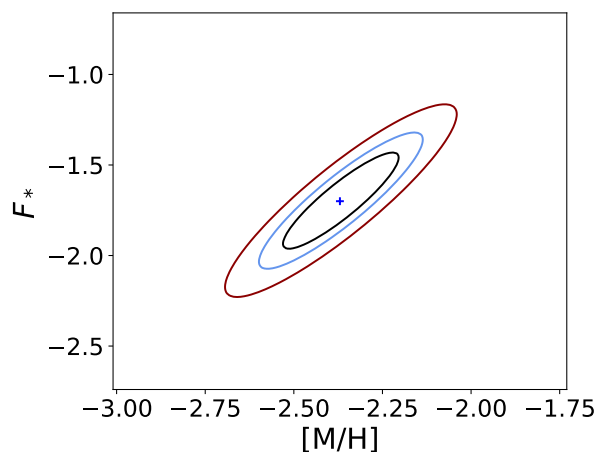


FIGURE 3.24: 1, 2, 3 $\sigma$  2D confidence levels for GRB 090926A

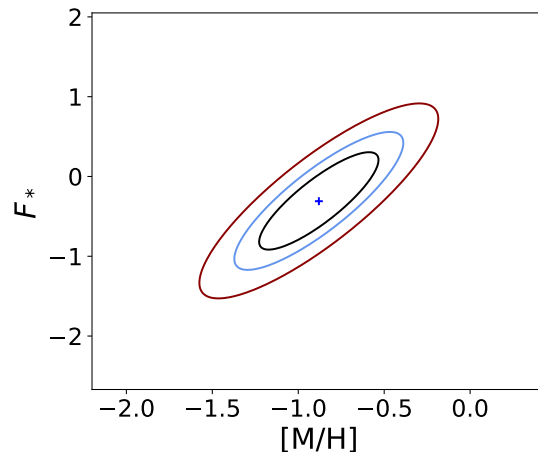


FIGURE 3.25: 1, 2, 3 $\sigma$  2D confidence levels for GRB 100219A

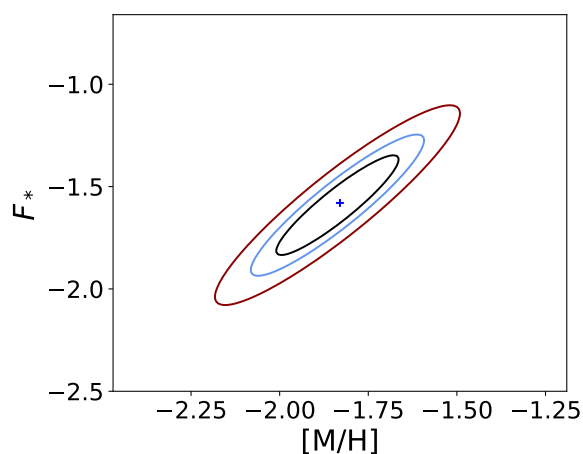


FIGURE 3.26: 1, 2, 3 $\sigma$  2D confidence levels for GRB 111008A

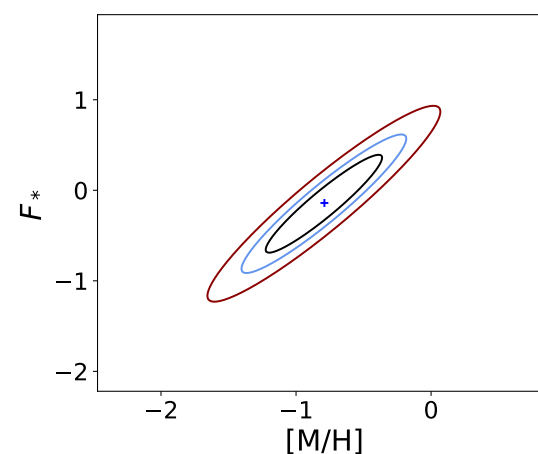
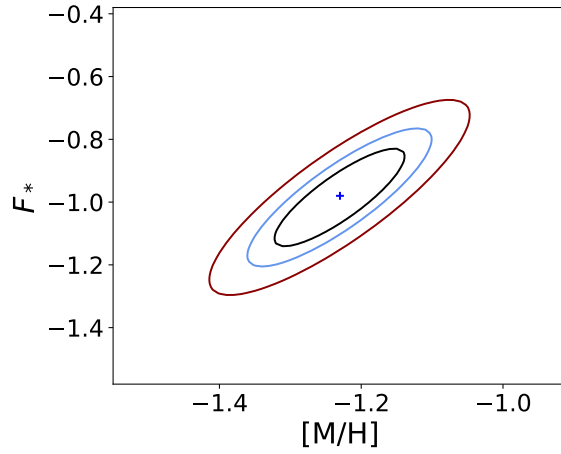
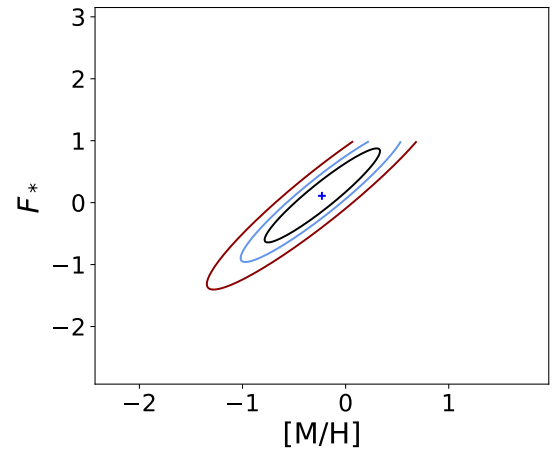
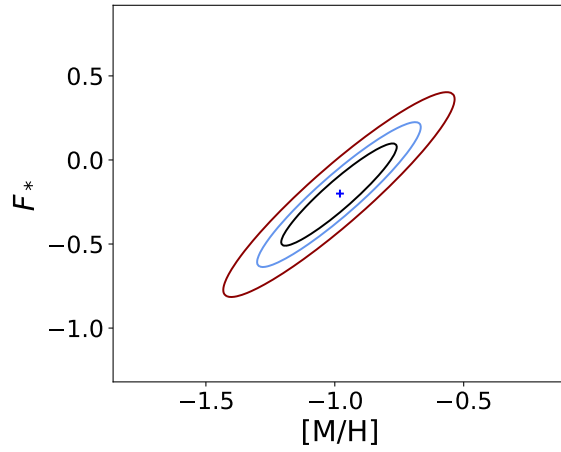
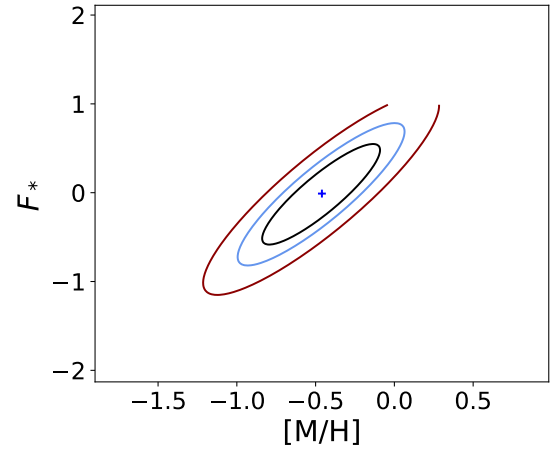


FIGURE 3.27: 1, 2, 3 $\sigma$  2D confidence levels for GRB 120119A

FIGURE 3.28: 1,2,3 $\sigma$  2D confidence levels for GRB 120327AFIGURE 3.29: 1,2,3 $\sigma$  2D confidence levels for GRB 120716AFIGURE 3.30: 1,2,3 $\sigma$  2D confidence levels for GRB 120815AFIGURE 3.31: 1,2,3 $\sigma$  2D confidence levels for GRB 120909A

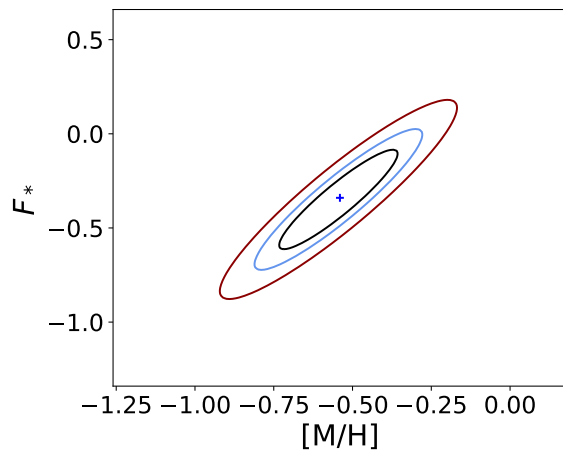


FIGURE 3.32: 1,2,3 $\sigma$  2D confidence levels for GRB 121024A

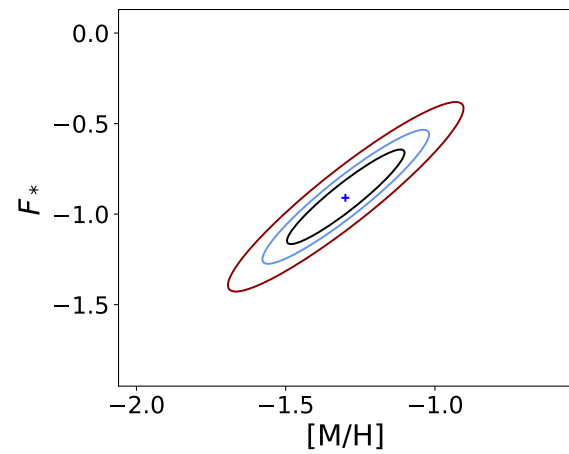


FIGURE 3.33: 1,2,3 $\sigma$  2D confidence levels for GRB 130408A

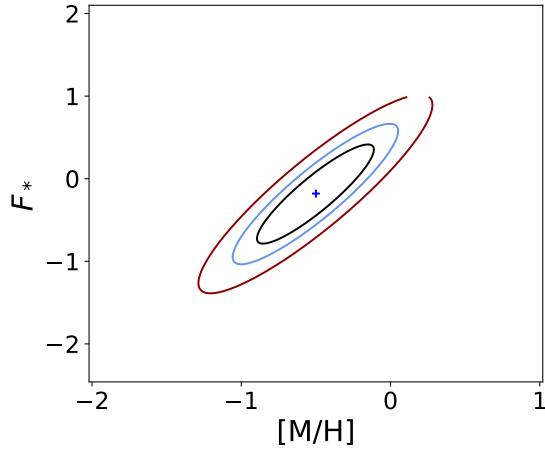


FIGURE 3.34: 1,2,3 $\sigma$  2D confidence levels for GRB 141028A

## Chapter 4

# Gas inflow and outflow in an interacting high-redshift galaxy

## The remarkable host environment of GRB 080810 at $z = 3.35$

As published in P. Wiseman, D. A. Perley, P. Schady, J. X. Prochaska, A. de Ugarte Postigo, T. Krühler, R. M. Yates, and J. Greiner, 2017, *Astronomy & Astrophysics*, in press, DOI 10.1051/0004-6361/201731065, reproduced with permission ©ESO.

### 4.1 Introduction

Far from their historical description as ‘island universes’, galaxies interact continuously with their immediate surroundings and their broader environments, known as the circumgalactic medium (CGM) and intergalactic medium (IGM). Over the past 40 years, it has been established that continued accretion of fresh metal-poor gas is required to fuel ongoing star formation in galaxies over cosmological timescales (Rees & Ostriker 1977; White & Rees 1978; White & Frenk 1991; Dekel et al. 2006). This star formation can be quenched and regulated by gaseous outflows and fountains that enrich the IGM and CGM with metals via regulatory winds powered by supernovae (SNe), stellar winds, and active galactic nuclei (e.g. Mathews & Baker 1971; Larson & B. 1974; Martin 1999; Dalla Vecchia & Schaye 2008, 2012). While observations of outflows have been made out to high redshifts (Shapley et al. 2003; Martin 2005; Weiner et al. 2009; Rubin et al. 2014; Finley et al. 2017), it is much harder to detect emission from infalling streams because of their lower surface brightness, which is a result of the lower metallicity and volume filling factor, although it has been possible to identify infalling gas through absorption lines in individual galaxy spectra (Rubin et al. 2012).

Instead of observing galaxies and their CGM by their emission, it is possible to measure their properties by absorption if they line up with a bright background point-source such as a quasar (QSO) or gamma-ray burst (GRB). At sufficiently high redshift<sup>1</sup>, some quasar spectra show the imprint of a dense column of neutral hydrogen in the form of a damped Lyman-alpha absorber (DLA), defined as a system with neutral hydrogen column density  $\log N_{\text{HI}} > 20.3$  (Wolfe et al. 2005)<sup>2</sup>.

Damped Lyman-alpha absorbers are associated with intervening galaxies between the observer and the QSO (Wolfe et al. 1986; Prochaska & Wolfe 1998), and are one of the most prominent tools used to study the properties of cold gas at high redshift (Dessauges-Zavadsky et al. 2006; Rafelski et al. 2012, 2014; De Cia et al. 2016). GRBs are produced during the deaths of very massive stars (Woosley & Bloom 2006), as proven by their association with type Ic supernovae (SNe; Galama et al. 1998; Hjorth et al. 2003; Greiner et al. 2015b; Cano et al. 2017).

<sup>1</sup>Because of the large optical depth of the Earth’s atmosphere to wavelengths bluer than  $\sim 3000 \text{ \AA}$ , Ly- $\alpha$  is only visible from the ground at  $z \gtrsim 1.6$

<sup>2</sup>Throughout the paper, column densities ( $N$ ) are given in units of  $\text{cm}^{-2}$

While QSO-DLAs tend to probe dense pockets in the outskirts of galaxies, the DLAs commonly seen in the afterglow spectra of GRBs represent the dense ISM and star-forming regions of their host galaxies (Fynbo et al. 2006; Prochaska et al. 2007b; Ledoux et al. 2009; Krühler et al. 2013). Along with detections of metal absorption lines redward of the Lyman-alpha ( $\text{Ly-}\alpha$ ) feature, these absorption spectra can be used to calculate the metallicity (e.g. Savaglio et al. 2012; Cucchiara et al. 2015; Wiseman et al. 2017b) and study the kinematics of the absorbing material (e.g. Prochaska et al. 2008a).

Because QSO lines of sight (LOS) are random, there is no preference for the occurrence of DLAs. There are thus large samples of QSO-sub-DLAs, which are also known as super-Lyman limit systems (SLLS;  $19 < \log N_{\text{HI}} < 20.3$ ; e.g. Peroux et al. 2007; Quiret et al. 2016). Similar studies extend to Lyman-limit systems (LLS;  $17.3 < \log N_{\text{HI}} < 19$ ; e.g. Prochaska et al. 2015; Fumagalli et al. 2016; Lehner & Nicolas 2016), partial Lyman-limit systems (pLLS), and the  $\text{Ly-}\alpha$  forest ( $\log N_{\text{HI}} < 17.3$ ; e.g. Aguirre et al. 2003; Pieri et al. 2013), all of which tend to be representative of different phases of the ISM, CGM, and IGM, respectively. LLSs have been the subject of particular interest recently as they are likely to represent absorption through dense cool pockets of the predominantly hot and ionised CGM. Simulations and observations suggest that they may trace the fresh gas that fuels star formation (Fumagalli et al. 2011b,c; Glidden et al. 2016; Lehner et al. 2016) and also outflowing metal-rich gas (Lehner et al. 2013), or indeed a combination of the two (Fumagalli et al. 2013).

While the physical conditions of GRB-DLAs and sub-DLAs have been extensively studied (e.g. Prochaska et al. 2007a; D’Elia et al. 2011; Schady et al. 2011; Sparre et al. 2014; Friis et al. 2015; Wiseman et al. 2017b), much less is known about the systems hosting GRBs with a much lower hydrogen column density. Typically, they are excluded from studies that are based on metals and dust because of the complicated effects of ionisation, which at higher column densities are rendered negligible (Viegas 1995; Wolfe et al. 2005; Peroux et al. 2007). They are also much rarer. Of the 75 GRBs identified by Cucchiara et al. (2015) as having measurable  $\text{H I}$  and at least one metal line, only 5 (6.7%) qualify as LLSs. Of these, GRB 060124 ( $\log N_{\text{HI}} = 18.5$ ; Fynbo et al. 2009) and GRB 060605 ( $\log N_{\text{HI}} = 18.9$ ; Ferrero et al. 2009) were observed with only low-resolution spectrographs and provide little information regarding their hosts. GRB 060607A ( $\log N_{\text{HI}} = 16.8$ ) and GRB 080310 ( $\log N_{\text{HI}} = 18.8$ ) have high-resolution spectra from VLT/UVES, and have been studied in Fox et al. (2008), who focused on high-ion absorption, particularly the prominence of blue-shifted absorption tails of these species.

In this paper, we present a detailed study of GRB 080810, whose spectrum shows a very small total  $N_{\text{HI}}$  distributed along several absorption components at the host redshift, which show dramatically different chemical and physical properties. Throughout the manuscript we use solar abundances from Asplund et al. (2009). We assume a flat  $\Lambda$ CDM cosmology with *Planck* parameters:  $H_0 = 67.3 \text{ km s}^{-1} \text{ Mpc}^{-1}$ ,  $\Omega_{\text{m}} = 0.315$ , and  $\Omega_{\Lambda} = 0.685$  (Planck Collaboration 2014). Errors are given at the  $1 \sigma$  confidence level.

## 4.2 Observations and data reduction

On 2008-08-10 at  $T_0=13:10:12$  UT, the Burst Alert Telescope (BAT; Barthelmy et al. 2005) on board *Swift* (Gehrels et al. 2004) triggered on GRB 080810 (Page et al. 2008), which at  $T_0 + 80\text{s}$  was detected as a bright source in the *Swift* X-ray Telescope (XRT; Burrows et al. 2005) and Ultra-violet and Optical Telescope (UVOT; Roming et al. 2005). The burst was localised to lie at RA = 23:47:10.48, Dec. = +00:19:11.3 (J2000+/- 0.6"), and Page et al. (2009) provided an overview of the prompt and subsequent follow-up observations carried out by numerous ground- and space-based observatories. We refer to that paper for a detailed analysis of the broadband spectral evolution of the GRB.



### 4.2.1 Keck/HIRES afterglow spectrum

Starting 37.6 minutes after the trigger at 13:47:50 UT, GRB 080810 was observed with the High Resolution Echelle Spectrometer (HIRES; Vogt et al. 1994) mounted on the 10-metre Keck I telescope of the W. M Keck Observatory located at the summit of Maunakea, Hawaii. A series of two exposures of 1000 s each were taken using the C5 decker, providing a FWHM spectral resolution of  $\approx 8 \text{ km s}^{-1}$ . The data were reduced with the HIRedux data reduction pipeline bundled within the XIDL software package<sup>3</sup>. Full details on the data reduction algorithms are given in Bernstein et al. (2015). The data were coadded optimally and normalised with low-order polynomial fits to individual echelle orders. The extracted 1D spectrum is shown in Fig. 4.1.

### 4.2.2 Late time imaging and spectral observations

We observed the host galaxy of GRB 080810 on several occasions. On 2014-07-22, we acquired  $6 \times 250 \text{ s}$  of imaging in the  $r$  band with the Optical System for Imaging and low-Intermediate-Resolution Integrated Spectroscopy (OSIRIS; Cepa et al. 2000) on the 10.4 m Gran Telescopio Canarias (GTC). We acquired imaging with the Low-Resolution Imaging Spectrograph (LRIS; Oke et al. 1995) mounted at Keck, in the  $B$ ,  $G$ ,  $R$ , and  $RG$  850 (similar to SDSS- $z$ ) filters on the nights of 2014-08-30 and 2014-08-31 (three exposures in each filter, totaling between six and nine minutes total on-source). A longslit spectrum was also acquired at a position angle of 35 degrees, with a total exposure time of 2400 s in the blue arm and 2200 s in the red arm. We also acquired near-infrared imaging using the Multi-Object Spectrograph For Infrared Exploration (MOSFIRE; McLean et al. 2012) on 2014-10-01 using the same telescope, in the  $K_s$  and  $J$  bands. In addition, on 2015-07-23, we acquired a further 600 s of imaging with GTC/OSIRIS in the  $i$  band, and we obtained deep FOcal Reducer/low dispersion Spectrograph 2 (FOR2)  $R$ -band imaging from the VLT archive (originally published in Greiner et al. 2015a). Finally, we have obtained *Spitzer* 3.6  $\mu\text{m}$  data as part of the SHOALS survey (Perley et al. 2016c).

## 4.3 Analysis of the afterglow spectrum

The normalised spectrum of GRB 080810 (Fig. 4.1) shows negligible flux bluewards of a cut-off at 3795 Å, corresponding to the Lyman limit at  $z \approx 3.35$ . Redwards of this is a dense Ly- $\alpha$  forest, which terminates with two deep Ly- $\alpha$  absorption troughs around 5300 Å, assumed in Page et al. (2009) to correspond to the GRB host system at an approximate redshift of 3.35. Further redwards, the spectrum is populated by mild metal absorption from the host systems, as well as by various metal lines associated with lower redshift systems.

### 4.3.1 Defining the host complex at $z = 3.35$

The large column densities in GRB-DLAs and sub-DLAs cause, through quantum mechanical effects, the Ly- $\alpha$  absorption feature to be saturated and often to span regions over 15 Å wide about its central rest-frame wavelength of 1215.8 Å. A fit to the damping of the red wing was therefore used to measure the  $N_{\text{H I}}$  for the entire host. The deep and wide trough from the DLA means that any additional Ly- $\alpha$  absorption only becomes evident at much shorter wavelengths, shifted significantly in redshift space (and thus much closer to Earth) or corresponding to a shift of several thousands of  $\text{km s}^{-1}$  in velocity space at the redshift of the DLA. This blueshifted Ly- $\alpha$  absorption is thus entirely unrelated to the GRB or its host galaxy and surrounding environment. The spectrum of GRB 080810 shows no such DLA, and therefore there is no clear distinction

<sup>3</sup><https://github.com/profxj/xidl>

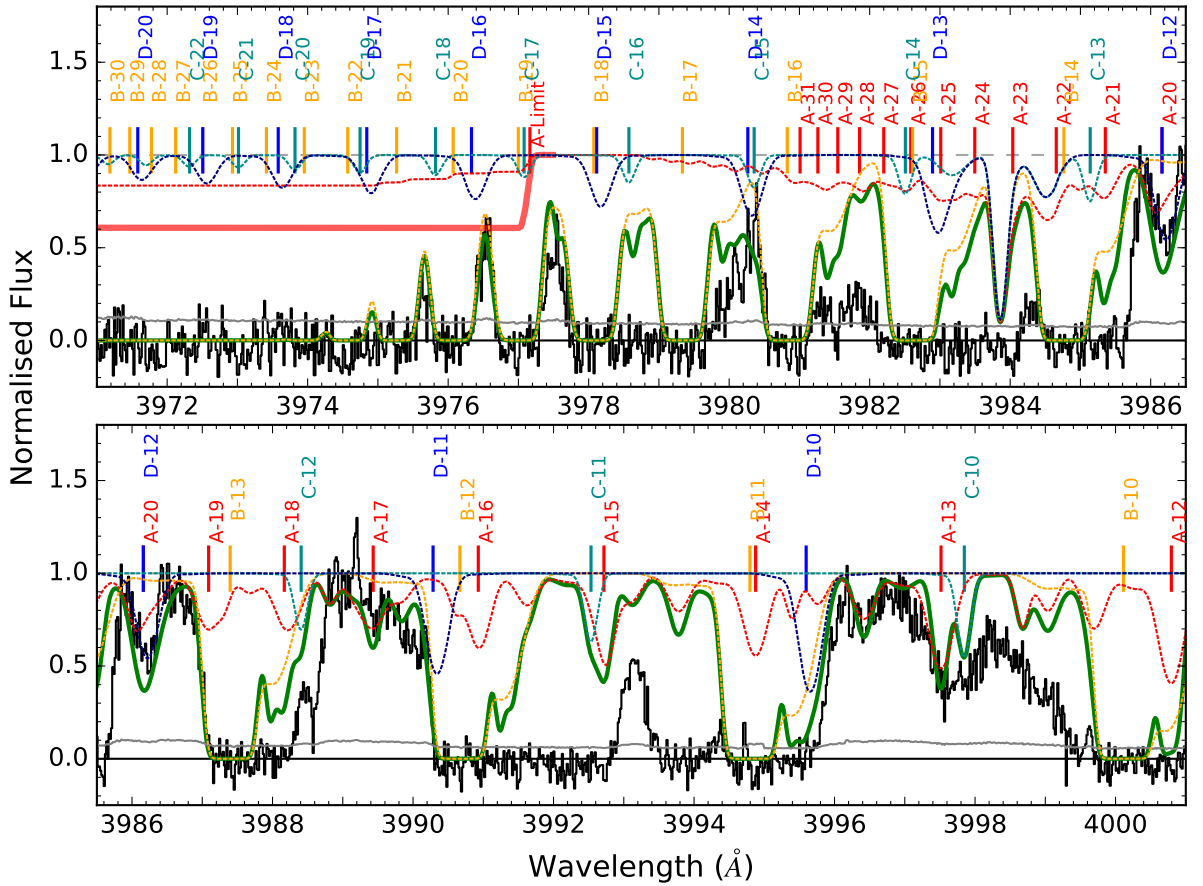


FIGURE 4.2: Normalised HIRES spectrum of GRB 080810 (black) around the Lyman limit of 911.8 Å. Fits to the absorption by H I by the four systems of the host are plotted as dashed lines in red, orange, cyan, and dark blue for systems A, B, C, and D, respectively, with the combined fit shown in solid green. Labels show the location of each order for each component. The error spectrum is shown in grey. The thick red line corresponds to the upper limit in system A of  $N_{\text{H I}} \leq 16.9$ .

between the absorption components that are related to the host and those that are Ly- $\alpha$  forest absorption from the IGM.

The reddest Ly- $\alpha$  absorption is centred around  $z = 3.361$ , which we denote system A. Roughly  $700 \text{ km s}^{-1}$  bluer at  $z = 3.351$  lies system B. These two objects are also detected in the late-time imaging and low-resolution spectroscopy, as detailed in Sect. 4.4.5. Furthermore, based on our subsequent analysis (Sect. 4.5.1), there is strong evidence to show that system B is in fact the host of the GRB. This means that A is in the foreground, and implies a positive relative velocity between A and B of  $\approx 700 \text{ km s}^{-1}$ . To simplify the analysis, we henceforth denote B as being at rest in relation to the Hubble flow, and thus define it as the point where the peculiar velocity  $v = 0 \text{ km s}^{-1}$ .

Farther bluewards, systems C and D are centred at  $z_c = 3.348$  and  $z_d = 3.346$ , a shift of  $-170 \text{ km s}^{-1}$  and  $-340 \text{ km s}^{-1}$ , respectively, with respect to B. These velocities satisfy the (observationally motivated) condition used by Prochaska et al. (2015) to define an LLS, in that they lie within  $500 \text{ km s}^{-1}$  of the point of deepest absorption and are thus treated as part of the same system. However, if we assume that C and D have no local velocity relative to B, they are 0.6 Mpc and 1 Mpc displaced from B, respectively, while if we instead take A and B to be systems falling at equal and opposite peculiar velocities towards each other, the respective separation to C and D increases to 1.6 and 2 Mpc. These values lie significantly

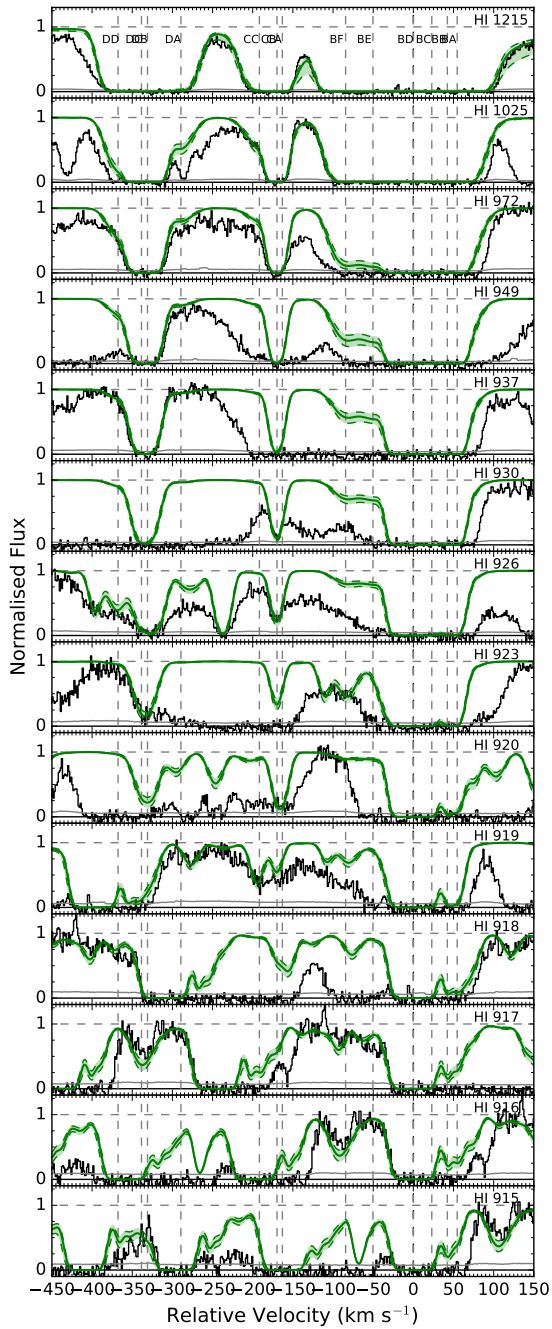


FIGURE 4.3: Selection of fits to the Lyman series for systems D, C, and B at  $z = 3.346$ , 3.348, and 3.351, respectively. Lines between the third and tenth orders allow systems C and D to be constrained well. Higher order Lyman-series transitions near the Lyman limit, where system B better is constrained, are shown in Fig. 4.2. Shaded regions show 0.3 dex deviations from the best fit. Grey vertical lines represent the centres of the corresponding components.

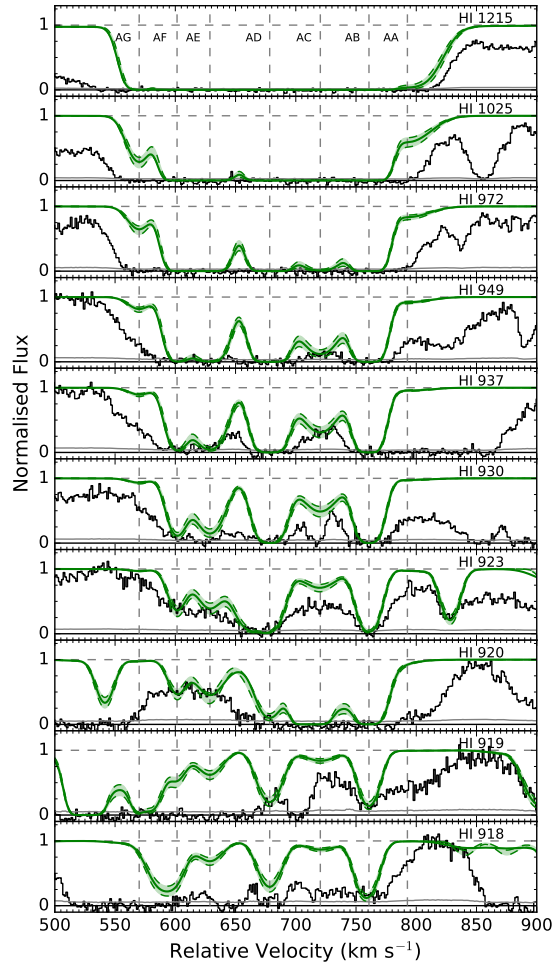


FIGURE 4.4: Selection of fits to the Lyman series for component A at  $z = 3.36$ . HI 937, 930, 923, and 920 are used to constrain components AD-AG, while the transitions at 923, 919, and 918 Å provide constraints on the main red component AB. Shaded regions show 0.3 dex deviations from the best fit. Grey vertical lines represent the centres of the corresponding components.

outside the average virial radius of 105 kpc for a dark matter halo containing a galaxy of the mass  $\log M_* = 10^{10} M_\odot$  (Henriques et al. 2015), a similar stellar mass to the mass we derive for this host in Sect. 4.4.5. Since we are unable to break the degeneracy between local velocities and cosmological redshift, it is not possible to determine for certain, based on redshift arguments alone, whether these two systems are also bound to the A-B system, but we include them in our analysis in an attempt to determine their nature. We return to this topic in the discussion section, where we use chemical and physical arguments to locate the systems in space. Lyman-series absorption from components A-D is shown in Figs. 4.3 and 4.4.

The next absorption systems, E and F, are found at  $z_E = 3.338$  and  $z_F = 3.330$ , respectively. When we assume that they are bound to the host system, they have relative velocities of  $\approx -1000$  and  $-1550 \text{ km s}^{-1}$  with respect to B, and thus fall outside the aforementioned criterion to be part of the same LLS. When we assume, on the other hand, that they are static relative to the expansion of the Universe, the separation between E (F) and the mean redshift of A and B is  $\sim 3.6 \text{ Mpc}$  ( $\sim 5.2 \text{ Mpc}$ ). Finally, there is no apparent low- or high-ionisation metal absorption associated with these redshifts, reducing the possibility that they are high-velocity outflows from the GRB progenitor or the host galaxy system. We conclude that E and F are very unlikely to be part of the host system and are probably located in the IGM. We therefore define the host complex as being comprised of systems A, B, C, and D.

#### 4.3.1.1 H I column densities

It is unusual for a GRB host galaxy to have no damping of the Ly- $\alpha$  lines, but this is the case in the presumed host of GRB 080810, which places an initial upper limit of  $\log N_{\text{H I}} < 19$  for each of the systems. As was the case in Page et al. (2009), a lower limit of  $\log N_{\text{H I}} > 17.3$  may be imposed because of 100% absorption below the Lyman limit. With Ly- $\alpha$  being saturated but not damped, a Voigt-profile fit to this line alone does not constrain  $N_{\text{H I}}$  much further. However, the excellent signal-to-noise ratio (S/N) and high resolution of the spectrum enable us to use higher order Lyman series lines to place much tighter constraints on the  $N_{\text{H I}}$ . A selection of these transitions is shown in Fig 4.3 for systems B, C, and D, and in Fig. 4.4 for system A. A more detailed view of the highest order Lyman series absorption and the Lyman limit is presented in Fig. 4.2.

The flux drops to zero around  $3975 \text{ \AA}$ , which is consistent with the Lyman limit at a redshift of 3.3598. However, the higher orders of the Lyman series of system A are unsaturated, and there is also non-zero flux blueward of  $3977 \text{ \AA}$ , which corresponds to the Lyman limit of the strongest metal absorber in system A at  $z = 3.36206$ . This implies that system A is a pLLS. The thick red line in in Fig. 4.2 corresponds to the flux drop caused by a column density of  $\log N_{\text{H I}} = 16.9$  at the redshift of system A, which means that this value is a strict upper limit. We deduce that the zero-flux at  $3975 \text{ \AA}$  is due to the saturated Ly-21 and 22 transitions from system B, which has a significantly larger column density.

Each of the four host systems are split up further into components at slightly different redshifts and with different column densities and other physical parameters. In order to measure column densities more accurately, it is necessary to define these velocity components. Absorption lines from species with similar ionisation potentials usually show very similar profiles, defined by their redshift  $z$  and broadening parameter  $b$ . The only remaining free parameter is then  $N$ , which can be varied to find the best fit for all of the available lines of the species in question. However, determining  $z$  and  $N$  for H I is non-trivial. H I lines are strong and saturate up to the highest orders even for low column densities. Because it is so abundant, the stronger H I lines (Ly- $\alpha, \beta, \gamma$ ) often show absorption at high velocities from their central redshift, where

there is no corresponding metal absorption. Additionally, the Lyman series is strongly contaminated by the Ly- $\alpha$  forest, so there is a degree of uncertainty created by not knowing whether absorption comes from the host or from intervening systems.

While H I is expected to follow components seen in the neutral and singly ionised metals (which are labelled with Greek letters), this is clearly not the case in system A: C II and Si II are only detected in one component, A $\alpha$ , while H I covers over 250 km s<sup>-1</sup> in velocity space. The typical  $b$ -parameter of absorption systems in GRB hosts is  $\sim 12$  km s<sup>-1</sup> (de Ugarte Postigo et al. 2012), which means that H I in A is clearly formed of several components. Owing to its low column density relative to most GRBs, many of the transitions from H I 949 to the Ly limit show sections of non-zero flux, therefore some velocity structure can be determined. It is apparent in Fig. 4.4 that the deeper absorption matches the central redshifts of the high-ionisation metals (high ions; Sect. 4.3.1.2), whose absorption components are spread across the entire velocity range traced by H I.

Proceeding with caution, we used the Voigt-profile fitting software `VPFit` (v. 10.2)<sup>4</sup>, with initial guesses for absorption lines at redshifts and  $b$  parameters taken from the high ions, and  $N$  given by the upper limit measured from the Ly limit. The fits to the entire available Lyman series (some lines such as H I 926 are entirely saturated and thus not used, since the amount of contamination from one or several Ly- $\alpha$  forest lines is unknown) were then simultaneously adjusted by eye until a satisfactory fit was found (this technique is commonly used for fitting of H I, e.g. Prochter et al. 2010; Rafelski et al. 2012; Jorgenson et al. 2013; Prochaska et al. 2015). This is necessary because of Lyman-alpha forest contamination, which cannot be accounted for in the fitting routine. The simultaneous fit is possible because the components are relatively narrow and thus independent of each other. The best fit becomes apparent when the green modelled line in Figs. 4.3 and 4.4 matches the data best. While `VPFit` provides a statistical uncertainty for each fit, this is often unrealistic given the blending of most of the Lyman series transitions. We therefore adopt a minimum uncertainty of 0.1 dex for these lines, although only a limit is given in the end.

Following this procedure, fits to H I 937, 930, 923, 920, 919, and 918 result in a total column density of  $\log N_{\text{H I}}^{\text{A}} = 16.45$ , which is consistent with the upper bound placed by the Lyman limit. Given the probability that all of the lines used in the fit are also to some degree contaminated by unrelated absorption, the values from individual components (given in Table 4.1) as well as the total are strictly upper limits. In reality, the H I is distributed in more sub-components than can be modelled (because the additional components do not have corresponding metal absorption), which makes the fits appear inconsistent with the data. However, these additional components must not add much extra column, or else they would contradict the strict upper limit placed by the Lyman limit.

In contrast to system A, there are no unsaturated Lyman transitions corresponding to system B, which causes difficulty in placing tight constraints on  $N_{\text{H I}}$ . Because of this saturation, it is not possible to determine whether the H I appears to follow the high or the low ions better. Nevertheless, we place upper limits on both BE (H I 917, 916) and BF (H I 920, 917), at  $\log N_{\text{H I}}^{\text{BE,BF}} < 16.0$ , with the  $b$  parameter not well constrained (and largely unimportant). These values are more than 2 dex lower than the main component and thus have negligible impact on the result. By far the strongest component is BD/B $\beta$ ,  $\gamma$ . The saturation of the Ly-20 and Ly-21 lines as well as a total lack of flux below the corresponding Lyman limit (accounting for the flux error of 0.1 in this part of the spectrum) place a lower limit of  $\log N_{\text{H I}}^{\text{BD}} > 17.9$ . When we assume the  $b$ -parameter from the high-ions of 7 km s<sup>-1</sup>, the lack of damping in the red wing of Ly- $\alpha$  as well as the flux peak between systems B and C place a constraint of  $\log N_{\text{H I}}^{\text{BD}} \leq 18.35$ ; this is traced by the solid green line in Fig. 4.3. The shaded region corresponds to column densities

<sup>4</sup>VPFit, R. F. Carswell & J. K. Webb, 2014: <http://www.ast.cam.ac.uk/rfc/vpfit.htm>

up to 0.3 dex away from this value, and it is clear that a value of  $\log N_{\text{H I}}^{\text{BD}} > 18.35$  does not fit the data well. Varying the  $b$ -parameter to as high as  $20 \text{ km s}^{-1}$  does not change this limit. The blue wing of component BD in H I 918, 917, 916, and 915 fits the observed flux best with a  $b$ -parameter of  $20 \text{ km s}^{-1}$ , which is significantly larger than that of both the corresponding low and high ions. While it is likely that in reality BD is formed of a number of smaller components with smaller  $b$ -parameters, and again allowing for contribution to the absorption from unrelated systems, it is with some confidence that we report the upper limit of  $\log N_{\text{H I}}^{\text{BD}} \leq 18.35$ . The components BA, BB, and BC are unresolved and either contaminated or saturated throughout most of the Lyman series. Assuming the same  $b$ -parameters as the high-ions and using the constraining red wing of H I 918, we estimate a conservative combined limit of  $\log N_{\text{H I}}^{\text{BA+BB+BC}} \leq 16.5$ . Component BD greatly dominates the  $N_{\text{H I}}$ , and given the lower limit from the Lyman limit and the upper limits from the remaining series, we estimate the total as  $\log N_{\text{H I}}^{\text{B}} = 18.1 \pm 0.25$ , where the probability distribution function is more likely flat than Gaussian, such that the true value is equally likely to lie anywhere within the uncertainty (Prochaska et al. 2015).

Systems C and D can be much more easily constrained by their unsaturated high-order Lyman transitions. For the central component of C we find the definite  $\log N_{\text{H I}}^{\text{CB}} = 15.53 \pm 0.05$ , fixed predominantly by H I 930 and 926 (Ly-6, 7). We note that the best fit results when  $b = 8 \text{ km s}^{-1}$ , which is lower than typically seen in H I. However, this value is a true convergence of the program, rather than a fit by eye, and we therefore assume it to be true. The value also matches that of the metal lines. The high-ion component CB is mirrored by the low-ion  $\text{C}\alpha$ , but for consistency with systems A and B, we use the capital letter notation for the H I in system C and D. The blended peripheral components are constrained to limits  $\log N_{\text{H I}}^{\text{CA,CC}} < 14.0$  in the same transitions, as are Ly- $\alpha$ ,  $-\beta$ , and  $-\gamma$ . For system D we again applied the restriction of fits to H I 937, 926, 923, and 917 (Ly- $\epsilon$ , 7, 8, and 12), which combine to give  $\log N_{\text{H I}}^{\text{DB+DC}} = 15.9 \pm 0.1$ . The red wing of Ly- $\alpha$  and the blue wing of H I 972, 937, 923, and 918 return values of  $\log N_{\text{H I}}^{\text{DA}} = 14.35 \pm 0.1$  and  $\log N_{\text{H I}}^{\text{DD}} = 14.0 \pm 0.1$ . Final measurements are presented in Table 4.1, and the summed column densities for each system are given in Table 4.5.

#### 4.3.1.2 Metal column densities

Systems A, B, and C show significant absorption from both low- and high-ionisation states of various metal elements, including C, Si, and O, while system D shows a possible detection of weak absorption from C II and Si II. These systems are further broken up into a subset of velocity components, some of which are resolved, while others are blended with one another. Systems B and C also exhibit significant absorption from excited states of C II and Si II. As it has a much larger H I column density and the largest corresponding columns of excited gas, we defined component  $\text{B}_\gamma$  as the component of zero relative velocity, which we keep consistent throughout the paper. We assumed the instrument resolution of  $\text{FWHM} = 8 \text{ km s}^{-1}$ , which we verified by measuring the width of the single telluric lines. To fit Voigt-profiles to the absorption lines, we used the same method as described in Wiseman et al. (2017b). To determine the number of components and their exact redshifts, we used unsaturated lines in high S/N regions of the spectrum, which are unaffected by blending from unrelated absorption. Following the criteria imposed on HIRES data by Prochaska et al. (2015), we defined an unsaturated line as a line whose minimum flux is greater than 0.1 times that of the continuum to avoid the limited hidden saturation that may occur. We selected these initial lines separately for the singly and higher ionised species as the properties of the absorbing systems are significantly different. For each ionisation level, we fit the above-defined lines with `VPFit` and measured the broadening parameter,  $b$ , and redshift,  $z$ . We let the program add components until the  $\chi^2$  parameter was minimised. In some cases, such as  $\text{B}\beta$ ,  $\gamma$ , this resulted in strongly blended components separated by only a few  $\text{km s}^{-1}$ , but this does not have a significant effect on the results. After they were

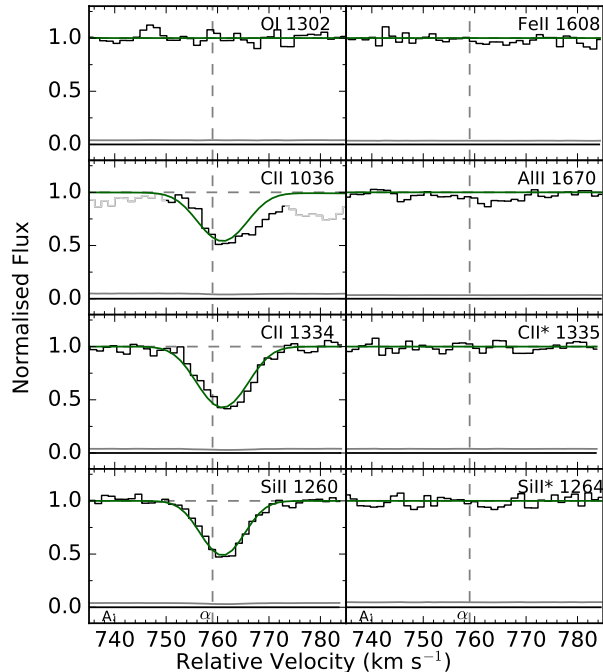


FIGURE 4.5: Low-ionisation metal transitions in system A with their respective Voigt-profile fits in green. Light grey data represents unrelated absorption, while the error spectrum is plotted in dark grey. Vertical dashed lines correspond to the respective velocity components. This scheme is used in Figs. 5-11.

determined from these ideal lines,  $z$  and  $b$  were fixed, and Voigt profiles were fit to all of the other lines in that component and ionisation level in order to measure the column density  $N$ . An exception to this is the O VI detected in system A, which displays a unique absorption profile (Fig. 4.9). We show the low-ionisation fits in Figs. 4.5, 4.6, and 4.7, and those for the high-ionisation states in Figs. 4.9, 4.10, and 4.11. The fits of system D are combined and shown in Fig. 4.8.

### 4.3.2 Intervening systems

Along with the absorption from the complex host galaxy system, the spectrum is populated with a vast number of intervening systems forming the Ly- $\alpha$  forest between Ly- $\alpha$  at the host redshift and its associated Lyman limit, corresponding to a redshift range of  $2.32 < z_{\text{abs}} < 3.34$ . A number of these show corresponding metal absorption, mostly in C IV and Si IV, which suggests pockets of IGM gas that have been enriched with metals. The absorbers at  $z = 2.32, 2.53, 3.157,$  and  $3.300$  also show significant absorption from singly ionised species.

## 4.4 Results

The column densities measured by Voigt-profile fitting of each individual component are presented in Table 4.1, and a summary for each system is given in Table 4.5. The four main systems are strikingly different in their absorption characteristics, and in the following section, we present their physical properties as revealed by the analysis.

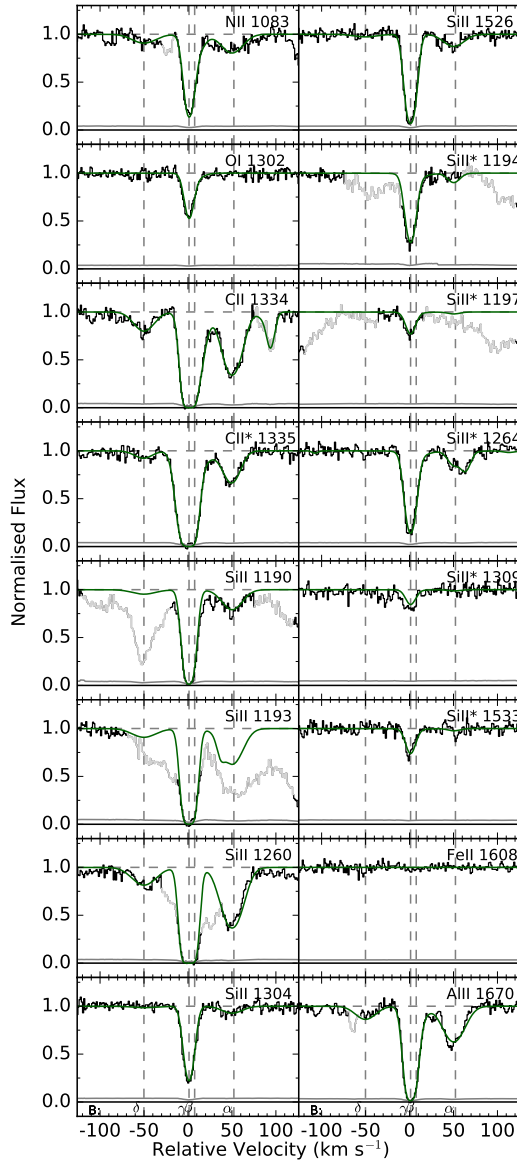


FIGURE 4.6: Low-ionisation metal transitions in system B with their respective Voigt-profile fits in green.

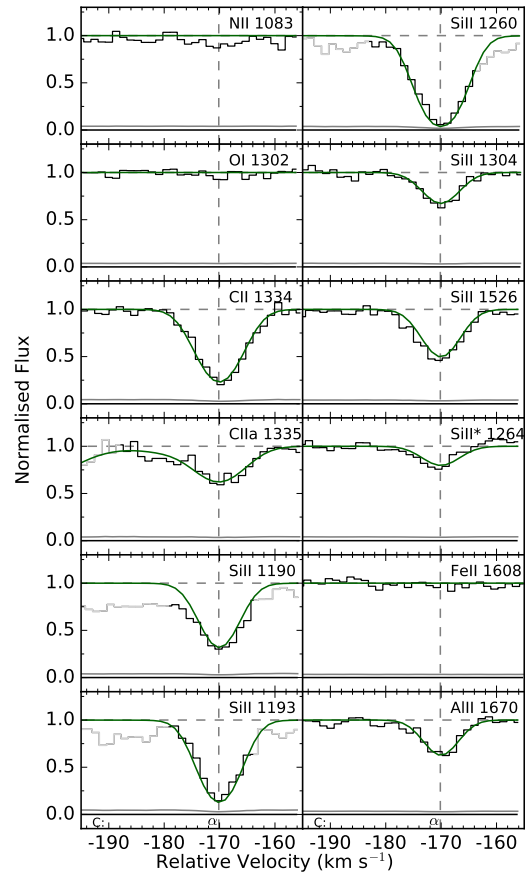


FIGURE 4.7: Low-ionisation metal transitions in system C with their respective Voigt-profile fits in green.

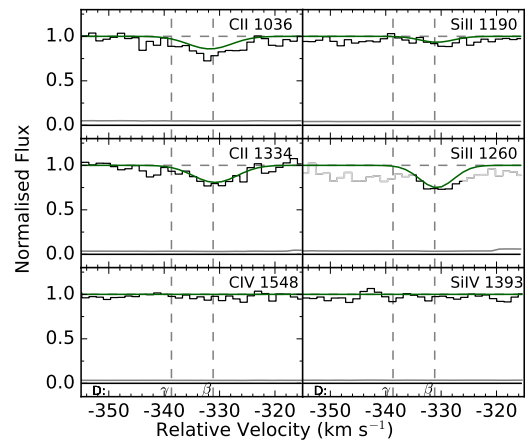


FIGURE 4.8: Marginal detection of C II is shown along side other metal transitions which provide limits in system D.

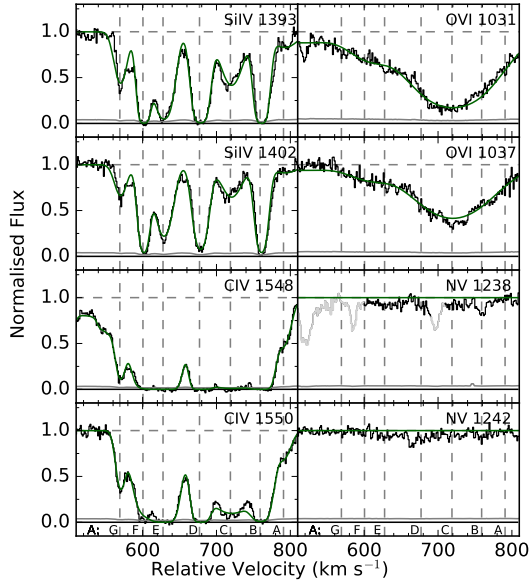


FIGURE 4.9: High-ionisation metal transitions in system A with their respective Voigt-profile fits in green.

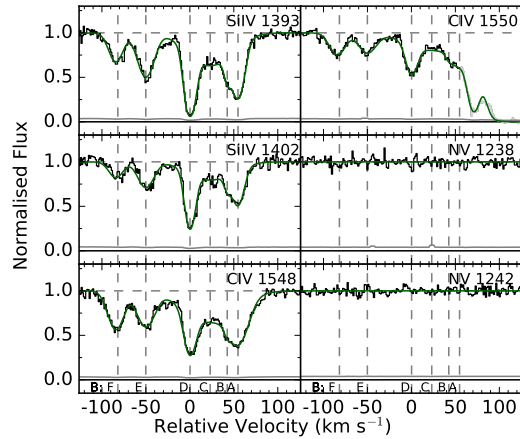


FIGURE 4.10: High-ionisation metal transitions in system B with their respective Voigt-profile fits in green.

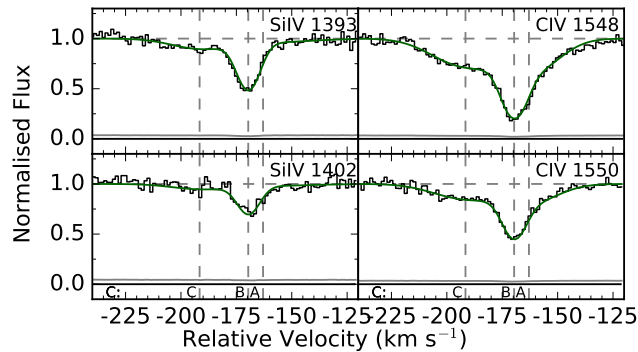


FIGURE 4.11: High-ionisation metal transitions in system C with their respective Voigt-profile fits in green.

#### 4.4.1 System A

System A, with  $\log N_{\text{HI}}^{\text{A}} < 16.9$ , is classed as a partial-Lyman limit system (pLLS). Its Lyman absorption is shown in Fig. 4.4, and low- and high-ionisation metals in Figs. 4.5 and 4.9, respectively. All C iv and Si iv transitions are affected by saturation in some or all of the seven main velocity components, which combine to give lower limits of  $\log N_{\text{CIV}}^{\text{A}} > 15.2$  and  $\log N_{\text{SiIV}}^{\text{A}} \geq 14.3$ . The singly ionised lines, on the other hand, are much weaker at  $\log N_{\text{CII}}^{\text{A}} = 13.32 \pm 0.02$  and  $\log N_{\text{SiII}}^{\text{A}} = 12.26 \pm 0.03$ , and are detected only in component A $\alpha$ . The ratios of singly-to-triply ionised absorption are presented in Table 4.6, and they are both around -2 dex, which indicates a very high degree of ionisation in the system. This assertion is reflected in oxygen, with the values of  $\log N_{\text{OVI}}^{\text{A}} = 14.8 \pm 0.05$  and  $\log N_{\text{OI}}^{\text{A}} < 12.05$ . For all other ions we report non-detections, including both N II and N v, despite good coverage in their respective wavelength regions.

The aforementioned ionic ratios are an average calculated over the whole of system A. In reality, the highly ionised gas appears as a series of clouds located at different relative velocities along the line of sight, while singly ionised absorption is only detected in one component. In this component (A $\alpha$ /AB), the ratios are less extreme, although the difference between singly

and triply ionised systems is still over 1 dex. In the other components, there is evidence that the ionisation is even stronger. The physical interpretation is that  $A\alpha$  is a denser, slightly less strongly ionised pocket along a sightline of highly ionised gas covering over  $300 \text{ km s}^{-1}$  in relative velocity. In general, however, the fact that H I traces the high ions well while the low ions are only found in one narrow component suggests that the system is highly ionised, and that H I traces a much more dominant H II component. This implies that the metals are also mostly in the more highly ionised state, leaving too few to be detected in the singly ionised state.

#### 4.4.2 System B

With  $17.9 < \log N_{\text{HI}}^{\text{B}} < 18.35$ , system B has the largest column density of neutral hydrogen in the complex by nearly two orders of magnitude, but the absence of evident damping of Ly- $\alpha$  (Fig. 4.3) means that it is also classed as an LLS. The singly ionised species show one strong and three weaker components ranging over  $100 \text{ km s}^{-1}$  (Fig. 4.6). The strongest component, B $\gamma$ , is effectively coincident with the high-ionisation component BD and is saturated in C II  $\lambda 1334$  and Si II  $\lambda \lambda 1190, 1193$ . High-ionisation lines, on the other hand, are much weaker than in system A and are unsaturated (Fig. 4.10), allowing for tight constraints to be placed on their column density and a comparison to the low ions to be made. The O VI doublet is located in the Ly- $\alpha$  forest, and strong blending prevents an unambiguous detection. The ionic ratios  $\log(N_{\text{Si II}}/N_{\text{Si IV}})_{\text{B}} = 0.24 \pm 0.03$  and  $\log(N_{\text{C II}}/N_{\text{C IV}})_{\text{B}} > 0.76$  are around 2 dex larger than system A, which implies that the ionisation is not as strong in system B. Similarly to system A, the ionic ratios vary substantially across system B: the gas associated with low-ion components B $\beta$ ,  $\gamma$ , and high-ion BD has a higher ratio of singly to triply ionised gas, while B $\delta$ /BE appears much more strongly ionised. BA and BF appear to be wings of highly ionised gas not detected in the low ions. Given that the low- and high-ion components do not trace each other exactly, it is not possible to calculate ratios for all individual components. Instead, we note that even within relatively small velocity ranges, ionic ratios appear to change on the order of a few tenths of a decade, which indicates a highly inhomogeneous ISM. Unfortunately, further analysis of the ionisation state of the system is limited through contamination by unrelated absorption in areas of the spectrum containing useful species, such as Si III and N I. Along with the large uncertainty on  $N_{\text{HI}}$ , this restricts our ability to constrain the metallicity of the system. With an unsaturated detection of O I, however, we can at least place some constraints that are independent of ionisation. This is because the neutral states of O and H are coupled by charge-exchange reactions (Prochaska et al. 2015), so they are likely to have similar ionisation fractions such that the relative abundance of the neutral state,  $\{\text{O I}/\text{H I}\}_{\text{B}} = \log(N_{\text{O I}}/N_{\text{H I}})_{\text{B}} - \log(N_{\text{O}}/N_{\text{H}})_{\odot}$ , represents the overall relative abundance,  $[\text{O}/\text{H}]_{\text{B}} = \log(N_{\text{O}}/N_{\text{H}})_{\text{B}} - \log(N_{\text{O}}/N_{\text{H}})_{\odot}$ . Following this method, we obtain  $-1.3 < [\text{O}/\text{H}]_{\text{B}} < -0.8$ . We note, however, that this assumption may break down at the low  $N_{\text{HI}}$  of this absorber and also at the high X-ray fluxes observed in GRB 080810 (Page et al. 2009).

System B shows strong absorption from the unstable fine-structure transitions C II\* and Si II\*. The C II and C II\* absorption lines are both saturated, preventing us from calculating the ratio of excited to ground-state C II. This saturation is very mild, and at such high resolution and S/N, it does not significantly affect the values obtained from the Voigt-profile fit. We conclude that the excited fraction is around 50%. Si II and Si II\*, on the other hand, are not saturated in some transitions, allowing an exact ratio to be calculated at  $\log(N_{\text{Si II}^*}/N_{\text{Si II}})_{\text{B}} = -0.93 \pm 0.04$ , or  $\sim 10\%$ . Interestingly, O I\*  $\lambda 1304$  and O I\*\*  $\lambda 1306$  are not detected, unlike GRB 050730 (Prochaska et al. 2006), for instance, where C II\* and Si II\* are also seen.



Table 4.1 cont: System B

Component									
$z$									
$v$ km s <sup>-1</sup> a									
$b$ km s <sup>-1</sup> b									
Ion	Transitions Observed <sup>c</sup>								
C II	$\lambda 1334$	$13.14 \pm 0.04$	$> 14.5$ (S)	$> 13.7$ (S)	$13.78 \pm 0.01$				
C II*	$\lambda 1335$	$12.65 \pm 0.1$	$> 14.5$ (S)	$> 13.2$ (S)	$13.33 \pm 0.02$				
N II	$\lambda 1083$	$13.03 \pm 0.08$	$13.89 \pm 0.03$	$13.29 \pm 0.07$	$13.33 \pm 0.04$				
O I	$\lambda 1302$	$< 12.95$	$13.65 \pm 0.02$	$12.93 \pm 0.14$	$< 13.1$				
Al II	$\lambda 1670$	$11.71 \pm 0.05$	$> 12.87$ (S)	$> 11.79$	$12.22 \pm 0.02$				
Si II	$\lambda 1190, \lambda 1193, \lambda 1260,$ $\lambda 1304, \lambda 1526$	$12.23 \pm 0.06$	$13.82 \pm 0.02$	$< 12.0$	$12.85 \pm 0.08$				
Si II*	$\lambda 1194, \lambda 1197, \lambda 1264,$ $\lambda 1309, \lambda 1533$	$< 11.0$	$12.87 \pm 0.03$	$11.7 \pm 0.3$	$11.9 \pm 0.1$				
Fe II	$\lambda 1608$		$< 12.70$						
Component									
$z$									
$v$ km s <sup>-1</sup> a									
$b$ km s <sup>-1</sup> b									
Ion	Transitions Observed <sup>c</sup>								
H I	Lyman series <sup>d</sup>	$\leq 15.0$	$17.9 < N_{\text{HI}} < 18.35$ (S)	$\leq 16.15$	$\leq 16.0$ (S) <sup>h</sup>				
C IV	$\lambda 1548, \lambda 1550$	$13.20 \pm 0.01$	$13.39 \pm 0.02$	$13.28 \pm 0.02$	$12.7 \pm 0.06$				$13.42 \pm 0.02$
N V	$\lambda 1238, \lambda 1242$		$< 12.3$						
Si IV	$\lambda 1393, \lambda 1402$	$12.60 \pm 0.02$	$13.25 \pm 0.01$	$13.16 \pm 0.02$	$12.28 \pm 0.05$				$12.99 \pm 0.02$

Table 4.1 cont: System C

Component		C $\alpha$	
$z$		3.348545	
$v$ km s $^{-1}$ <sup>a</sup>		-171	
$b$ km s $^{-1}$ <sup>b</sup>		4	
Ion	Transitions Observed <sup>c</sup>	$\log(N)$	
C II	$\lambda$ 1334	13.50 $\pm$ 0.02	
C II*	$\lambda$ 1335	13.11 $\pm$ 0.03	
N II	$\lambda$ 1083	< 12.75	
O I	$\lambda$ 1302	< 11.2	
Al II	$\lambda$ 1670	11.66 $\pm$ 0.04	
Si II	$\lambda$ 1190, $\lambda$ 1193, $\lambda$ 1260, $\lambda$ 1304, $\lambda$ 1526	13.04 $\pm$ 0.03	
Si II*	$\lambda$ 1194, $\lambda$ 1197, $\lambda$ 1264,	11.7 $\pm$ 0.1	
Fe II	$\lambda$ 1608	< 12.75	
Component		CC	CB
$z$		3.348234	3.348552
$v$ km s $^{-1}$ <sup>a</sup>		-193	-171
$b$ km s $^{-1}$ <sup>b</sup>		22	41
Ion	Transitions Observed <sup>c</sup>	$\log(N)$	
H I	Lyman series <sup>d</sup>	< 13.8	15.53 $\pm$ 0.05 <sup>i</sup>
C IV	$\lambda$ 1548, $\lambda$ 1550	13.2 $\pm$ 0.2	13.27 $\pm$ 0.06
N V	$\lambda$ 1238, 1242		< 13.05
Si IV	$\lambda$ 1393, $\lambda$ 1402	12.21 $\pm$ 0.08	12.66 $\pm$ 0.02
			12.01 $\pm$ 0.1
			CA
			3.348649
			-164
			54

Table 4.1 cont: System D

Component	DD	DC	DB	DA
$z$	3.345680	3.346103	3.346212	3.346816
$v$ km s <sup>-1</sup> <sup>a</sup>	-369	-339	-332	-290
$b$ km s <sup>-1</sup> <sup>b</sup>			4	
Ion	Transitions Observed <sup>c</sup>		log(N)	
H I	Lyman series <sup>d</sup>		15.55 ± 0.05	
C II	<b>λ1036, λ1334</b>		12.66±0.05	
N II	λ1083		< 12.15	
N V	λ1238, λ1242		< 11.85	
C IV	λ1548, λ1550		< 12.05	
O I	λ1302		< 12.5	
Al II	λ1670		≤ 11.2	
Si II	λ1190, λ1260		≤ 11.65 <sup>j</sup>	
Si II	λ1309		< 12.4	
Si IV	λ1393, λ1402		< 11.3	
Fe II	λ1608		< 12.5	

(S/B): line is saturated/blended.

<sup>a</sup> Relative velocity compared to component Bγ at  $z = 3.351030$ .

<sup>b</sup>  $b$  is the broadening parameter for the component determined from the fit to the highest S/N, unsaturated and unblended lines.

<sup>c</sup> Only transitions in bold have been used in the determining of column densities or upper limits

<sup>d</sup> see Section 4.3.1.1 and Figs 4.3,4,4

<sup>e,f,g</sup>  $z = 3.358461, 3.359810, 3.361463$  and  $b = 65, 36, 72$  km s<sup>-1</sup> respectively.

<sup>h</sup> Combined upper limit for BA+ BB + BC.

<sup>i</sup>  $b = 8.0$  km s<sup>-1</sup>.

<sup>j</sup> The significance of this measurement is discussed in Section 4.4.4.

TABLE 4.5: Total column densities in the four main systems of the host complex.

	A	B	C	D
Ion	$\log N$			
H I	$\leq 16.9$	$18.1 \pm 0.25^a$	$15.53 \pm 0.05$	$15.97 \pm 0.1$
C II	$13.32 \pm 0.02$	$> 14.5$	$13.50 \pm 0.02$	$12.66 \pm 0.05$
C II*	$< 12.35$	$> 14.5$	$13.11 \pm 0.02$	$< 12.55$
C IV	$> 15.2$	$14.03 \pm 0.01$	$13.70 \pm 0.07$	$< 12.05$
N II	$< 13.35$	$14.11 \pm 0.02$	$< 12.75$	$< 12.15$
N V	$< 12.0$	$< 12.3$	$< 13.05$	$< 11.85$
O I	$< 12.05$	$13.73 \pm 0.03$	$< 11.2$	$< 12.5$
O VI	$14.81 \pm 0.05$	-	-	-
Al II	$< 11.3$	$> 13.0$	$11.66 \pm 0.04$	$\leq 11.2$
Si II	$12.26 \pm 0.03$	$13.87 \pm 0.02$	$13.04 \pm 0.03$	$\leq 11.65$
Si II*	$< 12.25$	$12.94 \pm 0.03$	$11.7 \pm 0.1$	$< 12.4$
Si IV	$\geq 14.3$	$13.68 \pm 0.01$	$12.86 \pm 0.03$	$< 11.3$
Fe II	$< 12.65$	$< 12.70$	$< 12.75$	$< 12.5$

<sup>a</sup> PDF is not Gaussian, but more likely flat.

TABLE 4.6: Ionic and excitation ratios for the four components in silicon and carbon, given in the form  $X_A/X_B = \log(N_{X_A}/N_{X_B})$ . These ratios are derived for entire systems; the values for individual components vary somewhat.

	A	B	C	D
Ratio	$\log(N_{X_A}/N_{X_B})$			
C II/C IV	$< -1.9$	$\geq 0.8$	$-0.05 \pm 0.1$	$> 0.5$
Si II/Si IV	$\leq -2$	$0.24 \pm 0.03$	$0.22 \pm 0.04$	-
C II*/C II	$< -0.97$	$\approx 0$	$-0.39 \pm 0.03$	$< 0.11$
Si II*/Si II	$< 0$	$-0.93 \pm 0.04$	$-1.34 \pm 0.1$	-
O I/O VI	$< -2.75$	-	-	-

### 4.4.3 System C

System C has the lowest H I column density of the host complex with  $\log N_{\text{HI}}^{\text{C}} = 15.53 \pm 0.05$  (Fig. 4.3), but it shows strong metal absorption (Fig. 4.7), even from the low-ionisation lines of C, Si, and Al, suggesting that it has also been significantly enriched with metals. We compare the relative abundances of Si II and H I:  $\{\text{Si II}/\text{H I}\}_{\text{C}} = 2.00$  is over 1.5 dex more than that of system B, which is constrained to  $0.06 < \{\text{Si II}/\text{H I}\}_{\text{B}} < 0.56$ . This could be explained if the metal content were the same, but system C was much more ionised than system B, such that  $N_{\text{HI}}/N_{\text{H}} \ll 1$ , a hypothesis supported by the lack of an O I detection in C. However, the high-ionisation lines in system C are weaker than system B (Fig. 4.11), such that the ionisation strength appears not to be particularly high. We make qualitative inferences on the nature of systems B and C in Sect. 4.5.1.

Fine-structure lines of C II\* and Si II\* are also detected in system C, albeit significantly weaker than in B. All but two Si II\* transitions are contaminated by unrelated absorption: Si II\*  $\lambda 1264$  is detected, but with a small column density, such that the non-detection of Si II\*  $\lambda 1309$  is consistent. Ratios of  $\log(N_{\text{Si II}^*}/N_{\text{Si II}})_{\text{C}} = -1.34$  and  $\log(N_{\text{C II}^*}/N_{\text{C II}})_{\text{C}} = -0.39$  indicate less excitation than in B.

#### 4.4.4 System D

System D has an  $N_{\text{H I}}$  that is 0.4 dex larger than system C, but there is an almost total dearth of metal absorption except for a marginal ( $\sim 3\sigma$ ) detection of C II. Standout measurements include the lack of any highly ionised metal lines, with upper limits of  $\log N_{\text{C IV}}^{\text{D}} < 12.05$  and  $\log N_{\text{Si IV}}^{\text{D}} < 11.05$ . This places a limit of  $\log(N_{\text{C II}}/N_{\text{C IV}})_{\text{D}} > 0.5$  dex, which points towards a similar or lower ionisation fraction than in system C. The relative abundance, on the other hand, is much lower:  $\{\text{C II}/\text{H I}\}_{\text{D}} = 0.33$  compared to  $\{\text{C II}/\text{H I}\}_{\text{C}} = 1.69$ . Si II is very weak, but may be evident in the transition at 1260 Å. This part of the spectrum, at 5478 Å in the observer frame, is contaminated by C IV  $\lambda$  1550 absorption at  $z = 2.534$ , and no absorption from the other available Si lines is detected above the level of the noise. When we assume the null hypothesis that there is no Si II absorption, the upper limit we measure at the position of the 1190 Å, 1304 Å, and 1526 Å transitions is consistent with the column density measured from the tentative 1260 Å feature,  $\log N_{\text{Si II}}^{\text{D}} \leq 11.65$ . We thus estimate a conservative upper limit of  $\{\text{Si II}/\text{H I}\}_{\text{D}} \leq 0.24$ , consistent with that of C II. The wavelength region around Si III  $\lambda$  1206 (5424 Å in the observed frame) is contaminated by a Ly- $\alpha$  line at  $z = 3.313$ . Based on the loose assumption of a similar ionisation level to that in C, we infer a difference in metallicity of around 1.5 dex, which is vast when we take into account the small ( $160 \text{ km s}^{-1}$ ) difference in relative velocity.

#### 4.4.5 Imaging and emission spectrum

A galaxy is detected at the GRB afterglow location in all of the images we took of the GRB field. The deep VLT image is shown in the left panel of Fig. 4.12; the host exhibits an extended morphology with a bright compact region accompanied by a fainter secondary component offset 0.8" to the northeast. A strong drop in the flux in the  $g$  and  $B$  bands suggests that this source is indeed the host galaxy system. Our spectroscopy confirms this and reveals a strong detection of redshifted Ly- $\alpha$  centred at 5305 Å ( $z = 3.36$ ).

The host is marginally resolved in both position and velocity space. An extraction of the spectrum at the position of the primary component seen in the imaging shows two marginally resolved peaks in wavelength space separated by  $\sim 13$  Å (observer-frame): one at our defined central redshift of  $z = 3.35$ , and a second dominant peak redshifted by  $\sim 700 \text{ km s}^{-1}$ . There is no spatial offset evident between these components in the 2D spectrum. Our LRIS longslit was oriented to include both the “primary” component of the host system and the secondary source to the NE, so this secondary source is also visible on the trace, although it is partially blended with emission from the “primary”. It shows bright Ly- $\alpha$  emission redshifted by approximately  $+250 \text{ km s}^{-1}$  relative to the strongest emitter, placing it at  $+1000 \text{ km s}^{-1}$  redder than our systemic redshift.

Given the equivalent redshifts, it is natural to associate the strongest emitter in the host spectrum with component A in the afterglow absorption spectrum; and we associate the blueshifted (spatially coincident) emission with component B (Fig. 4.12b). The spatially offset source and its red tail have no counterpart in absorption, while sources C and D have no distinct counterparts in emission (however, the low resolution of the host spectrum means that any such counterpart would likely be hopelessly blended with emission from B). If the GRB occurred in component B, then component A must be in the foreground and therefore must be infalling towards the host given its higher redshift—most likely the result of an active merger (the lack of a detectable spatial offset places them within a distance of  $\sim 5 \text{ kpc}$  in projection, which means that unless they are an improbable line-of-sight projection, the merger must be actively ongoing.)

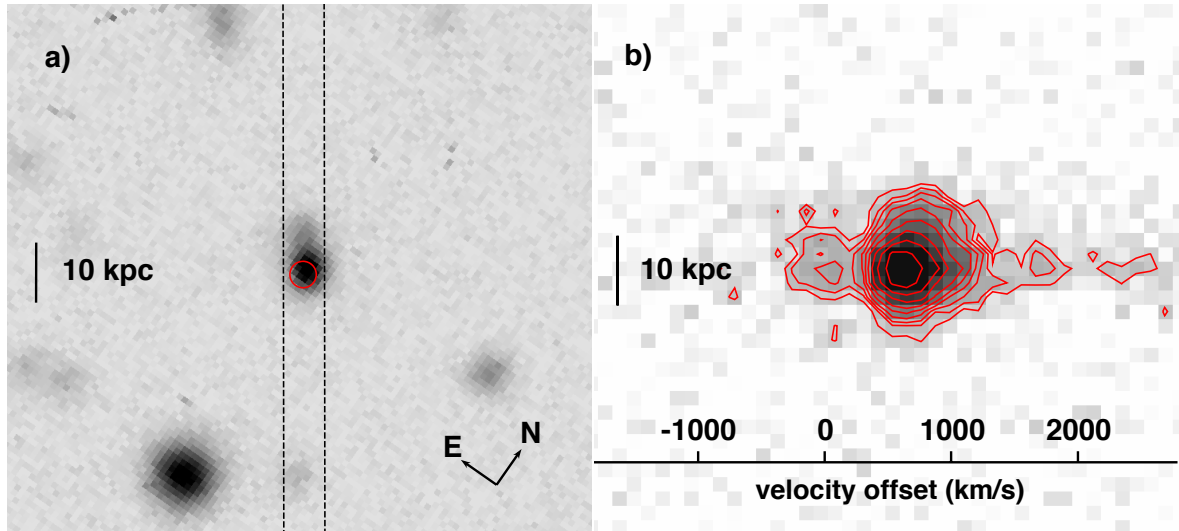


FIGURE 4.12: a) VLT/FORS2  $R$ -band image; the GRB location is marked with the red circle. The slit position used for the spectral observations is marked with vertical dotted lines; b) Keck/LRIS low-resolution 2D spectrum around the wavelength of  $\text{Ly-}\alpha$  at  $z \approx 3.35$ . The contours correspond to the relative flux of  $\text{Ly-}\alpha$  emission. The velocity scale is centred at the location of absorption component  $B\gamma$ .

We fitted all of our existing broadband photometry (presented in Table 4.7) with the Galaxy Builder photometric spectral energy distribution (SED) analysis software (first described in Perley et al. 2012, 2013<sup>5</sup>). All of the data points except for those in the  $K$  band and *Spitzer*  $3.6 \mu\text{m}$  are located at redshifts blueward of the redshifted Balmer break, and the  $K_s$  band is strongly contaminated by nebular emission from  $[\text{OIII}]$  and  $\text{H}\beta$ , which makes it difficult to constrain the presence of older stars in the population. However, it is clear that the star formation rate must be very high ( $\sim 10^2 M_\odot \text{yr}^{-1}$ ) in order to explain the luminous UV emission and  $K_s$ -band nebular excess. Extinction is modest ( $A_V \sim 0.4 \text{mag}$ ) and the inferred stellar mass (approximately  $\sim 3 \times 10^9 M_\odot$ ) is moderate, similar to the median for GRB hosts in general (Perley et al. 2016c).

<sup>5</sup>The fitting procedure was developed and executed, and the results supplied, by Dan Perley.

TABLE 4.7: Optical and NIR photometry of the host system.

Band	Magnitude <sup>a</sup>	Telescope/Instrument
$B$	$24.36 \pm 0.09$	Keck-I/LRISb
$g$	$24.13 \pm 0.07$	Keck-I/LRISb
$r$	$23.33 \pm 0.10$	GTC/OSIRIS
$R$	$23.25 \pm 0.04$	VLT/FORS2
$R$	$23.42 \pm 0.06$	Keck-I/LRISr
$i$	$23.22 \pm 0.06$	GTC/OSIRIS
$z$	$23.46 \pm 0.15$	Keck-I/LRISr
$J$	$23.44 \pm 0.22$	Keck-I/MOSFIRE
$K_s$	$22.23 \pm 0.12$	Keck-I/MOSFIRE
$3.6$	$23.57 \pm 0.07$	Spitzer/IRAC

<sup>a</sup> AB system, not corrected for foreground reddening.

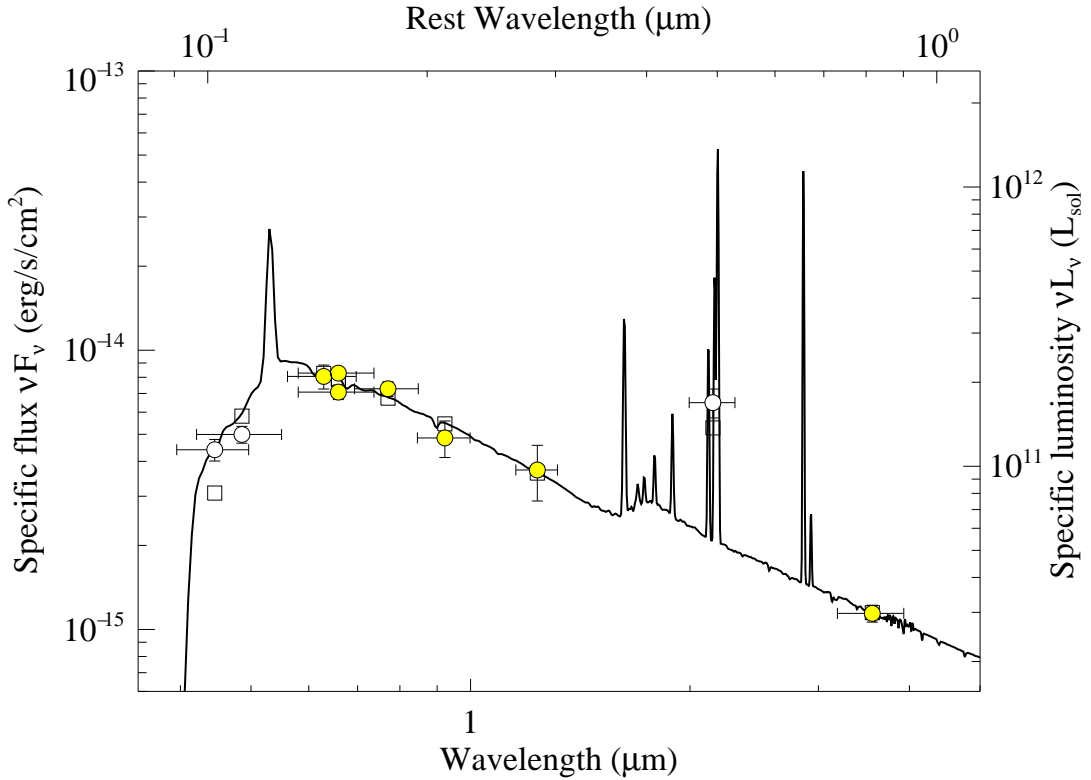


FIGURE 4.13: Spectral energy distribution of the host galaxy. We have obtained through multi-band photometry of this host as part of the SHOALS survey, showing it to be a remarkably luminous ( $MUV \sim -23$  mag) Lyman-break galaxy. A notable excess in the  $K_s$ -band photometry above the SED model suggests very strong high equivalent-width [OIII] emission. Clear circles show bands not used in the SED fit due to Ly- $\alpha$  forest or nebular contamination). Empty squares represent the value of the model integrated over the width of each band, and they show a relatively good fit.

## 4.5 Characterising the absorbing systems

Using the chemical, ionic, and kinematic properties presented in the previous section, we now classify the four distinct systems at the highest redshift along the extremely rich line of sight to GRB 080810 and build a picture of the entire complex, which we summarise in the cartoon Fig. 4.15.

### 4.5.1 Systems B and C

Several factors lead us to propose that system B lies nearest to the explosion site of GRB 080810. The most compelling factor is that system B is by far the largest reservoir of neutral hydrogen of the four systems we studied. This is a characteristic trait of the LOS probed by GRBs through their host galaxies. GRBs are associated with massive stars, and while they typically fully ionise their immediate surroundings, we expect the LOS to probe other regions of cool, dense, and predominantly neutral gas that is necessary for star formation inside the host galaxy. Although system B falls well below the average  $N_{\text{H I}}$  for a GRB (Cucchiara et al. 2015 reported a median of  $\log N_{\text{H I}} = 21.5$ ), its value is nearly two orders of magnitude higher than that of systems A, C, and D combined.

Secondly, we refer to the strong absorption by the fine-structure transitions of C II and Si II, which is often used as strong evidence that the physical location of the cloud is near to the GRB (Prochaska et al. 2006; Vreeswijk et al. 2013; D’Elia et al. 2014; Friis et al. 2015), as the intense UV radiation from the burst excites these unstable transitions. System C, however, also exhibits strong fine-structure absorption and might therefore also be close to the GRB. This observation is similar to the results Savaglio et al. (2012) obtained for the pair of interacting galaxies that form the host of GRB 090323, which both exhibit absorption from excited lines. It is known that lines may also be excited by UV radiation from a strong starburst (Pettini et al. 2002; Christensen et al. 2011), and the interpretation presented for GRB 090323 is that substantially increased star formation caused by the interaction is the reason for the excitation. Systems B and C may similarly be affected by intense background UV flux from the highly star-forming environment, but they would have to both be very close to the young hot stars. It is more likely that the majority of the excitation is caused by the GRB in both cases, as this can occur at distances of up to a few kiloparsecs from the burst. We note that the relative fraction of Si II in the excited state is 0.3 dex higher in system B, and a similar pattern is evident in C II. Assuming that both systems are exposed to the same background radiation field, we suggest that the additional excitation seen in B could be due to a higher influence of UV pumping from the GRB itself, and thus that it is located closer to the site of the burst.

System C is  $170 \text{ km s}^{-1}$  blueshifted from the central velocity component of B. However, it shows a fairly similar chemical composition. The similarities in the ionisation and excitation characteristics of B and C suggest that they are irradiated by a similar source, namely the GRB plus some UV background from nearby OB stars. Typically, it is expected that of two clouds exposed to similar ionising fields, the cloud with lower  $N_{\text{H I}}$  will be more strongly ionised because self-shielding is less efficient. For its very low  $\log N_{\text{H I}} = 15.53$ , the ionisation in C appears remarkably weak, based upon C IV and Si IV measurements (Table 4.6), which suggests that it could be similar to the ionisation in B. With comparable ionisation but much less H I, we infer that the total hydrogen content of system C is much lower than B. Thus, given that the metal detections are still strong, we assume metallicity is likely similar or even higher. Along with the negative relative velocity of nearly  $200 \text{ km s}^{-1}$ , we are led to propose that system C may trace an outflow driven by the intense star formation and associated supernovae in the galaxy in which the GRB exploded. Although the ionisation is relatively weak compared to system B, the system is still strongly ionised, with the H I tracing the high-ion components CA and CC that are not seen in low ions. This observation is consistent with other observations of strong ionisation in galactic outflows (Pettini et al. 2002; Grimes et al. 2009; Heckman et al. 2015; Chisholm et al. 2016).

#### 4.5.2 Lack of an Fe detection

In dense regions of the ISM, metals are often found to condense out of the gas phase and be locked into dust grains, an effect known as dust depletion (e.g. Savage & Sembach 1996; Vladilo 1998; Savaglio et al. 2003; De Cia et al. 2013). Furthermore, certain refractory elements such as Fe, Ni, and Ti are known to be much more heavily depleted than volatile elements such as Zn, S, and P. The relative depletion strengths of many elements have been well characterised by Jenkins (2009) and most recently De Cia et al. (2016), such that with a combination of measurements for volatile and refractory elements, it is possible to constrain the dust content of an absorbing system, which has been done for a sample of GRB host galaxies by Wiseman et al. (2017b). In that work, column density measurements for a minimum of four elements were required to constrain the depletion, but it is in practice possible to gain an insight into the dust content from just one volatile and one refractory element (e.g. Vladilo et al. 2011; De Cia et al. 2013).

In the case of system B of GRB 080810, we do not detect any strongly refractory elements. Furthermore, as a result of ionisation, the measurements of certain states cannot be treated as fully representative of the elements as a whole, meaning that it is not possible to measure the dust depletion directly. However, iron and silicon have very similar ionisation potentials as well as solar abundances, so that given the strong detection of Si II ( $N_{\text{Si II}}^{\text{B}} = 13.94$ ), we would expect a similar amount of Fe II. Instead, we measure only an upper limit of  $\log N_{\text{Fe II}}^{\text{B}} < 12.75$ . Assuming that iron follows a similar ionisation pattern to silicon, we can place a tentative constraint of  $[\text{Si/Fe}]_{\text{B}} > 0.9$ . If this value is due exclusively to dust, it means that system B shows stronger dust depletion than any of the 19 GRB-DLAs analysed in Wiseman et al. (2017b), at a level similar to that of the average Milky Way sight-line (Jenkins 2009; De Cia et al. 2016). There are many caveats to this analysis. It requires that the nucleosynthesis history of this galaxy, at  $z = 3.35$ , is similar to that in the solar neighbourhood, as well as that our assumptions about ionisation fractions are correct. We note that three separate studies have detected little or no dust in the afterglow SED:  $A_V = 0$  by Page et al. (2009);  $A_V = 0.16 \pm 0.02$  by Kann et al. (2010), and  $A_V < 0.35$  by Schady et al. (2012). We also find that the SED of the host gives an  $A_V$  of only  $\leq 0.5$  mag. Such a small amount of extinction is not expected for such a large amount of depletion, although these two measures of dust are indeed often inconsistent with each other (Watson et al. 2006; Friis et al. 2015; Wiseman et al. 2017b). Although there are many uncertainties in play, it is possible that some of this Fe/Si discrepancy could be due to dust. Such a detection could suggest that the gas has been ionised only recently, the cores of dust grains remaining intact.

Another possible reason for the lack of Fe is that at this redshift we expect a strong enhancement of the abundance of the alpha elements (usually denoted  $[\alpha/\text{Fe}]$ ), such that the relative abundances of Si, O, and C compared to Fe are positive. However, these enhancements are typically  $\sim 0.3$  dex at most in high-redshift absorption systems (Dessauges-Zavadsky et al. 2006; Rafelski et al. 2012; De Cia et al. 2016). Furthermore, we consider the relative abundance of another non-alpha element with similar ionisation potential to Fe: aluminium. The potentials for the first two ionisation states of Al are similar to those for Fe and Si, therefore the value  $\{\text{Al II}/\text{Si II}\} \approx 0.06$  suggests very little  $\alpha$  enhancement.

The depletion characteristics of Al are poorly understood, but is usually described as a refractory element (Phillips et al. 1982; Prochaska & Wolfe 2002). The similarity with the Si abundance thus suggests that the depletion is likely small, in contrast to the inference from the Si/Fe ratio. This could be explained by an abnormally high Al/Fe ratio, as seen in other GRBs (D’Elia et al. 2014; Hartoog et al. 2015), for which proton capture processes were highlighted as a possible cause. Were this the case in GRB 080810, then this would prevent the Al/Si ratio from ruling out  $\alpha$  enhancement being prominent.

While we cannot discount the possibility that all of these deviations from expected abundance patterns are primarily caused by the effects of strong ionisation, the non-detection of iron remains particularly puzzling.

### 4.5.3 System A

The absorption system A has a mean velocity of  $+690 \text{ km s}^{-1}$  relative to system B, consistent with the relative velocity seen in Ly- $\alpha$  emission. The implication is that system A lies in the foreground and is falling towards, and likely merging with, the host (including systems B and C). System A shows drastically different chemical and kinematic properties to system B. It is almost totally ionised and shows absorption from higher ionisation states over a  $320 \text{ km s}^{-1}$  range in relative velocity, which is traced by relatively weak neutral hydrogen. This velocity range is consistent with the range seen at intermediate impact parameters ( $\sim 30 \text{ kpc}$ ) in the CGM of a sample of Lyman-break galaxies (LBGs) at a similar redshift by Steidel et al. (2010). The

presence of such highly ionised gas, including strong O VI absorption, indicates that system A is a sight line through the CGM of the foreground galaxy. The high ionisation and wide velocity structure is indeed similar to that observed in the CGM of star-forming galaxies in the COS-Halos sample at  $z \approx 0.2$  (Werk et al. 2016; Prochaska et al. 2017). However, the imaging data presented in Sect. 4.4.5 imply that the LOS from the GRB passes within  $\lesssim 5$  kpc of the centre of this foreground galaxy. This is over an order of magnitude smaller than the impact parameters for the Steidel et al. (2010) sample, and also smaller than the impact parameters of the COS-Halos sample and the  $z \lesssim 1$  LLSs by Lehner et al. (2013). The fact that the LOS passes so close to the galaxy centre yet incurs such little neutral gas is unprecedented, and implies a very compact system — whereas in the aforementioned samples, we would expect at least a sub-DLA for such a sight line, here we see the typical signature of the CGM.

#### 4.5.4 System D

There is only a  $\sim 150$  km s<sup>-1</sup> difference in relative velocity between systems C and D, but they have strikingly different chemical properties. The almost total lack of metal absorption in D starkly contrasts with the comparatively metal-rich system C, and the lack of C IV and Si IV suggest a small ionised fraction. Together, these characteristics indicate that D is a cooler metal-poor cloud that is part of an inflow from the IGM. Although the marginal detection of carbon means that this is likely not primordial gas, it is much less enriched than that in the other systems, which have been processed in stars. The metals present could originate from mixing with more metal-rich gas ejected during previous epochs of intense star formation from nearby galaxies (see Fraternali & Filippo 2016 for a review).

## 4.6 Discussion

### 4.6.1 Conditions in the interacting galaxies

The analysis of the four main components paints a picture of a complex, compact environment that is host to GRB 080810. Denser gas is typically expected to be found at smaller impact parameters ( $R_{\perp}$ ), a trend seen in Werk et al. (2012), Lehner et al. (2013) and Prochaska et al. (2017). In the sample of LBGs presented in Steidel et al. (2010), there is also a strong decrease of absorption line strengths of Ly- $\alpha$  and metals with increasing impact parameter. As shown in Fig. 4.14, systems A, C, and D have some of the smallest column densities of neutral hydrogen ever observed at the host redshift of a GRB (compared to objects in the sample of GRB-DLAs by Cucchiara et al. 2015), with B also at the very low end of the distribution. We also contrast these column densities with two samples of QSO absorption line systems that probe the CGM, namely the samples reported by Prochaska et al. (2015) and Lehner et al. (2013). Whereas the QSO absorber samples typically probe gas at impact parameters of  $R_{\perp} \sim 10 - 100$  kpc, the sight line to GRB 080810 passes within 5 kpc, but it is evident that the  $N_{\text{H I}}$  is at the lower end of these populations as well. To find such a low  $N_{\text{H I}}$  in a system that is both a GRB host and lies at a small radius is highly unusual.

Systems A and B display comparable total metal column densities, but the fractions of C and Si in higher ionisation states are over two orders of magnitude larger in A than in B. This is reflected in the observed neutral hydrogen column density, which is 1.4 dex smaller in A. This result is consistent with the result from Prochaska et al. (2015), who found that the ionised fraction is higher in LLSs with lower  $N_{\text{H I}}$  (their Figure 9). We note that the sample presented in that paper has a lower  $\log N_{\text{H I}}$  cut-off of 17.3 and that trends evident there may not apply at the much lower column densities probed by A, C, and D. The vast difference in ionisation fractions and large velocity widths of systems A, B, C, and D imply highly turbulent media, reminiscent

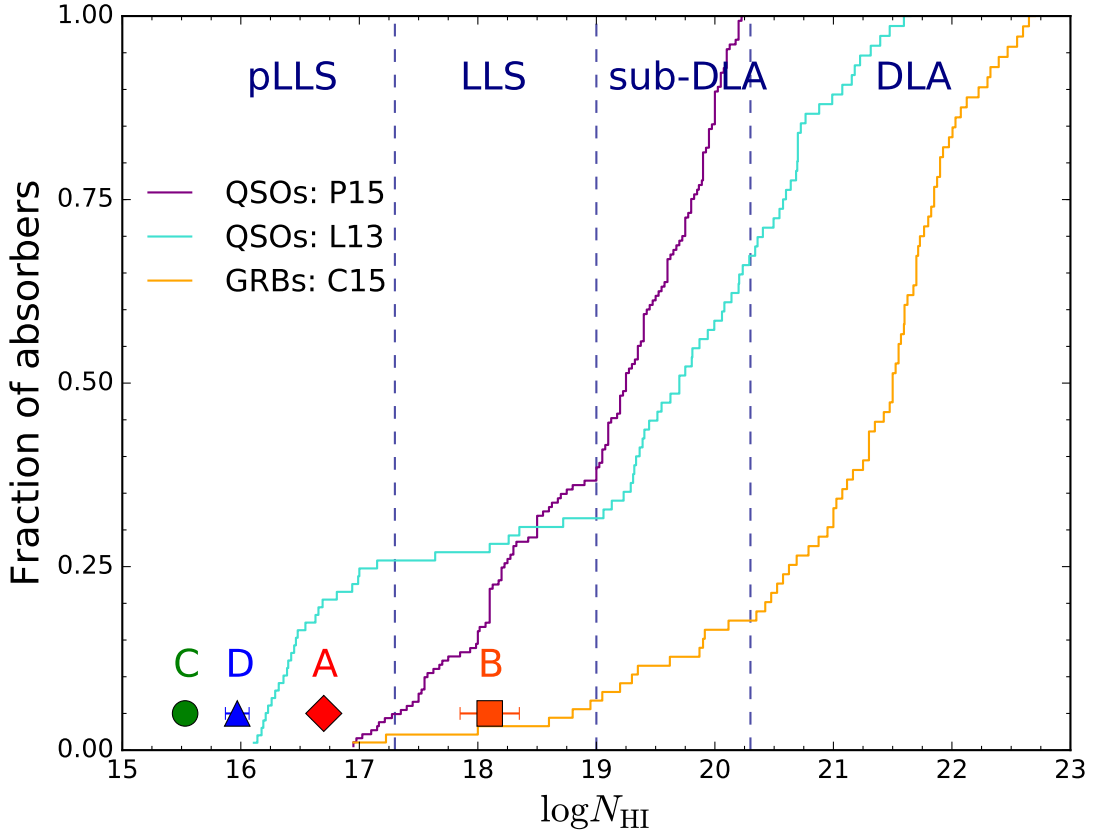


FIGURE 4.14: Neutral hydrogen column in the four systems (coloured shapes) compared to cumulative distributions of  $N_{\text{HI}}$  from three samples of Ly- $\alpha$  absorbing systems: GRB host galaxies (Cucchiara et al. 2015; C15, to which we have added GRBs 120119A and 141028A from Wiseman et al. 2017b), and QSO absorbers (Lehner et al. 2013; L13, Prochaska et al. 2015; P15).

of that found in CGM at larger ( $\sim 100$  kpc) radii (e.g. Crighton et al. 2013). We emphasise that in star-forming galaxies at high redshift there is a dynamic interplay between the the ISM and CGM (see e.g. Steidel et al. 2010), and the boundaries are largely undefined. It is clear that these are compact galaxies, with relatively small amounts of gas being probed. The gas observed is much more diffuse than expected for lines of sight passing so close to centres of star-forming galaxies.

While low H I column densities are rare in GRBs, a common trait exists among the small number of such objects, namely that multiple absorbing components separated by high ( $500 - 5000 \text{ km s}^{-1}$ ) velocities are often detected, as presented for GRB 080810 in this work. GRB 021004 ( $\log N_{\text{HI}} = 19.0$ ), GRB 060607A ( $\log N_{\text{HI}} = 16.8$ ), and GRB 080310 ( $\log N_{\text{HI}} = 18.8$ ) were all analysed in Fox et al. (2008), and GRB 060605 ( $\log N_{\text{HI}} = 18.9$ ) was analysed by Ferrero et al. (2009). These papers discussed the nature of the observed high-velocity components: whether they are winds originating from the GRB progenitor, are outflows on galactic scales, or are unrelated intervening systems. However, our analysis of the imaging and late-time spectroscopy of the host of GRB 080810 strongly suggests that the two largest absorbing systems correspond to two very compact interacting galaxies.

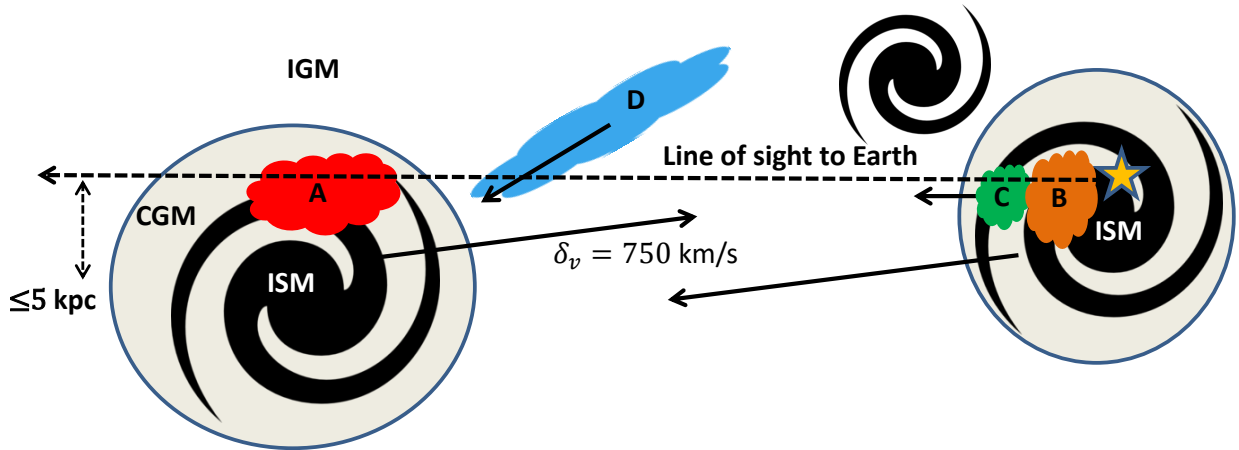


FIGURE 4.15: Scenario derived for the geometry of the host system. The GRB is represented by a yellow star, with the four absorption systems that trace strikingly different phases of gas coloured according to their apparent redshift in the absorption spectrum. The 5 kpc offset comes from the size of the foreground galaxy in the image along with the uncertainty on the GRB position. The additional component seen in the imaging data (Fig. 4.12), here shown between the two galaxies, does not intersect the line of sight and could be located at any horizontal position in this diagram.

#### 4.6.2 GRBs and SNe in interacting systems

The link between mergers and intense star formation has been studied for decades (e.g. Sanders et al. 1988; Bell et al. 2006; Robaina et al. 2009; see Bournaud 2011 for a review), and such events are a key ingredient in the theory of galaxy evolution (White & Rees 1978). Given that core-collapse SNe and GRBs are associated with massive stars, it is reasonable to expect a link between systems where mergers have caused starburst activity and thus a young and massive stellar population, and GRBs (Lopez-Sanchez & Esteban 2009; Chen 2011), and we propose that GRB 080810 could be one such system. There are other examples of potentially merging systems hosting cosmic explosions, detected in absorption line profiles such as GRB 090323 (Savaglio et al. 2012) and GRB 100219A (Thöne et al. 2013), and in imaging of the hosts (GRB 051022; Castro-Tirado et al. 2007; Rol et al. 2007, and GRB060814; Perley et al. 2013). Similarly, interacting systems have also been detected in the host systems of superluminous supernovae (Chen et al. 2017b; Perley et al. 2016b). However, the detection of mergers in GRB and SN hosts could be coincidental, especially at high redshift, where mergers are much more frequent (e.g. Callegari et al. 2009). Simulations and observations both show that at  $z \approx 3$  more than one in ten galaxies of stellar mass  $> 10^9 M_{\odot}$  have experienced a major merger in the preceding 1 Gyr (Rodríguez-Gomez et al. 2015). It remains to be clarified whether such GRBs are a result of the merger or are simply coincident.

#### 4.6.3 Inflows and outflows

The energetic turbulent medium present in system A, the strong ionisation, and the mixing of different gaseous phases all indicate inhomogeneous motion throughout the ISM and CGM of the galaxy system that is the host of GRB 080810, on small and large scales. While there is already evidence for the presence of large-scale outflows in GRB host galaxies (e.g. Schaefer et al. 2003; Chen et al. 2009), system C is one of the most convincing yet. It has been strongly enriched with metals, and its ionisation and excitation properties suggest an origin in the star-forming regions of its galaxy, near to the location where the GRB occurred. In contrast to system

A, which is highly ionised and likely representative of a hot wind-enriched galaxy halo, system C appears to have not yet reached its galaxy's CGM. Instead, it has maintained conditions similar to its conditions at launch.

A likely scenario for the geometry of the entire system is presented in Fig 4.15. The locations of systems A, B, and C are fairly well constrained by their metal absorption. System D is harder to place, as there is little to be learned from its negligibly low metal content. It is highly improbable that it is an outflow similar to C but with a higher velocity, or indeed that it has originated inside the galaxy at all. Instead we believe it to trace the metal-poor gas that acts as a replenishment mechanism of galaxies throughout the universe. It has indeed been suggested that GRB hosts in general are fuelled by recent metal-poor gas inflow (Michałowski et al. 2015, 2016). The  $-320 \text{ km s}^{-1}$  blueshift implies that it is not accreting onto galaxy B — if B hosted the GRB, then D must be in front of it, moving away at that velocity. The degeneracy between local velocities and cosmological redshift allows for a range of locations of system D. One possibility is that it is located between the two galaxies and is currently falling towards galaxy A, or has fallen from behind galaxy B and is being slowed by its gravity. Another possibility is that it has fallen from a large distance into the potential well of the complex and is now in the foreground, having initially passed both galaxies without being accreted, having joined in a disk-like structure (e.g. Bouché et al. 2013). For any of these scenarios, system D represents a rare detection of such a metal-poor inflow in a GRB galaxy, or indeed in absorption at such a small projected distance to any galaxy. Systems with positive velocities relative to the gas local to GRBs, and thus inferred to be falling in towards the star-forming regions of their hosts, have been detected previously (e.g. Prochaska et al. 2008a), but these have tended to be richer in metals than the gas observed here and may represent recycled gas that has previously been expelled from the galaxy. Ly- $\alpha$  emitters are thought to trace accretion in large halos around quasars (Cantalupo et al. 2014; Hennawi et al. 2015), and have been detected at impact parameters of  $\geq 70 \text{ kpc}$  from an LLS (Fumagalli et al. 2016). If system D is indeed bound to the host system, then it could be much closer to the galaxies than that. Finally, as discussed when defining the host complex in Section 4.3.1, it could in fact be a foreground system located  $\sim 1.5 \text{ Mpc}$  from the interacting complex. While this would exclude it from being a direct accretion flow onto the complex, it represents at the very least a reservoir of cool metal-poor gas residing in the IGM near the dark matter halo, available for star formation at some future epoch.

## 4.7 Summary and conclusions

The rapid follow-up observations of the extremely bright GRB 080810 with a high-resolution spectrograph at a 10m class telescope have provided us with an extremely rich window into the Universe at high redshift. Populated by numerous absorption systems from redshifts of upward of 2.3, the line of sight to the afterglow reveals a myriad of absorbing clouds in the IGM, sporadic denser systems with associated metal absorption, and a complex and extreme environment that is host to the GRB itself, dominated by an interacting star-forming Lyman-break galaxy system at  $z \approx 3.35$ .

In this paper, we have examined the properties of each of the four main systems at this redshift based on their absorption properties, through which we have provided one of the most detailed analyses of the multiple component nature of a galaxy at high redshift. The emerging picture is one of a complex environment, the outstanding results of which are summarised below.

(a) GRB 080810 exploded in the more distant partner of an interacting system. This component is hidden behind the compact foreground companion (which has the brightest Ly- $\alpha$  emission), and in total, the system is forming stars at a rate of  $\sim 10^2 M_{\odot} \text{ yr}^{-1}$ . The two systems are

closing with a relative velocity of  $\sim 700 \text{ km s}^{-1}$ .

(b) The column density of neutral hydrogen measured throughout the entire complex is very low: even the strongest absorption is limited to  $\log N_{\text{H I}}^{\text{B}} < 18.35$ , one of the lowest ever measured in a GRB host system, even though the LOS to the burst passes within  $\lesssim 5$  kiloparsecs of the centres of both galaxies. These are unprecedented scales for such a low level of neutral absorption.

(c) More neutral gas is found near the GRB site. The sight line through the interacting galaxy reveals a similar metal content, which is in a much higher ionisation state, however. This is representative of gas that has been expelled from the ISM into the hot turbulent halo. The implication that this is the CGM at a galactic radius of  $\lesssim 5$  kpc is remarkable.

(d) The mechanism by which such metals are expelled into the CGM is likely seen in the form of an outflowing cloud in the GRB host, which has a velocity of  $\sim -200 \text{ km s}^{-1}$  relative to the denser gas nearest to the GRB.

(e) The ongoing intense star formation is likely fueled by metal-poor inflowing gas. A candidate counterpart for this gas is seen in the spectrum, containing only marginal detections of heavy elements. Because of the degeneracy between cosmological redshift and local peculiar velocity, we cannot confirm that this gas is spatially coincident with the host galaxies. If it indeed belongs to the host complex, then it is one of the first detections to date of metal-poor gas in such close vicinity to star-forming galaxies.

# Chapter 5

## Discussion

In Chapters 3 and 4 I have presented results from two studies of gamma-ray burst host galaxies using absorption line spectroscopy as the main observational technique. In this chapter, I will discuss the issues arising from the work, regarding both the scientific implications as well as the experience gained relating to the data analysis.

### 5.1 Dust Properties of GRB host galaxies

In Chapter 3 I have presented the analysis of the dust depletion in a sample of 19 GRB-DLAs, through which I have published the largest sample of dust-corrected, absorption-line metallicities of GRB-DLAs to date. The principle scientific result of the analysis is the observed correlation between the dust-to-metals ratio and the metallicity. This result falls in line with the findings of De Cia et al. (2016), who studied the high-redshift ISM through QSO-DLAs. This is a conclusive result, conducted on two independent samples, using a thorough method. It is also consistent with the theoretical predictions of models such as those by Mattsson et al. (2014); Dwek (2016); Mattsson (2016); Schneider et al. (2016); Zhukovska et al. (2016); Aoyama et al. (2017); Popping et al. (2017). The current literature is converging to the consensus that grain growth of dust in the ISM is the dominant dust formation mechanism across the Universe, and is important even from early times (e.g. Draine 2003; Michałowski et al. 2010), although the paradigm still has opponents (e.g. Ferrara et al. 2016).

Recent observations have shown surprisingly large quantities of dust in some high-redshift galaxies (e.g. Watson et al. 2015), and theorists and observers alike are still not united on the mechanism which has produced it. Proponents for grain growth believe that this amount of dust cannot be produced by highly evolved stars, since they have not had enough time to reach the evolutionary stage at which they produce dust. While there are indeed high rates of SNe at high redshift, they are thought not to produce most of the dust: realistic dust formation rates (that take into account dust destruction by the SN reverse shock) indicate that the SN rate is not high enough to form the dust that is observed). The observed positive correlation between DTM and metallicity found in works such as that from Chapter 3 (Wiseman et al. 2017b) as well as De Cia et al. (2013) and De Cia et al. (2016) support this theory. This is because the dust forms directly out of the metals, such that at higher metallicity the efficiency of dust production is higher. Opponents believe in the simultaneous production of all dust and metals in the envelopes of evolved massive stars (known as post-AGB stars) and in the ejecta of SNe. In this case, the DTM is fixed and does not vary with metallicity. Ferrara et al. (2016) state that grain growth is inefficient, particularly at high redshift due to the temperature of the cosmic microwave background, which they theorise renders the growth of grains in the ambient ISM highly disfavoured. Observational evidence for this ‘stable state’ of dust production was presented by Zafar & Watson (2013), in a sample of GRB-DLAs, QSO-DLAs, and lensed galaxies. Given that the samples of Zafar & Watson (2013) actually overlap with De Cia et al. (2013) and Wiseman et al. (2017b), there is a clear tension between the methods used to quantify the

dust-to-metals ratio at high redshift, and this has been shown in explicit terms in Figs. 3.13, 3.14, and 3.15. I will not repeat the discussion of this tension that has been provided in Section 3.6.4, but instead present a widened discussion on the nature of dust at high redshift.

### 5.1.1 Dust at high redshift

The two different observational methods of calculating the DTM use different dust tracers. The definition from Zafar & Watson (2013) uses  $A_V$  taken from SED fits as the measure of dust, while that of De Cia et al. (2013, 2016) and Wiseman et al. (2017b) uses depletion. The question that needs addressing is as follows: why do  $A_{V;SED}$  and  $A_{V;DTM}$  not correlate with each other closely? Either one of the measurements must be incorrect or biased, or the two measures are actually tracing different dust clouds, or a different constituent of the same dust clouds.

#### 5.1.1.1 Inaccuracy of $A_{V;DTM}$

The first thing to investigate is the way that  $A_{V;DTM}$  is calculated. As explained in Section 3.6.2, typically used is the well known MW relation between  $N_H$  and  $A_V$ , that is:

$$A_{V;MW} = 0.45 \frac{N_H}{10^{21}} \text{ mag} . \quad (5.1)$$

The factor 0.45 is effectively a combination of the number of dust particles per  $\text{cm}^2$  of H, with the amount of extinction per dust particle. This therefore incorporates the metallicity and the DTM of the MW, i.e. the dust-to-gas ratio of the MW, which is constant to within a few percent, and then simply relates the dust column density to extinction. However, in DLAs the metallicity and DTM are often quite different to the MW, so to calculate the column of dust, the  $Z$  and DTM relative to the MW are included in the calculation:

$$A_{V;DLA} = 0.45 \frac{N_H}{10^{21}} \times \frac{DTM}{DTM_G} \times \frac{Z}{Z_\odot} \text{ mag} . \quad (5.2)$$

The extra factors are needed in order to calculate the dust column density — there are a factor of  $Z/Z_\odot$  more/fewer metals per H atom, and a factor of  $DTM/DTM_G$  more/fewer dust particles per metal atom. But as the results from Chapter 3 show, it appears that this relation, between dust column and  $A_V$ , does not hold so tightly in DLAs (Fig. 3.15).

One suggested reason for this is that  $N_H$  is being systematically overestimated due to the unresolvable nature of the damped Ly- $\alpha$  line. If it were the case that most of the depletion was coming from only a single component which had a lower  $N_H$  (which has just not been resolved), then the final calculation of total column density could be heavily overestimated. This issue is resolved by the inclusion of metallicity in the formula: the overcalculation of  $N_H$  is balanced by an equivalent undercalculation of  $Z$ . However, it is also possible to calculate the dust column without scaling the  $N_H$  by metallicity and DTM. Instead, the dust column can be calculated in a bottom up way, directly from the depletion measurement:

$$N_{X,dust} = \frac{N_{X,measured}}{10^{\delta_X}} , \quad (5.3)$$

where  $N_{X,measured}$  is the measured (or the value that would be measured, given the depletion strength factor  $F_*$  measured for that DLA) column density of the metal, i.e. in the gas phase, and  $\delta_X$  is the calculated depletion. The  $N_{X,dust}$  values can be summed over all of the abundant metals for which we have known dust depletion sequences in order to estimate the total dust column,  $N_{dust}$ . This bottom up approach to the measurement also has its caveats. One is that it misses the relatively abundant elements for which there are no well known depletion sequences, such

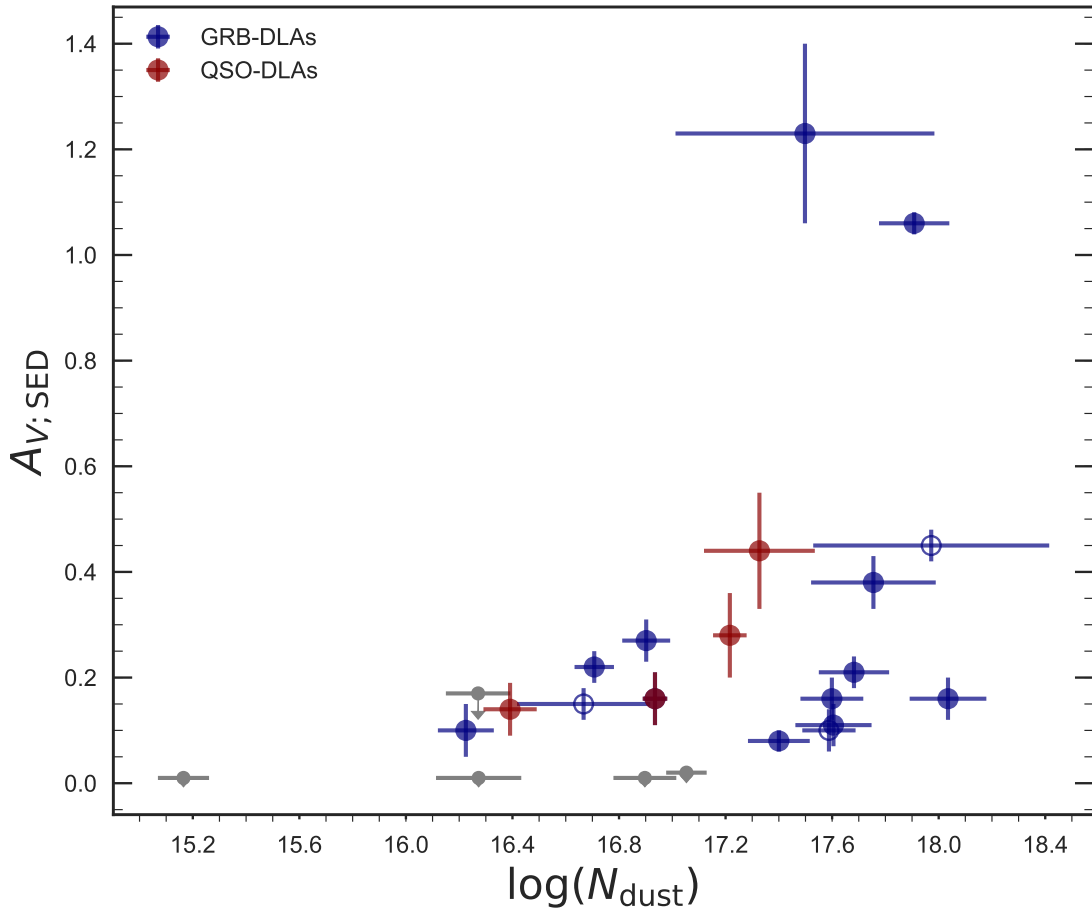


FIGURE 5.1: The  $A_{V;SED}$  compared to the dust column density in GRB-DLAs from Wiseman et al. (2017b) in blue, and three QSO-DLAs in red ( $A_{V;SED}$  from Vladilo et al. 2006,  $\log(N_{dust})$  from De Cia et al. 2016 and Péroux et al. 2006). Grey points are upper limits, and open circles correspond to depletion measured from low-resolution spectra.

as Al, Ne, Ar, Na, Ca, and importantly carbon. Carbon was included in the analysis of Jenkins (2009), but with very few data points the uncertainties on its dust depletion properties are large. Missing these elements out means that if anything the calculated column is an underestimate of the total dust column.

Fig. 5.1 shows the relation between  $N_{dust}$  and  $A_{V;SED}$  explicitly. The two distinct populations of GRB-DLAs, highlighted in Section 3.6.2, are evident once again. One population is made up of systems with an  $A_{V;SED}/N_{dust}$  significantly lower than the Milky way (appearing to the right in this figure), with the other population having more dust measured in the SED than in depletion. Despite the low number of objects, it is quite clear from this figure that in GRB-DLAs there is no simple, tight correlation between the column density of dust and the measured extinction. In other words, the number of dust particles in the line of sight does not mean a certain  $A_V$  will be measured.

It is unlikely that the depletion measurements are particularly inaccurate. The dust depletion sequences from the local group to high redshift, and from low to high metallicity, have been well studied (Jenkins 2009; De Cia et al. 2016; Tchernyshyov et al. 2015; Jenkins & Wallerstein 2017). The errors on the depletion slopes are small, and typically the relative abundances in GRB-DLAs fit these sequences very well. Following on, this means that the calculated amount

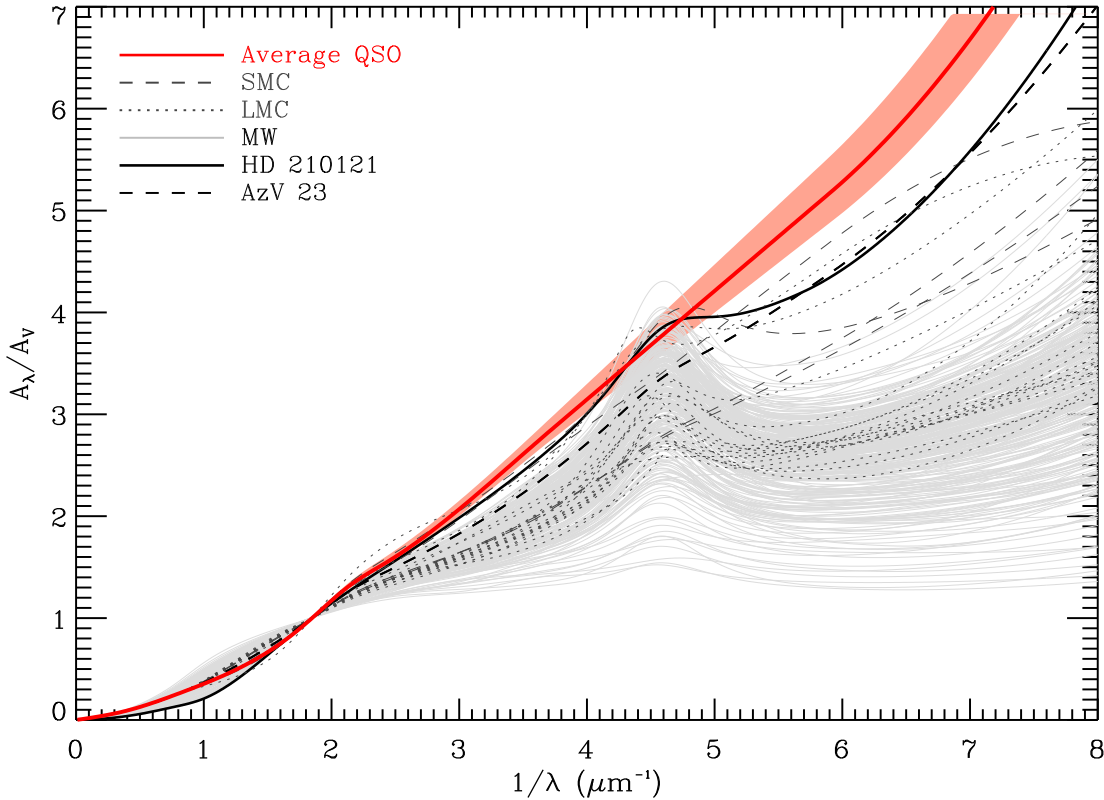


FIGURE 5.2: The average extinction curve measured from a sample of reddened quasars (red), showing their steepness and thus low  $R_V$ . These are compared to Milky Way sight lines from Fitzpatrick & Massa (2007), as well as those from the LMC and SMC (Gordon et al. 2003). HD 21012 is in the Milky Way, with AzV 23 in the SMC. Adapted from Zafar et al. (2015).

of each element in the dust phase is also accurate — we are not systematically underestimating the amount of, for example, iron or oxygen in the grains. If the aforementioned unused elements were the root of the problem, then Fig. 5.1 suggests that the fraction of these elements locked in dust grains relative to the elements measured must vary greatly, and not as a function of the total  $N_{\text{dust}}$ .

It appears that at  $\log N_{\text{dust}} > 17.5$  the lack of correspondence between the two different dust measurements is much greater, with  $A_V$  taking values from 0.1 to  $> 1$  mag. It could be that above this threshold, the properties of the dust change. For example, there could be an increase in the efficiency of forming carbonaceous dust grains. Carbon is thought to be the cause of the 2175 Å bump (e.g. Draine 1989), which is typically associated with systems with higher  $A_V$ , but with its currently poorly known depletion characteristics it is hard to tell whether it behaves linearly like the rest of the elements. However, to explain the large range of  $A_V$  for the same  $N_{\text{dust}}$ , the mechanism would have to take place in only some of the systems and thus be driven by an external factor. Alternatively, since the depletion of carbon is not included in the analysis, it could be that for these objects  $N_{\text{dust}}$  is significantly underestimated — that is, extinction is sensitive to both silicates and carbonaceous grains, whereas depletion misses many of the purely carbonaceous grains. To continue speculating about carbon as the physical cause of this large range of  $A_V$  is however not fruitful, as not enough is known about how it forms dust, but it would be worth investigating further in the future when its depletion properties are better known.

### 5.1.1.2 Varying extinction law at high $z$

Another possibility is that the two measurements are indeed tracing the same dust, but that the  $A_{V;\text{SED}}$  measurement is incorrect, if for example the extinction law used is wrong. The samples such as Kann et al. (2006); Schady et al. (2007, 2010); Greiner et al. (2011); Schady et al. (2012) have found good fits using average SMC and LMC extinction curves and the corresponding  $R_V$  values of 2.93 and 3.16, respectively. Other objects have displayed the 2175 Å bump (Krühler et al. 2008; Elíasdóttir et al. 2009; Perley et al. 2011; Zafar et al. 2011), typical of the MW extinction curve, once again meaning the  $R_V$  cannot vary too much from the average MW value of 3.08.

If the extinction law were to vary from those of the local group, however, then the measured  $A_V$  could be substantially off. The explanation of the discrepancy using the notion of grey dust, as discussed in Section 3.6.4, has been proposed in works such as Perley et al. (2008) and Friis et al. (2015). A flat extinction curve has also been suggested to explain the SED of GRB 050401 Watson et al. (2006). On the other side, some GRBs, such as GRB 080605 (Zafar et al. 2012) and GRB140506A (Fynbo et al. 2014) have shown evidence for steeper extinction curves, similar to those seen in SN of type Ia (e.g. Tripp 1998; Nobili & Goobar 2008). The evidence has been further increased by Zafar & Tayyaba (2016), who used optical/NIR spectra, rather than photometry, to fit the extinction curves, and found a mean  $R_V$  of 2.66, indicating an extinction curve steeper than the SMC. Even steeper extinction curves were found in a sample of reddened quasars (Zafar et al. 2015), with an average  $R_V$  of 2.2. For SNe Ia, one explanation for the steep extinction curves is that it mostly occurs from circumstellar dust (Wang 2005; Goobar 2008), although the latter suggest that this is due to multiple scattering events, which is not present in the ISM. This would not be the cause of steep extinction in GRB-DLAs, as all nearby material is strongly ionised by the intense radiation from the burst (e.g. Vreeswijk et al. 2007), and thus does not contribute to the extinction.

While it is certainly true that the use of Local Group extinction laws to determine  $A_V$  in GRB afterglows may cause some inaccuracies, it is unlikely that they are an order of magnitude off, which would need to be the case to explain the distribution of points in Fig. 5.1.

### 5.1.2 Future work on high- $z$ dust

The natural wish of an observer attempting to reconcile inconsistent measurements is for an increase in the amount of data, but for the analysis presented in this thesis this is unrealistic in the foreseeable future. The stringent selection criteria required to conduct the analysis with decent confidence have allowed only 19 GRBs to be studied; these 19 events have occurred over a 15 year period in which GRB research has been a strong focus of the astronomical community. No facilities are coming online which are expected to increase the number of GRBs observed with mid or high-resolution spectrographs. Instead, the different properties of the existing sample must be studied, as well as extending the analysis to different types of object.

De Cia et al. (2016) have made depletion measurements for a large sample of QSO-DLAs, but for only three have separate  $A_{V;\text{SED}}$  measurements been made beyond just upper limits. This is likely due to the difficulty in measuring reddening from a QSO spectrum, which is not as simple as that of a GRB. This is largely due to the fact that the DLA is usually at a different redshift to the QSO, but there could be significant dust in both the QSO itself as well as in the DLA. QSOs also have more complicated intrinsic spectra than GRBs. De Cia et al. (2016) discuss the three (Q0013-004, Q1157+014, J1323-0021) for which both depletion and extinction measurements have been possible, for which they report a relatively good agreement between  $A_{V;\text{SED}}$  and  $A_{V;\text{DTM}}$ . While the extinction measurements are small  $A_V = 0.44$  mag, 0.14 mag and 0.16 mag, it is still informative to calculate their values of  $N_{\text{dust}}$ , and they are plotted in Fig. 5.1.

Added to this is the object J 2225+0527 from Krogager et al. (2016b). While it is hard to draw any conclusions from so few objects, there is a hint that they fall into the lower-dust column group, in which the  $A_{V,SED}$  is higher than expected for the column of dust. It would be of great interest to put a large effort into the  $A_{V,SED}$  measurement of many QSO-DLAs that have known depletions in order to populate the diagram further. If indeed the QSO-DLAs also populate only the one group, in which the depletion appears weaker than in the majority of GRB-DLAs, then it could suggest a difference between the dust properties of GRB and QSO-DLAs. On the other hand, if they populate the two separate regions like the GRB-DLAs, it would suggest that the dust properties of the two classes of DLA are similar.

One complication in the measurement of extinction is the effect of intervening systems. Although this was touched upon in Section 3.6.4, no statistical investigation into the effects was conducted. It would be interesting to take a close look at each of the individual spectra (including those for which the column densities were taken from the literature) in order to search for intervening absorbers. It would then be possible to calculate the effect each absorber could have on the SED given its strength and redshift. Alternatively, it would be informative simply to plot the number of intervening systems and compare it to the difference between  $A_{V,SED}$  and  $A_{V,DTM}$ . However, such an analysis is not trivial, since it involves identifying all lines in the spectra in order to determine how many intervening absorbers there are, which at low S/N is often extremely difficult.

## 5.2 GRBs as probes of inflows

It is widely accepted that star formation in galaxies is fuelled by the continued accretion of gas (e.g. Rees & Ostriker 1977), otherwise they would exhaust their supplies well within the Hubble time (e.g. Genzel et al. 2010). This gas is thought to accrete onto galaxies via a number of mechanisms from the IGM. However, there is still little unambiguous observational evidence for this cornerstone of galaxy evolution theory. Studies have discovered gas infall in the form of redshifted Fe II and Mg II absorption lines in spectra of  $z \lesssim 1.4$  galaxies (Rubin et al. 2012; Martin et al. 2012). However, these signatures are rare and are based on transitions of heavy metals. Thus they may trace recycled gas which has previously been ejected from the galaxy and is re-accreting in the form of a galactic fountain, rather than the infall of pristine gas via the cosmic web. A second way of detecting infalling gas is through QSO absorbers. Typically, such systems probe dense pockets of IGM gas as well as cool regions of the CGM of galaxies. A fraction of these absorption systems are therefore predicted to trace cool, metal-poor gas falling from the IGM, through the CGM, into a galaxy (Fumagalli et al. 2011c; Lehner et al. 2013). The signatures of inflow include isolated systems with very low metallicities (Fumagalli et al. 2011a), or absorption systems detected at small impact parameters with velocity offsets matching rotation curves of their host galaxies (Bouché et al. 2013). Thirdly, there is expected to be an emissive signature of cool, accreting gas: Ly- $\alpha$  emission (Goerdt et al. 2012). There has been a detection of this signature around a quadruple quasar in a protocluster (Hennawi et al. 2015), as well as in an overdensity of radio galaxies (Vernet et al. 2017), but never around a more typical star-forming galaxy. Fumagalli et al. (2016) have searched for the Ly- $\alpha$  emission corresponding to a pristine ( $[M/H] \leq -3.8$ ) Lyman limit system at  $z \sim 3.1$ , finding an overdensity of Ly- $\alpha$ -emitting sources which show a tantalising possibility of being in alignment, and thus tracing a filament of cool gas. However, no star-forming Lyman-break galaxies (LBGs) were detected in the surroundings.

As has been discussed several times previously, GRBs provide a unique opportunity to study galaxies at high redshift, due to the strong preference for them to explode in central regions of their host galaxies. The light from the afterglow must then necessarily pass through the ISM

and CGM of the galaxy before reaching the IGM on its way towards Earth. It is also known that GRBs must occur in star-forming galaxies. It should therefore be possible, depending on the covering fraction, to detect metal-poor gas accretion in some form or another by its absorption signature in GRB afterglow spectra. The evidence for such inflow in absorption in a GRB host has however so far eluded detection at a high confidence level. Indirect evidence has been presented by Michałowski et al. (2015), who find high levels of H I in some hosts through radio observations of the 21 cm line. They suggest that the recent inflow of pristine gas has led to the large observed quantity of H I and the subsequent burst of star formation. Signs of infall have also been seen in a number of GRB absorption spectra in the form of metal lines that are redshifted relative to the bulk of the absorption (e.g. Prochaska et al. 2008a; Friis et al. 2015) as well as GRB 120119 in Chapter 3). However, these gas components are non-pristine, as their compositions include heavy elements only produced in massive stars and SNe.

In GRB spectra, the individual metallicities of the components in question cannot usually be measured accurately due to the unresolved nature of the damped Ly- $\alpha$  line. In the few cases where  $N_{\text{H I}}$  is low and Ly- $\alpha$  is weak and therefore resolvable, the S/N has typically been poor and a high resolution spectrograph, which is necessary in order to satisfactorily resolve potentially infalling components, has not been used,. That is of course excluding the case of GRB 080810, for which in Wiseman et al. (2017a) (Chapter 4) we have suggested the detection of a near-pristine infalling component. The other two GRBs with  $\log N_{\text{H I}} < 18$  and high resolution spectra are GRB 080310 and GRB 060607 (Fox et al. 2008). In GRB 080310, no infalling component is detected, although there is a weak C IV absorber at a relative velocity of  $-1400 \text{ km s}^{-1}$ , which could trace outflowing gas (or indeed infalling gas onto a foreground system, although this is not a pristine flow as it contains significant amounts of metals).

GRB 060607 has the lowest of all  $N_{\text{H I}}$  measured in a GRB spectrum, with 16.8. However, it is far from as rich in systems as GRB 080810. The high-ion lines are relatively weak and only cover a width of  $\sim 100 \text{ km s}^{-1}$ , and there is an even weaker system at  $-1800 \text{ km s}^{-1}$ . It would be interesting to make a detailed comparison of the characteristics of the three high-resolution, low  $\log N_{\text{H I}}$  spectra in order to identify similarities and differences between the absorption systems. Either GRB 080810 is an exception and a one off chance detection in an unusual environment, or it is representative of a larger population of GRBs which probe infall that do not get detected due to the aforementioned observational effects. The only way in which to test that hypothesis is to observe more GRBs with high-resolution spectrographs, which in the current climate of high competition on large telescopes is relatively difficult to realise. Even then, the vast majority of GRB hosts are DLAs, so the chances of improving the sample significantly are low.

One thing that the analysis of GRB 080810 has highlighted is the power of high-resolution spectroscopy, and the dangers of determining properties such as metallicity from lower-resolution instruments, and particularly at low  $N_{\text{H I}}$ , by showing the large differences in the physical properties of gas that in lower-resolution spectra would likely be strongly blended (although the case of 080810 is extreme). This notion leads on to the next section, namely on the synergy between and pitfalls of the different methods of measuring GRB host properties.

One way to confirm the nature of absorption systems is with integral field unit (IFU) spectroscopy, in which for every pixel a spectrum is measured. Future observations with the Multi Unit Spectroscopic Explorer (MUSE) would be able to identify accreting gas through Ly- $\alpha$  emission extended in a filamentary structure around the galaxies, which if detected would go a long way to confirming system D from GRB 080810 as a metal-poor inflow. Again, it would be informative to also observe other related targets with MUSE in order to understand what may give rise to the low total column densities along the lines of sight to such GRBs.

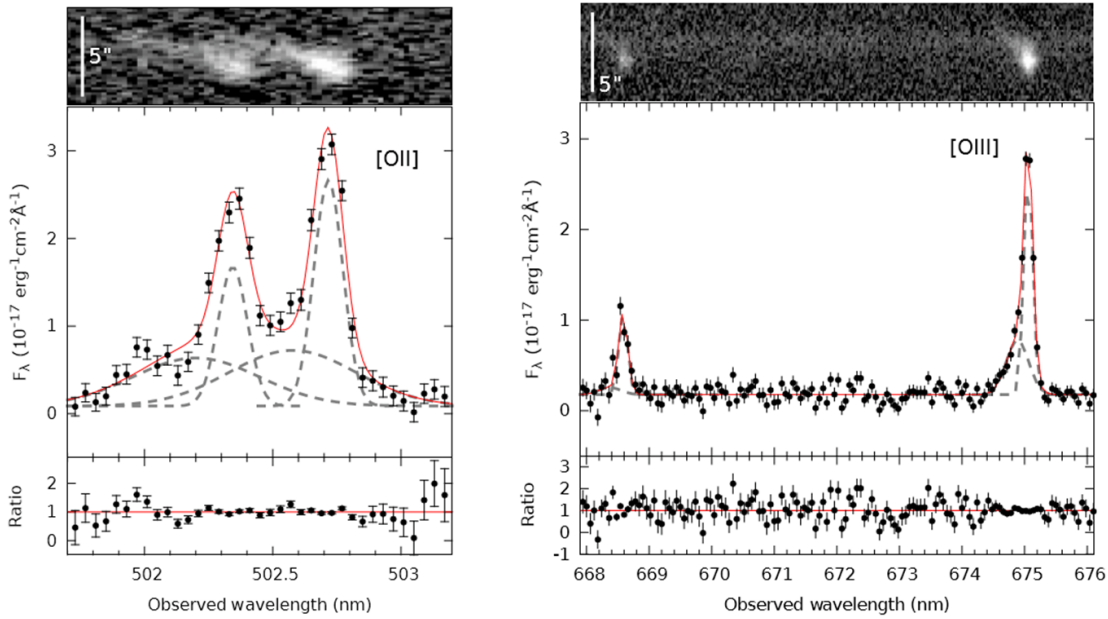


FIGURE 5.3: The O[II] and O[III] emission lines in the host of GRB 130427A. Adapted from Schady et al. (2015).

### 5.3 Accuracy of absorption and emission line measurements

While afterglow spectra are extremely rich and useful probes of the ISM of the hosts, they only probe a single line of sight, and as such do not provide information about the galaxy as a whole. By taking late time spectra in order to detect emission lines (Fig. 5.3), it is possible to gain a complementary understanding of the star-forming regions integrated over the entire host. This is because most hosts' angular sizes are smaller than the widths of the slits used; the spectrum taken is the integrated galaxy spectrum, dominated by the star-forming regions.

An excellent example of emission line spectroscopy complementing that from absorption lines can be found in Friis et al. (2015), who use the two methods to investigate the host of GRB 121024A in great detail. Metallicities measured from emission lines are typically calculated using the flux ratios of collisionally excited metal lines and hydrogen recombination lines, which are then put through their own unique formula, each of which has been calibrated differently. Different diagnostics use different combinations of different lines, and come in three distinct groups: the “direct” method uses the electron temperature measured from oxygen lines; electron temperatures can be used to calibrate certain line ratios to produce the “empirical” diagnostics (e.g. Pagel et al. 1979; Kobulnicky & Kewley 2004; Pettini & Pagel 2004; Marino et al. 2013); purely theoretical diagnostics derived from photoionisation models (e.g. Evans & Dopita 1985; Dopita et al. 2000; Kewley & Dopita 2002; Dopita et al. 2016). However, the results returned by the diagnostics can be significantly different depending on the galaxy properties such as stellar mass, as they can be sensitive to environmental conditions such as ionisation and temperature (e.g. Kewley & Ellison 2008; Yates & Kauffmann 2014). Most of them are well calibrated (or modelled) for the conditions observed in the nearby Universe, although empirical and theoretical diagnostics can still differ by up to 0.7 dex at low redshift (Kewley & Ellison 2008). It is not at all clear whether these conditions remain at high redshift; there is in fact evidence to suggest that the ionisation parameter is systematically larger at higher redshift (e.g. Steidel et al. 2014; Kewley et al. 2015). If these systematics are unaccounted for, they can lead to large errors in widely used relations such as the mass-metallicity relation (MZR; Tremonti et al. 2004), metallicity

gradients, outflows, and our general understanding of the chemical evolution of galaxies. It is therefore of utmost importance to calibrate the diagnostics to as high a precision as possible.

### 5.3.1 Metallicity diagnostics from integral field units

Integral field units combine the spatial dimensions of imaging with the spectral capabilities of spectrographs in order to create a 3D “data cube”. For objects that are spatially resolved, such as relatively nearby galaxies, IFUs provide the ability to make spectral maps. These can be useful for assessing the rotation curves of galaxies (e.g. Übler et al. 2017; Genzel et al. 2017 who used KMOS, an NIR IFU at the VLT). Using emission-line diagnostics, one can also create maps of metallicity, ionisation, and dust (using the Balmer decrement; Osterbrock 1989). This technique has been used with the VIMOS IFU on the VLT for the nearest GRBs known, such as GRB 980425/SN 1998bw (Christensen et al. 2008) and GRB 060505 (Thöne et al. 2014), and have shown that GRBs appear in the lowest-metallicity regions of their hosts. Follow up observations with the state-of-the-art VLT instrument MUSE (Bacon et al. 2010) have revealed the host of GRB 980425 in exquisite detail, resolving individual H II regions (Krühler et al. 2017). From such highly resolved studies, it is possible to measure the ages of the stellar populations of the H II regions through the equivalent width of the H $\alpha$  line, which relates directly to the mass of the stars and thus can place constraints on the GRB progenitor.

By calculating the metallicity for each spaxel based on the different emission line diagnostics, it is possible to assess their differences in relation to other physical parameters such as ionisation. With the unprecedented resolution of MUSE, Krühler et al. (2017) have shown that the O3N2 diagnostic (Pettini & Pagel 2004) appears to show decreasing metallicity towards the centre of the H II regions, which is physically unexpected. The map instead shows a very strong similarity with that of [S III]/[S II], a good tracer of the ionisation parameter. The result suggests that O3N2 is strongly dependent on ionisation, and may not be a reliable metallicity diagnostic, especially at high spatial resolution. The Dopita et al. (2016) diagnostic appears to be relatively independent of ionisation and shows a weak gradient in the galaxy, as would be expected; there are certainly not the dramatic gradients within the H II regions as seen in O3N2.

### 5.3.2 GRBs as metallicity calibrators

Gamma-ray bursts offer a unique opportunity to compare emission and absorption observations, and in particular metallicity. This is made possible by their transient nature - the afterglow provides the background continuum for absorption-line measurements, and then once it has faded the emission-line measurements can be made. The emission lines originate in star-forming H II regions of the host, and the measured value is typically integrated over the entire galaxy (save for when the galaxy is resolved, and/or observed with an IFU). On the contrary, the absorption measurement probes only one line of sight. However, the line-of-sight absorption is also likely to occur predominantly in and around star-forming regions, as they are the densest in the galaxy. It is therefore believed (see e.g. Friis et al. 2015) that the two measurements should indeed trace very similar values of metallicity, and thus could be good testbeds to cross-calibrate absorption-and emission-line diagnostics. However, reliable absorption-based metallicities are only possible above  $z \gtrsim 1.6$  with ground-based telescopes, while above  $z \gtrsim 2.3$  emission lines are relatively faint and the important [N II] 6584 Å line is not observable due to the brightness of the sky or indeed a blocking filter in the K-band (e.g. on X-shooter). For this reason, along with the difficulty of achieving a high enough quality spectrum to calculate an absorption metallicity, there are only three GRBs to date with metallicities that have been measured from both methods: GRB 120119A, GRB 121024A, and GRB 120815A, which have been plotted in Fig. 5.4. The emission line diagnostics used are N2 (using [N II]/H $\alpha$ ; Pettini & Pagel 2004), O3N2 (using the

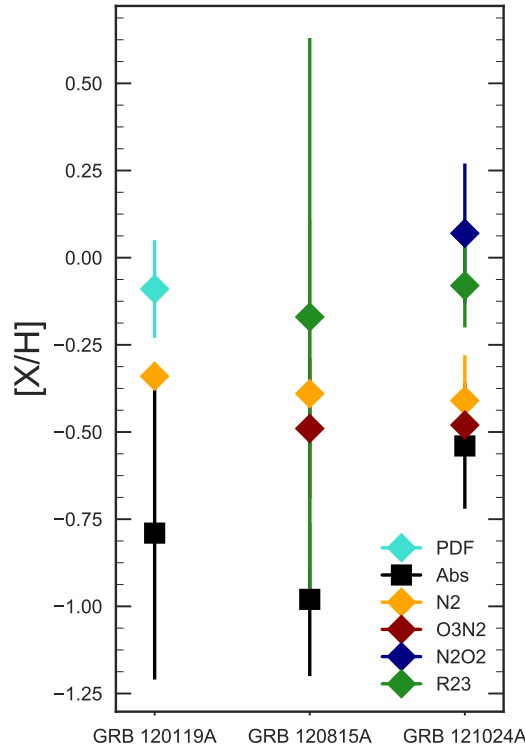


FIGURE 5.4: Metallicities of three GRBs calculated using the emission line diagnostics described in Section 5.3.2 (coloured diamonds) and absorption line method (black squares).

ratio of  $[\text{O III}]/\text{H}\beta$  to  $[\text{N II}]/\text{H}\alpha$ ; Pettini & Pagel 2004), R23 ( $([\text{O II}] + ([\text{O III}]))/\text{H}\beta$ ; e.g. Pagel et al. 1979; Kobulnicky & Kewley 2004), and a probability distribution function (PDF) combining several diagnostics (e.g. Nagao et al. 2006; Maiolino et al. 2008; Krühler et al. 2015). It is clear from the figure that there is no good agreement among the emission line diagnostics, and they are systematically higher than the absorption based value. There is a large uncertainty on the absorption metallicity from GRB 120119A (0.4 dex; Wiseman et al. 2017b) due to low S/N around Ly- $\alpha$  which lies at the end of the spectral range; the scatter on the emission line measurements for GRB 121024A is greater than 0.5 dex, despite Friis et al. (2015) claiming that they are consistent; originally, Krühler et al. (2015) did not report the emission line metallicity for GRB 120815A due to low significance. It is therefore clear that there is not a significant sample on which to cross-calibrate the methods. There remain two hosts that could be added to the sample, the redshifts of which allow both types of measurement, and whose absorption metallicities of  $[\text{M}/\text{H}] > -1$  indicate, via the MZR, that they are not likely to be small and thus too faint. However, observing time has not yet been secured for these targets. Furthermore, launch of the *James Webb Space Telescope* (see Section 6.2) will open up a much larger redshift range for the cross-calibration, and the sample will hopefully increase to a significant size.

# Chapter 6

## Outlook

### 6.1 GRBs, SLSNe and FRBs in similar hosts - implications for the progenitors

Despite intensive SNe and GRB research over the past century and half century respectively, in the last decade a new related class of explosive transient has been discovered - the superluminous supernovae (SLSNe), that are 10-100 times brighter than the ‘standard’ SNe (e.g. Gal-Yam 2012). The reason they were missed is due to observing strategy: previously, SNe searches focused on large, bright, star-forming galaxies, since the CCSNe rate correlates with SFR. SLSNe, on the other hand, tend to occur in small, faint galaxies (e.g. Neill et al. 2011) that were never targeted by such surveys. Instead, SLSNe have been recently detected in significant numbers due to large area, autonomous sky surveys which image the entire sky on a regular basis, such as the Panoramic Survey Telescope And Rapid Response System (Pan-STARRS; Kaiser et al. 2010), the Palomar Transient Factory (PTF; Rau et al. 2009), and La Silla Quest (LSQ; Baltay et al. 2013).

There are three competing theories as to the power source of SLSNe: the ‘central engine’ such as a spinning-down magnetar (e.g. Woosley 2010; Dessart et al. 2012); pair instability (PISNe; e.g. Gal-Yam et al. 2009; Kasen et al. 2011); interaction of the SN ejecta with the circum-stellar medium (CSM; e.g. Chevalier & Irwin 2011; Yan et al. 2015). The nature of the central engine may also vary depending on the class of event: SLSN are also split into types I and II based on the lack or presence of hydrogen respectively. The modelling and fitting of light curves and spectral evolution is critical in the quest to distinguish between the three paradigms (e.g. Chen et al. 2015; Jerkstrand et al. 2017; Inserra et al. 2017), but is also important to study the host galaxies, as has been done for GRBs over the last 20 years. Only very recently have large enough samples of SLSNe host been available in order to draw conclusions about their population.

The general consensus is that SLSNe occur in low-mass, low-metallicity galaxies. The first major sample study by Lunnan et al. (2014) suggested that SLSNe-I occur in similar galaxies to GRBs, thus inferring that the progenitor stars require low metallicity. Similar to GRBs, there is a debate as to the nature and the value of the metallicity cut-off. Lunnan et al. (2014) find the cut to be at  $0.45Z_{\odot}$ ; Perley et al. (2016b) find the rate of SLSN-I to be heavily suppressed for metallicities  $< 0.5Z_{\odot}$ , and Chen et al. (2017a) also argue for a half-solar metallicity threshold. Schulze et al. (2016) suggest that a very high specific star-formation rate ( $sSFR = SFR/M_*$ ) and a very short stellar population lifetime is needed alongside a  $0.4Z_{\odot}$  metallicity cut. The inference of a similar host population would be that GRB and SLSN progenitors require similar conditions, particularly high angular momentum (see e.g. Graham & Fruchter 2017), and could suggest that some GRBs and SLSN might share a magnetar origin, an example being the ultra-long GRB 111209A associated with a luminous SN 2011kl (Greiner et al. 2015b; Kann et al. 2016, 2017). On the other a hand, it has been shown that the combined energy needed to produce a typical, cosmological GRB and an associated supernova cannot be provided by a magnetar

alone (see e.g. Metzger et al. 2015; Cano et al. 2016 for a discussion). Angus et al. (2016) debate the previous notion that GRB and SLSN-I host populations are the same, suggesting that SLSNe hosts are distinctly fainter and less massive. They also suggest that the apparent similarity in metallicity arises from selection effects of obtaining reliable emission-line metallicities from the faint SLSN host population. Leloudas et al. (2015) find that SLSNe-I are often found in extreme emission-line galaxies, that the environments are more extreme than those hosting GRBs and that the SLSNe may explode even sooner than GRBs after a starburst. Future IFU observations of SLSN hosts will greatly enhance our understanding on the progenitors and the environmental conditions that they require (i.e. high sSFR or low metallicity).

A further class of recently discovered transient are the fast radio bursts (FRBs; Lorimer et al. 2007). They are bright bursts of GHz radio emission lasting a few milliseconds, and their dispersion measure (measured burst arrival time as a function of wavelength) suggests an extragalactic origin (see Katz 2016 for a review). In the decade since their discovery, no FRBs were localised well enough to be able to identify a counterpart at other wavelengths, nor a host galaxy. That was until the sub-arcsecond localisation of the repeating FRB 121102 (Chatterjee et al. 2017), consistent with a faint persistent radio source as well as a faint galaxy. Optical observations (Tendulkar et al. 2017; Kokubo et al. 2017; Bassa et al. 2017) have shown that the FRB location aligns with a bright star-forming region in the outskirts of a faint, irregular, low-metallicity host galaxy, similar to those commonly associated with GRBs and SLSNe. This discovery has provided a tangible link between the three classes of transient, raising the possibility that they are all (especially SLSNe and FRBs) powered by the same progenitors: magnetars (e.g. Piro 2016; Metzger et al. 2017). The theory is still speculative, and while the volumetric rates appear to match (Nicholl et al. 2017), the number statistics on FRBs are still very small. Similarly, black holes are still the preferred objects in GRB central engines, and it is by no means clear whether SLSNe are caused by magnetars either. Still, it could be that a sub-class of each of those transients are indeed driven by magnetars. In the coming decade, the introduction of new radio facilities such as the Square Kilometer Array (SKA) is expected to increase the FRB detection rate by orders of magnitude; with statistical samples of host galaxies, it should be possible to place constraints on the progenitor, as well as to search for coincident SNe in order to test the magnetar model even further.

## 6.2 The next decade: entering the LSST/JWST/E-ELT era of explosive transients

The coming decade is an exciting time for astronomy, with several world-leading facilities due to come online with capabilities across the electromagnetic spectrum. Many of these facilities will provide jumps in performance that will be of great use to the GRB host community, as well as those of related fields such as SLSNe.

With a 6.5 m mirror, and without the hindrance of sky lines or turbulence, the range of redshifts for which the emission-line metallicity measurement window overlaps with that for absorption lines will increase significantly with the launch of the *James Webb Space Telescope* (*JWST*), scheduled for 2018. The NIRspec instrument, a low/mid-resolution spectrograph operating in the NIR (0.6-5.3  $\mu\text{m}$ ), will have an IFU operating mode, allowing similar analyses to those facilitated by MUSE (although at much lower spatial resolution) but at the higher redshifts where the bulk of GRB host galaxies lie. With *JWST*, it should be possible to vastly increase the synergy between absorption and emission line studies, GRB hosts therefore playing a crucial role as a “Rosetta Stone” sample on which to calibrate metallicities between the local and distant Universe.

The deep infrared imaging and spectroscopic capabilities of *JWST* will also allow the detection of GRB hosts in general to higher redshifts. It should be possible to verify the redshifts of bursts which until now have those values measured only photometrically, and to detect any changes in the properties of GRB hosts beyond the limits reached by current surveys. The capabilities of *JWST* would also be perfectly complimentary to the proposed *THESEUS* mission, if it is selected to be the European Space Agency (ESA) M5 mission. However, with the M5 launch scheduled for  $\sim 2030$ , the overlap would likely be small, if at all. The mission is designed primarily to detect all GRBs to a redshift of 10, probing deep into the epoch of reionisation. With an on-board NIR instrument, it will be possible to detect high-redshift afterglows within seconds or minutes of the trigger, increasing the completeness of GRB catalogues. With follow-up from another new flagship facility, the European Extremely Large Telescope (E-ELT), GRBs could be used to pinpoint the very stars and galaxies causing the reionisation of the Universe, as well as to push our knowledge of the star-formation history back to much earlier epochs.

Relating to the work in this thesis, the extended use of radio/sub-mm arrays such as the Atacama Large Millimeter/submillimeter Array (ALMA) to follow up GRBs will help place additional constraints on gas and dust masses of hosts, allowing further constraints to be placed on the dust-to-gas and dust-to-metals ratios. With overlap between samples measured by depletion and by thermal emission, useful and necessary calibrations could be calculated and used in a wide range of research topics.

Currently under construction in Chile is the revolutionary Large Synoptic Survey Telescope (LSST). With an 8.4 m primary mirror and a 3.5 square degree field of view, LSST will image the whole sky in multiple optical bands every few nights, providing an extremely deep, high cadence survey. One of the primary outputs will be a vast number of SNe, including a large increase in the number of SLSNe (as many as  $\sim 10^5$ ; LSST Science Collaboration 2009; Scovacicchi et al. 2016). A sample of such size will signify a step-change in the amount of information available from SLSNe, allowing them to be used as drivers of high-redshift astronomy. Such large numbers will allow large number statistics to be used, and subtle differences in properties compared to GRB hosts or the general galaxy population will become apparent. Not only will such a sample allow SLSNe to be used as probes of small, faint galaxies out to high redshifts, or even standard candles, but also for much tighter constraints to be placed on their production mechanism and progenitor stars. The survey may also discover “orphan” afterglows of GRBs: bursts whose prompt emission was not aligned with Earth and thus not detected by energies, but whose jet opening angle becomes wider at later times, allowing the afterglow to be seen. Ghirlanda et al. (2015) suggest orphan GRB rates of  $50 \text{ yr}^{-1}$  may be detectable with LSST (roughly half that of *Swift* GRBs), which may open up a new window into GRB research, allowing refinement of rates and investigation into other selection effects that may be introduced by beaming.



# Bibliography

- Aguirre, A., Schaye, J., Kim, T.-S., et al. 2003, *The Astrophysical Journal*, 602, 38
- Angus, C. R., Levan, A. J., Perley, D. A., et al. 2016, *Monthly Notices of the Royal Astronomical Society*, 458, 84
- Aoyama, S., Hou, K.-C., Shimizu, I., et al. 2017, *Monthly Notices of the Royal Astronomical Society*, 466, 105
- Arabsalmani, M., Moller, P., Fynbo, J. P. U., et al. 2014, *Monthly Notices of the Royal Astronomical Society*, 446, 990
- Arnaud, K. A. 1996, in *Astronomical Data Analysis Software and Systems V*, ed. George H. Jacoby and Jeannette Barnes, Vol. 101 (Astronomical Society of the Pacific (ASP)), 17
- Asplund, M., Grevesse, N., Sauval, A. J., & Scott, P. 2009, *Astrophysics and Space Science*, 47, 481
- Atwood, W. B., Althouse, W., Anderson, B., et al. 2009, *The Astrophysical Journal*, 697, 1071
- Bacon, R., Accardo, M., Adjali, L., et al. 2010, in *Proceedings of the SPIE*, ed. I. S. McLean, S. K. Ramsay, & H. Takami, Vol. 7735, 773508
- Baltay, C., Rabinowitz, D., Hadjiyska, E., et al. 2013, *Publications of the Astronomical Society of the Pacific*, 125, 683
- Barthelmy, S. D., Barbier, L. M., Cummings, J. R., et al. 2005, *Space Science Reviews*, Volume 120, Issue 3-4, pp. 143-164, 120, 143
- Bassa, C. G., Tendulkar, S. P., Adams, E. A. K., et al. 2017, *The Astrophysical Journal*, 843, L8
- Battistini, C. & Bensby, T. 2015, *Astronomy & Astrophysics*, 577, id.A9, 18 pp.
- Bell, E. F., Phleps, S., Somerville, R. S., et al. 2006, *The Astrophysical Journal*, 652, 270
- Berger, E. & Edo. 2011, *New Astronomy Reviews*, 55, 1
- Bernstein, R. A., Burles, S. M., & Prochaska, J. X. 2015, *Publications of the Astronomical Society of Pacific*, 127, 911
- Bernstein, R. A., Freedman, W. L., & Madore, B. F. 2002, *The Astrophysical Journal*, 571, 56
- Bianchi, S. & Ferrara, A. 2005, *Monthly Notices of the Royal Astronomical Society*, 358, 379
- Bohlin, R. C., Savage, B. D., & Drake, J. F. 1978, *The Astrophysical Journal*, 224, 132
- Bouche, N., Lehnert, M. D., Aguirre, A., Peroux, C., & Bergeron, J. 2007, *Monthly Notices of the Royal Astronomical Society*, 378, 525
- Bouché, N., Murphy, M. T., Kacprzak, G. G., et al. 2013, *Science*, 341, 50

- Bournaud, F. 2011, *EAS Publications Series*, 51, 107
- Burrows, D. N., Hill, J. E., Nousek, J. a., et al. 2005, *Space Science Reviews*, 120, 165
- Callegari, S., Mayer, L., Kazantzidis, S., et al. 2009, *The Astrophysical Journal Letters*, 696, L89
- Campana, S., Thone, C. C., Postigo, A. d. U., et al. 2009, *Monthly Notices of the Royal Astronomical Society*, Volume 402, 402, 2429
- Cano, Z., de Ugarte Postigo, A., Pozanenko, A., et al. 2014, *Astronomy & Astrophysics*, 568, A19
- Cano, Z., Johansson Andreas, K. G., & Maeda, K. 2016, *Monthly Notices of the Royal Astronomical Society*, 457, 2761
- Cano, Z., Wang, S.-Q., Dai, Z.-G., & Wu, X.-F. 2017, in *Advances in Astronomy: GRB in the Swift/Fermi Era and Beyond*, Accepted Review in
- Cantalupo, S., Arrigoni-Battaia, F., Prochaska, J. X., Hennawi, J. F., & Madau, P. 2014, *Nature*, 506, 63
- Cardelli, J. A., Clayton, G. C., & Mathis, J. S. 1989, *The Astrophysical Journal*, 345, 245
- Castro-Tirado, A. J., Bremer, M., McBreen, S., et al. 2007, *Astronomy and Astrophysics*, 475, 101
- Cenko, S. B., Kelemen, J., Harrison, F. A., et al. 2009, *The Astrophysical Journal*, 693, 1484
- Cepa, J., Aguiar-Gonzalez, M., Gonzalez-Escalera, V., et al. 2000, in *Society of Photo-Optical Instrumentation Engineers (SPIE) Conference Series*, ed. M. Iye & A. F. M. Moorwood, Vol. 4008, 623
- Chatterjee, S., Law, C. J., Wharton, R. S., et al. 2017, *Nature*, 541, 58
- Chen, B., Dai, X., Kochanek, C. S., & Chartas, G. 2013, arXiv: 1306.0008
- Chen, H.-W. 2011, arXiv: 1110.0487
- Chen, H.-W., Johnson, S. D., Zahedy, F. S., Rauch, M., & Mulchaey, J. S. 2017a, arXiv: 1706.04645
- Chen, H.-W., Perley, D. A., Pollack, L. K., et al. 2009, *The Astrophysical Journal*, 691, 152
- Chen, T.-W., Nicholl, M., Smartt, S. J., et al. 2017b, *Astronomy & Astrophysics*, 602, A9
- Chen, T.-W., Smartt, S. J., Jerkstrand, A., et al. 2015, *MNRAS*, 452, 1567
- Chevalier, R. A. & Irwin, C. M. 2011, *The Astrophysical Journal*, 729, L6
- Chisholm, J., Tremonti, C. A., Leitherer, C., Chen, Y., & Wofford, A. 2016, *Monthly Notices of the Royal Astronomical Society*, 457, 3133
- Christensen, L., Fynbo, J. P. U., Prochaska, J. X., et al. 2011, *The Astrophysical Journal*, 727, 73
- Christensen, L., Hjorth, J., & Gorosabel, J. 2004, *Astronomy and Astrophysics*, 425, 913

- Christensen, L., Vreeswijk, P. M., Sollerman, J., et al. 2008, *Astronomy and Astrophysics*, 490, 45
- Costa, E., Frontera, F., Heise, J., et al. 1997, *Nature*, 387, 783
- Covino, S., Melandri, A., Salvaterra, R., et al. 2013, *Monthly Notices of the Royal Astronomical Society*, Volume 432, Issue 2, p.1231-1244, 432, 1231
- Crighton, N. H. M., Hennawi, J. F., & Prochaska, J. X. 2013, *The Astrophysical Journal Letters*, 776, 18
- Cucchiara, A., Fumagalli, M., Rafelski, M., et al. 2015, *The Astrophysical Journal*, 804, 51
- Dalla Vecchia, C. & Schaye, J. 2008, *Monthly Notices of the Royal Astronomical Society*, 387, 1431
- Dalla Vecchia, C. & Schaye, J. 2012, *Monthly Notices of the Royal Astronomical Society*, 426, 140
- De Cia, A., Ledoux, C., Mattsson, L., et al. 2016, *Astronomy & Astrophysics*, 97, 1
- De Cia, A., Ledoux, C., Savaglio, S., Schady, P., & Vreeswijk, P. M. 2013, *Astronomy & Astrophysics*, 560, A88
- de Ugarte Postigo, A., Fynbo, J. P. U., Thöne, C. C., et al. 2012, *Astronomy & Astrophysics*, 548, A11
- Dekel, A., Birnboim, Y., K., A., et al. 2006, *Monthly Notices of the Royal Astronomical Society*, 368, 2
- D'Elia, V., Campana, S., Covino, S., et al. 2011, *Monthly Notices of the Royal Astronomical Society*, 418, 680
- D'Elia, V., Fynbo, J. P. U., Covino, S., et al. 2010, *Astronomy & Astrophysics*, 523, A36
- D'Elia, V., Fynbo, J. P. U., Goldoni, P., et al. 2014, *Astronomy & Astrophysics*, 564, A38
- Dessart, L., Hillier, D. J., Waldman, R., Livne, E., & Blondin, S. 2012, *Mon. Not. R. Astron. Soc.*, 426, 76
- Dessauges-Zavadsky, M., Prochaska, J. X., D'Odorico, S., Calura, F., & Matteucci, F. 2006, *Astronomy & Astrophysics*, 445, 93
- Dopita, M. A., Kewley, L. J., Heisler, C. A., & Sutherland, R. S. 2000, *The Astrophysical Journal*, 542, 224
- Dopita, M. A., Kewley, L. J., Sutherland, R. S., & Nicholls, D. C. 2016, *Astrophysics and Space Science*, 361, 61
- Draine, B. 2003, *Annual Review of Astronomy and Astrophysics*, 41, 241
- Draine, B. 2009, in *Cosmic Dust - Near and Far*, ed. T. Henning, E. Grün, & J. Steinacker, Vol. 414, 453
- Draine, B. T. 1989, in *IAU Symposium 135, Interstellar Dust*, ed. L. J. Allamandola & A. G. G. M. Tielens (Santa Clara: Cambridge University Press), 313

- Draine, B. T., Dale, D. a., Bendo, G., et al. 2007, *The Astrophysical Journal*, 866
- Draine, B. T. & Salpeter, E. E. 1979a, *The Astrophysical Journal*, 231, 438
- Draine, B. T. & Salpeter, E. E. 1979b, *The Astrophysical Journal*, 231, 77
- Dwek, E. 1998, *Astrophysical Journal* v.501, p.643, 501, 643
- Dwek, E. 2016, *ApJ*, 825, 136, 6 pp
- Edmunds, M. G. & Eales, S. A. 1998, *Monthly Notices of the Royal Astronomical Society*, 299, L29
- Elíasdóttir, Á., Fynbo, J. P. U., Hjorth, J., et al. 2009, *The Astrophysical Journal*, 697, 1725
- Elliott, J., Greiner, J., Khochfar, S., et al. 2012, *Astronomy & Astrophysics*, 539, A113
- Elliott, J., Krühler, T., Greiner, J., et al. 2013, *arXiv*, 1306, 892
- Ellison, S. L., Prochaska, J. X., Hennawi, J., et al. 2010, *Monthly Notices of the Royal Astronomical Society*, 406, 1435
- Evans, I. N. & Dopita, M. A. 1985, *The Astrophysical Journal Supplement Series*, 58, 125
- Evans, P. A., Beardmore, A. P., Page, K. L., et al. 2009, *Monthly Notices of the Royal Astronomical Society*, 397, 1177
- Feldmann, R. 2015, *Monthly Notices of the Royal Astronomical Society*, 449, 3274
- Ferland, G. J., Chatzikos, M., Guzmán, F., et al. 2017, *arXiv:1705.10877*
- Ferrara, A., Viti, S., & Ceccarelli, C. 2016, *Monthly Notices of the Royal Astronomical Society: Letters*, 463, L112
- Ferrero, P., Klose, S., Kann, D. A., et al. 2009, *Astronomy & Astrophysics*, 497, 729
- Filgas, R., Greiner, J., Schady, P., et al. 2012, *A&A*, 546
- Filippenko, A. V. 1997, *Annu. Rev. Astron. Astrophys*, 35, 309
- Finley, H., Bouché, N., Contini, T., et al. 2017, *arXiv: 1701.07843*
- Firmani, C., Ghisellini, G., Ghirlanda, G., & Avila-Reese, V. 2005, *Mon. Not. R. Astron. Soc*, 360, 1
- Fitzpatrick, E. L. & Massa, D. 2007, *The Astrophysical Journal*, 663, 320
- Fox, A. J., Ledoux, C., Petitjean, P., & Srianand, R. 2007, *Astronomy and Astrophysics*, 473, 791
- Fox, A. J., Ledoux, C., Vreeswijk, P. M., Smette, A., & Jaunsen, A. O. 2008, *Astronomy & Astrophysics*, 491, 189
- Fox, A. J., Savage, B. D., Wakker, B. P., et al. 2004, *The Astrophysical Journal*, 602, 738
- Franco, J. & Cox, D. P. 1986, *Astronomical Society of the Pacific*, 98, 1076
- Fraternali, F. & Filippò. 2016, in *Gas Accretion onto Galaxies, Astrophysics and Space Science Library*, eds. A. J. Fox & R. Dave, 2017, published by Springer

- Friis, M. 2015, Phd dissertation, University of Iceland, Reykjavik
- Friis, M., De Cia, A., Krühler, T., et al. 2015, *Monthly Notices of the Royal Astronomical Society*, 451, 167
- Fruchter, A. S., Levan, A. J., Strolger, L., et al. 2006, *Nature*, 441, 463
- Fruchter, A. S., Thorsett, S. E., Metzger, M. R., et al. 1999, *The Astrophysical Journal*, 519, L13
- Fumagalli, M., Cantalupo, S., Dekel, A., et al. 2016, *Monthly Notices of the Royal Astronomical Society*, 462, 1978
- Fumagalli, M., O'Meara, J. M., & Prochaska, J. X. 2011a, *Science*, 334, 1245
- Fumagalli, M., O'Meara, J. M., & Prochaska, J. X. 2011b, *Science*, 334, 1245
- Fumagalli, M., O'Meara, J. M., Prochaska, J. X., & Worseck, G. 2013, *The Astrophysical Journal*, 775, 78
- Fumagalli, M., Prochaska, J. X., Kasen, D., et al. 2011c, *Monthly Notices of the Royal Astronomical Society*, 418, 1796
- Fynbo, J. P. U., Jakobsson, P., Prochaska, J. X., et al. 2009, *The Astrophysical Journal Supplement Series*, 185, 526
- Fynbo, J. P. U., Krühler, T., Leighly, K., et al. 2014, *Astronomy & Astrophysics*, 572, A12
- Fynbo, J. P. U., Ledoux, C., Noterdaeme, P., et al. 2011, *Monthly Notices of the Royal Astronomical Society*, 413, 2481
- Fynbo, J. P. U., Prochaska, J. X., Sommer-Larsen, J., Dessauges-Zavadsky, M., & Moller, P. 2008, *The Astrophysical Journal*, 683, 321
- Fynbo, J. P. U., Starling, R. L. C., Ledoux, C., et al. 2006, *Astronomy and Astrophysics*, 451, L47
- Gal-Yam, A. 2012, *Science*, 337, 927
- Gal-Yam, A., Mazzali, P., Ofek, E. O., et al. 2009, *Nature*, 462, 624
- Galama, T. J., Vreeswijk, P. M., van Paradijs, J., et al. 1998, *Nature*, 395, 670
- Gehrels, N., Chincarini, G., Giommi, P., et al. 2004, *Astrophysical Journal*, 611, 1005
- Genzel, R., Lutz, D., Sturm, E., et al. 1998, *Astrophysical Journal*, 498, 579
- Genzel, R., Schreiber, N. M. F., Übler, H., et al. 2017, *Nature*, 543, 397
- Genzel, R., Tacconi, L. J., Gracia-Carpio, J., et al. 2010, *Monthly Notices of the Royal Astronomical Society*, 407, 2091
- Ghirlanda, G., Salvaterra, R., Campana, S., et al. 2015, *Astronomy & Astrophysics*, 578, A71
- Glidden, A., Cooper, T. J., Cooksey, K. L., et al. 2016, *The Astrophysical Journal*, 833, 270
- Goerdt, T., Dekel, A., Sternberg, A., Gnat, O., & Ceverino, D. 2012, *Monthly Notices of the Royal Astronomical Society*, Volume 424, Issue 3, pp. 2292-2315., 424, 2292

- Goldoni, P., Royer, F., François, P., et al. 2006, *Ground-based and Airborne Instrumentation for Astronomy*. Edited by McLean, 6269, 80
- Goobar, A. 2008, 103
- Gordon, K. D., Clayton, G. C., Misselt, K. A., Landolt, A. U., & Wolff, M. J. 2003, *The Astrophysical Journal*, 594, 279
- Graham, J. F. & Fruchter, A. S. 2015, *The Astrophysical Journal*, 834, 1
- Graham, J. F. & Fruchter, A. S. 2017
- Graham, J. F. & Schady, P. 2016, *The Astrophysical Journal*
- Greiner, J., Bornemann, W., Clemens, C., et al. 2008, *Publications of the Astronomical Society of the Pacific*, 120, 405
- Greiner, J., Fox, D. B., Schady, P., et al. 2015a, *The Astrophysical Journal*, 809, 76
- Greiner, J., Krühler, T., Klose, S., et al. 2011, *Astronomy and Astrophysics*, 526, A30
- Greiner, J., Mazzali, P. a., Kann, D. A., et al. 2015b, *Nature*, 523, 189
- Grimes, J. P., Heckman, T., Aloisi, A., et al. 2009, *The Astrophysical Journal Supplement Series*, 181, 272
- Güver, T. & Özel, F. 2009, *Monthly Notices of the Royal Astronomical Society*, 400, 2050
- Hartoog, O. E., Malesani, D., Fynbo, J. P. U., et al. 2015, *Astronomy & Astrophysics*, 139, 1
- Hartoog, O. E., Wiersema, K., Vreeswijk, P. M., et al. 2013, *Monthly Notices of the Royal Astronomical Society*, Volume 430, Issue 4, p.2739-2754, 430, 2739
- Heckman, T. M., Alexandroff, R. M., Borthakur, S., Overzier, R., & Leitherer, C. 2015, *The Astrophysical Journal*, 809, 147
- Hennawi, J. F., Prochaska, J. X., Cantalupo, S., & Arrigoni-Battaia, F. 2015, *Science*, 348, 779
- Henriques, B., White, S., Thomas, P., et al. 2015, *Monthly Notices of the Royal Astronomical Society*, 451, 2663
- Hjorth, J. & Bloom, J. S. 2012, in Chapter 9 in "Gamma-Ray Bursts", *Cambridge Astrophysics Series 51*, eds. C. Kouveliotou, R. A. M. J. Wijers and S. Woosley, Cambridge University Press (Cambridge), 169–190
- Hjorth, J., Sollerman, J., Møller, P., et al. 2003, *Nature*, 423, 847
- Hunt, L. K., Palazzi, E., Michałowski, M. J., et al. 2014, *Astronomy & Astrophysics*, 565, A112
- Inoue, A. K. 2003, *Publications of the Astronomical Society of Japan*, 55, 901
- Insera, C., Nicholl, M., Chen, T.-W., et al. 2017, *Mon. Not. R. Astron. Soc.*, 000
- Issa, M. R., MacLaren, I., & Wolfendale, A. W. 1990, *Astronomy and Astrophysics*, 236, 237
- Japelj, J., Vergani, S. D., Salvaterra, R., et al. 2016, *A&A*, 590
- Jenkins, E. B. 2009, *The Astrophysical Journal*, 700, 1299

- Jenkins, E. B. & Wallerstein, G. 2017, *The Astrophysical Journal*, 838, 85
- Jerkstrand, A., Smartt, S. J., Inserra, C., et al. 2017, *The Astrophysical Journal*, 835, 13
- Jones, A. P., Tielens, A. G. G. M., & Hollenbach, D. J. 1996, *The Astrophysical Journal*, 469, 740
- Jorgenson, R. A., Murphy, M. T., & Thompson, R. 2013, *Monthly Notices of the Royal Astronomical Society*, 435, 482
- Kaiser, N., Burgett, W., Chambers, K., et al. 2010, in *Ground-based and Airborne Telescopes III*. Edited by Stepp, Larry M.; Gilmozzi, Roberto; Hall, Helen J. *Proceedings of the SPIE, Volume 7733*, article id. 77330E, 14 pp. (2010)., ed. L. M. Stepp, R. Gilmozzi, & H. J. Hall, Vol. 7733, 77330E
- Kajisawa, M., Ichikawa, T., Yoshikawa, T., et al. 2011, *Publications of the Astronomical Society of Japan*, 63, S403
- Kalberla, P. M. W., Burton, W. B., Hartmann, D., et al. 2005, *Astronomy & Astrophysics*, 440, 775
- Kann, D. A., Klose, S., & Zeh, A. 2006, *The Astrophysical Journal*, 641, 993
- Kann, D. A., Klose, S., Zhang, B., et al. 2010, *The Astrophysical Journal*, 720, 1513
- Kann, D. A., Schady, P., E., F. O., et al. 2016, arXiv:1606.06791
- Kann, D. A., Schady, P., E., F. O., et al. 2017, arXiv:1706.00601
- Kasen, D., Woosley, S. E., & Heger, A. 2011, *The Astrophysical Journal*, 734, 102
- Katz, J. I. 2016, *Modern Physics Letters A*, 31, 1630013
- Kelly, P. L. & Kirshner, R. P. 2012, *The Astrophysical Journal*, 759, 107
- Kewley, L. J. & Dopita, M. A. 2002, *The Astrophysical Journal Supplement Series*, 142, 35
- Kewley, L. J. & Ellison, S. L. 2008, *The Astrophysical Journal*, 681, 1183
- Kewley, L. J., Zahid, H. J., Geller, M. J., et al. 2015, *The Astrophysical Journal*, 812, L20
- Kistler, M. D., Yüksel, H., Beacom, J. F., Hopkins, A. M., & Wyithe, J. S. B. 2009, *The Astrophysical Journal*, 705, L104
- Klebesadel, R. W., Strong, I. B., & Olson, R. A. 1973, *The Astrophysical Journal*, 182, L85
- Kobulnicky, H. A. & Kewley, L. J. 2004, *The Astrophysical Journal*, 617, 240
- Kokubo, M., Mitsuda, K., Sugai, H., et al. 2017, arXiv:1705.04693
- Kouveliotou, C., Meegan, C. A., Fishman, G. J., et al. 1993, *The Astrophysical Journal*, 413, L101
- Krogager, J.-K., Fynbo, J. P. U., Heintz, K. E., et al. 2016a, *The Astrophysical Journal*, 832, 49
- Krogager, J.-K., Fynbo, J. P. U., Noterdaeme, P., et al. 2016b, *Monthly Notices of the Royal Astronomical Society*, 455, 2698

- Krühler, T., Kuncarayakti, H., Schady, P., et al. 2017, *Astronomy & Astrophysics*, In Press
- Krühler, T., Küpcü Yoldaş, A., Greiner, J., et al. 2008, *The Astrophysical Journal*, 685, 376
- Krühler, T., Ledoux, C., Fynbo, J. P. U., et al. 2013, *Astronomy & Astrophysics*, 557, A18
- Krühler, T., Malesani, D., Fynbo, J. P. U., et al. 2015, *Astronomy & Astrophysics*, 581, A125
- Lambert, D. L. 1987, *Journal of Astrophysics and Astronomy*, 8, 103
- Larson, R. B. & B., R. 1974, *Monthly Notices of the Royal Astronomical Society*, 169, 229
- Ledoux, C., Petitjean, P., Fynbo, J. P. U., Moller, P., & Srianand, R. 2006a, *Astronomy & Astrophysics*, 457, 71
- Ledoux, C., Petitjean, P., & Srianand, R. 2006b, *The Astrophysical Journal*, 640, L25
- Ledoux, C., Vreeswijk, P. M., Smette, A., et al. 2009, *Astronomy & Astrophysics*, 506, 661
- Lehner, N., Howk, J. C., Tripp, T. M., et al. 2013, *The Astrophysical Journal*, 770, 138
- Lehner, N. & Nicolas. 2016, in *Gas Accretion onto Galaxies*, *Astrophysics and Space Science Library*, eds. A. J. Fox & R. Dave, 2017, published by Springer
- Lehner, N., O’Meara, J. M., Howk, J. C., Prochaska, J. X., & Fumagalli, M. 2016, *The Astrophysical Journal*, 833, 283
- Leloudas, G., Schulze, S., Kruehler, T., et al. 2015, *Monthly Notices of the Royal Astronomical Society*, 449, 917
- Lin, H.-N., Li, X., Wang, S., & Chang, Z. 2015, *Monthly Notices of the Royal Astronomical Society*, 453, 128
- Lopez-Sanchez, A. R. & Esteban, C. 2009, *Astronomy and Astrophysics*, 508, 615
- Lorimer, D. R., Bailes, M., McLaughlin, M. A., Narkevic, D. J., & Crawford, F. 2007, *Science*, 318, 777
- LSST Science Collaboration. 2009, arXiv:0912.0201
- Lunnan, R., Chornock, R., Berger, E., et al. 2014, *The Astrophysical Journal*, 787, 138
- Madau, P. & Dickinson, M. 2014, *Annual Review of Astronomy and Astrophysics*, 52, 415
- Maiolino, R., Nagao, T., Grazian, A., et al. 2008, *Astronomy & Astrophysics*, 488, 463
- Mannucci, F., Salvaterra, R., & Campisi, M. A. 2011, *Monthly Notices of the Royal Astronomical Society*, 414, 1263
- Marino, R. A., Rosales-Ortega, F. F., Sánchez, S. F., et al. 2013, *Astronomy & Astrophysics*, 559, A114
- Martin, C. L. 1999, *The Astrophysical Journal*, 513, 156
- Martin, C. L. 2005, *The Astrophysical Journal*, 621, 227
- Martin, C. L., Shapley, A. E., Coil, A. L., et al. 2012, *The Astrophysical Journal*, 760, 127
- Mathews, W. G. & Baker, J. C. 1971, *The Astrophysical Journal*, 170, 241

- Mattsson, L. 2016, *Planetary and Space Science*, 133, 107
- Mattsson, L., De Cia, A., Andersen, A. C., & Zafar, T. 2014, *Monthly Notices of the Royal Astronomical Society*, 440, 1562
- Mazets, E. P., Golenetskii, S. V., Il'Inskii, V. N., et al. 1981, *Astrophysics and Space Science*, 80, 3
- McKee, C. C. F. & Ostriker, E. C. E. 2007, *Annual Review of Astronomy and Astrophysics*, 45, 565
- McKee, C. F. 1989, *The Astrophysical Journal*, 345, 782
- McKinnon, R., Torrey, P., & Vogelsberger, M. 2016, *Monthly Notices of the Royal Astronomical Society*, 457, 3775
- McLean, I., Steidel, C., Epps, H., et al. 2012, in *Society of Photo-Optical Instrumentation Engineers (SPIE) Conference Series*, Vol. 8446
- McWilliam, A. 1997, *Annual Review of Astronomy and Astrophysics*, 35, 503
- Meegan, C., Lichti, G., Bhat, P. N., et al. 2009, *The Astrophysical Journal*, 702, 791
- Ménard, B. & Fukugita, M. 2012, *The Astrophysical Journal*, 754, 116
- Meszáros, P. & Rees, M. J. 1997, *The Astrophysical Journal*, 476, 232
- Metzger, B. D., Berger, E., Margalit, B., et al. 2017, *The Astrophysical Journal*, 3, 14
- Metzger, B. D., Margalit, B., Kasen, D., & Quataert, E. 2015, *Monthly Notices of the Royal Astronomical Society*, 454, 3311
- Metzger, M. R., Djorgovski, S. G., Kulkarni, S. R., et al. 1997, *Nature*, 387, 878
- Michałowski, M. J., Ceron, J. M. C., Wardlow, J. L., et al. 2016, *Astronomy & Astrophysics*, 595, A72
- Michałowski, M. J., Gentile, G., Hjorth, J., et al. 2015, *Astronomy & Astrophysics*, 582, A78
- Michałowski, M. J., Kamble, A., Hjorth, J., et al. 2012, *The Astrophysical Journal*, 755
- Michałowski, M. J., Watson, D., & Hjorth, J. 2010, *The Astrophysical Journal*, 712, 942
- Mishenina, T., Gorbaneva, T., Pignatari, M., Thielemann, F. K., & Korotin, S. A. 2015, *Monthly Notices of the Royal Astronomical Society*, Volume 454, Issue 2, p.1585-1594, 454, 1585
- Modigliani, A., Goldoni, P., Royer, F., et al. 2010, *Observatory Operations: Strategies*, 7737, 56
- Morgan, A. N., Perley, D. A., Cenko, S. B., et al. 2014, *Monthly Notices of the Royal Astronomical Society*, Volume 440, Issue 2, p.1810-1823, 440, 1810
- Nagao, T., Maiolino, R., & Marconi, A. 2006, *Astronomy & Astrophysics*, 459, 85
- Nakar, E. 2007, *Physics Reports*, 442, 166
- Neill, J. D., Sullivan, M., Gal-Yam, A., et al. 2011, *The Astrophysical Journal*, 727, 15
- Nicholl, M., Williams, P. K. G., Berger, E., et al. 2017, *The Astrophysical Journal*, 843, 84

- Nobili, S. & Goobar, A. 2008, *Astronomy and Astrophysics*, 487, 19
- Oke, J., Cohen, J., Carr, M., et al. 1995, *PASP*, 107, 375
- Osterbrock, D. E. 1989, *Astrophysics of gaseous nebulae and active galactic nuclei* (Mill Valley, CA: University Science Books)
- Paciesas, W. S., Meegan, C. A., Pendleton, G. N., et al. 1999, *THE ASTROPHYSICAL JOURNAL SUPPLEMENT SERIES*, 122, 465
- Page, K. L., Barthelmy, S. D., Burrows, D. N., et al. 2008, *GRB Coordinates Network*, 8080
- Page, K. L., Willingale, R., Bissaldi, E., et al. 2009, *Monthly Notices of the Royal Astronomical Society*, 400, 134
- Pagel, B. E. J., Edmunds, M. G., Blackwell, D. E., Chun, M. S., & Smith, G. 1979, *Monthly Notices of the Royal Astronomical Society*, 189, 95
- Peek, J. E. G., Ménard, B., & Corrales, L. 2015, *The Astrophysical Journal*, 813, 7
- Peeples, M. S., Werk, J. K., Tumlinson, J., et al. 2014, *The Astrophysical Journal*, 786, 54
- Peeters, E., Spoon, H. W. W., & Tielens, A. G. G. M. 2004, *The Astrophysical Journal*, 613, 986
- Pei, Y. C. 1992, *Astrophysical Journal*, 395, 130
- Perley, D. A., Bloom, J. S., Butler, N. R., et al. 2008, *The Astrophysical Journal*, 672, 449
- Perley, D. A., Cenko, S. B., Bloom, J. S., et al. 2009, *The Astronomical Journal*, 138, 1690
- Perley, D. A., Krühler, T., Schulze, S., et al. 2016a, *The Astrophysical Journal*, 817, 7
- Perley, D. A., Krühler, T., Schulze, S., et al. 2015, *The Astrophysical Journal*, 817, 7
- Perley, D. A., Levan, A. J., Tanvir, N. R., et al. 2013, *The Astrophysical Journal*, 778, 128
- Perley, D. A., Modjaz, M., Morgan, A. N., et al. 2012, *The Astrophysical Journal*, 758
- Perley, D. A., Morgan, A. N., Updike, A., et al. 2011, *The Astronomical Journal*, 141, 36
- Perley, D. A., Quimby, R. M., Yan, L., et al. 2016b, *The Astrophysical Journal*, 830, 13
- Perley, D. A., Tanvir, N. R., Hjorth, J., et al. 2016c, *The Astrophysical Journal*, 817, 8
- Perlmutter, S., Aldering, G., Goldhaber, G., et al. 1999, *The Astrophysical Journal*, 517, 565
- Peroux, C., Dessauges-Zavadsky, M., D'Odorico, S., Kim, T.-S., & McMahon, R. G. 2007, *Monthly Notices of the Royal Astronomical Society*, Volume 382, Issue 1, pp. 177-193., 382, 177
- Péroux, C., Kulkarni, V. P., Meiring, J., et al. 2006, *Astronomy & Astrophysics*, 450, 53
- Pettini, M. & Pagel, B. E. J. 2004, *Monthly Notices of the Royal Astronomical Society*, 348, L59
- Pettini, M., Rix, S. A., Steidel, C. C., et al. 2002, *The Astrophysical Journal*, 569, 742
- Phillips, A. P., Gondhalekar, P. M., & Pettini, M. 1982, *Monthly Notices of the Royal Astronomical Society*, 200, 687

- Pieri, M. M., Mortonson, M. J., Frank, S., et al. 2013, *Monthly Notices of the Royal Astronomical Society*, 441, 1718
- Piro, A. L. 2016, *The Astrophysical Journal*, 824, L32
- Planck Collaboration. 2014, *Astronomy & Astrophysics*, 571, A16
- Popping, G., Somerville, R. S., & Galametz, M. 2017, *Monthly Notices of the Royal Astronomical Society*, 471, 3152
- Predehl, P. & Schmitt, J. H. M. M. 1995, *Astronomy and Astrophysics*, 293, 889
- Prochaska, J. X. 2006, *The Astrophysical Journal*, 650, 272
- Prochaska, J. X., Chen, H., & Bloom, J. S. 2006, *The Astrophysical Journal*, 648, 95
- Prochaska, J. X., Chen, H., Bloom, J. S., et al. 2007a, *The Astrophysical Journal Supplement Series*, 168, 231
- Prochaska, J. X., Chen, H., Dessauges-Zavadsky, M., & Bloom, J. S. 2007b, *The Astrophysical Journal*, 666, 267
- Prochaska, J. X., Chen, H., Wolfe, A. M., Dessauges-Zavadsky, M., & Bloom, J. S. 2008a, *The Astrophysical Journal*, 672, 59
- Prochaska, J. X., Dessauges-Zavadsky, M., Ramirez-Ruiz, E., & Chen, H. 2008b, *The Astrophysical Journal*, 685, 344
- Prochaska, J. X., O'Meara, J. M., Fumagalli, M., Bernstein, R. A., & Burles, S. M. 2015, *The Astrophysical Journal Supplement Series*, 221, 2
- Prochaska, J. X., Werk, J. K., Worseck, G., et al. 2017, *The Astrophysical Journal*, 837, 169
- Prochaska, J. X. & Wolfe, A. M. 1998, *The Astrophysical Journal Supplement Series*, 121, 369
- Prochaska, J. X. & Wolfe, A. M. 2002, *THE ASTROPHYSICAL JOURNAL*, 566, 68
- Prochaska, J. X., Wolfe, A. M., Howk, J. C., et al. 2007c, *The Astrophysical Journal Supplement Series*, 171, 29
- Prochter, G. E., Prochaska, J. X., O'Meara, J. M., Burles, S., & Bernstein, R. A. 2010, *The Astrophysical Journal*, 708, 1221
- Quiret, S., Péroux, C., Zafar, T., et al. 2016, *Monthly Notices of the Royal Astronomical Society*, 458, 4074
- Racusin, J. L., Liang, E. W., Burrows, D. N., et al. 2009, *The Astrophysical Journal*, 698, 43
- Rafelski, M., Neeleman, M., Fumagalli, M., Wolfe, A. M., & Prochaska, J. X. 2014, *The Astrophysical Journal Letters*, 782, L29
- Rafelski, M., Wolfe, A. M., Prochaska, J. X., Neeleman, M., & Mendez, A. J. 2012, *The Astrophysical Journal*, 755, 89
- Rau, A., Kulkarni, S. R., Law, N. M., et al. 2009, *Publications of the Astronomical Society of Pacific*, 121, 1334
- Rau, A., Savaglio, S., Krühler, T., et al. 2010, *The Astrophysical Journal*, 720, 862

- Rees, M. J. & Ostriker, J. P. 1977, *Monthly Notices of the Royal Astronomical Society*, 179, 541
- Riess, A. G., Filippenko, A. V., Challis, P., et al. 1998, *The Astronomical Journal*, 116, 1009
- Robaina, A. R., Bell, E. F., Skelton, R. E., et al. 2009, *The Astrophysical Journal*, 704, 324
- Robertson, B. E. & Ellis, R. S. 2012, *The Astrophysical Journal*, 744, 95
- Rodriguez-Gomez, V., Genel, S., Vogelsberger, M., et al. 2015, *Monthly Notices of the Royal Astronomical Society*, 449, 49
- Rol, E., van der Horst, A., Wiersema, K., et al. 2007, *The Astrophysical Journal*, 669, 1098
- Roming, P. W. A., Kennedy, T. E., Mason, K. O., et al. 2005, *Space Science Reviews*, 120, 95
- Roming, P. W. A., Koch, T. S., Oates, S. R., et al. 2009, *The Astrophysical Journal*, 690, 163
- Rubin, K. H. R., Prochaska, J. X., Koo, D. C., & Phillips, A. C. 2012, *The Astrophysical Journal Letters*, 747, 26
- Rubin, K. H. R., Prochaska, J. X., Koo, D. C., et al. 2014, *The Astrophysical Journal*, 794, 156
- Salvaterra, R., Campana, S., Vergani, S. D., et al. 2012, *The Astrophysical Journal*, 749, 68
- Sanders, D. B. & Mirabel, I. F. 1996, *Annual Review of Astronomy and Astrophysics*, 34, 749
- Sanders, D. B., Soifer, B. T., Elias, J. H., et al. 1988, *The Astrophysical Journal*, 325, 74
- Sari, R., Piran, T., & Narayan, R. 1998, *Astrophysical Journal Letters* v.497, 497, L17
- Savage, B. D. & Mathis, J. S. 1979, *Annual Review of Astronomy and Astrophysics*, 17, 73
- Savage, B. D. & Sembach, K. R. 1991, *The Astrophysical Journal*, 379, 245
- Savage, B. D. & Sembach, K. R. 1996, *Annual Review of Astronomy and Astrophysics*, 34, 279
- Savaglio, S. 2001, in *The Extragalactic Infrared Background and its Cosmological Implications IAU Symposium, Vol. 204*, 307
- Savaglio, S. & Fall, S. 2004, *The Astrophysical Journal*, 614, 293
- Savaglio, S., Fall, S. M., & Fiore, F. 2003, *The Astrophysical Journal*, 585, 638
- Savaglio, S., Glazebrook, K., & Le Borgne, D. 2009, *The Astrophysical Journal*, 691, 182
- Savaglio, S., Rau, A., Greiner, J., et al. 2012, *Monthly Notices of the Royal Astronomical Society*, 420, 627
- Schady, P., Dwelly, T., Page, M. J., et al. 2012, *Astronomy & Astrophysics*, 536, A15
- Schady, P., Krühler, T., Greiner, J., et al. 2015, *Astronomy and Astrophysics*, 579
- Schady, P., Mason, K. O., Page, M. J., et al. 2007, *Monthly Notices of the Royal Astronomical Society*, 377, 273
- Schady, P., Page, M. J., Oates, S. R., et al. 2010, *Monthly Notices of the Royal Astronomical Society*, 401, 2773

- Schady, P., Savaglio, S., Krühler, T., Greiner, J., & Rau, A. 2011, *Astronomy & Astrophysics*, 525, 1
- Schaefer, B. E., Gerardy, C. L., Hoflich, P., et al. 2003, *The Astrophysical Journal*, 588, 387
- Schlafly, E. F. & Finkbeiner, D. P. 2011, *The Astrophysical Journal*, 737, 103
- Schlegel, D. J., Finkbeiner, D. P., & Davis, M. 1998, *The Astrophysical Journal*, 500, 525
- Schneider, R., Hunt, L., & Valiante, R. 2016, *Arxiv astroph*, 10, 10
- Schulze, S., Chapman, R., Hjorth, J., et al. 2015, *The Astrophysical Journal*, 808, 73
- Schulze, S., Krühler, T., Leloudas, G., et al. 2016, *arXiv:1612.05978*
- Scovacricchi, D., Nichol, R. C., Bacon, D., Sullivan, M., & Prajs, S. 2016, *MNRAS*, 456, 1700
- Shapley, A. E., Steidel, C. C., Pettini, M., & Adelberger, K. L. 2003, *The Astrophysical Journal*, 588, 65
- Skúladóttir, Á. 2010, Master thesis, Univ. Copenhagen
- Smette, A., Sana, H., Noll, S., et al. 2015, *Astronomy & Astrophysics*, 576, A77
- Sparre, M., Hartoog, O. E., Krühler, T., et al. 2014, *The Astrophysical Journal*, 785, 150
- Spitzer, L. 1978, *Physical Processes in the Interstellar Medium*, ed. L. Spitzer (New York: Wiley-Interscience)
- Starling, R. L. C., Wijers, R. a. M. J., Wiersema, K., et al. 2007, *The Astrophysical Journal*, 661, 787
- Steidel, C. C., Erb, D. K., Shapley, A. E., et al. 2010, *The Astrophysical Journal*, 717, 289
- Steidel, C. C., Rudie, G. C., Strom, A. L., et al. 2014, *The Astrophysical Journal*, 795, 165
- Tanga, M., Schady, P., Gatto, A., et al. 2016, *A&A*, 595
- Tanvir, N. R., Barnard, V. E., Blain, A. W., et al. 2004, *Monthly Notices of the Royal Astronomical Society*, 352, 1073
- Tanvir, N. R., Fox, D. B., Levan, a. J., et al. 2009, *Nature*, 461, 1254
- Tchernyshyov, K., Meixner, M., Seale, J., et al. 2015, *The Astrophysical Journal*, 811, 78
- Tendulkar, S. P., Bassa, C. G., Cordes, J. M., et al. 2017, *The Astrophysical Journal*, 834, L7
- Thöne, C. C., Christensen, L., Prochaska, J. X., et al. 2014, *MNRAS*, 441, 2034
- Thöne, C. C., Fynbo, J. P. U., Goldoni, P., et al. 2013, *Monthly Notices of the Royal Astronomical Society*, 428, 3590
- Tremonti, C. A., Heckman, T. M., Kauffmann, G., et al. 2004, *The Astronomical Journal*, 613, 898
- Trenti, M., Perna, R., Levesque, E. M., Shull, J. M., & Stocke, J. T. 2012, *The Astrophysical Journal*, 749, L38
- Tripp, R. 1998, *Astronomy and Astrophysics*, 331, 815

- Übler, H., Schreiber, N. M. F., Genzel, R., et al. 2017, arXiv:1703.04321
- van Paradijs, J., Groot, P. J., Galama, T., et al. 1997, *Nature*, 386, 686
- Varela, K., van Eerten, H., Greiner, J., et al. 2016, *Astronomy & Astrophysics*, 589, A37
- Vernet, J., Lehnert, M. D., De Breuck, C., et al. 2017, *Astronomy & Astrophysics*, 602, L6
- Viegas, S. M. 1995, *Monthly Notices of the Royal Astronomical Society*, Volume 276, Issue 1, pp. 268-272., 276, 268
- Vladilo, G. 1998, *The Astrophysical Journal*, 493, 583
- Vladilo, G. 2004, *Astronomy and Astrophysics*, 421, 479
- Vladilo, G., Abate, C., Yin, J., Cescutti, G., & Matteucci, F. 2011, *Astronomy & Astrophysics*, 530, A33
- Vladilo, G., Centurión, M., Levshakov, S. A., et al. 2006, *Astronomy and Astrophysics*, 454, 151
- Vogt, S. S., Allen, S. L., Bigelow, B. C., et al. 1994, *Society of Photo-Optical Instrumentation Engineers (SPIE) Conference Series*, 2198, 362
- Vreeswijk, P. M., Ledoux, C., Raassen, A. J. J., et al. 2013, *Astronomy & Astrophysics*, 549, A22
- Vreeswijk, P. M., Ledoux, C., Smette, A., et al. 2007, *A&A*, 468, 83
- Wang, L. 2005, *The Astrophysical Journal*, 635, L33
- Watson, D. 2011, *Astronomy & Astrophysics*, 533, A16
- Watson, D., Christensen, L., Knudsen, K. K., et al. 2015, *Nature*, 519, 327
- Watson, D. J., Fynbo, J. P. U., Ledoux, C., et al. 2006, *The Astrophysical Journal*, 652, 1011
- Weiner, B. J., Coil, A. L., Prochaska, J. X., et al. 2009, *The Astrophysical Journal*, 692, 187
- Werk, J. K., Prochaska, J. X., Cantalupo, S., et al. 2016, *The Astrophysical Journal*, 833, 54
- Werk, J. K., Prochaska, J. X., Thom, C., et al. 2012, *The Astrophysical Journal Supplement Series*, 198, 3
- Wheeler, J. C., Sneden, C., & Truran, James W., J. 1989, *Annual Review of Astronomy and Astrophysics*, 27, 279
- White, S. D. M. & Frenk, C. S. 1991, *The Astrophysical Journal*, 379, 52
- White, S. D. M. & Rees, M. J. 1978, *Monthly Notices of the Royal Astronomical Society*, 183, 341
- Wiseman, P., Perley, D. A., Schady, P., et al. 2017a, *Astronomy & Astrophysics*, Accepted;
- Wiseman, P., Schady, P., Bolmer, J., et al. 2017b, *Astronomy & Astrophysics*, 599, A24
- Wolfe, A. M., Gawiser, E., & Prochaska, J. X. 2005, *Annual Review of Astronomy and Astrophysics*, 43, 861

- Wolfe, A. M., Lanzetta, K. M., Foltz, C. B., & Chaffee, F. H. 1995, *The Astrophysical Journal*, 454, 698
- Wolfe, A. M., Prochaska, J. X., & Gawiser, E. 2003, *The Astrophysical Journal*, 593, 215
- Wolfe, A. M., Turnshek, D. A., Smith, H. E., & Cohen, R. D. 1986, *The Astrophysical Journal Supplement Series*, 61, 249
- Woosley, S. E. 1993, *The Astrophysical Journal*, 405, 273
- Woosley, S. E. 2010, *The Astrophysical Journal*, 719, L204
- Woosley, S. E. & Bloom, J. S. 2006, *Annu. Rev. Astron. Astrophys.*, 44, 507
- Woosley, S. E. & Heger, A. 2006, *The Astrophysical Journal*, 637, 914
- Yamasawa, D., Habe, A., Kozasa, T., et al. 2011, *The Astrophysical Journal*, 735, 44
- Yan, L., Quimby, R., Ofek, E., et al. 2015, *Astrophysical Journal*, 814, 108
- Yates, R. M. & Kauffmann, G. 2014, *MNRAS*, 439, 3817
- Yoon, S.-C. & Langer, N. 2005, *A&A*, 443, 643
- Yüksel, H., Kistler, M. D., Beacom, J. F., & Hopkins, A. M. 2008, *The Astrophysical Journal*, 683, L5
- Zafar, T., Møller, P., Watson, D., et al. 2015, *Astronomy & Astrophysics*, 584, A100
- Zafar, T. & Tayyaba. 2016, *Planetary and Space Science*, 133, 14
- Zafar, T. & Watson, D. 2013, *Astronomy & Astrophysics*, 560, A26
- Zafar, T., Watson, D., Elíasdóttir, Á., et al. 2012, *The Astrophysical Journal*, 753, 82
- Zafar, T., Watson, D., Fynbo, J. P. U., et al. 2011, *Astronomy & Astrophysics*, 532, A143
- Zhukovska, S., Dobbs, C., Jenkins, E. B., & Klessen, R. 2016



## *Acknowledgements*

I would like to acknowledge the help of everyone who has made my time in Munich so fruitful, and who have aided in the smooth and rewarding completion of this project.

First of all I would like to thank my supervisor Patricia. Her door is always open, and I must have knocked an average of three or four times a day for three whole years; for the patience and thoroughness with which she always responded to my questions, ideas, plots and drafts, I am extremely grateful. Similarly, many thanks to Jochen for his ever useful input on the direction of the papers as well as teaching me a lot about GRBs and science in general.

I extend these thanks to the rest of the GROND team, past and present: Thomas, for helping to teach me the entire field of spectroscopy among many other things; Fabian, Julia, and Jan, for putting up with and improving my German skills; Rob, for never quite convincing me that Ronaldo is better than Messi (and everything about galaxies); Mohit, Tassilo, and John, for assisting my first GROND remote shifts and imparting wisdom at all times; Corentin, for showing me how to observe on the mountain; Karla, for teaching me how to dance; Janet, for teaching me everything I know about supernovae; Michael, for being so enthusiastic about the Eisbach, and opening my eyes to statistics; as well as the rest of the MPE high energy group for entertaining lunch and coffee discussions, even if most of them were about Brexit and Trump.

I am grateful for the interesting discussions with other colleagues on the subject of GRBs, DLAs, and dust - the help from Sandra, Tayyaba and Annalisa in my first few months was invaluable in helping me understand what my task was and how to go about it. I am of course very grateful for Dan and his provision of the most beautiful GRB spectrum, and letting me loose on it.

I'd like to thank the IMPRS reps over the years for their help with planning the parties, BBQs, and excursions, and all of the other PhD students in Garching.

Ich bedanke mich beim geilsten Rugby-Club der Welt: StuSta München. Ohne StuSta, wäre meine Zeit in München viel langweiliger gewesen. Da habe ich Deutsch gelernt, da habe ich Spaß gehabt, da habe ich meine beste Freunde kennengelernt. Danke Jethro, dass du mich zur StuSta mitgebracht hast! Einmal StuSta, immer StuSta.

Thank you to all of the friends who made the trip out here from the UK, even if just to use it as free accommodation for Oktoberfest. And thanks especially to my family, who have made it out several times per year and helped me get out of the bubble with every visit.

Finally, I huge thank you to my girlfriend Emileigh, who has listened to my daily rants about my computer, my code, mornings, weather, bike inner tubes, inanimate objects, animate objects, opposition teams' tactics... you name it. You have supported me so well, especially with a non-stop flow of cat videos, and I am so lucky and grateful to have you by my side.